

# Investigation of the thermal conductivity of SiC/SiC cladding before and after irradiation

THÈSE N° 7378 (2017)

PRÉSENTÉE LE 20 JANVIER 2017

À LA FACULTÉ DES SCIENCES ET TECHNIQUES DE L'INGÉNIEUR

INSTITUT DES MATÉRIAUX

PROGRAMME DOCTORAL EN SCIENCE ET GÉNIE DES MATÉRIAUX

ÉCOLE POLYTECHNIQUE FÉDÉRALE DE LAUSANNE

POUR L'OBTENTION DU GRADE DE DOCTEUR ÈS SCIENCES

PAR

Loïc Guillaume FAVE

acceptée sur proposition du jury:

Prof. P. Bowen, président du jury

Prof. C. Hébert, Dr M. A. Pouchon, directeurs de thèse

Prof. P. M. Mummery, rapporteur

Dr D. Staicu, rapporteur

Dr R. Schäublin, rapporteur



ÉCOLE POLYTECHNIQUE  
FÉDÉRALE DE LAUSANNE

Suisse  
2016





# Acknowledgements

This doctoral thesis would not have been possible without the scientific, technical, organisational and personal help of many people. Therefore, I would like to express my gratitude to those who helped me in the present work.

First of all, I am deeply grateful for the support and guidance of my thesis director, Prof. Cécile Hébert. She made it possible for me to get into the world of electron microscopy, and this work would not be what it is without our many discussions and her most valuable input.

I also would like to thank my supervisor, Dr. Manuel Pouchon, for giving me the opportunity to carry out this work in his group and laboratory.

There are many people at PSI who contributed to this work. Most importantly, I am thankful to Dr. Elisabeth Müller, who introduced me to TEM, FIB and overall sample preparation, and to Tomislav Rebac, whose technical expertise and help made the construction and implementation of my experimental apparatus possible. Additionally, I would like to thank my colleagues for their discussions and friendship, especially Ignasi Villacampa Rosés, who coped with me for the last two and a half years, Serafin Knittel, Dr. Cédric Cozzo, Dr. Maria Cabanes Sempere, Dr. Lyubomira Veleva, Vladimir Brankov, Sean Vetsch and Anna Dal Farra, as well as other members of the ANM group and LNM laboratory.

I would like to express my thanks to all the members of CIME for their warm welcome every time I was coming to EPFL to do some microscopy. Particularly, I am thankful to Dr. Duncan Alexander and Dr. Theresa Dennenwaldt for showing me the ropes on the JEOL 2200FS and doing most of the work on the Titan. I am also grateful to Danièle Laub and Colette Vallotton for introducing me to sample preparation techniques.

The CSNSM staff, primarily Dr. Cédric Baumier, are acknowledged for their help with the in-situ experiments at JANNuS, as well as The EMIR network of French accelerators for granting me beamtime.

Funding from the GIF VHTR, the CARAT (DE-NE0000566), the EU Fp7 MaTISSE (EU grant n°604862) and MeAWaT ([ccem.ch/meawat](http://ccem.ch/meawat)) projects made this project possible from a financial standpoint. I am thankful for this support as well as for CEA and Westinghouse contributions, namely supplying samples, thus giving the material needed for my experimental work. Thank

## Acknowledgements

---

you to Dr. Cédric Sauder from CEA, Dr. Edward Lahoda, Dr. Christian Deck and Herbert Feinroth for their contributions, be it supplying samples, giving needed information or engaging in fruitful discussions.

Finally, I would like to thank my family for supporting me through my education, be it during high school, university or, finally, this doctorate, and for always encouraging me to achieve my goals and dreams. Most of all, I want to thank Maude for her love and support during the past years; this thesis would not exist without her help.

*Villigen, September 11<sup>th</sup> 2016*

L. F.

## Abstract

Silicon carbide based composites are candidates for structural components and fuel claddings in nuclear power plants. In the frame of accident tolerant fuel research, the effective through-thickness thermal conductivity of SiC/SiC prototype claddings is investigated. This property, which is both material- and geometry-dependent, has been measured with a custom-made radial heat flow apparatus. Conductivities ranging between 0.5 and  $\sim 4 \text{ W}\cdot\text{m}^{-1}\cdot\text{K}^{-1}$  have been measured at temperatures between the ambient and  $800^\circ\text{C}$ , well below the literature values of 8 to  $15 \text{ W}\cdot\text{m}^{-1}\cdot\text{K}^{-1}$ . This significant difference is due to several factors. Firstly, with the method used here, the components of the conductivity, parallel and perpendicular to the fibre weave, are fully separated. Secondly, the complex multilayered architectures of the tubes are detrimental, acting as barriers against heat transport. Indeed, to be water- and gas-tight, the tubes have to include dense ceramic or metallic layers. The poor adhesion between these and SiC/SiC results in a severely reduced heat transfer. Moreover, the matrix of the composite shows a heterogeneously distributed porosity – about 20 to 45%. This leads to an inhomogeneous thermal conductivity, along both the length and the circumference of the cladding. Although the total porosity should be lessened in future development steps, it currently contributes to the transport of heat through Mie forward scattering of infrared radiation, an effect known as radiation thermal conductivity.

In parallel to these activities, a specific component of SiC/SiC, the pyrolytic carbon interphase, has been investigated using analytical electron microscopy. This work showed that this layer, linking the fibres to the matrix, becomes partially amorphous after irradiation. Ion irradiations evidenced radiation-induced dimensional changes of the said layer, the impact of which would mostly be on the mechanical properties of the composite. Using continuous medium modelling, the effect of a partial amorphisation of the PyC is estimated to lead to a thermal conductivity loss of 20 to 25%. In their current state, SiC/SiC clads do not have a thermal conductivity high enough for them to be used in power plants. Indeed, a thermal conductivity locally as low as  $1 \text{ W}\cdot\text{m}^{-1}\cdot\text{K}^{-1}$  results in fuel temperatures high enough for  $\text{UO}_2$  to reach its melting point.

**Key words:** silicon carbide composites (SiC/SiC), thermal conductivity, radial heat flow, pyrolytic carbon (PyC), amorphisation, energy-filtered transmission electron microscopy (EFTEM), electron spectroscopic imaging (ESI)



## Résumé

Les composites basés sur le carbure de silicium sont actuellement au cœur de la recherche portant sur les combustibles nucléaires résistants aux accidents. Dans le cadre du présent travail, la conductivité thermique effective de prototypes de gaines SiC/SiC a été étudiée. Cette propriété, qui dépend du matériau ainsi que de sa géométrie, a été mesurée au moyen de la technique du flux de chaleur radial. Une conductivité de  $0,5$  à  $4 \text{ W}\cdot\text{m}^{-1}\cdot\text{K}^{-1}$  a été mesurée à des températures comprises entre  $25^\circ\text{C}$  et  $800^\circ\text{C}$ , bien en-deçà des valeurs de la littérature, entre  $8$  et  $15 \text{ W}\cdot\text{m}^{-1}\cdot\text{K}^{-1}$ . Cette grande différence découle de plusieurs facteurs. Tout d'abord, la méthode expérimentale utilisée dans ce travail sépare les composantes de la conductivité, parallèles et perpendiculaires au tissage des fibres, et obtient des valeurs plus basses que celles habituellement obtenues par flash laser. Deuxièmement, la mauvaise adhésion du SiC/SiC sur les couches métalliques ou céramiques, parties nécessaires à l'étanchéité des tubes, contribue à réduire l'efficacité du transport de chaleur. Enfin, le degré de porosité de la matrice est élevé – entre  $20$  et  $45\%$  – et non homogène. Par conséquent, la conductivité thermique des tubes est hétérogène, tant sur la longueur que sur la circonférence de ceux-ci. Bien qu'il soit nécessaire de diminuer la porosité de la matrice, en raison de la diffusion préférentielle du rayonnement infrarouge entre les pores, celle-ci contribue actuellement à la conductivité du SiC/SiC.

Parallèlement à ces activités, un composant particulier du SiC/SiC, l'interface de carbone pyrolytique, a été étudié à l'aide de méthodes de microscopie électronique analytique. Il a été démontré que, du fait de l'endommagement de radiation, ces interfaces deviennent partiellement amorphes. Des irradiations in-situ ont également mis en évidence que, de par l'effet d'un bombardement ionique, ces couches changent de dimensions, ce qui influence les propriétés mécaniques du composite. La théorie des milieux continus a permis d'estimer que l'amorphisation susmentionnée induit une perte de conductivité de  $20$  à  $25\%$ . Dans leur état actuel, les gaines SiC/SiC ne sont pas suffisamment conductrices pour être utilisées dans des centrales. En effet, lorsqu'elles affichent une conductivité de  $1 \text{ W}\cdot\text{m}^{-1}\cdot\text{K}^{-1}$  ou moins, le combustible  $\text{UO}_2$  atteint des températures excédant son point de fusion.

**Mots clefs :** composites carbure de silicium (SiC/SiC), conductivité thermique, flux de chaleur radial, carbone pyrolytique (PyC), microscopie électronique à transmission filtrée en énergie (EFTEM), imagerie par spectroscopie des électrons (ESI)



# Contents

<b>Acknowledgements</b>	<b>i</b>
<b>Abstract</b>	<b>iii</b>
<b>Résumé</b>	<b>v</b>
<b>Table of Contents</b>	<b>vii</b>
<b>List of figures</b>	<b>xi</b>
<b>List of tables</b>	<b>xvii</b>
<b>List of abbreviations</b>	<b>xix</b>
<b>List of symbols</b>	<b>xxiii</b>
<b>Introduction</b>	<b>1</b>
<b>1 Silicon carbide composites</b>	<b>23</b>
1.1 Introduction to silicon carbide . . . . .	24
1.1.1 Basics and properties overview . . . . .	24
1.1.2 Radiation damage in SiC . . . . .	27
1.2 Silicon carbide based composites . . . . .	31
1.3 Architectures of SiC/SiC composites . . . . .	35
1.3.1 SiC fibres . . . . .	36
1.3.2 SiC matrices . . . . .	42
1.3.3 Interphase layers . . . . .	44
1.4 Pyrolytic carbons . . . . .	45
1.5 Samples . . . . .	50
1.5.1 Non-tubular samples . . . . .	50
1.5.2 Prototype cladding tubes . . . . .	52
1.5.3 Summary of samples and measurements . . . . .	55
	<b>vii</b>

## Contents

---

<b>2</b>	<b>Electron Microscopy</b>	<b>57</b>
2.1	Introduction . . . . .	58
2.2	Spectroscopic techniques in the TEM . . . . .	59
2.2.1	Electron scattering . . . . .	60
2.2.2	Magic angle conditions . . . . .	63
2.2.3	Energy-filtered TEM . . . . .	68
2.2.4	Spectrum imaging . . . . .	70
2.2.5	Thickness estimates: log-ratio . . . . .	71
2.2.6	Instrumentation . . . . .	74
2.3	Carbon hybridisation . . . . .	77
2.3.1	Orbital theory . . . . .	77
2.3.2	$sp^2$ to $sp^3$ ratio quantification . . . . .	81
2.4	Experimental . . . . .	84
2.4.1	EFTEM . . . . .	84
2.4.2	STEM-EELS . . . . .	84
2.4.3	JANNuS . . . . .	85
2.5	Data processing . . . . .	88
2.5.1	Drift correction . . . . .	89
2.5.2	Multivariate statistical analysis . . . . .	90
<b>3</b>	<b>Thermal conductivity measurements</b>	<b>93</b>
3.1	Thermal conductivity measurement methods . . . . .	94
3.2	Radial heat flow method . . . . .	94
3.2.1	Basics . . . . .	94
3.2.2	Heat equation . . . . .	96
3.3	Radiosity . . . . .	100
3.3.1	View factors . . . . .	103
3.3.2	Effect of thermocouples . . . . .	112
3.4	Experimental . . . . .	114
3.4.1	Experimental apparatus . . . . .	114
3.4.2	Thermocouple positioning and gluing . . . . .	115
3.4.3	Experimental procedure . . . . .	115
<b>4</b>	<b>Modelling</b>	<b>117</b>
4.1	Introduction . . . . .	118
4.2	Conductivity of a composite tube . . . . .	118
4.3	Modelling of the effective conductivity of SiC/SiC layers . . . . .	120
4.3.1	Effective medium models . . . . .	121
4.3.2	Three cylinders model . . . . .	122
4.3.3	Effect of porosity . . . . .	125



<b>5</b>	<b>Results and discussion</b>	<b>129</b>
5.1	Electron microscopy . . . . .	130
5.1.1	JANNuS results . . . . .	130
5.1.2	EFTEM and STEM-EELS . . . . .	140
5.2	Thermal conductivity . . . . .	145
5.2.1	Steel tube measurement . . . . .	145
5.2.2	SiC/SiC tubes . . . . .	146
5.2.3	Discussion . . . . .	152
5.2.4	Comparison with laser flash . . . . .	152
5.2.5	Radiative thermal conductivity . . . . .	155
5.3	Modelling . . . . .	162
5.3.1	SiC/SiC thermal conductivity . . . . .	162
5.3.2	Application to an actual case . . . . .	163
5.4	Effect of cladding conductivity on fuel temperature . . . . .	165
5.4.1	Thermal analysis of a fuel element . . . . .	165
5.4.2	Fuel pellet temperature profiles . . . . .	169
	<b>Conclusion and perspectives</b>	<b>173</b>
	<b>Appendices</b>	<b>181</b>
<b>A</b>	<b>Thickness maps</b>	<b>183</b>
A.1	GA1 . . . . .	183
A.1.1	Unirradiated material . . . . .	183
A.1.2	Irradiated material . . . . .	185
A.2	GA4 . . . . .	186
A.2.1	Unirradiated material . . . . .	186
A.2.2	Irradiated material . . . . .	187
A.3	GA6 . . . . .	188
A.3.1	Unirradiated material . . . . .	188
A.3.2	Irradiated material . . . . .	189
A.4	GA7 . . . . .	190
A.4.1	Unirradiated material . . . . .	190
A.4.2	Irradiated material . . . . .	191
A.5	GA9 . . . . .	192
A.5.1	Unirradiated material . . . . .	192
A.5.2	Irradiated material . . . . .	193
A.6	A034 . . . . .	194
A.6.1	Unirradiated material . . . . .	194
A.6.2	Irradiated material . . . . .	195

## Contents

---

<b>B EFTEM and STEM-EELS maps</b>	<b>197</b>
B.1 References . . . . .	197
B.1.1 HOPG . . . . .	197
B.1.2 Lacey carbon . . . . .	198
B.2 A034 . . . . .	199
B.2.1 Unirradiated material . . . . .	199
B.2.2 Ion irradiated material . . . . .	200
B.2.3 Neutron irradiated material . . . . .	201
B.3 GA . . . . .	203
B.3.1 Unirradiated material . . . . .	203
B.3.2 Ion irradiated material . . . . .	204
B.4 H1-4 . . . . .	207
<b>Bibliography</b>	<b>209</b>
<b>Curriculum Vitae</b>	<b>231</b>

# List of Figures

1	Manmade greenhouse gas emissions and average yearly temperatures . . . . .	2
2	Plot showing the risk and corresponding consequences of the failure of electricity production technologies. . . . .	3
3	Diagrams of the very-high temperature and gas-cooled fast reactors . . . . .	4
4	Thermal conductivity of SiC . . . . .	7
5	Phonon-phonon scattering . . . . .	11
6	Range of ions in matter . . . . .	17
1.1	Atomic structure and phase diagram of the Si-C system . . . . .	25
1.2	Thermal conductivity of selected materials . . . . .	26
1.3	Microstructural irradiation damage in SiC . . . . .	28
1.4	Swelling in SiC . . . . .	29
1.5	Crack tip bridging mechanism . . . . .	32
1.6	Ashby material selection maps . . . . .	34
1.7	SiC fibres generations . . . . .	39
1.8	Types of multi-directional-dimensional fibre reinforcements . . . . .	41
1.9	Sketch of a 2.5/3D weave . . . . .	42
1.10	SEM micrographs of PyC, (PyC/SiC) <sub>n</sub> and BN interphases . . . . .	44
1.11	Atomistic models of PyC types . . . . .	46
1.12	Thermal conductivity of carbon allotropes . . . . .	47
1.13	Microstructural damages in PyC . . . . .	49
1.14	DLR SiC/SiC . . . . .	51
1.15	Cross-section views of the GA samples . . . . .	52
1.16	Cross-section view of the neutron irradiated GA sample . . . . .	53
1.17	SEM micrographs showing cross-section views of CEA SiC/SiC tubes. . . . .	54
2.1	De Broglie wavelength of electrons . . . . .	58
2.2	Classical representation of electron scattering . . . . .	60
2.3	Densities of State in a solid . . . . .	61
2.4	Example EELS spectrum . . . . .	62
2.5	BN K-edge spectra out of magic angle conditions . . . . .	63

## List of Figures

---

2.6	Magic angle skematic drawing . . . . .	64
2.7	BN K-edge spectra out of magic angle conditions . . . . .	66
2.8	carbon K-edge characteristic angle and electron velocity . . . . .	67
2.9	Demonstration of the MAC on carbon at zero and high tilt . . . . .	68
2.10	Skematic representation of an EFTEM stack . . . . .	69
2.11	Skematic representation of a spectrum image . . . . .	70
2.12	EELS spectrum with intensities $I_0$ and $I_t$ for the log-ratio method . . . . .	72
2.13	Example absolute thickness map . . . . .	73
2.14	Castaing-Henry and Madoline filters . . . . .	74
2.15	Ray diagram of operating $\Omega$ -filter . . . . .	75
2.16	Sketch of a Gatan Image Filter . . . . .	76
2.17	Orbital diagram of the ground state of a carbon atom . . . . .	77
2.18	$1s$ , $2p_x$ , $2p_y$ and $2p_z$ electron orbitals. . . . .	77
2.19	Orbital diagrams of the $sp$ , $sp^2$ and $sp^3$ molecular orbitals of hybridised carbon atoms . . . . .	78
2.20	Sketch of the $sp^2$ hybrid orbital formation . . . . .	79
2.21	Sketch of the $\pi$ hybrid orbital formation . . . . .	79
2.22	Sketch of the $sp^3$ hybrid orbital formation . . . . .	80
2.23	Carbon allotropes K-edge spectra . . . . .	80
2.24	Gaussian fitting method . . . . .	82
2.25	Two windows method . . . . .	83
2.26	TEM at JANNuS . . . . .	86
2.27	Beam coincidence in the TEM at JANNuS . . . . .	86
3.1	Simplified geometry of the experimental setup . . . . .	96
3.2	Heat equation solution geometry . . . . .	97
3.3	Heat map and axial temperature profiles computed by FEM . . . . .	99
3.4	Radiant heat exchange between arbitrary surfaces . . . . .	101
3.5	View factor $F_{AB}$ definition . . . . .	104
3.6	View factors describing the apparatus . . . . .	105
3.7	Geometry of the view factor $F_{14,tot}$ . . . . .	107
3.8	View factor between the hot part of the heating rod and the sample. . . . .	108
3.9	View factors between the sample and cold parts of the heating wire . . . . .	109
3.10	View factor of the inner surface of the sample with itself . . . . .	110
3.11	View factors with the vacuum chamber . . . . .	111
3.12	Thermal resistance across a slab . . . . .	112
3.13	Thermal resistance series at the measurement points . . . . .	113
3.14	CAD render of the apparatus . . . . .	114
3.15	Example of experimental data . . . . .	116
3.16	Example of processed experimental data . . . . .	116

4.1 Thermal resistance of a multilayered composite tube . . . . .	119
4.2 Geometry for the 3 cylinders model . . . . .	123
4.3 Parallel, Maxwell-Eucken and Landauer models . . . . .	127
5.1 dpa maps of the samples irradiated at JANNuS . . . . .	130
5.2 TEM micrographs of the GA1- sample at JANNuS . . . . .	132
5.3 Thickness maps of the sample GA1 before and after irradiation . . . . .	133
5.4 TEM micrographs of the GA4 sample at JANNuS . . . . .	133
5.5 Thickness maps of the sample GA4 before and after irradiation . . . . .	134
5.6 TEM micrographs of the GA6 sample at JANNuS . . . . .	134
5.7 Thickness maps of the sample GA6 before and after irradiation . . . . .	135
5.8 TEM micrographs of the GA9 sample at JANNuS . . . . .	135
5.9 Thickness maps of the sample GA9 before and after irradiation . . . . .	136
5.10 TEM micrographs of the GA7 sample at JANNuS . . . . .	136
5.11 Thickness maps of the sample GA7 before and after irradiation . . . . .	137
5.12 TEM micrographs of the A034 sample at JANNuS . . . . .	137
5.13 Thickness maps of the sample A034 before and after irradiation . . . . .	138
5.14 Changes of the width, thickness and volume of the PyC interphases irradiated at JANNuS . . . . .	138
5.15 Width increases measured on the JANNuS samples . . . . .	139
5.16 R-ratio measurements of the A034 sample . . . . .	141
5.17 R-ratio maps calculated with the TWM method overlaid on EFTEM images acquired on pristine A034 . . . . .	141
5.18 R-ratio maps calculated with the TWM method overlaid on EFTEM and HAADF images acquired on ion irradiated A034 . . . . .	142
5.19 R-ratio maps calculated with the TWM method overlaid on HAADF images acquired on neutron irradiated A034 . . . . .	142
5.20 R-ratio maps calculated with the TWM method overlaid on EFTEM images acquired on pristine GA SiC/SiC . . . . .	143
5.21 R-ratio maps calculated with the TWM method overlaid on EFTEM images acquired on pristine A034 . . . . .	143
5.22 R-ratio maps calculated with the TWM method overlaid on EFTEM and HAADF images acquired on ion irradiated GA SiC/SiC . . . . .	144
5.23 Map and boxplot of the R-ratio calculated with the TWM method overlaid on an HAADF image acquired on neutron irradiated H1-4 SiC/SiC . . . . .	144
5.24 Measured thermal conductivity of 316L tube . . . . .	146
5.25 Measured thermal conductivity of CEA SiC/SiC tubes . . . . .	148
5.26 Measured thermal conductivity of CEA sandwich tubes . . . . .	149
5.27 Measured thermal conductivity of CEA pre-damaged sandwich tubes . . . . .	149
5.28 Measured thermal conductivity of pristine GA/Westinghouse SiC/SiC tubes . .	150

## List of Figures

---

5.29 Measured thermal conductivity of neutron irradiated GA/Westinghouse SiC/SiC tubes . . . . .	151
5.30 Representation surface of the thermal conductivity of an anisotropic material .	153
5.31 2D view of the effective thermal conductivity of a composite with $k_{xx} = k_{yy}$ . .	154
5.32 Wavelength of the IR photons and corresponding refractive index of SiC . . . .	157
5.33 Absorption coefficient of silicon carbide . . . . .	159
5.34 Skematic representation of Rayleigh and Mie scattering . . . . .	160
5.35 Types of porosities found in SiC/SiC composite tubes. . . . .	160
5.36 Dimensionless size parameter of SiC/SiC microstructural features . . . . .	161
5.38 Measured thermal conductivity of CEA sandwich tubes . . . . .	163
5.39 Cross-sectional view of a CEA sandwich cladding, with associated temperature profile . . . . .	164
5.40 Cross-sectional view of a fuel element . . . . .	166
5.41 Flow channel in a fuel assembly . . . . .	169
5.42 Fuel temperature profiles for $\text{UO}_2$ , UN and UC pellets . . . . .	170
5.43 Temperature profiles across claddings with different conductivities . . . . .	170
5.44 Fuel system temperature profiles with different fuels . . . . .	171
7 Carbon K-edge absorption spectrum fitted with four Gaussians . . . . .	178
A.1 Thickness maps and histograms of the unirradiated GA1 lamella . . . . .	183
A.2 Thickness maps and histograms of the unirradiated GA1 lamella . . . . .	184
A.3 Thickness maps and histograms of the ion irradiated GA1 lamella . . . . .	185
A.4 Thickness maps and histograms of the unirradiated GA4 lamella . . . . .	186
A.5 Thickness maps and histograms of the ion irradiated GA4 lamella . . . . .	187
A.6 Thickness maps and histograms of the unirradiated GA6 lamella . . . . .	188
A.7 Thickness maps and histograms of the ion irradiated GA6 lamella . . . . .	189
A.8 Thickness maps and histograms of the unirradiated GA7 lamella . . . . .	190
A.9 Thickness maps and histograms of the ion irradiated GA7 lamella . . . . .	191
A.10 Thickness maps and histograms of the unirradiated GA9 lamella . . . . .	192
A.11 Thickness maps and histograms of the ion irradiated GA9 lamella . . . . .	193
A.12 Thickness maps and histograms of the unirradiated A034 lamella . . . . .	194
A.13 Thickness maps and histograms of the irradiated A034 lamella . . . . .	195
B.1 ESI quantified maps of HOPG . . . . .	197
B.2 ESI quantified maps of Lacey . . . . .	198
B.3 EFTEM and ESI quantified maps of unirradiated A034 . . . . .	199
B.4 EFTEM and ESI quantified maps of ion irradiated A034 . . . . .	200
B.5 EFTEM and ESI quantified maps of neutron irradiated A034 . . . . .	201
B.6 EFTEM and ESI quantified maps of unirradiated GA lamellae . . . . .	203
B.7 EFTEM quantified maps of ion irradiated GA lamellae . . . . .	204

B.8 EFTEM and ESI quantified maps of ion irradiated GA lamellae . . . . .	205
B.9 EFTEM and ESI quantified maps of neutron irradiated A034 . . . . .	206
B.10 EFTEM and ESI quantified maps of neutron irradiated H1-4 lameallae . . . . .	207





# List of Tables

1	Time and energy scales of radiation damage events . . . . .	15
2	Ion and neutron irradiation characteristics . . . . .	19
1.1	Properties of pristine and irradiated SiC composites . . . . .	35
1.2	Properties of SiC fibres . . . . .	38
1.3	GA samples irradiations details . . . . .	54
1.4	Samples studied in the project . . . . .	56
2.1	Parameters to calculate magic angle and operation conditions at the MAC at different voltages . . . . .	67
2.2	Strengths and weaknesses of EFTEM and STEM EELS . . . . .	69
2.3	JANNuS experimental details . . . . .	87
3.1	Summary of the view factors implicated in the radiosity calculations determining the heat fluxes in the experimental rig. . . . .	106
5.1	316L tube dimensions . . . . .	145
5.2	Fit parameters for Equation 5.11 . . . . .	158
5.3	EPR parameters for radial temperature distribution analysis . . . . .	166
5.4	Thermophysical properties of 300°C water at 155 bar . . . . .	169



## List of abbreviations

<b>ANM</b> .....	Advanced Nuclear Materials group
<b>ATF</b> .....	Accident Tolerant Fuel
<b>BWR</b> .....	Boiling Water Reactor
<b>CAD</b> .....	Computer Assisted Design
<b>CARAT</b> .....	Collaboration for Advanced Research on Accident Tolerant fuel
<b>CEA</b> .....	Commissariat à l'Énergie Atomique et aux Énergies Alternatives
<b>CIME</b> .....	Centre Interdisciplinaire de Microscopie Électronique
<b>CMC</b> .....	Ceramic Matrix Composite
<b>CSNSM</b> .....	Centre de Science Nucléaire et de Sciences de la Matière
<b>CTE</b> .....	Coefficient of Thermal Expansion
<b>CVD</b> .....	Chemical Vapour Deposition
<b>CVI</b> .....	Chemical Vapour Infiltration
<b>DDSCS</b> .....	Double Differential Scattering Cross-Section
<b>DLR</b> .....	Deutsches Zentrum für Luft- und Raumfahrt
<b>DM</b> .....	Digital Micrograph
<b>DNB</b> .....	Departure from Nucleate Boiling
<b>DOS</b> .....	Density of States
<b>dpa</b> .....	Displacement per Atom
<b>EDX</b> .....	Energy Dispersive X-ray Spectroscopy

## List of abbreviations

---

<b>EELS</b>	.....	Electron Energy-Loss Spectroscopy
<b>EFTEM</b>	.....	Energy-Filtered Transmission Electron Microscopy
<b>EPR</b>	.....	European/Evolutionary Pressurised Reactor
<b>ESI</b>	.....	Electron Spectroscopic Imaging
<b>FEI</b>	.....	Field Electron and Ion Co.
<b>FEM</b>	.....	Finite Elements Modelling
<b>FIB</b>	.....	Focused Ion Beam
<b>FWHM</b>	.....	Full Width at Half Maximum
<b>GA</b>	.....	General Atomics
<b>GFR</b>	.....	Gas-cooled Fast Reactor
<b>GIF</b>	.....	Gatan Image Filter
<b>HAADF</b>	.....	High-Angle Annular Dark-Field
<b>HNLS</b>	.....	Hi-Nicalon Type S
<b>HOPG</b>	.....	Highly Oriented Pyrolytic Graphite
<b>HTR</b>	.....	High Temperature Reactor
<b>IAEA</b>	.....	International Atomic Energy Agency
<b>IEA</b>	.....	International Energy Agency
<b>IPCC</b>	.....	Intergovernmental Panel on Climate Change
<b>JANNuS</b>	.....	Joint Accelerators for Nano-science and Nuclear Simulation
<b>JEOL</b>	.....	Japan Electron Optics Laboratory
<b>LWR</b>	.....	Light Water Reactor
<b>MAC</b>	.....	Magic Angle Conditions
<b>MatISSE</b>	.....	Materials' Innovations for Safe and Sustainable Nuclear in Europe
<b>MDSC</b>	.....	Modulated Differential Scanning Calorimetry
<b>MOX</b>	.....	Mixed Oxide fuel

<b>MSA</b> .....	Multivariate Statistical Analysis
<b>NRC</b> .....	United States Nuclear Regulatory Commission
<b>PCA</b> .....	Primary Component Analysis
<b>PKA</b> .....	Primary Knocked-on Atom
<b>ppm</b> .....	Parts per million
<b>PSI</b> .....	Paul Scherrer Institut
<b>PWR</b> .....	Pressurized Water Reactor
<b>PyC</b> .....	Pyrolytic Carbon
<b>RSSR</b> .....	Relative Sum of Squared Residuals
<b>SDSD</b> .....	Statistically Determined Spatial Drift
<b>SEM</b> .....	Scanning Electron Microscopy
<b>SRIM</b> .....	Stopping and Range of Ions in Matter
<b>STEM</b> .....	Scanning Transmission Electron Microscopy
<b>SVD</b> .....	Singular Value Decomposition
<b>TC</b> .....	Thermal Conductivity or Thermocouple
<b>TEM</b> .....	Transmission Electron Microscopy
<b>TRIM</b> .....	Transport of Ions in Matter
<b>TWM</b> .....	Two Windows Method
<b>VHTR</b> .....	Very High Temperature Reactor
<b>ZLP</b> .....	Zero-Loss Peak
<b>Zry</b> .....	Zircaloy



# List of symbols

$\alpha$ .....	convergence semi-angle (section 2) or thermal diffusivity (section 3)
$\tilde{\alpha}_0$ .....	Scaled convergence semi-angle
$\beta$ .....	Collection semi-angle
$\gamma$ .....	relativistic factor
$\Gamma$ .....	Gebhart matrix
$\Gamma_{ij}$ .....	Gebhart factor
$\Delta E$ .....	Energy loss
$\varepsilon$ .....	Emissivity
$\theta_B$ .....	Bragg angle
$\theta_e$ .....	Inelastic scattering characteristic angle
$\Theta$ .....	Collection semi-angle
$\tilde{\Theta}$ .....	Scaled collection semi-angle
$\kappa$ .....	Thermal conductivity
$\lambda$ .....	Mean free path
$\mu$ .....	Dynamic viscosity
$\nu$ .....	Porosity fraction
$\rho$ .....	Mass density
$\rho_i$ .....	Absorptance of surface $i$
$\sigma$ .....	Double differential scattering cross-section (page 65)

## List of symbols

---

$\sigma$ .....	Stefan-Boltzmann constant
$\tau$ .....	Characteristic time
$\Phi_e$ .....	radiant heat flux
$\chi$ .....	Neutron inelastic scattering mean energy loss
$\omega$ .....	Frequencies
$\Omega$ .....	Solid angle
$a_0$ .....	Bohr radius
$A$ .....	Atomic mass
$A_i$ .....	area of surface $i$
$c$ .....	Speed of light
$C_p$ .....	Heat capacity
$D_h$ .....	Hydraulic diameter
$E$ .....	Energy
$E_0$ .....	Incident particle (ion, electron or neutron) energy
$E_m$ .....	Material dependent energy in thickness measurements
$F$ .....	Relativistic factor
$F_{ij}$ .....	View factor between surfaces $i$ and $j$
$h$ .....	Heat transfer coefficient
$\hbar$ .....	Reduced Planck constant
$I_t$ .....	Total intensity of EELS spectrum
$I_0$ .....	ZLP intensity of EELS spectrum
$J_e$ .....	Radiosity
$k$ .....	Thermal conductivity
$k_b$ .....	Boltzmann constant
$k_{\text{eff}}$ .....	Effective thermal conductivity



$k_{\text{eq}}$ .....	Equivalent thermal conductivity
$\vec{k}_f$ .....	Electron wave vector after inelastic scattering
$\vec{k}_i$ .....	Electron wave vector before inelastic scattering
$K$ .....	Thermal resistance
$L$ .....	Length
$N_a$ .....	Avogadro's Number
$Nu$ .....	Nusselt number
$Pr$ .....	Prandtl number
$\vec{q}$ .....	Momentum transfer vector
$\dot{q}''$ .....	Heat flux in $\text{W}\cdot\text{m}^2$
$\dot{q}'$ .....	Linear heat rate
$\dot{Q}$ .....	Heat rate
$r$ .....	Radial position, radius
$R$ .....	Thermal resistance
$Re$ .....	Reynolds number
$S_{n,e,r}$ .....	Nuclear, electronic and radiative stopping powers
$S(\vec{q}, E)$ .....	Dynamic form factor
$t$ .....	Thickness
$T$ .....	Temperature
$T_d$ .....	Displacement threshold energy
$U$ .....	Internal energy
$v$ .....	Particle velocity
$V_f$ .....	Volume fraction of fibres
$z$ .....	Axial position (length)
$Z$ .....	Atomic number
$Z_{\text{eff}}$ .....	Effective atomic number



# Introduction

## General Background

Large scale energy production and the consequences thereof on the environment are one – if not the biggest – challenge humanity is facing in the 21<sup>st</sup> century. Since the dawn of the industrial age in the eighteenth century, mankind has been rapidly increasing its needs in energy in all of its forms. This trend is nowhere near ending, with both the IPCC and the IEA projecting an increase of the worldwide consumption by at least a third of what it currently is by 2035 [1]. Global population growth and the rapid economic development of countries such as China, India and Brazil will not slow down before the middle of this century.

Electricity production is responsible for about 40% [2] of the energy-related worldwide CO<sub>2</sub> emissions. The current technologies capable of producing electricity from hundreds of megawatts to gigawatts are all based on the use of fossil fuels, with the exception of hydro power plants<sup>1</sup>. The constant burning of coal, oil and natural gas is having a catastrophic impact on our environment through the release of enormous quantities of greenhouse gases such as CO<sub>2</sub>, which have been steadily increasing the earth temperature for the last two centuries.

Although renewable energy sources like solar, wind, bio-fuels or tidal energy are showing great potential, these technologies are still too young to reach production levels where they would be able to compete or even replace the still much cheaper fossil systems. Furthermore, since most renewable energy are intermittent in their production, their reliability also depends on the availability of electrical energy storage systems such as hydrogen production combined with fuel cells.

---

<sup>1</sup>In reality, hydro power plants such as the Swiss gravity dams also depend on fossil sources to pump the water after it has been turbined.

## Introduction

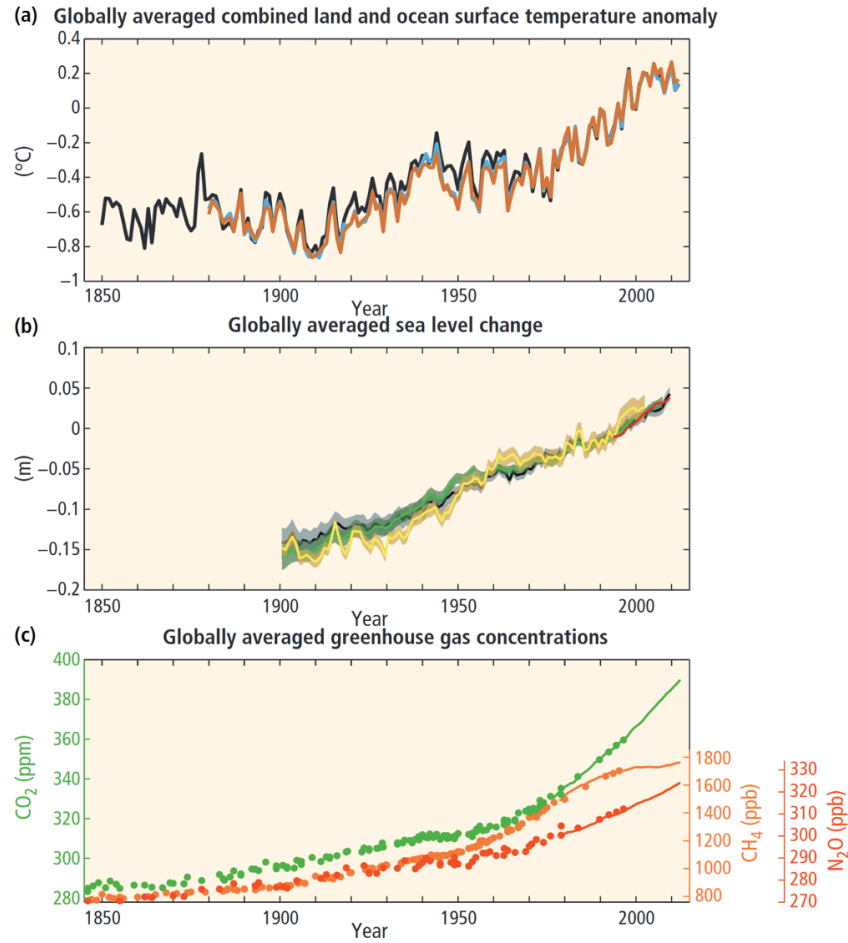


**Figure 1** – Correlation of man-made greenhouse gas emissions and yearly average temperatures over the last 150 years ([3])

In this context, the production of electricity via nuclear fission is a reliable energy source which environmental impact, as far as global warming is concerned, is much less than other fossil fuels. The risk involved in using this technology is undeniable since the consequences of a single nuclear disaster can be much worse than those of any of the other energy production chains.

Figure 2 shows the risks in terms of accident frequency and consequences of various industrial and energy production processes. Though nuclear fission has the lowest accident frequency with probabilities ranging in the  $10^{-4}$  to  $10^{-6}$ , the outcome of a nuclear disaster such as Chernobyl is extreme, with a long-term death toll estimated upwards of ten thousand victims, and the contamination of large territories for the centuries to come. In this regard, nuclear research activities aim at increasing the safety of power plants in many ways. Advances in thermohydraulics guarantee the core coolability. Neutronics assure the constant monitoring of

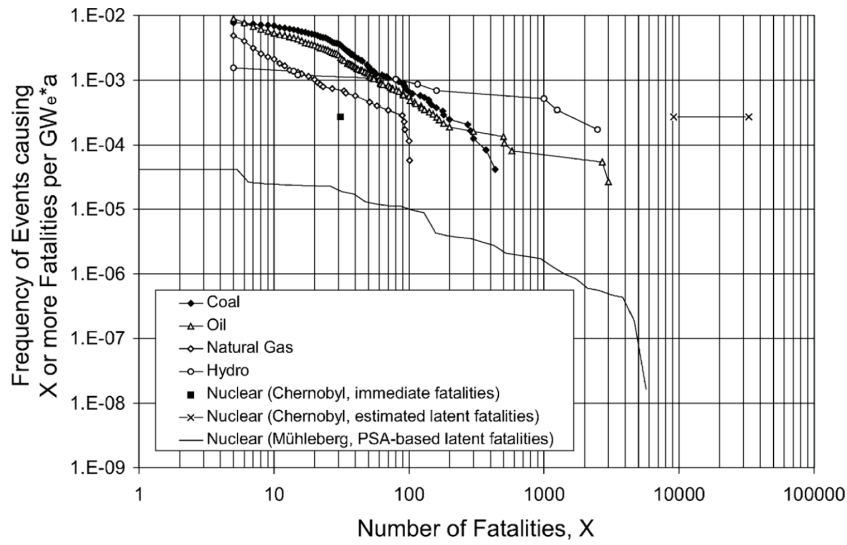


**Figure 2** – Risk-consequence curves of several energy production systems calculated by probabilistic risk assessment [4]

neutron fluxes and core temperatures during operation. Finally, nuclear materials research is focused on the development of materials which safety would be increased compared to those currently in use and on the monitoring of ageing mechanisms of current reactor materials to ensure safe operations.

## Nuclear Context

This work is embedded in research activities towards new structural materials for nuclear applications. The interest in silicon carbide as a nuclear material is twofold. It is considered as potentially applicable in fourth generation (GenIV [5]) reactor designs such as the gas-cooled fast reactor (GFR) or the very high temperature reactor (VHTR). Both designs are helium-cooled systems, with the difference being in the type of neutron spectrum, as well as in the operating temperature of the reactors.

The GFR would be a fast reactor system, by which the use of a more energetic neutron spectrum is meant. The consensus on neutron temperature<sup>2</sup> is that a *fast* neutron has an energy above 1 MeV; a typical fast reactor spectrum has a majority of neutrons with energies in the intermediate (0.3 keV to 1 MeV) and in the fast ranges. In this type of reactors, some structural elements would be made of silicon carbide composites. Since this reactor would operate at a temperature of 850°C, ceramics are a material of choice. On the other hand, the high or very-high temperature reactor (HTR or VHTR) is a thermal reactor, i.e. the neutrons are

<sup>2</sup>In neutronics, the term *temperature* is usually used to refer to the neutron energy.

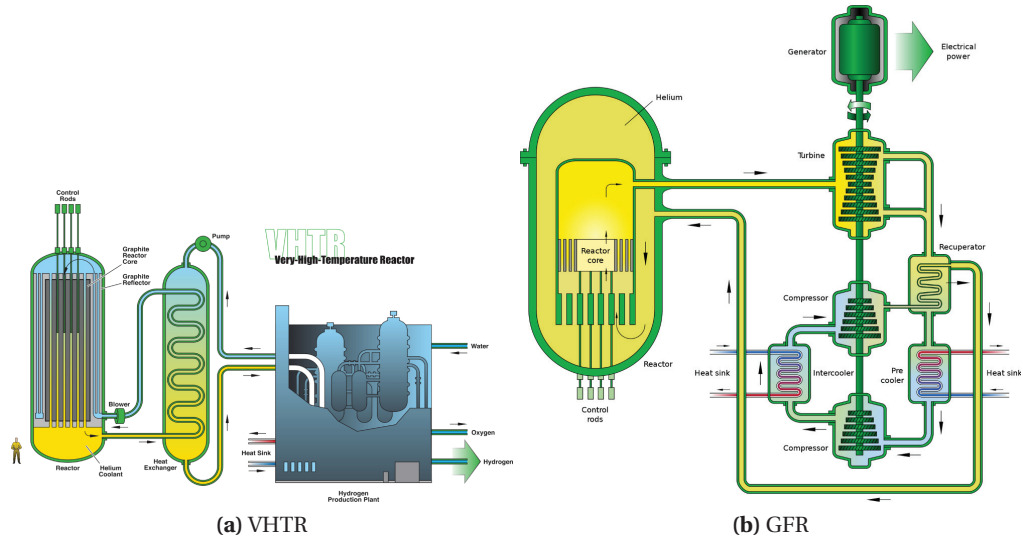


**Figure 3** – Diagrams of the very-high temperature (a) and gas-cooled fast (b) reactors [6, 7]

moderated to thermal energies (0.025 eV). This type of reactor would operate at temperatures above 800°C, potentially up to 1000°C – temperatures at which, once again, ceramics are very interesting structural materials.

In addition, following the Fukushima nuclear accident in 2011 and the recent trend pushing towards the development of accident tolerant fuel systems (ATF), silicon carbide also meets a strong interest in the nuclear community. The motivation for these research and design activities is to develop new systems, be it the fuel itself (silicide, nitride or metallic fuels) or the cladding (SiC/SiC), which would tolerate or potentially be able to cope with accidental conditions such as a loss of coolant accident. Here, the overarching goal is to find ways to give more time, generally called *grace time*, to the operators and emergency response to overcome the accident by restoring cooling to the core, in order to avoid a nuclear disaster.

In this frame, SiC composites are currently at an experimental stage as a replacement to the zirconium-based Zircaloy (Zry) used for light water reactor fuel clads. Zry has a major oxidation issue in high temperature steam: as it oxidises to  $\text{ZrO}_2$ , large amounts of hydrogen are produced. The issue is manifold; firstly, the fuel cladding loses all of its mechanical properties and will inevitably break once oxidised throughout, thus leading to release of molten fuel in the reactor pressure vessel. Secondly, the oxidation reaction is exothermic and escalates as temperature rises. In a loss of coolant accident, both the decay heat of the reactor and the oxidation reaction itself contribute to the elevation of the temperature. Consequently, the oxidation reaction can rapidly run out of control. Lastly, the production of hydrogen

through this reaction is significant. In the absence of hydrogen recombining systems<sup>3</sup>, the amount of H<sub>2</sub> in the reactor containment can reach concentrations high enough to detonate. This is what happened to units 1, 3 and 4 of the Fukushima Daiichi power plant.

The study of the thermal properties of this material over a wide temperature range, and in the shape in which it would be implemented is important for several reasons. First of all, in normal operating conditions, the cladding will face temperatures ranging from 50°C and shall not exceed 1205°C [8] (depending on the phase of the plant operation cycle). Secondly, in accidental conditions, the temperatures which it would have to withstand and at which it must still ensure as much heat transfer as possible easily exceed 1500°C. Indeed, it is well known that coping with the temperature rise accompanied by an uncooled reactor is no trivial task; for a full core, the decay heat emanating from the fuel accounts for several megawatts. Finally, the foreseen operating temperatures of both the GFR and VHTR systems are much higher than what is currently the case in light water reactors. In addition to all of this, the fact that SiC is a ceramic and behaves in a completely different way with respect to radiation damage is a concern. Indeed, contrarily to metallic systems such as Zry, where radiation damage does not significantly influence the thermal conductivity, the thermal conductivity of ceramics strongly suffers from the radiation generated point defects.

## **Materials aspects**

### **Properties**

#### **Thermal properties**

The thermal conductivity of a material is a transport property. It is the proportionality constant linking the rate at which energy flows through a piece of material to the temperature difference between two points along the said flow. The formalism describing the relationship given in Equation 1 was laid out in the early nineteenth century by Fourier [9].

$$k = -\frac{\dot{q}''}{\Delta T} \quad (1)$$

In Equation 1,  $k$  is the thermal conductivity of a material,  $\dot{q}''$  is the heat flux per unit area to which it is subjected and  $\Delta T$  is the resulting temperature drop.

---

<sup>3</sup>These are systems in which H<sub>2</sub> is either burned in a control way or recombined through catalytically enhanced  $\text{H}_2 + 1/2\text{O}_2 \rightarrow \text{H}_2\text{O}$

## Introduction

---

The thermal conductivity of materials depends on their state and generally increases with density, i.e. gases are less conductive than liquids, which in turn are less conductive than solids. The reason for the correlation between density and thermal conductivity is that the denser a material is, the closer from each other its building blocks (atoms or molecules) are. This is particularly true in gases and liquids, where the furthest apart the molecules are, the less they will collide and exchange heat.

In all three common states of matter, the rate of heat transfer is linked to the average velocity of the heat carrier, its mean free path and the specific heat capacity per unit volume of the carrier. In gases, this translates into Equation 2.

$$\kappa = \frac{n \langle v \rangle \lambda c_v}{3N_a} \quad (2)$$

Where  $n$  is the gas number density,  $\langle v \rangle$  the average velocity of the gas molecules,  $\lambda$  their mean free path,  $c_v$  the molar heat capacity of the gas and  $N_a$  Avogadro's number.

## Thermal conductivity

In modern physics, a solid is seen as a lattice of atoms. In metals, the lightly bond electrons are collectively shared in the conduction band, thereby forming an electron *gas*. On the other hand, the electrons of semi- and non-conductors such as ceramics, are more tightly bound to the lattice position of the atom. In either case, the same underlying principle as the one at the basis of the conductivity of gases applies. The difference here is that, since the atoms or molecules making the solid are not mobile like in gases or liquids, the thermal energy carriers are electrons and lattice vibrations. The abundance of free electrons in metals is such that the lattice contribution (phonons) is negligible, whereas most non-metals usually have a large band gap. This means that the phonons are almost the only contributors to heat transport. Therefore, an equation like the one valid for gases can be written:

$$\kappa = \frac{1}{3} C \langle v \rangle \lambda \quad (3)$$

In Equation 3, the terms  $C$ ,  $\langle v \rangle$  and  $\lambda$  account for the same quantities as in Equation 2, namely the specific heat capacity of the heat carrier, its average velocity and the average distance it travels between two collision events, i.e. its mean free path. As mentioned above, the carriers are either free electrons or lattice vibrations. The former are much more efficient at



transporting heat, which is the reason why metals practically always exhibit higher thermal conductivities than the other material classes. Although the electrons of non-conductive materials such as ceramics are not free as in metals, electronic thermal conduction can be observed at elevated temperatures in some of these materials, but is almost absent in SiC.

In ceramics, the thermal conductivity is dictated by the ability of phonons to travel through the crystalline lattice. The energy carried by a phonon in a mode  $n$  is given by Equation 6, and their mean free path  $\lambda$  is discussed later in this section. One often encounters equations where the phonon relaxation time  $\tau$  is used in place of the mean free path  $\lambda = v\tau$ . Hence, Equation 3 is also written as a function of the phonon frequency  $\omega$ :

$$\kappa = \frac{1}{3} C \langle v(\omega) \rangle^2 \tau(\omega) \quad (4)$$

Figure 4 shows collected data on many types of cubic silicon carbide (monocrystalline, polycrystalline, porous, large and small grained SiC) by Snead et al. [10, 11].

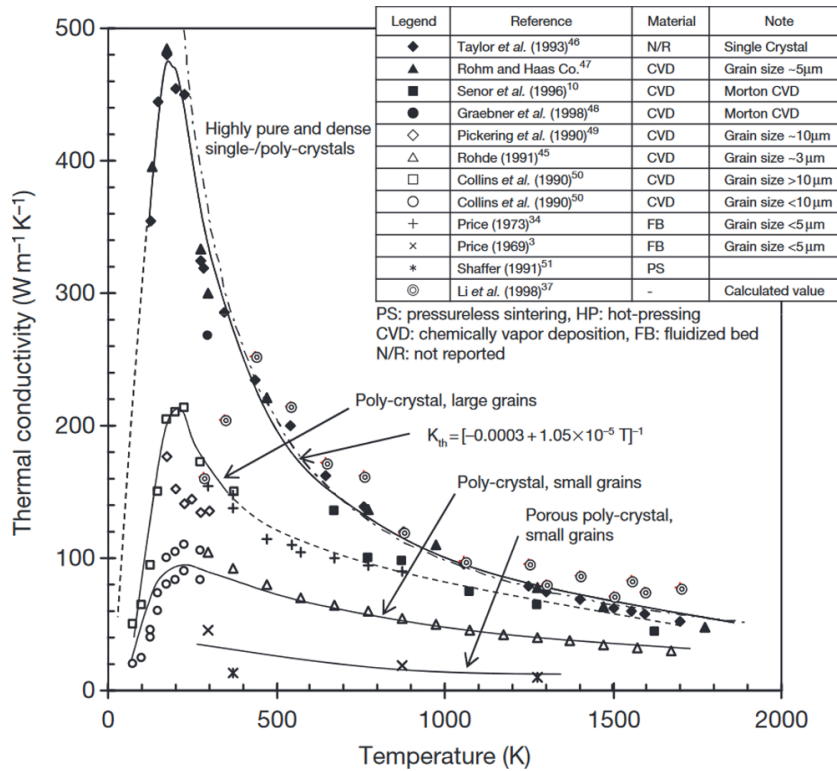


**Figure 4** – Collected thermal conductivity data measured on various grade of 3C silicon carbide. Reproduced from [11]. The original data can be found in [10].

## Introduction

---

### Heat Capacity

The ability of a solid to store and to transport heat are interdependent because both are caused by the same phenomenon, i.e. the number and energy of heat carriers found at a given state. These properties are related through the definition of the thermal diffusivity  $\alpha$ , given in  $\text{m}^2\text{s}^{-1}$ .

$$\alpha = \frac{k}{\rho C_p} \quad (5)$$

Where  $\rho$  is the density,  $k$  the thermal conductivity and  $C_p$  the heat capacity of the material. Linking this expression with the definition given in Equation 4 makes it necessary to discuss the heat capacity of the material. In a solid, the heat capacity tends towards the Dulong-Petit limit [12], which states that the specific heat of a material is given by  $3k_b N_a$ . This law holds at high temperatures, but not as temperature decreases, since the Maxwell-Boltzmann statistics used by Dulong and Petit do not include the necessary quantum treatment required at very low temperatures. The corrections to this model were made by Einstein and Debye in the early twentieth century. In ceramics, the conduction band is practically empty, with a very low density of electrons populating these energy states. As a result, only the lattice vibrations of the crystal can act as a thermal energy carrier to ensure heat transport [13]. Furthermore, electrons do not significantly contribute to the heat capacity of a material. The reason for this is that electrons carrying heat and contributing to thermal transport are close to the Fermi level<sup>4</sup>. For the valence electrons to contribute to the specific heat of the material, they would have to have an additional amount of energy equal to  $k_b T$ . However, since  $E_f \gg k_b$ , there are very few available states close to  $E_f$  which could accommodate such small amounts of energy. Hence, phonons are the mode of energy storage mostly responsible for the heat capacity of materials. The energy carried by such vibrational waves, described as harmonic oscillators, is given by Equation 6.

$$E_n = \left(n + \frac{1}{2}\right) \hbar \omega(k) \quad (6)$$

---

<sup>4</sup>The *Fermi level* is defined as the highest occupied energy state in a given atom at the absolute zero.

Where  $n$  is the excitation number of a particular oscillator associated with a wave vector  $k$ ,  $\hbar$  is the reduced Planck constant and  $\omega$  is the frequency of the oscillation. One can see that this amount of energy is quantised and can be seen as a wave/particle called a *phonon*. Thus, the energy of any vibrational mode  $n$  depends on the probability of having this particular mode, which is given by Planck's distribution:

$$U_n = \int \frac{\hbar\omega}{\exp\left(\frac{\hbar\omega}{k_b T}\right) - 1} d\omega \quad (7)$$

The internal energy of a crystal is then given by summing the integral of Equation 7 over the frequencies for all possible modes.

$$U = \sum_m \int \frac{\hbar\omega}{\exp\left(\frac{\hbar\omega}{k_b T}\right) - 1} D_m(\omega) d\omega \quad (8)$$

Where  $D_m(\omega)$  is the number of phonons in a mode  $m$  with a frequency  $\omega$ , given by Bose-Einstein statistics. The heat capacity is by definition the amount of thermal energy stored per degree, i.e. it is given by the derivative of  $U$  relative to  $T$ .

$$C = \frac{dU}{dT} = k_b \sum_m \frac{x^2 \exp(x)}{[\exp(x) - 1]^2} \text{ with } x = \frac{\hbar\omega}{k_b T} \quad (9)$$

One needs then to express  $D_m(\omega)$  as a function of  $x$  and the famous results of Debye can be derived, i.e. the proportionality of  $C_V$  to  $T^3$  and the departure from this behaviour to a quasi linear temperature dependence above the Debye temperature [14].

### Defects and phonon scattering

In a real solid, the mean free path of phonons is limited not only by the limits of the medium, but also by the presence of imperfections. Indeed, phonons are likely to scatter against each other (N and U processes, see below), as well as against impurities, electrons or boundaries [15,

## Introduction

---

16]. These scattering mechanisms contribute to the decrease of the phonon mean free path or relaxation time, respectively. To account for the individual contributions, Matthiessen's rule is used [16, 17].

$$\frac{1}{\tau(\omega)} = \sum_i \frac{1}{\tau_i(\omega)} \quad (10)$$

These phenomena occur at different phonon frequencies and can thus be separated as individual contributions to the thermal resistance of a given material per their respective strengths. Equation 11 is the common form found in the literature related to the thermal conductivity of ceramics such as SiC [11].

$$\frac{1}{K} = \frac{1}{K_{gb}} + \frac{1}{K_u} + \frac{1}{K_d} \quad (11)$$

### Phonon-phonon interactions

The interaction between two phonons can result in two different outcomes. Depending on whether the sum of two wave vectors  $k_1$  and  $k_2$  stays inside the first Brillouin zone or not, the outgoing phonon  $k_3$  will either conserve the incoming momentum or not. These situations are schematically represented in Figure 5a and 5b, respectively. In the first case, the process is called normal scattering or N-process, whilst the second is known as Umklapp scattering or U-process. In the latter case, the outgoing wave vector  $k'_3$  which is outside of the first Brillouin zone is equivalent to  $k_3$  by mathematically adding a reciprocal lattice vector  $G = \frac{2\pi}{a}$  parallel to the axis  $k_x$ . In either case, the energy is conserved, meaning that  $\omega_1 + \omega_2 = \omega_3$ .

Umklapp scattering is likely to occur at high temperatures, i.e. when it exceeds the Debye temperature of the material. In this case, all phonons modes are excited, since  $k_b T \geq \hbar\omega_{\max}$  and most phonon collisions will result in a change of momentum. In a defect free crystal, the U-process is the driving force behind thermal resistivity at elevated temperatures and is inversely proportional to temperature [15].

### Grain boundary scattering

In polycrystalline solids, grains have a finite size, meaning that an additional limit is imposed on the mean free path of the phonons. In such solids, the apparent mean free path  $\lambda$  in Equation 3 is comparable to the size of the largest grains [18] and increases as temperature decreases. The presence of grain boundaries effectively limits  $\lambda$  to values smaller or equal to

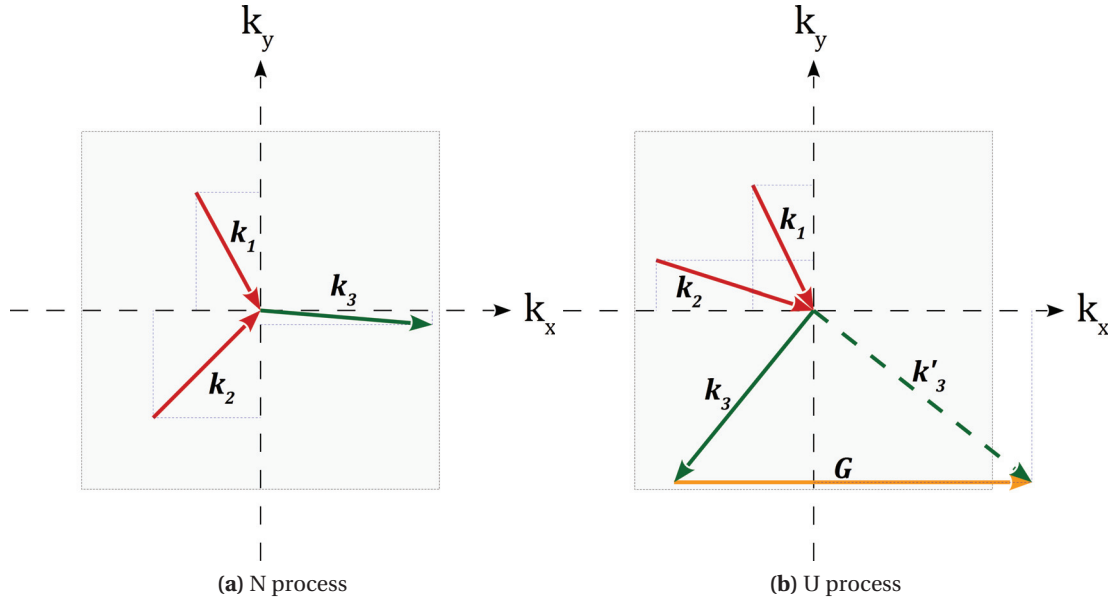


**Figure 5** – Normal (N) and Umklapp (U) phonon scattering. The first Brillouin zone in the phonon  $k$ -space is represented by the grey areas. After a sketch by Kittel [15].

the grain size  $D$ . At intermediate and high temperatures, the intrinsic mean free path  $\lambda_i$  is inversely proportional to the squared frequency  $\omega$ , and the limited mean free path is written according to Equation 12.

$$\lambda = \frac{D\lambda_i(\omega)}{D + \lambda_i(\omega)} \quad (12)$$

From this expression, it appears that grain boundaries influence  $\lambda$  only at the lowest frequencies, and the overall reduction in the mean free path caused by grain boundaries is given by:

$$\delta\lambda_{GB} = \lambda_i \left( \frac{\omega_{GB}}{\omega_D} \right) \arctan \left( \frac{\omega_D}{\omega_{GB}} \right) \quad (13)$$

In Equation 13,  $\omega_D$  stands for the Debye frequency, i.e. the maximum frequency at which the atoms can vibrate and  $\omega_{GB}$  is the frequency at which  $\lambda_i(\omega_{GB}) = D$ . More details concerning different types of grain boundaries and their scattering potential can be found in Klemens [18].

### Defect scattering

Many types of defects are able to influence the thermal conductivity of ceramics by scattering phonons. Each type of crystal defect, starting from the smallest, i.e. vacancies, interstitials and antisite<sup>5</sup> defects to planar defects (dislocation loops) and up to the largest such as vacancy cluster, also known as voids, all affect the mean free path of phonons in different ways. Papers by Walker and Pohl as well as Snead et al. [19, 17] are good sources of information on this particular topic. The discussion below summarises parts of these discussions. For all three types of defect, Equation 13 is used to determine how they impact thermal resistivity. Depending on the case, a particular frequency  $\omega_i$ , where  $i$  stands for vacancies, voids or loops, associated to the relaxation time of the appropriate phonon-defect scattering, is used.

At the temperatures of relevance for the foreseen applications of silicon carbide, antisite defects are mobile enough to diffuse and recombine at favourable locations. Therefore, only vacancies are hindering the lattice vibrations. The relaxation time associated to scattering with vacancies is directly proportional to the density of this type of defects. It is expressed with Equation 14.

$$\frac{1}{\tau_v} = \frac{9C_v\Omega}{4\pi v^3} \quad (14)$$

With  $C_v$  the vacancy concentration and  $\Omega$  the atomic volume. The intrinsic relaxation time is given by  $\frac{1}{\tau_u} = \frac{vT}{aT_m\omega_D^2}\omega^2$ ,  $a$  is related to the lattice spacing and  $T_m$  is the melting temperature. One defines  $\omega_P$ , the frequency at which the intrinsic relaxation time equates that of the point defects. Depending on the magnitude of  $\omega_P$ , two regimes are identified. Firstly, when the scattering due to vacancies is weak, i.e.  $\omega_P > \omega_D$ , the thermal resistivity increase caused by these defects is independent from the temperature and linearly proportional to the concentration of vacancies. The second regime is that of strong vacancy scattering, where  $\omega_P < \omega_D$ . In this case, the vacancy thermal resistance is proportional to the square root of the vacancy density, and comparably to the case of point defects, one defines

$$\frac{1}{\tau_{\text{loop}}} = \frac{24\pi h^2 R^2}{v} n_{\text{loop}} \omega^2$$

---

<sup>5</sup>vacancies are "holes" in the lattice, whereas interstitials are atoms occupying a usually empty locations and antisite defects are substitutional defects, where an atom A of a compound AB occupies a lattice position of atom B, or vice-versa.

with  $h$  and  $R$  being the thickness and radii of the loops and  $n_{loop}$  the loop density. Introducing the associated frequency  $\omega_{loop}$  in Equation 13 lets one obtain an expression where the thermal resistivity caused by scattering against dislocation loops is proportional to their density and the square of their physical characteristics  $h$  and  $R$ . Lastly, the case of extended defects such as voids is similar to that of point defects. Here, the relaxation time  $\tau_E$  is inversely proportional to the defect density and the square of their radii. Again, an associated frequency  $\omega_E$  is found when the phonon frequency is equal to the previously introduced intrinsic relaxation frequency. At any concentration, the mean free path between void scattering events is much greater than the lattice spacing, meaning that  $\omega_E < \omega_D$ , i.e. the scattering caused by extended defect clusters such as voids, is always significant. The strength of this effect on thermal resistivity is proportional to  $N^{1/2}$  as well as  $T^{1/2}$ . These three mechanisms increase the thermal resistivity of the material and explain why the thermal conductivity of ceramics is very sensitive to the presence of defects.

### **Other properties**

Other properties such as chemical stability and mechanical properties are of course of importance in the designing of any engineering material. However, since this work is focused on the thermal properties of silicon carbide-based CMCs, only a few facts regarding these will be discussed here. The case of nuclear fuel cladding is a good illustration of the importance of mechanical properties and their stability. Indeed, these long and thin hollow cylinders are subjected to a large range of loadings. Firstly, the pressure in the primary coolant loop is around 70 to 75 bar in boiling water reactors and about 155 bar in pressurised water reactors. In addition to this, the fuel pins are pressurised with helium at 15.2 bar for thermal transfer purposes, as well as to give a free space for gaseous fission products. As a result, an external hoop stress of around 35 MPa [20] is applied during normal operation, meaning that sufficient tensile properties are required from any potential cladding material. The fuel pin must also be rigid enough to avoid bowing during operation. If this was not the case, deformations along the axis of the pin could lead to the blockage of the cooling channels, with the potential for local dry-out and temperatures rising beyond safety limits. Lastly, the combination of the elevated core temperature and pressure means that creep is often an issue, which can be further enhanced depending on the neutron spectrum. It is then known as irradiation creep, which usually occurs at lower stresses than thermal creep.

### **Degradation mechanisms**

Materials used for in-core structures in a nuclear reactor are submitted to a wide range of degradation mechanisms caused by the extremely harsh environment they are exposed to. Thus, most of their properties degrade over time, be it their mechanical, thermal or chemical

## Introduction

---

characteristics. In most cases, degradation mechanisms act in a synergistic manner, further enhancing the rate at which properties such as the yield strength or the hardness of these materials vary during exposure. A typical example would be the case of *stress-corrosion cracking* (SCC), where irradiation effects such as the introduction of helium in the material or irradiation enhanced diffusion give rise to more pronounced SCC. This phenomenon is called *irradiation assisted stress-corrosion cracking* (IASCC) and is only one of the possible irradiation induced or assisted degradation phenomena occurring in nuclear materials.

## Radiation damage

In nuclear environments, neutrons,  $\alpha$ - and  $\beta^\pm$  particles, fission fragments and  $\gamma$  quanta are produced either through nuclear fission or via nuclear decay. These radiation sources are able to interact and damage materials to a certain extent. Nevertheless, only neutrons are of real relevance as far as structural material are concerned. Indeed, the other particles with a large damaging potential –  $\alpha$  particles and fission products – usually do not reach the fuel cladding since they are stopped either within the fuel itself or in the helium filled gap between the fuel and the clad. Furthermore, if they do reach the cladding, they are stopped in the first micrometres of the tube wall. In any case, mechanisms of radiation damage always start with atomic level displacements. Radiation damage is quantified in terms of *displacement per atom* (dpa), i.e. the number of atomic displacements induced by a single particle integrated over the total number of particles bombarding and atoms in a given sample<sup>6</sup>. In the case of silicon carbide composites, the type of microstructural damage expected to occur is the introduction of point defects such as vacancies and interstitials and amorphisation, i.e. loss of crystallinity. Irradiation induced swelling might also be observable depending on the irradiation conditions.

The basic mechanisms through which a particle will shed its kinetic energy as it travels through a material are either elastic and inelastic scattering or nuclear reactions. Most of the displacement damage results from scattering events, either elastic or not. The first atom struck by the incoming particle is called the *primary knocked-on atom* (PKA), if the energy transferred to this particular atom is higher than a given threshold  $T_d$ , it will be knocked out of its lattice position. In cases like this, a vacancy-interstitial pair, called a *Frenkel pair* is created. The threshold energy  $T_d$  is typically only a few tens of eV. The exact figures depend on the irradiated atom and recommended values can be found in the ASTM norm E521-96 [21]. In a nuclear reactor, the incoming particles have energies ranging from sub-eV to MeV levels. Thus, the PKA often receives enough energy to displace neighbouring atoms in addition to itself. In such occurrences, one speaks then of displacement cascades. Aside from displacement

---

<sup>6</sup>Typical damage levels in Zry cladding ranging between 20 and 40 dpa are reached in 3 to 5 years of in-core exposure.



damage, interactions between an incoming particle and atoms of the irradiated material can lead to ionisation, electron transfer or exchange and finally, nuclear reactions can be triggered by neutrons or highly energetic charged particles.

The sequence over which radiation damage events take place is summarised in Table 1. From the creation of a PKA to the thermalisation of the energy dissipated through the event, many order of magnitudes, in both time and energy scales, are involved.

**Table 1** – Characteristic time and energy scales of radiation damage events. PKA: Primary knocked-on atom, SDA: secondary displaced atom.

Event	Time [s]	Energy carrier	E [eV]
Cascade Creation	$10^{-13}$	Incoming particle	$10^6$
Unstable matrix	$10^{-11}$	PKA	$10^4$
Interstitial diffusion	$10^{-6}$	SDA	$10^2$
Vacancy diffusion	1	Matrix	1
Microstructure evolution	$10^4$	Thermal diffusion	$k_b T$

### Interactions of neutrons and matter

The case of neutrons is particular because of their charge neutrality. Indeed, in the absence of nuclear reactions, neutron – atom interactions can be described as hard sphere collisions. When a neutron scatters inelastically against an atom, the mean logarithmic energy loss is given by Equation 15.

$$\chi = \ln \frac{E_0}{E} = 1 + \frac{(A-1)^2}{2A} \ln \left( \frac{A-1}{A+1} \right) \sim \frac{2}{A+1} \quad (15)$$

Where  $E_0$  and  $E$  are the energy of the neutron before and after the scattering event respectively, and  $A$  the atomic mass of the scattering atom. Thus, when neutrons travel through a silicon carbide target, scattering events will reduce the neutron energy by an average of 15.4% if the struck object is a carbon nucleus, or 6.9% if it scatters against silicon. Considering that the energy of a fission neutron can be as high as 2 MeV, the PKA can have a maximum energy of 300 keV or 138 keV in collisions against carbon or silicon atoms, respectively

The other particularity of neutron interactions with matter is that it can trigger a wide range of nuclear reactions. The mechanisms involved here are following one general trend. First, the neutron can interact with the target atom. The probability of such an event depends on the cross-sections of the reaction involved. Neutron reaction cross-sections practically always

## Introduction

---

depend on the energy of the neutron itself. A very famous example of this is the fission reaction of  $^{235}\text{U}$  which is very likely to occur with thermal neutrons, i.e. at sub-eV neutron energies. As far as irradiation damage is concerned, fission is not a key player, since such reactions will not occur in structural materials. Nevertheless, reactions such as  $(n, \alpha)$ ,  $(n, \gamma)$  and  $(n, \beta^\pm)$  produce particles whose energies are most of the times high enough to create PKAs in the material. Furthermore, reactions yielding  $\alpha$ -particles or protons lead to the production of gases within the material, what has a particularly negative impact on its properties<sup>7</sup>.

### Interactions of charged particles and matter

Interactions between ions and atoms are important in the study of radiation damage. Indeed, ions are very often used to simulate neutron damage because of the technical complications ensuing from the handling of radioactive materials, as well as the time requirements and the high costs that come with neutron irradiations.

The physics behind these interactions has been formalised in 1911 by Rutherford. This formalism uses so-called *interatomic potentials* to model the Coulomb potential in the target's lattice. The interaction of a moving charged particle with the electric field surrounding an atom can be described with the electrostatic forces involved in the collision. Many authors have published different interatomic potentials to describe the interactions of various charged particles and energies. Depending on the mass and energy of the incoming particle, screening effects may have to be accounted for. A detailed discussion of this topic can be found in [22]

A central parameter of any ion irradiation experiment is the range of the said ions in the material. The distance travelled by an energetic particle before it stops is a function of the stopping power of the target. This quantity accounts for the entirety of the mechanisms through which the incoming ion can lose its energy, i.e. elastic and inelastic collisions, interactions with electrons, Bremstrahlung and nuclear reactions. Mathematically, the stopping powers are defined as shown in Equation 16 and take units of  $\text{eV}\cdot\text{nm}^{-1}$ .

$$\left(\frac{dE}{dx}\right) = \left(\frac{dE}{dx}\right)_n + \left(\frac{dE}{dx}\right)_e + \left(\frac{dE}{dx}\right)_r = N(S_n + S_e + S_r) \quad (16)$$

Here, the indices  $n$ ,  $e$  and  $r$  stand for nuclear, electronic and radiative,  $N$  is the number density of the target and the  $S_i$ s are the stopping powers themselves. The first two mechanisms are usually dominating, and the ratio between each other gives an indication as to the nature of

---

<sup>7</sup>This is especially true for the mechanical properties of irradiated materials, where helium bubbles can form and embrittle whole components.

the collisions (pure or screened Coulomb). The accurate modelling of these quantities has been studied at length, and several functions have been proposed for nuclear stopping [22, 23, 24].

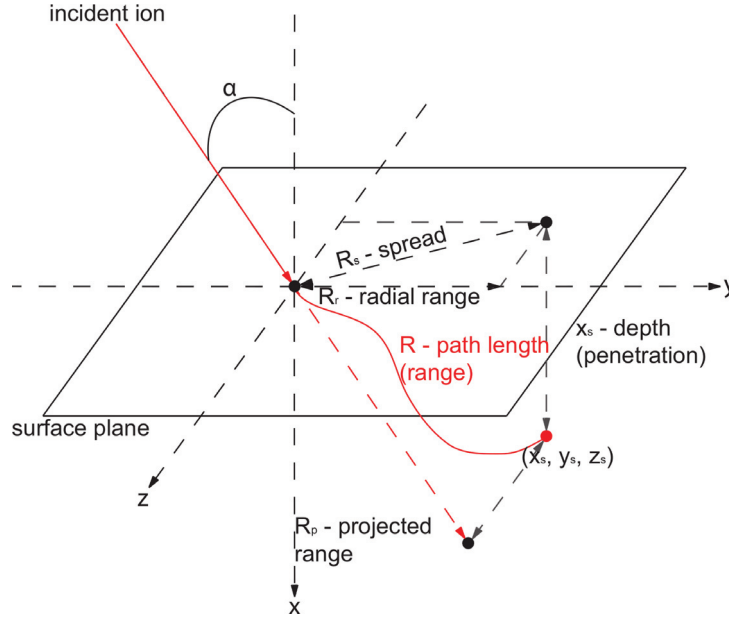


**Figure 6** – Geometry of the penetration of an ion into a target material. After an illustration from Nastasi and Mayer [25].

The result of these considerations is that the average total range of the ion, in nanometres, can be calculated with Equation 17.

$$R = \int_0^x dx = \frac{1}{N} \frac{dE}{S_n(E) + S_e(E)} \quad (17)$$

However, this quantity is not the range perpendicular to the surface of the target,  $R_p$  in Figure 6. The complete derivations leading to the expression given in Equation 18 can be found in Was and Nastasi [22, 25].

$$R_p = \frac{6EM_1(M_1 + M_2)(Z_1^{2/3} + Z_2^{2/3})^{1/2}}{\rho Z_1 Z_2 M_2} \quad (18)$$

## Introduction

---

Where  $E$  is the energy of the incoming particle in keV,  $\rho$  is the target density in gram per cubic centimetre,  $Z_1$ ,  $Z_2$ ,  $M_1$  and  $M_2$  are the atomic numbers and masses of the ion and target, respectively. Was and Nastasi have shown that the function above follows a Gaussian distribution. From this, the implantation of the ion at a given depth  $x$  is given by Equation 19, in  $\text{at}\cdot\text{nm}^{-3}$ .

$$N(x) = N_p \exp \left[ \frac{1}{2} \left( \frac{\Delta R_p}{x - R_p} \right)^2 \right] \quad (19)$$

With  $N_p$  the peak concentration at  $R_p$ , and  $\Delta R_p \sim R_p/2.5$  the standard deviation of the Gaussian distribution. This expression can then be integrated over  $x$  to obtain the implantation per unit area.

## Simulation of neutron damage with ions

Ions are widely used to simulate radiation damage caused by neutrons because of several factors such as the easiness of handling, the limited number of neutron sources and the short irradiation times.

The first reason follows from the fact that neutrons transmute the target material because of neutron capture processes. Therefore, neutron irradiated samples are often activated, thus requiring careful handling and use of adapted facilities such as closed hoods or hot cells. Little activation arises from ion irradiations, which makes the post-irradiation analysis much easier to carry out. Nevertheless, since the irradiated material does not undergo transmutation, the influence of new foreign atoms in the target is absent and effects may be missed. The second factor mentioned above, is the limited number of neutron sources available for research. Whilst nuclear power stations are found in many countries, inserting test rods or capsules, in a commercial reactor is difficult and requires a very lengthy commissioning process of the experimental apparatus. Finally, even using research reactors, the time required to reach damage levels worth investigating is often a deciding factor. Indeed, the time needed to reach a single dpa in a thermal neutron flux is about a year whereas this can be achieved within hours of ion irradiation.

These three factors are the main reasons for which ion irradiation is often used in the first stages of radiation phenomena studies. A summary of the main advantages and disadvantages of the different modes of irradiation available in nuclear material research is shown in Table 2.

**Table 2** – Summary of the most important characteristics of irradiation experiments using neutrons, light ions and heavy ions. From the book of Gary S. Was [22].

Advantages	Disadvantages
<b>Neutrons</b>	
<ul style="list-style-type: none"> <li>• Real damage data</li> <li>• Displacement cascades</li> <li>• Transmutation</li> </ul>	<ul style="list-style-type: none"> <li>• Very long irradiation time</li> <li>• High sample activation</li> <li>• Scarcity of sources</li> <li>• Costs</li> </ul>
<b>Light ions</b>	
<ul style="list-style-type: none"> <li>• Moderate dose rates</li> <li>• Reasonable irradiation time</li> <li>• Good penetration depth</li> </ul>	<ul style="list-style-type: none"> <li>• Implantation</li> <li>• Minor cascades</li> <li>• No transmutation</li> </ul>
<b>Heavy ions</b>	
<ul style="list-style-type: none"> <li>• High dose rates</li> <li>• Short irradiation time</li> <li>• Displacement cascades</li> <li>• No activation</li> </ul>	<ul style="list-style-type: none"> <li>• Very small penetration</li> <li>• No transmutation</li> <li>• High implantation</li> <li>• High dpa rate (annealing)</li> </ul>

A critical question following from the differences between ion and neutron irradiation is that of the representativeness of such experiments. Like most damage mechanisms of materials, knowledge of the initial and final states of a material is not sufficient; more often than not, the damaging process history has to be known as well. The same is true with radiation damage, where, although many processes such as swelling mostly depend on the dose, the rate at which the damage is introduced often plays a role. Therefore, irradiation experiments must be planned carefully in order to make sure that they actually make sense. The ASTM norm E521-96 is a good starting point in the preparation of experimental work using ion beams [21].

### Computer simulations of ion irradiations

Simulating the experiment prior to any practical work is always amongst the first steps of radiation damage studies using ions. For this, the software SRIM (Stopping and Range of Ions in Matter) is very often used to carry out TRIM<sup>8</sup> calculations. In these calculations, the interaction

<sup>8</sup>TRIM stands for *TR*ansport of *I*ons and *M*atter

## Introduction

---

between ions and a chosen target is simulated with the Monte Carlo approach. SRIM simulates collisions with screened Coulomb collisions, including exchange and correlation interactions between the overlapping electronic shells [26, 24]. The algorithm considers that the ion jumps from one collision to another and averages the collision results over the gap that separates these collisions. Long range interactions by electron excitation and plasmons in the target material are also included by considering the target collective electronic and interatomic bond structures. In order to simulate future irradiations and their resulting damage, the SRIM input should be set up with '*Detailed calculation and full damage cascades*'. This option follows every recoiling atom until its remaining energy is lower than the energy required to displace any of the target atoms. Thus, all collisional damage is accounted for and fully analysed. The physics behind the creation of vacancies is modelled as being the sum of the created interstitials and of the atoms leaving the target volume. The collision cascades resulting from the knock-on of incident atoms or ions, having a mass  $Z_1$  and an energy  $E_0$  with target atoms of mass  $Z_2$ , are calculated with the following scheme:

- All target atomic species are attributed a displacement energy  $E_d$ , a binding energy to their lattice position  $E_b$ , and the final energy below which an atom struck by the ion does not move from its lattice position  $E_f$ .
- After a collision, the incoming atom  $Z_1$  has an energy  $E_1$  and the struck atom  $Z_2$  has an energy  $E_2$ .
- Displacements occur in cases where  $E_2 > E_d$ . A vacancy is however not necessarily created in this case: the creation of a vacancy requires both  $E_1 > E_d$  and  $E_2 > E_d$ , i.e. both atoms have enough energy to leave the location where the collision occurred.
- In cases where  $E_1 < E_d$  and  $E_2 > E_d$ , either  $Z_1 = Z_2$  or  $Z_1 \neq Z_2$ , i.e. the incident atom is identical or different from its target. In the first case, the collision is called a replacement collision, and the incident atom remaining energy  $E_1$  is dissipated in the form of thermal energy through phonons. In the second case,  $Z_1$  is stopped as an impurity.
- The last possible case is that  $E_1 < E_d$  and  $E_2 < E_d$ , in which case  $Z_1$  becomes an interstitial, and the remaining energy  $E_1 + E_2$  is released as phonons.

SRIM is a very handy tool where the user can simulate irradiations of mono- or multilayers with given compositions. The energy and atomic species as well as the incidence of the ion beam are adjustable at will. In this work, it has been used in the planning and post-processing of ion beam irradiations carried out at the JANNuS facility in Orsay, France (see page 85).

### Other degradation mechanisms

Similarly to non-thermal properties, other degradation mechanisms are only shortly discussed here through three examples of either pure mechanical damage or issues arising from the combination of high temperatures, corrosion effects and mechanical loadings.

The rather high temperatures found in light water reactors are not a predominant damage mechanism for in-core and structural materials. Nevertheless, creep shall be mentioned because of the elevated temperature. The external pressure applied onto the cladding is about 15 MPa [27], which is sufficient to induce an inwards strain in the cladding tube. A fuel pin is under a complex combination of mechanical loadings, some of which can lead to severe degradation and potential failure. Because of the high flow rate of the cooling water<sup>9</sup>, the fuel pins are subjected to vibrations. Since they are held in position in the bundle with spacer grids – in part to avoid bowing –, they experience abrasion at these locations. The pins must thus be made with materials able to cope with this type of high cycle interaction.

Mechanical damage can also be caused by the interaction between fuel pellets and the cladding, which can suffice to bring the cladding to failure. This phenomenon is called *pellet-cladding mechanical interaction* (PCMI). The cause of PCMI is on one side the inwards creep of the clad, and on the other the thermal expansion and fission gas swelling of the fuel pellet. The combination of both these effects can lead to a closure of the 50 to 200  $\mu\text{m}$  wide helium gap [27], see Figure 5.40, separating these components of the fuel system. This typically occurs during power ramping after low-power periods and is more prone to happen in boiling than in pressurised water reactors since the reactivity control of the former via control rods is less smooth than in the latter, where boric acid plays this role. If the stresses applied at the contact point between fuel and cladding become high enough, the cladding may crack and even burst. Corrosion from the coolant, and especially via the free radicals created by radiolysis of the water, are an issue for the coolant facing side of structural materials. The controlled water chemistry of the reactor, as well as the pre-oxidation of the surfaces of some components, are measures taken to mitigate overall corrosion of core internals. Nevertheless, corrosion is often part of the reason why components fail in a reactor. As is the case of the high temperatures, it is the combination of several factors which lead to conditions where design limits are exceeded.

An example of such conditions is the *pellet-cladding interaction* (PCI) phenomenon. Contrarily to PCMI, where the local mechanical loading between fuel and cladding might lead to failure, PCI includes the presence of stress-corrosion cracking agents such as iodine, caesium or cadmium. In this case, a crack appears at stress levels well below the expected limits because

---

<sup>9</sup>Typically about 20 tons per second, i.e.  $\sim 5 \text{ m}\cdot\text{s}^{-1}$

## **Introduction**

---

I, Cs or Cd [28], which have diffused into the inner side of the cladding locally, lower the mechanical properties of Zry. Like PCMI, this failure mechanism usually occurs during power ramping or in short power transients during operations.



# **1 Silicon carbide composites**

In this first chapter, the materials studied in this thesis, silicon carbide, as well as the ceramic matrix composites based on this carbide are introduced. The discussion then moves on to the characteristics of SiC fibres and matrices, before discussing the pyrolytic carbon interphases at the core of this work. Finally, the different samples studied in this PhD work are introduced.

### 1.1 Introduction to silicon carbide

Silicon carbide is a binary compound of silicon and carbon whose chemical formula is SiC. Interestingly enough, the synthesis of this material was achieved in 1891, twelve years before the discovery of the extremely rare natural mineral moissanite. Thanks to its very high hardness, scoring between 9 and 9.5 on the Mohs scale, this ceramic has been used as an abrasive ever since its discovery in the early twentieth century.

Further uses of silicon carbide are found in parts requiring high endurance such as car brakes and has been researched for high temperature and high strength uses such as gas turbine blades. However, it was not successful due to its brittleness and low fracture toughness. It is also used for armouring purposes in defence applications such as bullet proof vests or vehicle armour [29]. The electronic properties of SiC were discovered by H.J. Round when he built a LED made with a SiC crystal. Since then, it has become rather common in electronics subjected to high temperatures and/or high voltages. Many manufacturers of high temperature ovens use SiC heating elements because of its stability at high temperature. In the frame of energy production, silicon carbide has been used in pebble bed gas cooled nuclear reactors as a component of the TRISO fuel particles. The thermal stability of silicon carbide is exceptional: this ceramic does not melt, but directly decomposes into gaseous compounds at extreme temperatures. Snead et al. put forward a decomposition temperature of 2818 K, at which point solid SiC decomposes in Si, SiC<sub>2</sub> and Si<sub>2</sub>C [10].

#### 1.1.1 Basics and properties overview

##### Structure

Silicon carbide has many different polytypes, a broad panel of hexagonal and rhombohedral structures as well as a single zinc blende cubic phase. The hexagonal and cubic silicon carbide structures are usually noted  $\alpha$ - and  $\beta$ -SiC (or 3C), respectively. Because of its anisotropic radiation induced swelling, hexagonal SiC is not used in the nuclear industry. The three main SiC polytypes (3C, 4H and 6H) are shown in Figure 1.1a. The phase diagram of the silicon/carbon system is shown next to these sketches in Figure 1.1b.

SiC is not a purely covalent ceramic: the atomic bonds are in fact partially ionic in nature due to the difference in electronegativity between silicon and carbon atoms. In its cubic form, silicon carbide has a theoretical density of 3.215 g·cm<sup>-3</sup>, and the lattice parameter  $a$  is 4.3589 Å [10]. This particular phase is the most stable of the SiC polytypes, featuring very little change in the lattice parameter, even at temperatures as high as 1273 K.

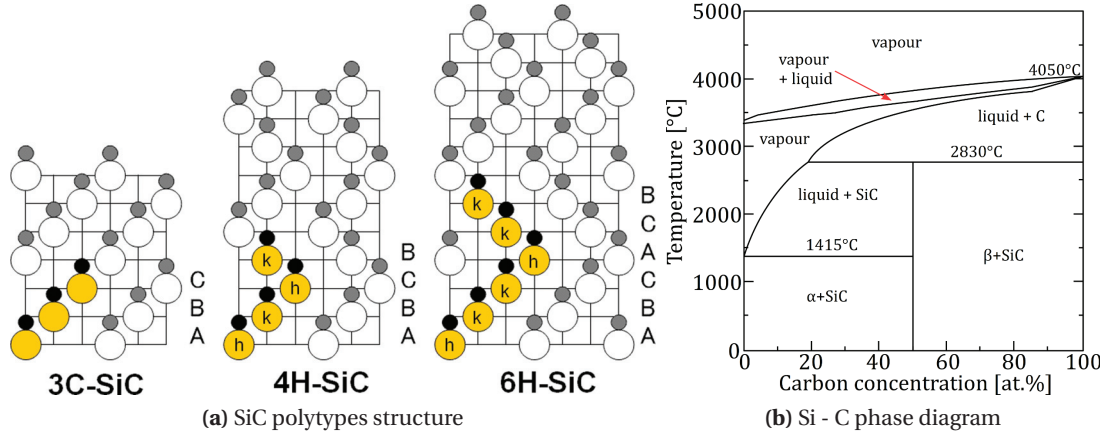


**Figure 1.1** – Crystal structure of the main SiC polytypes (a) and phase diagram of the silicon/carbon system (b)

### Mechanical properties

As most ceramic materials, silicon carbide exhibits a high elastic modulus, about 460 GPa for very dense CVD SiC. In terms of hardness, values in the range of 20 to 27.7 GPa have been measured with various techniques such as Vickers, Knoop or nano-indentation measurements. SiC shows weaknesses as far as its fracture toughness and fracture strength are concerned: it ranges between 2.4 and 5.1 MPa·m<sup>1/2</sup>, with a slight increase at elevated temperatures. The large scatter of these figures results from the different measurement techniques used, as well as from the grain size of the tested CVD SiC. As it is the case with most ceramic materials, fracture data is statistical in nature. Therefore, the fracture strength is a preferable parameter to the usual ultimate tensile strength (UTS). However, because of the brittleness of ceramics such as SiC, Weibull statistics are commonly used to describe the fracture probability instead of an actual fixed value defining the strength of the material.

$$P = 1 - \exp \left\{ - \frac{\int \left( \frac{\sigma}{\sigma_0} \right)^m dV}{V_0} \right\} \quad (1.1)$$

The terms  $\sigma_0$ ,  $m$  and  $V_0$  in Equation 1.1 are scaling factors related to the average strength, an exponent accounting for the scatter of the fracture data and a reference volume, typically 1 m<sup>3</sup> [30]. Snead et al. have reported a large range of values for  $m$ , going from 2 to 12 [10]. The corresponding parameters for a CVI SiC/SiC composite have been measured as  $\sigma_0 = 10.5$  MPa,  $m = 6.1$ , with  $V_0 = 1\text{m}^3$  [30].

### Thermal properties

The thermal conductivity (TC) of silicon carbide is very high. Stoichiometric monocrystalline SiC has a maximum thermal conductivity which can range from  $360 \text{ W}\cdot\text{m}^{-1}\cdot\text{K}^{-1}$  (3C-SiC) to  $490 \text{ W}\cdot\text{m}^{-1}\cdot\text{K}^{-1}$  (6H-SiC) at room temperature. To put this figure in perspective, it is 1.5 times higher than that of aluminium and is close to the  $385 \text{ W}\cdot\text{m}^{-1}\cdot\text{K}^{-1}$  of copper. Gathered thermal conductivity data of several nitride and oxide ceramics as well as of the aforementioned metals and the types of carbon discussed in this work are presented in Figure 1.2.

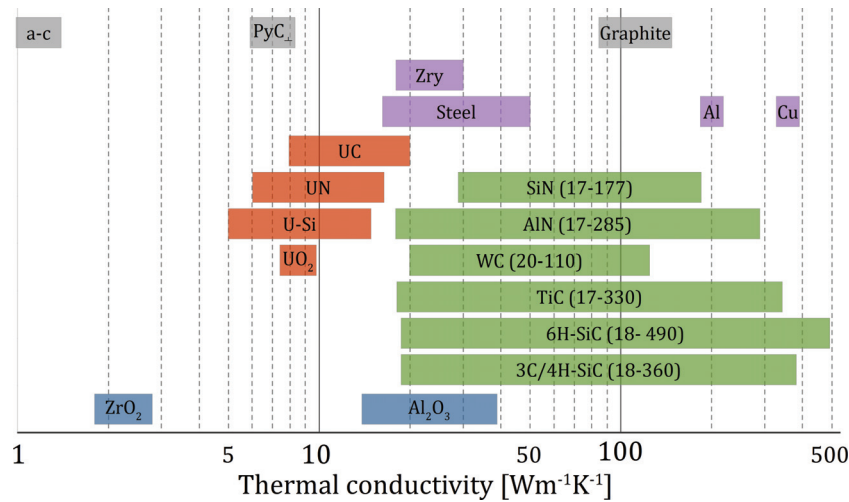


**Figure 1.2** – Collected thermal conductivity values for oxide ( $\text{ZrO}_2$ ,  $\text{Al}_2\text{O}_3$ ), nitride ( $\text{SiN}$  [31],  $\text{AlN}$ ) and carbide ( $\text{SiC}$  [32, 33],  $\text{TiC}$ ,  $\text{WC}$ ) ceramics, nuclear fuel systems ( $\text{UO}_2$  [34],  $\text{USi}$  [35],  $\text{U}_3\text{Si}$  [36],  $\text{U}_3\text{Si}_2$  [37],  $\text{U}_3\text{Si}_5$  [38],  $\text{UC}$  [39] and  $\text{UN}$  [40]), metals ( $\text{Steel}$ ,  $\text{Zry}$ ,  $\text{Al}$  and  $\text{Cu}$ ) and carbon allotropes discussed in the thesis (amorphous carbon,  $\text{PyC}$  and graphite [41]). Data from non-referenced sources was obtained from Matweb [42]. The large spread of the carbides and nitrides data is due to grain size and density effects.

At temperatures below 200 K, thermal conductivity strongly increases with temperature, up to a peaking value of about  $480 \text{ W}\cdot\text{m}^{-1}\cdot\text{K}^{-1}$ . Past this point, it significantly decreases with increasing temperature because of the enhanced scattering of phonons. The low temperature behaviour of thermal conductivity is linked to that of the specific heat described below, since these properties are interdependent through the thermal diffusivity of the material. Furthermore, the thermal conductivity of silicon carbide depends strongly on its structure. Both the density and the size of SiC crystals have a dramatic impact, a topic which is further discussed in following sections.

In terms of specific heat, silicon carbide is quite different from other carbide and nitride ceramics. Though it is comparable to other compounds such as  $\text{SiN}$ ,  $\text{TiC}$  or  $\text{AlN}$  at room temperature (capacity of about  $671 \text{ J}\cdot\text{kg}^{-1}\cdot\text{K}^{-1}$ ), it rapidly increases to  $1000 \text{ J}\cdot\text{kg}^{-1}\cdot\text{K}^{-1}$  at 500 K.

Its dependence on temperature is divided in two regimes, a strong increase at temperatures ranging from 0 to 200 K, which is followed with a much smaller increase beyond 200 K. More details on this are available in reviews by Snead and Lamont [10, 30].

Lastly, the thermal expansion of SiC is rather low. As previously mentioned, the cubic crystal of 3C is very stable at elevated temperatures. As a result, *coefficients of thermal expansion* (CTE) of  $4.5$  to  $6 \cdot 10^{-6} \cdot \text{K}^{-1}$  are usually measured [10, 30]. This is lower than most metals and in the range of other refractory materials. As an example, tungsten features a similar CTE of  $4.3 \cdot 10^{-6} \cdot \text{K}^{-1}$ .

### Activation and transmutation

With the current tendency of favouring low activation materials, SiC/SiC does rather well compared to other candidates. Having a simple composition means that only a limited number of activation products result from transmutation reactions. In a fission neutron spectrum, the predominant activation products are  $^{40}\text{P}$ , and magnesium isotopes, with the addition of  $^{22}\text{Na}$ . In the case of the neutron irradiated samples obtained from GA/Westinghouse, the most active isotopes were not activation products but contaminants from the loop, namely  $^{60}\text{Co}$ . Though low activation cladding is not the highest priority in the nuclear energy industry, the limited extent to which SiC transmutes under neutron irradiation is interesting for the stability of its properties in GenIV or fusion systems. Sawan et al. [43] reported on this topic as well as on the enhanced transmutation of SiC in a harder fusion spectrum. Indeed, if the neutrons have much higher energies and are more numerous in high energy ranges, the production of metallic isotopes such as Mg can reach up to 1.3 wt.% per year.

### 1.1.2 Radiation damage in SiC

#### Damage microstructure

Irradiation induced damage in cubic silicon carbide results in the introduction of point defects and vacancies. Depending on the dose and irradiation temperature, these defects can either cluster, migrate or annihilate. The current state of knowledge on this topic is summarised in Figure 1.3. Three regimes are identified on this plot. Firstly, at low doses and high temperatures, high doses and low temperatures or an intermediate combination of both, *black spot defects* (BSD), expected to be interstitial clusters with a size of about one nanometre and small disordered Frank loops appear. At combinations of intermediate dose and temperature, in addition to both aforementioned types of defect clusters, voids can start to grow. Lastly, when both the doses and irradiation temperature are high, voids are more prominent, whilst BSDs are not present any more. Additionally, loop networks have been reported under such

irradiation conditions. A comprehensive summary of data has been collected to make a visual representation of these three dose/irradiation temperature regimes by Snead et al. [11]. This is shown in Figure 1.3.

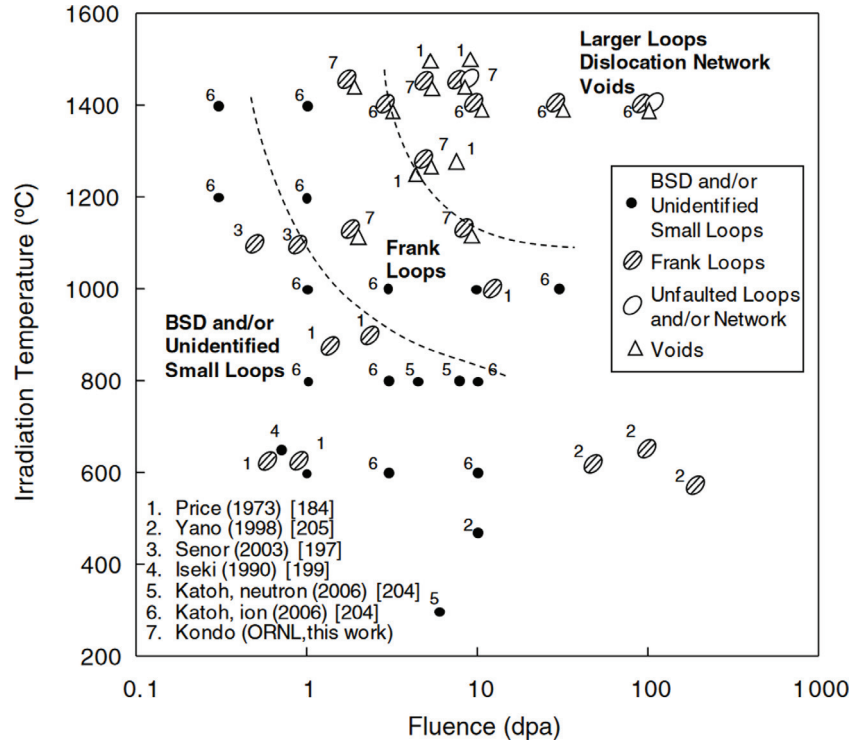


**Figure 1.3** – Types of microstructural defects caused by neutron and self-ion irradiation in cubic silicon carbide. Reproduced from Snead et al. [11].

The consequences of the creation of these defect clusters on the microstructure depends strongly on the irradiation temperature. At temperatures below 423 K, the accumulation of strain due to the production of interstitial clusters can become high enough to amorphise the SiC crystals. This temperature threshold is known as the *critical amorphisation temperature*,  $T_c$ . Above this limit, the crystallinity is maintained, and swelling becomes the main damage mechanism. On a side note, it shall be mentioned that Chen and Weber [44] have reported seeing amorphisation of SiC under  $\text{Kr}^{2+}$  irradiation at high temperature and very high dose rates<sup>1</sup>.

<sup>1</sup>These results show that amorphisation can occur above  $T_c$ . However, because of the extreme dose rate, these are not relevant for nuclear applications.

### Irradiation induced swelling

Swelling has been reported to increase logarithmically with increasing doses until it saturates. Depending on which type of defect clusters fuels the swelling, two regimes are recognised. Firstly, at temperatures ranging between 423 and 1073 K, the accumulation of point defect clusters such as BSDs and Frank loops are driving the phenomenon in the so-called *point defect swelling* regime. Secondly, at higher irradiation temperatures, i.e. ranging between 1173 and 1700-1800 K, the formation and growth of voids is the driving force behind the increase in volume. Figure 1.4 shows data collected by Snead et al. [11] featuring the aforementioned radiation induced swelling regimes.

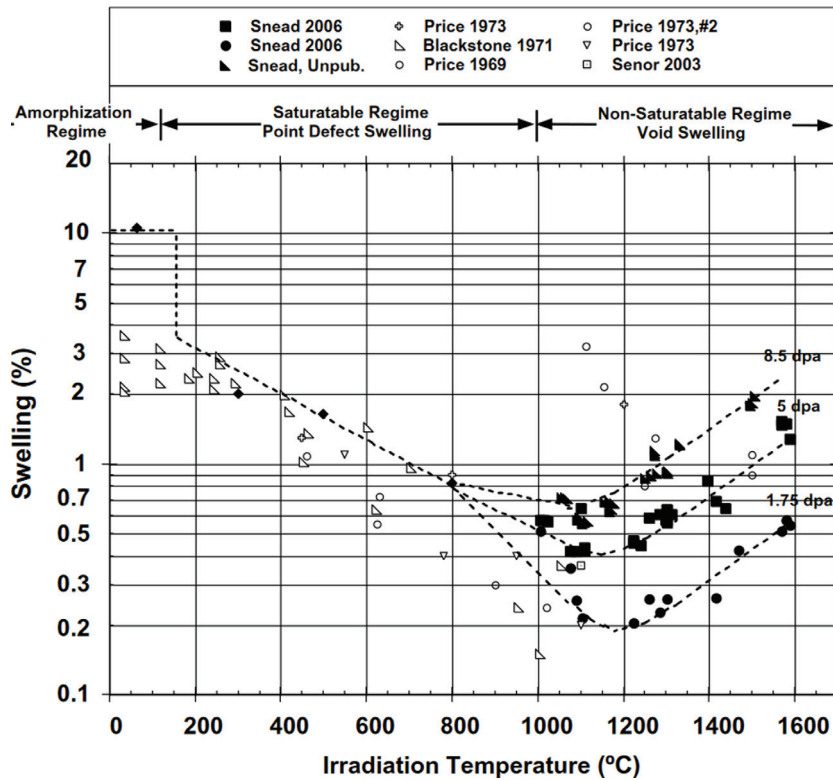


**Figure 1.4** – Irradiation induced swelling in cubic SiC as function of irradiation temperature and dose. Reproduced from [11], the original data was first published in [10].

The first swelling regime has two characteristics setting it apart from the one governed by voids:

- The saturation limit is a function of the irradiation temperature, the higher the irradiation the lower the dose at which swelling will saturate. This is due to the increased mobility of point defects at elevated temperature, meaning that as recombination is enhanced, the clustering of interstitials in BSDs or Frank loops becomes less likely.

- The doses at which swelling saturates are rather low, with reports of saturation at 1 dpa in samples irradiated at 1073 K. As a consequence, no radiation induced dimensional changes are expected beyond the first year of in-core exposure.

At intermediate temperatures between 1073 and 1173 K, silicon vacancies begin to gain some mobility. This temperature range is where the transition between the low temperature point defect swelling and the higher temperature void swelling regime occurs. Vacancies gain sufficient mobility to start diffusing and clustering, leading to the formation of voids. At this point, these cavities will keep growing without saturation of this final swelling regime.

### Thermal conductivity degradation

Radiation damage has a very strong impact on the thermal conductivity of silicon carbide. As previously introduced, heat transfer occurs via either electronic or phononic conduction. Being a ceramic, SiC has electrons tightly bound to the nucleus. The band gap of 3C SiC is 2.36 eV at 300 K [32], meaning that electronic conduction is negligible at temperature below more than a thousand Kelvin, where some electrons would have enough energy to cross it because of Boltzmann statistics. Therefore, lattice vibrations are the main mechanism through which heat is transported in this material. The strength of the different phonon scattering mechanisms was introduced with Equation 11 on page 10. Since the main result of the irradiation of silicon carbide is the increase of point defects and clusters, the term  $K_d$  becomes dominant over the other two, increasing until the aforementioned defect saturation level is reached. This contribution to the overall thermal conductivity can become so high that the Umklapp mechanism is effectively negated, hence removing the temperature dependence of thermal conductivity in highly damaged SiC [11]. The effect of irradiation on the thermal conductivity of silicon carbide and other ceramics is often expressed using the concept of *thermal defect resistance*. This quantity is defined as the difference between the inverse of the thermal conductivity of irradiated and pristine material [11, 17, 45].

$$\frac{1}{K_{rd}} = \frac{1}{K_{irr}} - \frac{1}{K_{pristine}} \quad (1.2)$$

The magnitude of  $K_{rd}$  can then be related to the density of the different types of radiation induced defects using the concepts introduced in the previous chapter. Most measurements carried out on irradiated SiC have been conducted in the range of temperatures expected to be of relevance either in LWRs or GFRs, i.e. from the ambient up to some 850°C. It has been observed that  $K_{rd}$  is directly proportional to the swelling in this temperature range. This can be explained by the previously introduced phonon-defect scattering mechanisms, which



are all proportional to the defect density or its square root. Given that the density of small point defects such as BSDs increases with dose until saturation and that point defect swelling follows linearly with this increase, thermal defect resistance will follow the same trend in this temperature regime. One should however note that although point defect production and clustering does saturate at a given point,  $K_{rd}$  will not. The reason here is that phonon scattering due to both loops and voids are also proportional to their densities. Since they do not saturate and keep growing as the irradiation dose increases, the thermal defect resistance does not saturate either [11].

## 1.2 Silicon carbide based composites

Like practically all ceramic materials, silicon carbide is brittle by nature, which means that using it as a structural material in any system requires to overcome this major drawback. The issue of brittleness is solved by making a composite material based on both a SiC matrix and SiC fibres. The underlying principle of composite materials is to bring together different materials in a way which takes advantage of either components strengths, whilst avoiding their respective weaknesses. There are several approaches through which this synergy is achieved. The most produced and used man-made material, concrete, is actually a composite material made out of aggregate and cement. Plywood is another example of a very common construction material which is a composite. Nevertheless, fibre reinforced polymers are usually the first composite material that comes to mind and are very prominent members of the composites family, in which an often weaker matrix is reinforced by strong but rather brittle fibres. Other possible combinations such as matrices reinforced by dispersions of particles are also good examples of synergistic combinations of properties.

The basics behind fibre reinforced composites such as SiC/SiC is the use of fibres to bear the mechanical load, which in turn is transferred to the surrounding matrix in order to not exceed the elastic limit of the fibres. In addition to this, fibres act as features hindering the propagation of cracks through the matrix. This effect is known as *crack tip opening bridging* [46]. A schematic representation of damage mechanisms in fibre reinforced composites is shown in Figure 1.5. These include the bridging effect as well as fibre to matrix debonding.

The case of ceramic matrix composites (CMC) such as SiC/SiC is different from other composite materials based on fibre reinforcement. Indeed, the desired properties are not gained from a fibre and matrix combination alone. Both the fibres and matrix are brittle taken individually, meaning that a third component called the *interphase* needs to be added to the fibre/matrix combination to obtain viable properties. In SiC/SiC, the interphase, also called *interlayer*, takes the form of a thin material layer deposited by chemical vapour deposition (CVD) prior to the infiltration of the matrix into the weave.

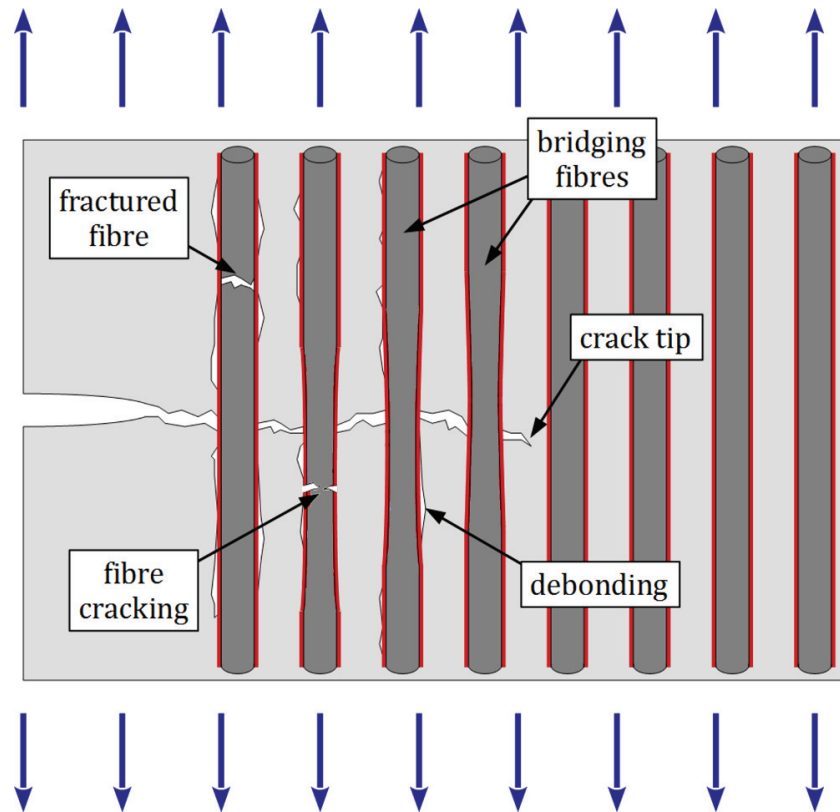


**Figure 1.5** – Schematic representation of damage mechanisms occurring in fibre reinforced composite materials such as SiC/SiC. The red outline around the fibres represents the PyC interphase. Inspired from a figure by Dassios et al. [46].

The use of SiC as a CMC goes back to the 1980s, when the chemical vapour infiltration process was improved to the point of enabling the production of full scale industrial components. This pioneering work was mostly heralded by SEP (SNECMA nowadays) and a few other companies. The first applications of these composites were either in the aerospace industry, e.g. spacecraft re-entry tiles, propulsion chambers for solid fuel rockets, or for military uses in aircraft and missile components. Since then, other uses in high temperature/high strength industrial applications have become customary, mostly in the frame of cleaner combustion engines (low NO<sub>x</sub> furnaces), power generation with parts such as high temperature gas turbine components and chemical industry components facing high temperatures.

Lately, silicon carbide-based CMCs feature properties close to other materials considered for nuclear fuel cladding. The Ashby diagrams shown in Figure 1.6 show three combinations of properties relevant to the operation conditions and design requirements that nuclear cladding has to meet. Both stainless steels and zirconium based alloys have been highlighted next to pure silicon carbide as well as SiC/SiC composites. The ellipses accounting for the properties

of pristine SiC/SiC and Zry have been gathered from literature reviews such as [30, 45, 47] for SiC/SiC and [48] for Zry. The first diagram shows the yield strengths of many materials plotted against their respective fracture toughness. The diagonal lines represent the ratio  $K_{IC}/\sigma_f$ , commonly known as the *yield before break* (YBB) criterion, whilst the flatter one seen on the upper left corner of the figure shows the *leak before break* (LBB) criterion. Both criteria are used in power generation industries for the safe design of parts such as heat exchangers. The LBB criterion is common practice in the nuclear industry [49]. The second of the Ashby maps features the thermal conductivity of materials plotted against their thermal expansion coefficient. This specific combination is also relevant for nuclear fuel clad design, since the lines of constant  $\lambda/\alpha$  ratios feature materials with similar susceptibilities to thermal distortions. The higher the ratio, the less the material will be prone to deformation caused by thermal stresses. Finally, the third diagram shown in Figure 1.6 contains a plot of the maximum operation temperature against the strength of the materials at these temperatures.

Looking at these diagrams, one can rapidly see that SiC/SiC composites feature YBB criterion very close to that of Zry, it even sits on the same YBB line as some of the strongest stainless steels. It also has a very good score as far as thermal distortions are concerned. This is of utmost importance for nuclear cladding, since a typical LWR fuel rod is about 4 metres long and should be as dimensionally stable as possible to ensure optimal coolability of the core at all times. Last, it is not surprising that it sits very high in the strength versus maximum operating temperature diagram. Here, the fact that it is a ceramic based composite makes it stand out compared to both zirconium based alloys and stainless steels.

Further properties of relevance for nuclear materials are their behaviour in a neutron field, i.e. their resistance against radiation damage as well as radiation induced phenomena such as swelling, radiation creep, segregation or amorphisation. In addition to this, the corrosion properties of any nuclear material have to be given special attention as any structural material in the primary circuit of a light water reactor would be immersed in high temperature pressurised water<sup>2</sup>. Katoh et al. [45] have published an extensive survey on the known radiation effects occurring in SiC/SiC composites in 2014. Table 1.1 is reproduced from this paper and gives a good overview of the current state of the art regarding SiC CMCs and their use in nuclear environments.

---

<sup>2</sup>275-315°C at 155 bar or 285°C at 70-75 bar in pressurised and boiling water reactors, respectively.

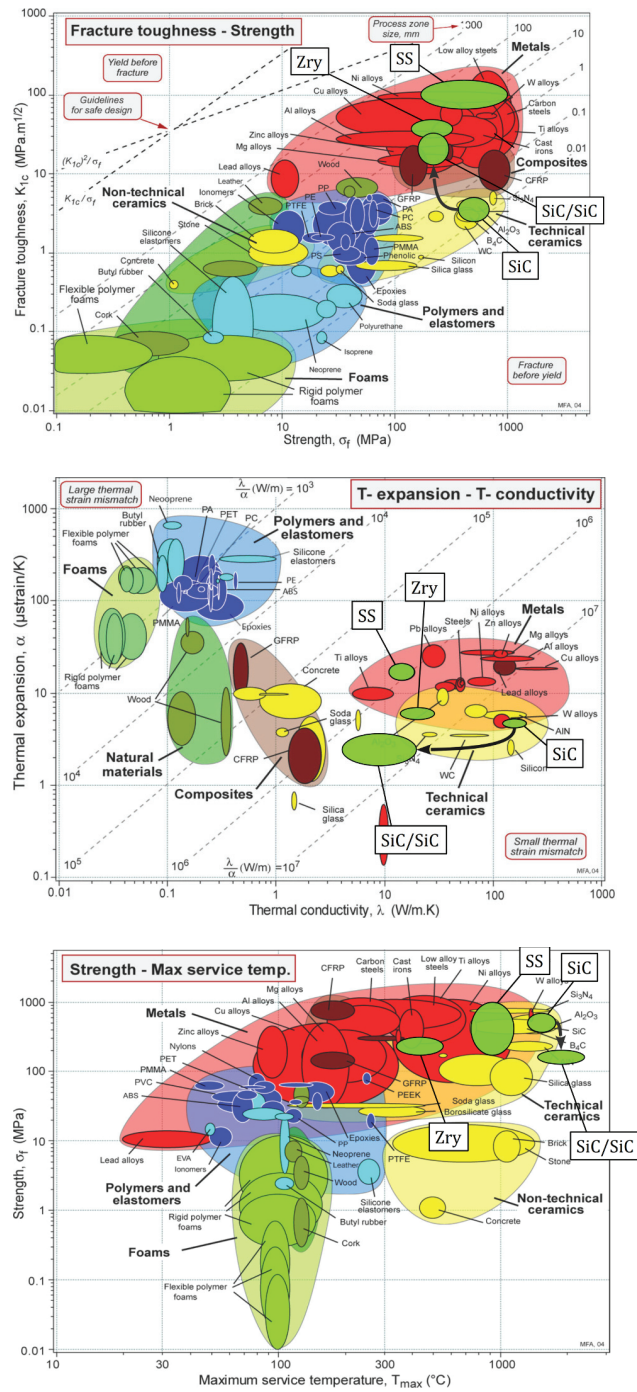


**Figure 1.6** – Ashby material selection maps of the yield strength against the fracture toughness (top left), thermal conductivity against thermal expansion coefficient (top right) and maximum operating temperature against yield strength (bottom). The materials most commonly used or foreseen for nuclear claddings (stainless steels and Zircaloy) as well as pure SiC and SiC/SiC composites have been highlighted. Based on figures from [50].

### 1.3. Architectures of SiC/SiC composites

**Table 1.1** – Collected properties of pristine and irradiated SiC/SiC composites. After Katoh et al. [45].

Property	Pristine	Irradiated
Density	2.5 to 2.7 g·cm <sup>-3</sup>	
Porosity	15 to 20%	No changes
Volume fraction (fibres)	35-40%	
CTE	Values of CVD SiC	
	• 8-15 W·m <sup>-1</sup> ·K <sup>-1</sup> with HNLS	
Thermal conductivity	• 15-24 W·m <sup>-1</sup> ·K <sup>-1</sup> with TSA3	Significant reduction: 85-90% lower
Specific heat $C_p$	CVI SiC values	No changes
Elastic modulus	200-280 GPa at RT	$\frac{\Delta E}{E_0} \sim -\frac{10}{3} \frac{\Delta V}{V_0}$
	• ~ 0.13 (0°/90° weave)	
Poisson ratio	• ~ 0.25 (±45° weave)	
in plane $\epsilon_{0.2}$ (PLS)	90-120 MPa	
UTS	250-350 MPa (0°/90° weave)	
Statistical strength (Weibull)	PLS	No changes
Trans-laminar shear strength	25-35 MPa	
Trans-thickness tensile strength	20-25 MPa	
Damage tolerance	Macro-crack resistance ~3 kJ·m <sup>-2</sup>	
Time-dependent fracture	Larson-Miller approach	

### 1.3 Architectures of SiC/SiC composites

The stringent tightness requirements imposed onto nuclear cladding cannot be met by SiC/SiC alone. Typical porosity values for composite tubes ranges from 15 to 20%. Furthermore, the scale at which the material is porous is twofold. Indeed, large pores with sizes of several tens of micrometres are common occurrences between tows of fibres. In addition to this, a second type of porosity with a much smaller size distribution, typically below a fibre diameter is found between individual fibres within the tows themselves. To ensure the tightness of a composite tube, manufacturers such as the French *Commissariat à l'énergie atomique et aux énergies alternatives* (CEA) and Westinghouse have been developing multilayered concepts in which

a tube is made out of one or more layers of SiC/SiC composite as well as of layers of a dense material such as monolithic SiC or metallic liners. These concepts are discussed in details later in section 1.5.

### 1.3.1 SiC fibres

Nowadays, there are many types of commercially available SiC fibres. Depending on the applications they are fabricated for, these fibres can have widely different compositions, grain sizes and properties. Ever since the growing interest of the nuclear industry for CMCs, a tendency towards purer and near stoichiometric silicon carbide fibres has become prevalent. There are currently four main companies present on the market, selling SiC fibres under the trade names of Nicalon<sup>TM</sup>, Tyranno<sup>TM</sup>, Sylramic<sup>TM</sup> and SCS<sup>TM</sup>. Only specific variations of the first three fibres are considered here, the fourth being a large-diameter, large-grained fibre available in the form of monofilaments, i.e. these are more CVD SiC monofilaments grown onto a carbon substrate than actual fibres.

For nuclear applications, near stoichiometric, large-grained polycrystalline fibres are desirable. Larger grain materials are less sensitive to diffusion-controlled creep mechanisms. In Equation 1.3,  $\dot{\epsilon}$  is the creep strain rate,  $C$  is a material and creep mechanism dependent constant,  $d$  is the grain size of the said material,  $m$  and  $b$  are mechanism-dependent exponents and the exponential term is a typical Arrhenius activation energy term.

$$\dot{\epsilon} = \frac{C\sigma^m}{d^b} \exp\left(\frac{-Q}{k_b T}\right) \quad (1.3)$$

In the case of intragranular diffusion creep, commonly known as Nabarro-Herring [51, 52], the exponent  $b$  is equal to 2, whereas in grain boundary diffusional creep, known as Coble creep [53], it takes the value of 3, meaning that the latter mechanism is more sensitive to grain size than the former. This implies that such a microstructure is desirable in SiC fibres intended to be used in nuclear reactors, where creep is further enhanced by irradiation. However, one should keep in mind that creep occurring through dislocation climb does not depend on the grain size.

Another reason for which large grains are desirable arises from the fact that SiC is a ceramic material in which thermal conductivity is almost purely phononic<sup>3</sup>. Having large grains automatically involves less grain boundaries, thus decreasing the number of obstacles to the motion of phonons. Thus, phonons have a larger mean free path in large grained materials, from which a higher thermal conductivity ensues.

The other requirement SiC fibres have to meet in order to be considered as nuclear grade is stoichiometry. The more chemically and structurally similar to the CVI/CVD SiC matrix the SiC fibre is, the better. An issue reported by several authors in the early stages of development of SiC/SiC composites as structural material for nuclear applications was the pronounced shrinkage of the fibres. This dimensional change was due to the use of either hexagonal  $\alpha$ -SiC or non-stoichiometric fibres of the first and second generations; these types of SiC fibres exhibited an irradiation induced swelling significantly different from that of the chemical vapour grown cubic  $\beta$ -SiC matrices. This specific issue has since then been fixed thanks to the progresses made towards high-purity, large-grained cubic SiC fibres, known as third generation or *nuclear grade* fibres. In terms of weight percentages, a perfect atomic ratio Si:C of one translates in weight percentages of 29.95% C and 70.05% Si.

Table 1.2 shows collected data on the SiC fibres found on the market. The four highlighted fibres, Hi-Nicalon Type S, Tyranno SA 1-3 and Sylramic/iBN are the only fibres used in structural applications for nuclear power generation. As mentioned before, these are all large-grained, high-density fibres with compositions close to stoichiometry in the case of the first two. The result of both the purity and large grain size of the fibres is visible in their respective thermal conductivities, with values ranging from 18 to 65 W·m<sup>-1</sup>·K<sup>-1</sup> and densities between 3.02 and 3.05 g·cm<sup>-3</sup>, which translates in 94% and 95% of the theoretical density, respectively.

---

<sup>3</sup>However, electronic conduction does occur at very high temperatures.

**Table 1.2** – Characteristics and properties of commercially available SiC fibres. The three highlighted fibres, Hi-Nicalon Type S, Tyranno SA 1-3 and Sylramic are the ones used for structural applications in the nuclear industry. Based on tables by Di Carlo and Yun [33].

Product Name	Composition [wt. %]	Grain size [nm]	Diameter [ $\mu\text{m}$ ]	Density [ $\text{g}\cdot\text{cm}^{-3}$ ]	k [ $\text{W}\cdot\text{m}^{-1}\cdot\text{K}^{-1}$ ]	CTE [ $\text{ppm}\cdot\text{C}^{-1}$ ]
Nicalon, NL200	56 Si + 32 C + 12 O	2	14	2.55	3	3.2
Hi-Nicalon	62 Si + 37 C + 0.5 O	5		2.74	8	3.5
Hi-Nicalon Type S	69 Si + 31 C + 0.2 O	100	12	3.05	18	
Tyranno Lox M	55 Si + 35 C + 10 O + 0.2 Ti	1	11	2.48	1.5	
Tyranno ZMI	557 Si + 31 C + 7.6 O + 1.0 Zr	2			2.5	3.1
Tyranno SA 1-3	68 Si + 32 C + 0.6 Al	200	7.5-10	3.02	65	
Sylramic	67 Si + 29 C + 0.8 O + 2.3 B + 0.4 N + 2.1 Ti	100	10	3.02	46	5.4
Sylramic-iBN		>100		3.0	>46	
SCS-6-9/Ultra SCS	70 Si + 30 C + Si and C traces	~ 100 by 10	70-140	3	~ 70	4.6



### Fabrication of SiC fibres

Silicon carbide fibres are produced by spinning and heat treating precursors. Yajima et al. [54] reported in 1978 on the use of organometallic polymers for the production of continuous  $\beta$ -SiC fibres. As a starting point, dimethyldichlorosilane  $(\text{CH}_3)_2\text{SiCl}_2$  is converted into a polymer, polydimethylsilane  $[(\text{CH}_3)_2\text{Si}]_n$ , via dechlorination. Following a pyrolysis at  $400^\circ\text{C}$ , fibres of the “preceramic” polycarbosilane  $[\text{SiH}_2\text{CH}_2]_n$ <sup>4</sup> are produced. Further heat treatment steps, including cross-linking and densification through pyrolysis and sintering, are required until a SiC fibre is obtained. SiC fibres prepared through this processing route typically have very small grain sizes, in the nanometre range<sup>5</sup>.

The mechanical, thermal and microstructural properties of SiC fibres are strongly dependent on the processing sequence leading from a green to a densified SiC fibre. DiCarlo and Yun discuss this topic in details in their review paper [33]. The grain size of the fibres listed in Table 1.2 are plotted against their processing temperature in Figure 1.7. Displaying these two quantities next to one another clearly shows the difference between the three generations of SiC fibres.

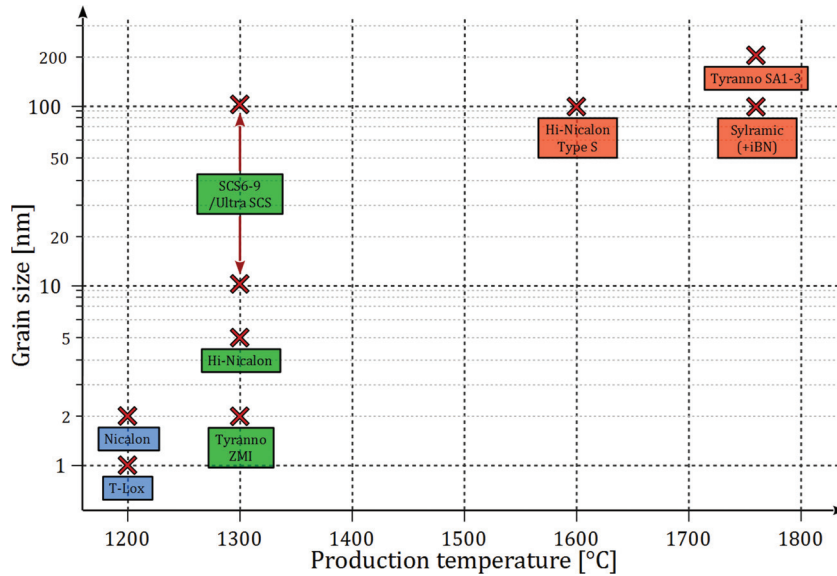


**Figure 1.7** – Grain size against production temperature of commercially available SiC fibres. First generation in blue, second in green and third in red.

The earliest SiC fibres, by which one understands the Nicalon NL200 and Tyranno Lox M fibres, picked up large amounts of oxygen during curing, thus forming carbon and oxygen impurity phases. These were then densified at  $1200^\circ\text{C}$ , a processing step at which the aforementioned

<sup>4</sup>“Preceramic” fibres such as polycarbosilane are usually referred to as green fibres, in analogy to the green forms used in the processing of ceramics.

<sup>5</sup>Yajima et al. reported that the SiC particles found in their fibres had an average diameter of 7 nm [54].

oxy-carbides decompose in gases, hence leaving much porosity behind. As a result, densities of only 77 to 79% of the theoretical density were attained. Furthermore, as a result of the low sintering temperature, first generation fibres featured very fine grains (see Table 1.2). The combination of both microstructural features had a negative impact on practically all of their mechanical and thermal properties (tensile strength, modulus, thermal conductivity and expansion coefficient, see [33] for more details) as well as on their maximum usage temperature due to enhanced creep rates.

No major changes resulted from the transition between first and second generation fibres. In terms of processing, the Hi-Nicalon fibre undergoes an electron irradiation at the curing stage, thence considerably lowering oxygen pickup in the green form. Thus, less porous fibres are produced, with a density reaching about 85%, i.e. a 6% reduction of the total porosity. The addition of different sintering additives to the Tyranno ZMI fibre does not result in much difference in terms of microstructure or thermal properties. Both these fibres are also processed at slightly higher temperatures – 1300°C instead of 1200°C – the effect of which is seen with the slightly larger grains.

The third and currently most advanced SiC fibre generation comprises the Hi-Nicalon Type S, Tyranno SA and Sylramic fibres. Just as the Hi Nicalon fibre, the Type S version is also subjected to electron irradiation at the curing stage. This is followed by sintering at 1600°C. Thanks to the much higher processing temperature, a large-grained fibre is obtained, with typical grain diameters around 100 nm. In addition to this, a higher density is gained, in part because of the near-stoichiometric composition. The other two types of fibres follow another oxygen-content reducing route. In both cases, oxide impurities are decomposed by heat-treating the green fibres at 1200°C. Because of this additional process, sintering additives are required to reinforce the weakened fibres. Tyranno SA1-3 fibres are fabricated using aluminium additives, whereas boron is added to the Sylramic fibres. Both types are then sintered at temperatures above 1700°C. Nevertheless, the use of boron containing sintering aids in the fabrication of Sylramic fibres limits their use in nuclear applications because of  $(n, \alpha)$  reactions, leaving only the Hi-Nicalon Type S and Tyranno SA3 fibres. All three of these fibres are very close to a perfect one-to-one stoichiometry, with their weight percent distribution being fairly close to the theoretical 29.95 wt.% of carbon and 70.05 wt.% of silicon.

### Types of SiC fibre weave

The strengthening of fibre reinforcement depends on the way the fibres are organised in the matrix. There are several types of fibre distribution, starting from a random distribution up to multi-directional weaving (2D, 3D, 4D).

- **Randomly distributed fibres**

The simplest way of reinforcing a matrix with fibres consists in distributing short sections of fibres  $5 < L/d < 1000$ , called *whiskers*, into a matrix. This type of reinforcement is not seen in any end-product such as cladding tubes since, since such composites do not feature properties comparable with uni-directional and other more complex woven products. Generally speaking, it is advantageous because of the low price of fibre whiskers as well as the possibility of large scale production by hot-pressing of high-pressure injection.

- **1D weave**

Uni-directional (UD) fibre reinforced composites are the simplest type of materials reinforced with long fibres rather than whiskers. One takes a simple fabric of uni-axial fibres to make a preform, which is then densified by CVI. These composites exhibit a high strength along the fibre direction but do not gain much from the reinforcement in the other directions. For this reason, as well as because of their easiness of implementation, UD composites are very often used in early process development stages.

- **Multidirectional weaves**

All SiC/SiC composites actually in use or at the prototype development stage use both multi-dimensional and multi-directional fibre reinforcement. The classification of these types of fibre weaves can be misleading since both the directionality and dimensionality of the weaves are shortened with the letter d. Generally, a capital “D” refers to the number of dimensions (X, Y and Z), whereas a lower case “d” is used to refer to the number of directions in which the fibres are woven. A good example of such a case, the 3D4d braid, is shown in Figure 1.8c.

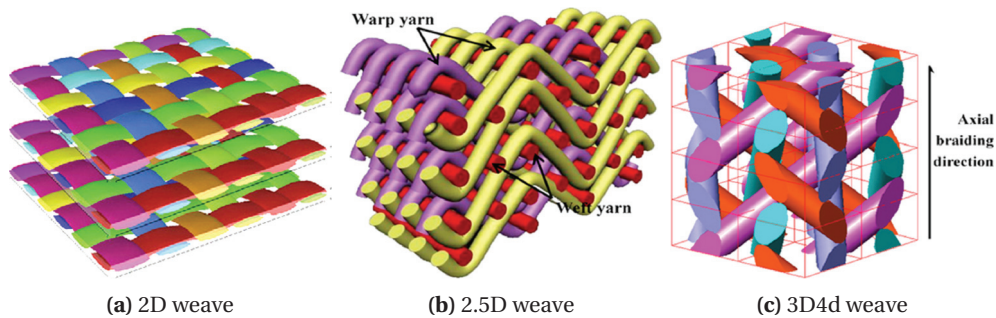


**Figure 1.8** – Types of multi-directional-dimensional fibre reinforcements: (0°/90°) 2D, (a), 2.5D (b) and 3D4d woven fibres (c). From Zhao et. al [55].

The composites studied in this work are made with either 2D weaves with a  $0^\circ/90^\circ$ , shown in Figure 1.8a, or  $0^\circ/45^\circ$  fabrics or 3D (2.5) woven fibres similar to Figure 1.8b. The sketch presented in Figure 1.9 shows what a cross-section view of a “3D” SiC/SiC composite looks like. The grey fibre tows seen in cross-section make what is known as a  $0^\circ/45^\circ$  2D weave, whilst the blue tows are cross-linking the 2D weave in a direction parallel to the circumferential direction of the tube. This type of composites is usually called 2.5 or 3D composites. The 2.5D denomination is more accurate since the parallel tows are only partially oriented in the radial direction of the hollow cylinder. The illustration shown in Figure 1.8b gives a good 3D representation of this type of weave.

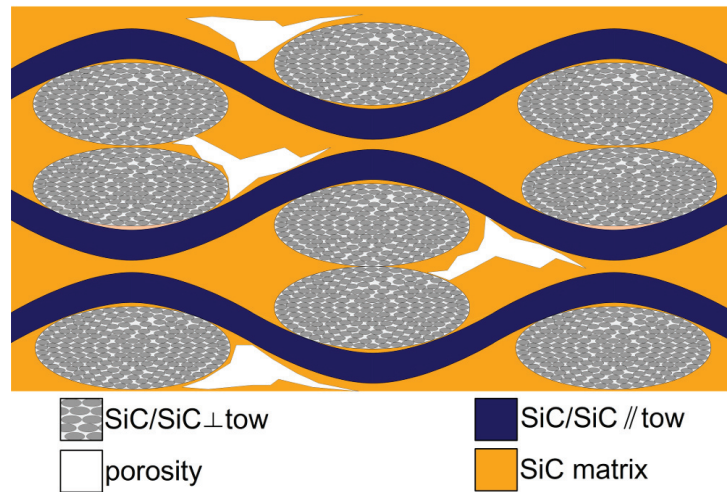


**Figure 1.9** – Schematical representation of 2.5/3D reinforced SiC/SiC composite seen in cross section

These more complicated architectures are preferable to obtain satisfactory mechanical properties. 2D and 3D SiC/SiC composites have properties close to those of metals commonly used for claddings (see the Ashby diagrams in Figure 1.6). However, these depend on the type of weave selected, as illustrated by the Poisson's ratio of  $0^\circ/90^\circ$  and  $\pm 45^\circ$  2D weaves shown in Table 1.1.

### 1.3.2 SiC matrices

Three main processes are used to densify woven SiC fibres with a SiC matrix. These share the common goal of creating a large-grained silicon carbide matrix between and inside the fibre tows making the weave. The matrix should be as dense and close to stoichiometric SiC as possible. In all three cases, a precursor, either gaseous or solid, is infiltrated into the preform made of woven fibres. It is then densified, and SiC grains are allowed to grow via different heat treatment steps.

#### CVD and CVI SiC

Both chemical vapour deposition (CVD) and infiltration (CVI) are based on the same principle. The main difference between them is the size of the parts which can be densified. CVD is used for small samples, whereas the densification of fuel-pin sized tubes can be achieved only through CVI. In both cases, gaseous precursors are used to either deposit the ceramic on another material or infiltrate it into a preform typically made of woven fibres. To produce SiC/SiC composite tubes, the woven fibres are often supported by a cylinder made of graphite, which is subsequently disposed of by pyrolysis [56]. In a first step, the interphase layer is deposited on top of the woven fibres by CVD. After this, methylchlorosilane is introduced in the infiltration chamber. This gaseous precursor is converted to SiC at a given rate, depending on the pressure and temperature conditions. The most commonly used CVI process is the isobaric isothermal CVI (I-CVI) process [57], where the chamber is kept at constant temperature and pressure. The physical mechanism behind the infiltration is gaseous diffusion through the woven fibres, which is driven by the MTS concentration gradient between the outer and inner surfaces of the preform. An issue commonly met in CVI SiC/SiC is that surface porosity closes during the process, hence leaving inner parts of the preform less densified as the gas flow is blocked at the surface. Intermediate machining steps or more complicated CVI procedures adding additional driving forces such as pressure gradients (F-CVI), pulsed precursor introduction (P-CVI) or thermal gradients give more satisfactory results at different scales. More details on the topic of CVI and its use in the production of SiC/SiC CMCs can be found in a comprehensive review by Lamon [57].

#### NITE SiC

The acronym NITE stands for *Nanopowder Infiltration and Transient Eutectic* phase processing. This process has been developed some years ago at Kyoto University [58]. It is based on the use of a slurry of nano-powder made of a mixture of  $\beta$ -SiC and sintering additives such as  $\text{Al}_2\text{O}_3$ ,  $\text{Y}_2\text{O}_3$  and  $\text{SiO}_2$ . The slurry is then infiltrated into the fibre weave and hot-pressed at elevated temperatures ( $>1700^\circ\text{C}$ ) [59]. The NITE process has produced the densest matrices thus far, nearing the theoretical density [60]. Complex shapes such as hollow tubes and small cooling panels made from a 2D weave densified with NITE were produced by Kohyama et al. [61]. Nevertheless, bringing the NITE process from a laboratory to an industrial scale production whilst keeping similar quality levels has not been successful so far.



### PIP SiC

The third process by which weaves of SiC fibres are bound together in a SiC matrix is the Polymer Impregnation and Pyrolysis, shortened PIP process. The principle of this technique is to infiltrate the structure to densify with a mixture of pre-ceramic polymer precursors such as polycarbosilane and polymethylsilane [55]. This process is advantageous as far as the fabrication of large and complex components at an industrial scale is concerned. Nevertheless, PiP SiC matrices do not present the same quality level as those produced by CVI or NITE. Indeed, PiP produces low density, non-stoichiometric, amorphous SiC [55]. Although this issue can be overcome by raising the pyrolysis temperature and changing the precursors, PiP is a much less frequently used process than the well-established CVI process.

### 1.3.3 Interphase layers

Over the last couple of decades, several types of interface layers have been investigated. Papers by Bertrand et al. as well as Taguchi et al. [62, 63, 64] discuss the properties of composites where a single layer of pyrolytic carbon (PyC), a multi-layered structure of PyC and SiC, noted  $(\text{PyC}/\text{SiC})_n$ , or a monolayer of boron nitride are used for the interphase. Yu et al. [65] as well as Taguchi et al. [66] have reported results on C/SiC and SiC/SiC composites prepared with an interphase made with carbon nanotubes.

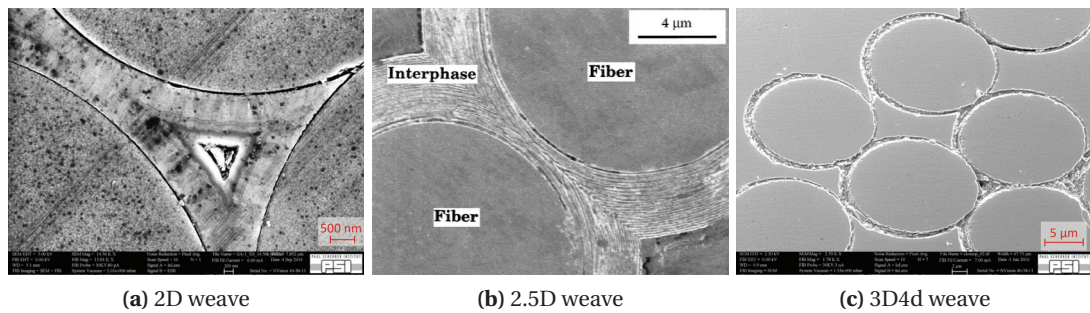


**Figure 1.10** – SEM micrographs showing a single PyC (a), multilayered  $(\text{PyC}/\text{SiC})_n$  [62] (b) and BN interphases (c)

The primary function of the interphase is to ensure that stresses can be transferred between the fibres and the matrix so that the whole composite behaves in pseudo-ductile<sup>6</sup> manner. To this end, the interfacial friction strength of the interlayer is of the highest relevance to the manufacturing of viable SiC/SiC composites. Shear stresses at the interphase can result from many phenomena.

<sup>6</sup>Pseudo-ductility is the term used to describe the manner in which CMCs deform. Thanks to crack-tip bridging by the fibres, these composites exhibit stress-strain curves similar to those of ductile materials, whilst being made with brittle components.

- The thermal expansion of the fibres and matrix is not homogeneous. Indeed, a fibre is effectively a cylinder with a very high aspect ratio. Even though the fibre is made of polycrystalline cubic SiC which expansion coefficient is isotropic, the end product will still feature preferential dilatation along its length.
- Irradiation-induced swelling has the same consequences as thermal expansion, with the difference that this phenomenon is not reversible. The extent of this source of shear stresses is rather limited since hexagonal  $\alpha$ -SiC has been abandoned in favour of the more stable isotropic cubic  $\beta$ -SiC.
- Thermal and irradiation creep will also cause the interphase to experience some stresses along the fibre length axis.
- In addition to the role it has on the mechanical performance of the composite, the interphase acts as a barrier against thermal transport between the fibre and matrix. As introduced in the abstract, the study of this contribution to the overall thermal conductivity is at the core of this work and discussed in the next chapters.

Thanks to their easiness of preparation as well as low price compared to the other options, PyC monolayers are the most commonly seen interphases.  $(\text{PyC}/\text{SiC})_n$  is not used in prototype clads from CEA or Westinghouse. Despite having a microstructure similar to graphite-like PyC, the use of BN in a neutron field would severely hamper the durability of the interlayer; the very high cross-section of the  $^{10}\text{B}$  ( $n, \alpha$ )  $^7\text{Li}$  which would produce helium at the interphase itself and result in undesirable neutron capture. This can be avoided by using enriched  $^{11}\text{B}$ , which does not produce helium via ( $n, \alpha$ ) reactions. Because of the more expensive and complicated process involved in the deposition of these nano-featured interphases, multilayered PyC/SiC is not common either. The specifics of PyC monolayers are further discussed in the following section.

## 1.4 Pyrolytic carbons

Pyrolytic carbons are a group of carbon allotropes prepared by CVD at rather low pressures and temperatures. They are the result of the dehydrogenisation of hydrocarbons such as methane, propane, ethane, ethylene, etc. at temperatures ranging from 900 to 1300°C [67]. This type of carbons is quite prevalent in the composite industry for its use as an interphase layer in many applications such as aerospace parts, high performance brakes, as well as in a few medical applications. The interest in PyCs in the nuclear industry started in the 1960s with pebble bed reactors [68] such as the German AVR [69]. In this type of reactors, PyC was used for the inner buffer of the pebbles made from an outer SiC shell containing TRISO fuel particles [70].

PyC come in many forms, depending on the CVD parameters. There are four widely recognised classes of pyrocarbons. These are traditionally differentiated by their optical properties under polarised light [67, 71], with three main categories, the rough laminar (RL), the smooth laminar (SL) and the isotropic (I) pyrolytic carbons [67], dating back to the 1970s. Since then, an additional class, the regenerated laminar (ReL) PyC, has been identified by TEM [72, 73]. The differences between these classes of pyrocarbons is their structure, which can be either graphite-like (RL, SL and ReL) or isotropic (I-PyC). In terms of optical properties, RL and SL PyC feature partial or full Maltese crosses under polarised light. The isotropic PyC has no optical anisotropy, and features no phase shift such as the one seen with RL and SL PyCs.

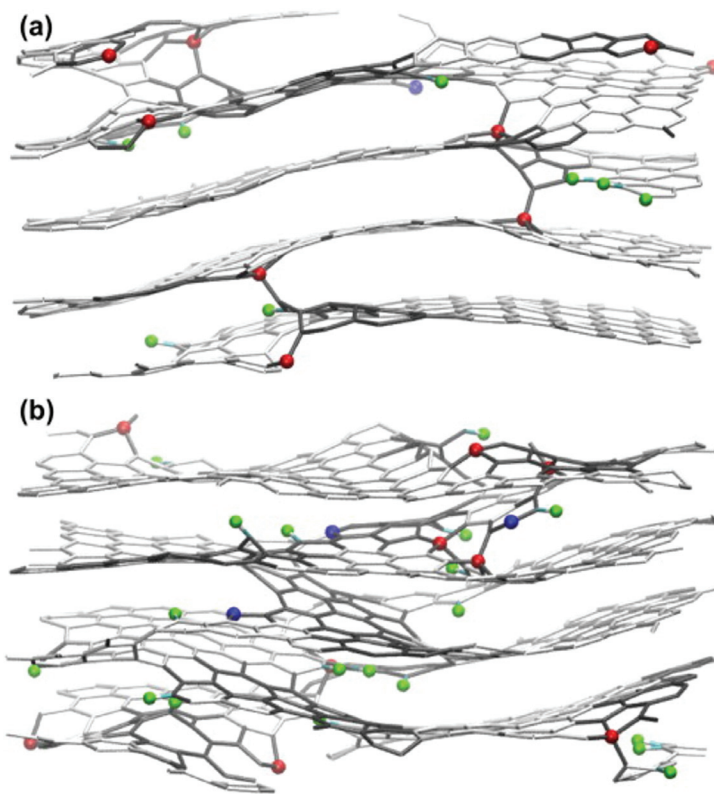


**Figure 1.11** – Atomistic models of (a) rough laminar (RL) and (b) regenerated laminar (ReL) pyrolytic carbons. From Farbos et al. [74].

The more recently identified ReL PyC has properties similar to those of rough laminar pyrocarbon. However, it has a different structure, with additional links in the c-axis, i.e. more numerous and extensive bonds across the graphene sheets [74]. In SiC/SiC composites, the PyC layers deposited onto the fibres are of the rough laminar type. Indeed, its mechanical properties are close to those of graphite, thus enabling a smooth glide of the fibres in the matrix under loading.



### Thermal properties of graphite-like carbon

The physics governing heat transfer in pyrolytic carbon are identical to what was introduced in the section dedicated to the thermal conductivity of silicon carbide and its degradation. Generally speaking, carbon allotropes feature thermal conductivities over a surprisingly large span. Carbon has the largest range of conductivity of any single element. At the ambient, it covers more than three orders of magnitude, starting with amorphous carbon, which conductivity is slightly less than  $1 \text{ W}\cdot\text{m}^{-1}\cdot\text{K}^{-1}$ , whilst diamond exhibits a conductivity of  $\sim 2'000 \text{ W}\cdot\text{m}^{-1}\cdot\text{K}^{-1}$  [41]

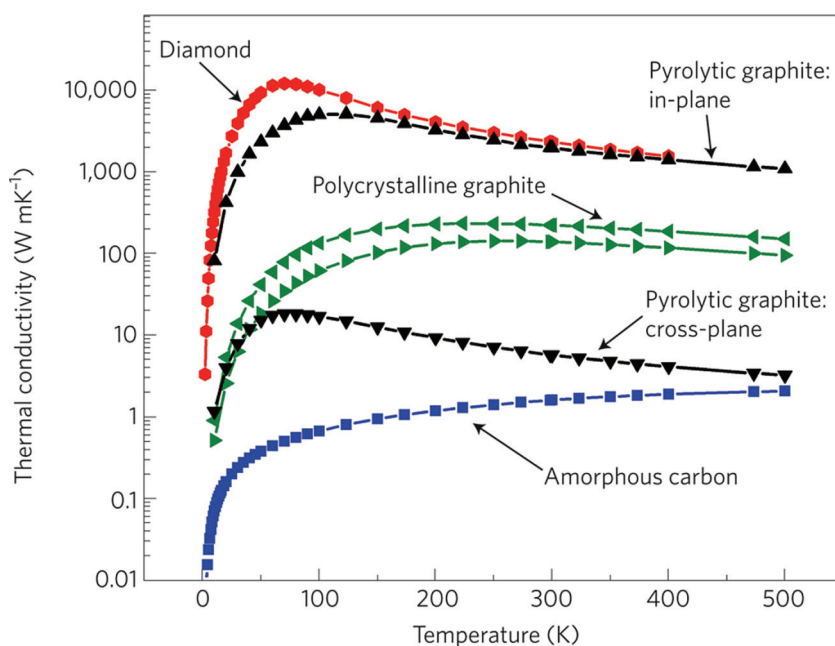


**Figure 1.12** – Thermal conductivity of carbon allotropes: amorphous carbon, pyrolytic and polycrystalline graphite and diamond. From [41].

Carbon allotropes such as diamond, in-plane graphite and graphene owe their high conductivities to their crystalline nature as well as to the efficient phonon transport granted by the strong  $\sigma$  molecular orbitals<sup>7</sup>. On the other hand, the  $\pi$  orbitals binding the graphene sheets of graphite transport phonons much more poorly, essentially because of their weaker binding.

Aside from these particularities due to the quasi two-dimensional structure of graphite, the same principles of phonons scattering against other phonons, grain boundaries or point- and planar-defects discussed in pages 9 to 13 apply here.

<sup>7</sup>Consult section 2.3 on page 77 for details on the hybridisation of carbon atoms.

### Radiation damage in graphite and PyC

Carbon atoms are rather easy to move from their lattice position. Indeed, the binding energy of atoms in graphite is about 7 eV, and the threshold energy  $T_d$  is reported to be somewhere between 24 and 60 eV [75]. However, several authors are making the point that a single  $T_d$  cannot be used for graphite-like carbon because of the difference in bonding strength along the c-axis and in the basal planes. Banhart proposes a  $T_d$  of 12 to 20 eV for displacement along the c-axis and another of about 30 eV in the basal planes [76]. Nevertheless, these energies are negligible compared to the potential 300 keV that the PKA can gain from the collision with a 2 MeV neutron, and displacements will indeed occur in graphitic structures such as PyC. Just as in most materials, interstitials and vacancies are created in the early stages of radiation damage. These defects do not have the same mobility: vacancies tend to stay at the location where they have been created, whereas interstitials easily migrate and cluster. The consequences of irradiation on the microstructure of graphite-like carbons is significant. Asymmetric dimensional changes have been shown to occur; the mechanisms driving these are the clustering of point defects into prismatic dislocation loops between graphitic planes, which can then grow into new planes. Figure 1.3 (d) and (e) show the two principal types of interplanar defects, known as *spiro*- and *divacancy* configurations [77]. Antisite defects do not migrate and cluster within the basal layers because the associated configurations are much less favourable in terms of energy compared to clustering between planes [78]. Thus, the material grows along the c-axis; this elongation has been shown to be significant with growth up to 300% in unconstrained HOPG [79]. One shall note that not all interstitials contribute to the formation of additional crystalline plane. Part of these also serve as nucleation sites for amorphous pockets [80, 81], which are further discussed later. The dimensional changes are asymmetrical because, while elongation along the c-axis occurs, shrinkage in the basal planes takes place. This contraction in the planes is associated with several mechanisms. Firstly, the topology of the atomic arrangement can significantly change while keeping the same bonding characteristics. Figure 1.3 (a), (b) and (c) show the break-up of the original hexagons into pentagons, heptagons or octagons. All these new configurations retain the in-plane  $sp^2$  bonding, but are accompanied with dimensional changes.

In addition, shrinkage is partly due to Poisson contraction caused by the elongation along the c-axis and the formation and concentration of vacancy lines in the planes. This process saturates at some point because of the elastic repulsion between the ends of different lines [77].

The most famous radiation effect in graphite is the accumulation of self- and strain-energy known as the *Wigner energy* [82]. The amount of stored energy associated with these non-ideally placed atoms can reach tremendous figures. The highest stored energy in graphite has been reported to be about  $2.7 \text{ kJ}\cdot\text{g}^{-1}$  [83]. This amount of energy, which given the heat capacity of graphite  $-0.72 \text{ kJ}\cdot\text{g}^{-1}\text{C}^{-1}$  – could result in extreme temperature elevations. The

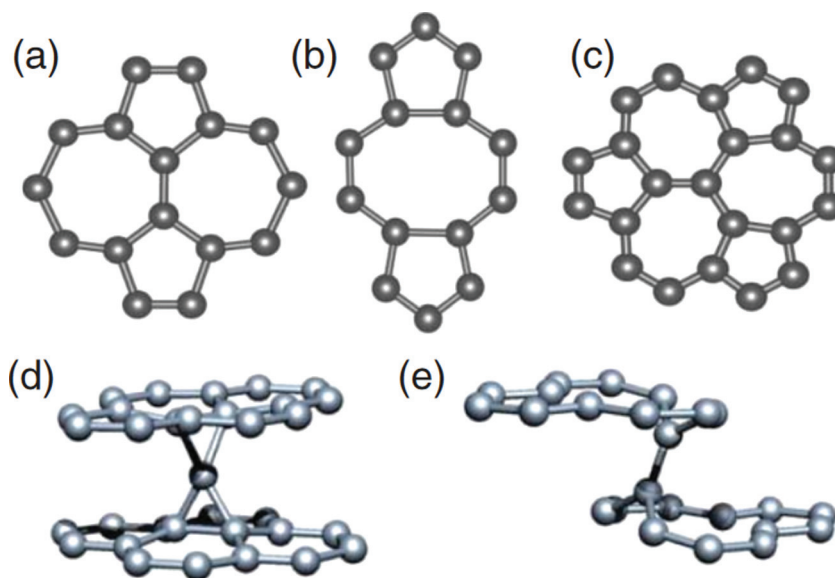


**Figure 1.13** – Types of planar (a), (b) and (c) and interplanar defects (d) and (e) in graphite. Reproduced from [78].

risk associated with this phenomenon is very real; a sudden release of this energy would result in temperature spikes exceeding 3500 K, which can potentially set fire to graphite structural components. This is believed to have been in part the cause of the Windscale nuclear accident [84].

Lastly, graphite and pyrocarbons are known to amorphise under irradiation. This damage mechanism usually appears after dimensional changes since it relies on the succession of three phenomena. As is the case for the other two radiation damage effects, amorphisation starts with the creation and accumulation of point defects in the microstructure. The clustering of vacancies in lines results in the destruction of long-range ordering. The outcome is a microstructure made of nanocrystalline domains connected by dislocation dipoles [80] and small amorphous pockets [81]. Due to their pinning by amorphous domains, the graphene sheets start to buckle and ripple. Indeed, interstitials and pockets are bridging the graphene planes, which hinders the accommodation of associated stresses through dimension changes in the basal directions. In a final stage, as the amorphous domains increase in size and number density, the graphene sheets start to break in smaller layers, which finally disappear. Although the long-range order is completely lost, and the material is fully amorphised, a fraction of the carbon atoms retain their original coordination number of 3, i.e. they are still hybridised in  $sp^2$  states, which is the reason why amorphous carbon does have a mixture of  $sp^2$  and  $sp^3$  hybrids [81].

### 1.5 Samples

SiC/SiC samples have been acquired from several industry key players, as well as from former research activities. These came either in form of plates or other small featureless volumes or as prototype cladding tubes produced by General Atomics/Westinghouse and CEA. In the first category, an aerospace grade SiC/SiC and a nuclear grade composite have been used either for training purposes in the case of the former or as a subject of study for the latter.

The second type of samples was obtained through the participation in the *Materials' Innovations for Safe and Sustainable Nuclear in Europe* (MatISSE) and the *Collaboration for Advanced Research on Accident Tolerant Fuel* (CARAT) research programs. In both cases, sections of experimental cladding were obtained from industrial partners.

#### 1.5.1 Non-tubular samples

Prior to the beginning of this project, SiC/SiC composites were obtained from two sources. These came in the shape of a large plate and small platelets and were placed at our disposal by the *Deutsches Zentrum für Luft- und Raumfahrt* (DLR), as well as CNRS-SNECMA. Details on these materials are given in the following pages.

##### DLR training material

A plate of composite material produced by DLR was used in the early stages of the project as training material to learn TEM sample preparation techniques such as dimple and tripod polishing and, more importantly, focused ion beam (FIB) milling. This material was not worth further studying in the frame of the thesis, since it neither came in a form which could be used for thermal conductivity measurements, nor was it representative of nuclear grade silicon carbide CMCs [85]. The SEM micrograph featured on Figure 1.14 shows the polished surface of a piece of this material. The organisation of the fibres in tows with varying orientation is typical for all the SiC/SiC composites investigated in this work. The seemingly much larger fibres on the right-hand side of the image are simply not seen with their axis perpendicular to the surface normal and is a result of the 2D weave used in most fibre reinforced composite materials.

This SiC/SiC sample shares most of its features with nuclear grade composites, since the fact that the fibres are not nuclear grade cannot be seen on a SEM micrograph. The porosity of this sample is actually higher than that of the other samples studied in the dissertation.

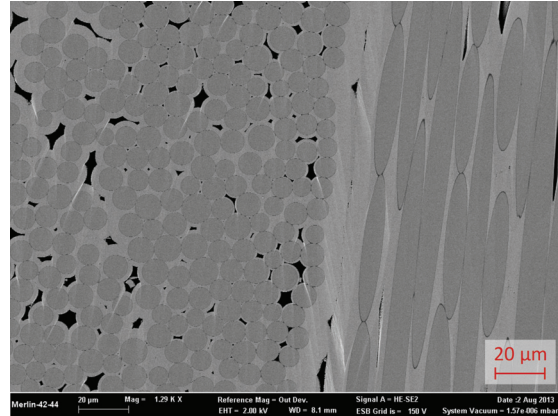


**Figure 1.14** – SEM micrograph showing the architecture of the DLR SiC/SiC composite

### CNRS SNECMA SiC/SiC

Both pristine and neutron irradiated SiC/SiC prepared by the SEP laboratory of the university of Bordeaux (Laboratoire d'ingénierie des matériaux et de hautes pressions) and the *Société nationale d'étude et de construction de moteurs d'aviation* (SNECMA), now Safran [86], were obtained prior to the beginning of this project via a collaboration with the Nuclear Research and Consultancy Group (NRG) [87]. These samples are made of a three-directional weave of Hi-Nicalon fibres densified with a CVI SiC matrix. The density of the composite is  $2.55 \text{ g}\cdot\text{cm}^{-3}$ , which translates in an average porosity of 21.5%. A disc, with a diameter of ca 2 mm, was put with other samples in the sixth drum of the SICCROWD [88] experiment, in the high flux test reactor (HFR) in Petten, Netherlands [89]. The neutron irradiation occurred at temperatures ranging between 782 and 810°C, with an average of 796°C [90]. The fast neutron dose<sup>8</sup> was measured in the range of  $2.7$  to  $3.5\cdot 10^{25} \text{ n}\cdot\text{cm}^{-2}$ . The fast neutron fluence was translated into dpa by Ralph Hania [90]. In the case of the A034 sample, the irradiation resulted in  $1.92\pm 15\%$  dpa. Little irradiation-induced swelling of these sample was measured by linear variable differential transducer (LVDT [91]) and reported by Hegeman and al. [88]: this particular sample experienced 0.09% of longitudinal, 0.5% of width and 0.5% of height swelling, translating into an average volume change of 1%.

This material has been used for the microscopy part of the thesis only. Because the only available material came in form of small platelets and discs, no thermal conductivity measurements could have been carried out using our radial heat flow apparatus<sup>9</sup>. FIB lamellae were extracted from both the pristine and neutron irradiated bulk material and characterised

<sup>8</sup>Radiation damage in neutron irradiations is usually calculated on the basis of the fluence of fast neutrons ( $E > 0.1 \text{ MeV}$ ), since collision events with less energetic neutrons will not cause much damage.

<sup>9</sup>The thermal diffusivity of these samples was measured with the laser flash method by Hegeman et al. [88]

by EFTEM. A lamella of pristine material was also irradiated in-situ at the JANNuS, Orsay facility [92]. This material is later referred to as either the “Petten” SiC/SiC or by its designation A034.

### 1.5.2 Prototype cladding tubes

Through the participation of ANM to the CARAT and MatISSE programs, prototype fuel cladding was obtained from General Atomics/Westinghouse and CEA, respectively. These samples feature the two main design routes selected for solving tightness issues against both cooling water ingress and fission gases egress. GA/Westinghouse has a design based on the use of monolithic SiC layers, whereas CEA has taken an approach involving a metallic liner.

#### General Atomics/Westinghouse

Samples obtained from the CARAT program will be referred to as *GA samples* from this point forward. Both pristine and neutron irradiated sections of cladding tubes were obtained via our participation to CARAT. The overall concept of the composite cladding developed by GA is known as a *triplex* cladding. It consists in having a tube composed of three consecutive layers, out of which the inner and outer ones are made of monolithic silicon carbide, and only the central layer is a SiC/SiC composite. The pristine GA/Westinghouse samples are fabricated using a 2D weave of Hi-Nicalon Type-S fibres reinforcing a CVI SiC matrix. The PyC interphases found in these samples are about 50 to 100 nm thick.

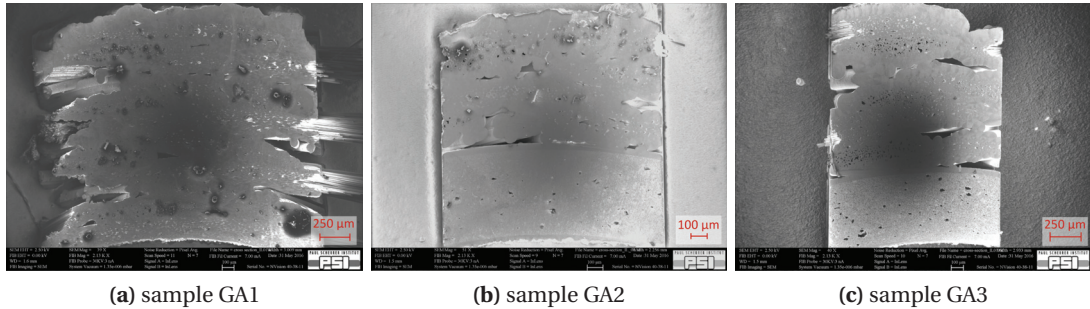
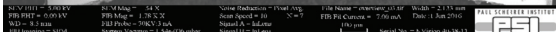


**Figure 1.15** – Cross-sectional views of the GA1, GA2 and GA3 samples. The difference within this batch is the thickness of the inner SiC monolith. The inner and outer radii of the tubes are seen at the bottom and top of the micrographs.

Two batches of samples were obtained through our participation to the CARAT project. Firstly, three sections of about 12 cm were received. These are made of either pure SiC/SiC (GA1) or have a duplex architecture (GA2 and GA3), with a  $\sim 460 \mu\text{m}$  SiC monolith on the inside of the tube whilst the outer layer is composite. A representative view of the cross-section of





## Chapter 1. Silicon carbide composites

**Table 1.3** – Specifics of the neutron irradiated GA/Westinghouse samples. Dimensions in millimetres.

Sample name	R7 (10-2)	H1-4	F4-5
Length [mm]	45	34.5	47.5
Outer diameter [mm]	10.05	10.80	10.60
Inner diameter [mm]	8.15	8.80	8.80
Exposure [MWd]	1871	933	848
Dose [dpa]	1.26	0.66	0.6

### CEA

Lastly, samples prepared according to the patented *Sandwich* [95] architecture were obtained from CEA through membership in the MatISSE research program. About twenty tube sections have been received; the thermal conductivity of most of these has been measured using our custom-made apparatus. The sandwich sections, a cross-section of which is shown in Figure 1.17b, contains a metallic liner made of tantalum. The choice of this metal over other possibilities is motivated by its properties at elevated temperatures as well as its low impact on the neutron economy.

These samples come in three main categories, two of which are shown in Figure 1.17; simple SiC/SiC (Figure 1.17a) and sandwich (Figure 1.17b).

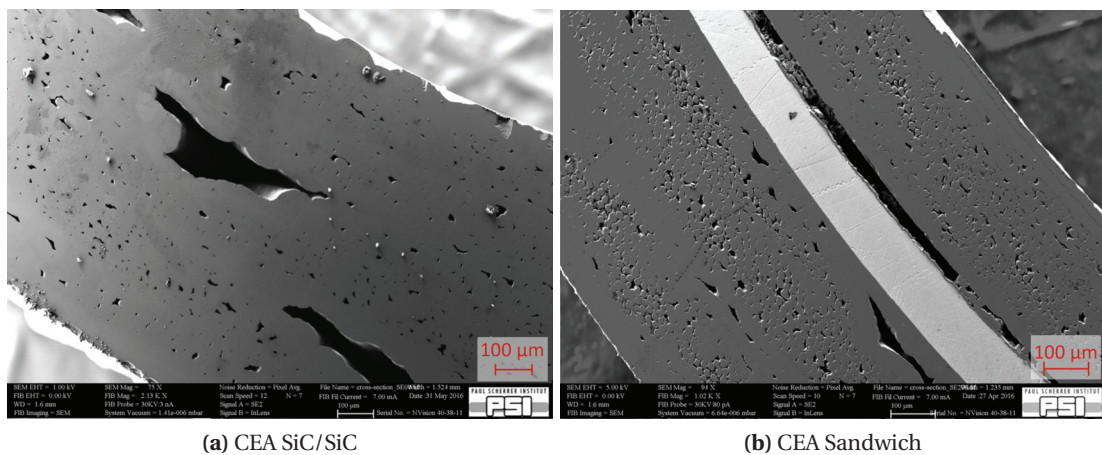


**Figure 1.17** – SEM micrographs showing cross-section views of a SiC/SiC tube **(a)** and a sandwich cladding section **(b)**. The bright layer in **(b)** is the tantalum liner “sandwiched” between the two SiC/SiC layers.



The reason for measuring pre-damaged tubes is to investigate whether the additional cracks have a detrimental effect on the thermal conductivity of the clad.

### **1.5.3 Summary of samples and measurements**

Not all the experimental techniques were applied on all of the samples obtained from our different suppliers. As an example, CEA prototypes were sent in groups of three sections, two longer ones of about 20 cm, and a shorter one of about 10 cm. The long ones have been used for the thermal conductivity measurements, whilst the shorter samples have been prepared for SEM observation.

Similarly, the neutron irradiated samples obtained from GA/Westinghouse proved extremely difficult to prepare. Only the H1-4 sample could be fully characterised. The other two samples, 10-2 and F4-5, featured extensive cracking, thus making them hard to polish. Though they nevertheless could be polished, they featured practically no carbon interlayer.

Table 1.4 on page 56 shows the entirety of the samples, as well as the tests carried out on these.

**Table 1.4** – Sample studied in this work with their characteristics, as well as measurements carried out on them. In the "design" column, *sand* stands for sandwich and SiC/SiC for simple composite architectures. The bracketed dashes mean that experiments were carried out, but that no relevant results are worth reporting. The porosities  $v$  are those of the composite layers only, since as far as modelling is concerned, this quantity is the relevant one.

Supplier	Group	Name	L [mm]	D <sub>in</sub> [mm]	D <sub>out</sub> [mm]	Mass [g]	$v$ [%]	Fibres	design	TC	SEM	TEM	Irradiation
CEA	SAND	I2-1	190.57	7.71	9.82	23.23	44.1			✓	✓	✓	✓
		I2-2	191.53	7.72	9.83	23.84	47.5			✓	✓	✓	✓
		I2-3	100.33	7.72	9.78	12.07	44.5			✓	✓	✓	✓
		I3-1	192.95	7.71	9.78	23.32	45.2			✓	✓	✓	✓
		I3-2	190.05	7.71	9.78	23.03	45.8	HNLS	sand	✓	✓	✓	✓
		I3-3	100.07	7.71	9.78	12.00	43.4			✓	✓	✓	✓
		L3-1-pre	138.88	7.7	9.78	16.96	46.4			✓	✓	✓	✓
		L3-2-pre	145.02	7.71	9.78	17.33	43			✓	✓	✓	✓
		L3-3-pre	142.24	7.71	9.78	17.23	45.4			✓	✓	✓	✓
	SIC	I2-1	96.95	7.81	9.74	7.44	55.2			✓	✓	✓	✓
		I2-2	190.58	7.81	9.77	14.97	55.8	HNLS	SiC/SiC	✓	✓	✓	✓
		I2-3	192.32	7.81	9.75	14.78	54.8			✓	✓	✓	✓
GA/Westinghouse	GA	1	102.68	7.39	10.91	12.07	27.1			✓	✓	✓	ions
		2	103.00	8.23	10.92	9.65	34.5	HNLS	duplex	✓	✓	✓	
		3	102.80	8.15	11.63	13.43	28.1			✓	✓	✓	
	H1-4 (R7) 10-2 F4-5		34.75	8.80	10.80	2.76	20.7	Sylramic		✓	✓	✓	neutrons
			45	8.15	10.05	3.18	31.5	HNLS	triplex	✓	✓	✓	
			47.5	8.8	10.6	2.64	21.4			✓	✓	(✓)	
	A034				n.a.				SiC/SiC	✓	✓	✓	ion & neutrons
SNECMA													
DLR			n.a.						SiC/SiC	✓	(✓)	(✓)	✓

## 2 Electron Microscopy

The electron microscopy techniques used in this thesis are discussed in the present chapter. The necessary theoretical background of energy-filtered TEM and electron energy-loss spectroscopy as well as the instrumentation used in these techniques are presented. Additionally, the measurement and quantification of the  $sp^2$  to  $sp^3$  ratio, used to characterise the graphitic degree of the PyC interlayers, are explained. Details concerning the acquisition, experimental conditions and data processing are also discussed.

## 2.1 Introduction

Ever since their inception in the 1930s [96, 97], electron microscopy techniques – be it in the transmission (TEM) or later in the scanning (SEM from the 1950s) modes – have become common practice in materials science. The reason for using electrons in the frame of microscopy is their much smaller De Broglie wavelength than that of visible light<sup>1</sup>. Figure 2.1 shows a plot of the wavelength in nanometres of electrons accelerated to typical SEM and TEM voltages<sup>2</sup>.

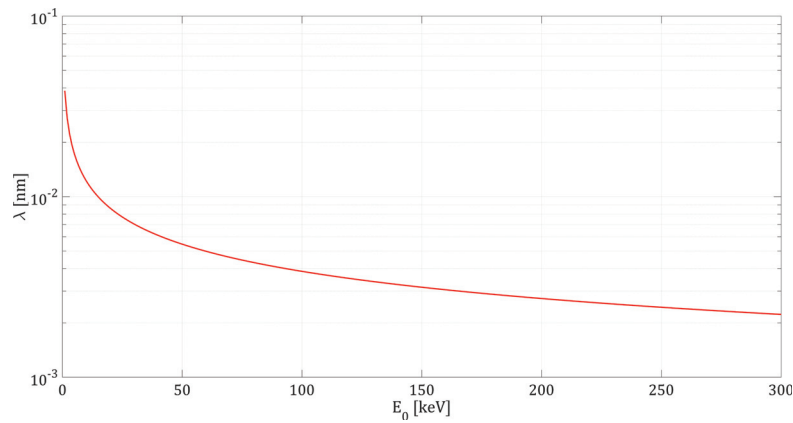


**Figure 2.1** – De Broglie wavelength of electrons accelerated at voltages typical for electron microscopy

The actual resolution of a TEM is not as high as the theoretical limit given by De Broglie. Due to the many aberrations introduced by the electromagnetic lenses used to condense and project the electron beam, what a user can realistically expect ranges between 2.5 – for a conventional TEM – and 0.5 Å in the case of a top-of-the-line  $C_s$ -corrected TEM. In addition to their very high resolution, the interactions between the incident electrons and the studied sample give rise to many signals such as X-rays, secondary electrons, cathodoluminescence and Auger electrons. This results in a very wide panel of analytical techniques, such as electron diffraction, various imaging modes, chemical analysis and spectroscopy, making SEMs and TEMs one of the most common tools in materials science.

In the frame of the present PhD work, electron microscopy has been extensively used as an analytical technique and as an in-situ irradiation facility. SEM was used to characterise the cross-sectional structure of the SiC/SiC cladding tubes and to a limited extent in combination with the Focused Ion Beam (FIB) to address the three-dimensional organisation of the PyC interphase and the small-scale porosity found within strands of fibres. More importantly,

<sup>1</sup> 200 nm with violet light (shortest  $\lambda$ ) from the Rayleigh criterion [98]

<sup>2</sup>  $\lambda = h/p \approx 1.22/\sqrt{E}$ , with  $h$  the Planck constant,  $p$  the momentum of the electron and  $E$  its speed in eV [99]

PSI's Zeiss Nvision40 FIB-SEM was used to produce thin samples extracted from areas of interest of the SiC/SiC tubes. This samples preparation route has been chosen primarily because mechanical polishing to thicknesses reasonable for a subsequent ion milling (PIPS) is extremely difficult. Indeed, in most cases, the fibres and matrix start losing their cohesion when the sample thickness approaches 100 to 60  $\mu\text{m}$ . Thinning via electro-polishing is also not possible because of the architecture of the composite. Indeed, the solutions of HF,  $\text{H}_2\text{SO}_4$  and  $\text{HClO}_4$  required to thin SiC would attack and dissolve the PyC interphase well before the sample is thin enough to be electron-transparent.

There is a major drawback coming along with the use of FIB as the sole preparation technique. The necessity of preparing samples where fibres and interphase are seen along their axial direction, i.e. in cross-section, makes the preparation more difficult. Since the FIB lamellae are extracted normal to the sample surface, one needs to polish sections of tubes on their circumference and in a radial direction. Though such an operation is not very difficult with a tripod polisher, the fibres are mostly invisible once the sample is polished and ready to be brought in the FIB. Therefore, the time required to prepare lamellae with the FIB is significantly increased, since one needs to find a fibre to start with. In addition to this, the size of the lamellae must be sufficiently large to accommodate at the very least the intersection of two fibres. Samples are typically 20 to 35  $\mu\text{m}$  wide, 15 to 25  $\mu\text{m}$  high and about 80 to 140 nm thick.

TEM was used for different purposes, from simple sample quality checks to EFTEM mapping. A JEOL 2010 was used at PSI as a training microscope as well as to control whether TEM lamellae were ready for further analysis at EPFL. Energy-filtered TEM was carried out at EPFL using CIME's JEOL 2200FS, and STEM-EELS spectrum imaging was performed on a FEI Titan Themis. In addition to this, an in-situ ion irradiation was carried out with a modified FEI Tecnai G<sup>2</sup> 20 at the JANNuS Orsay facility in France.

## 2.2 Spectroscopic techniques in the TEM

Electron energy-loss spectroscopy, abbreviated EELS, is a very powerful analytical technique available in the TEM. In EELS, the energy spectrum of the electrons going through a sample is recorded and analysed. Since we are dealing with highly energetic electrons, typically accelerated between 100 and 300 keV, and thin samples which are at most a few hundreds of nanometres thick, most of the incident electrons are simply transmitted without losing energy. Nevertheless, some electrons interact with the atoms found in the volume of the sample. When such interactions occur, the electrons can either lose some energy or not. We then speak of *inelastic* or *elastic* scattering, respectively. EFTEM is another technique based on the observation of inelastically scattered electrons. The difference here is that images are

recorded instead of spectra. In either case, inelastic scattering is at the core of the observed physical phenomena. It is therefore important to understand the quantities and mechanisms involved in the energy loss of electrons.

### 2.2.1 Electron scattering

Since the analytical techniques used in this thesis are based on inelastic scattering, no detailed discussion of elastic scattering will be made. Figure 2.2 shows the classical representation of elastic (a) and inelastic scattering (b) and (c).

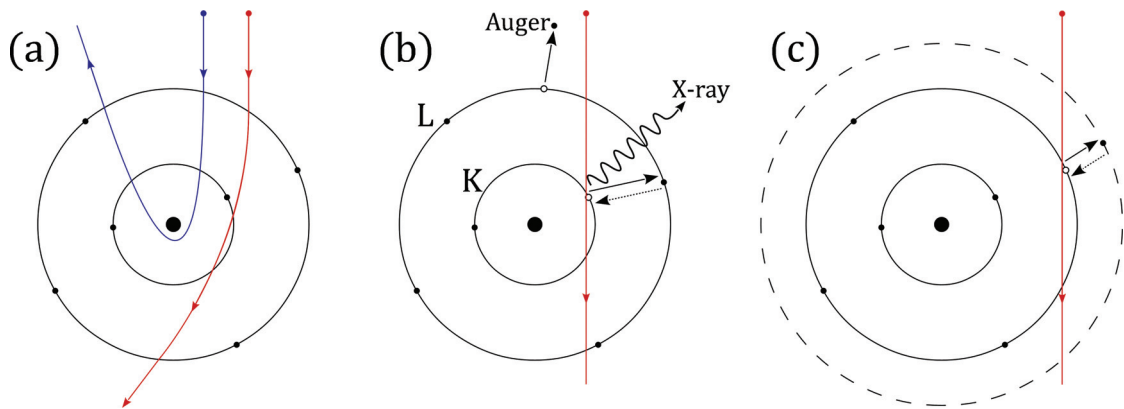


**Figure 2.2** – Elastic scattering of an incident electron with the nucleus (a), inelastic scattering with an inner-shell atomic electron (b) and with an outer-shell atomic electron (c). Based on [100].

Inelastic scattering occurs via Coulomb interactions with either inner-shell, or outer shell electrons, schematically represented in Figure 2.2 (b) and (c), respectively. In the latter case, an atomic electron lying on a low energy level below the Fermi level is excited to a higher energy state above the Fermi level. Thus, this electron gains at least its binding energy from the incident fast electron, leaving the atom in an ionised state. Upon relaxation to the ground state, one of the electrons occupying energy levels higher than the hole left by the aforementioned excitation process will transition to this lower energy state. During this process, the excess energy is released as a photon (X-ray) or is shed as kinetic energy to another electron, leading to the emission of an Auger electron (right-hand side of Figure 2.3).

The other mechanism through which an incident electron might lose some of its energy is through Coulomb scattering with outer-shell electrons, sketched on Figure 2.2 (c). This can occur either with a single outer-shell electron, in which case it jumps to a higher empty energy state, or with the electron gas of the sample. This is schematically represented in the centre of Figure 2.3. More details are available in Egerton [100]. In the de-excitation process, the excess

energy can be released as photons, which can be in the visible spectrum. In this case we speak of *cathodoluminescence*, represented on the right of Figure 2.3. Alternatively, the energy is simply dissipated as heat within the material.

In the second option, the excitation takes the form of a collective resonance which can be described by a quasi-particle called a *plasmon*. The energy of the plasmon is quantified and characteristic of the element with which the electron is interacting, typically between 5 and 20 eV [100, 101]. The fingerprints of plasmon oscillations are visible in the low-loss part of an EELS spectrum, a few tens of eV after the zero-loss peak (ZLP). Depending on the thickness of the sample, plasmon scattering is characterised by a series of peaks at multiples of the plasmon energy  $E_p$ , which can be a hindrance to the interpretation of spectral data.

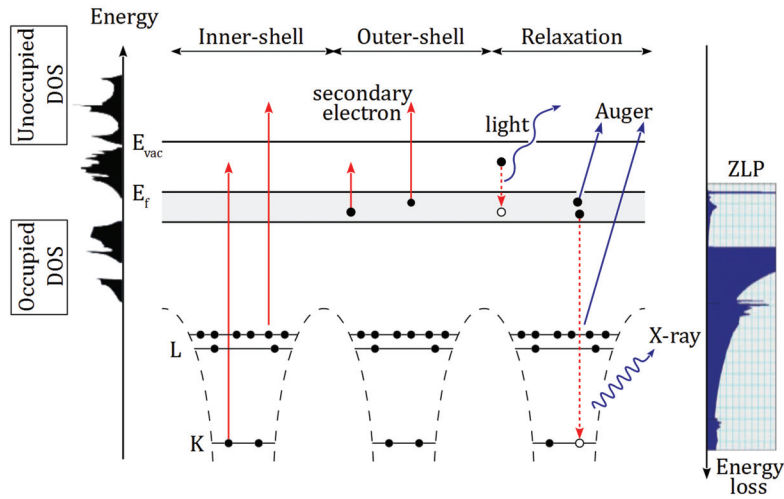


**Figure 2.3** – Diagram of the energy levels of a solid.  $E_f$  is the Fermi level, and  $E_{vac}$  is the vacuum energy. The grey area below  $E_f$  represents the delocalised states of a valence band. A representation of the DOS, both occupied and unoccupied, are shown on the left-hand side of the figure. Last, an example of an EELS spectrum is displayed on the right of the sketch. This figure is based on drawings from [100] and lecture material from Prof. Hébert.

An EELS spectrum is usually separated in three domains, according to the increasing energy involved in the scattering interaction, i.e. increasing energy losses. Firstly, the zero-loss peak includes the electrons which have either lost so little energy that it cannot be measured or no energy at all. Secondly, the low-loss part of the spectrum, which corresponds to inelastic scattering with outer shell electrons, and thirdly, the core-loss part, which is due to interactions with inner-shell electrons. A spectrum acquired on a SiC/SiC lamella is displayed in Figure 2.4. The lower-left part shows the zero-loss peak (ZLP) and low-loss part of the spectrum, whereas

the top right part shows the core-loss taken at the carbon ionisation K-edge. All of these structures are lying on an exponentially decreasing background, made of the high-energy tails of the scattering events which took place at lower energy levels.

The fine structure of the core-loss part of the spectrum is the part that is analysed to identify the carbon allotropes through a quantification of the ratio between the peaks corresponding to  $sp^2$  to  $sp^3$  states. In Figure 2.4, no noticeable features can be distinguished since this spectrum was acquired over a large area of about  $1\ \mu\text{m}$  radius containing silicon carbide and pyrolytic carbon.

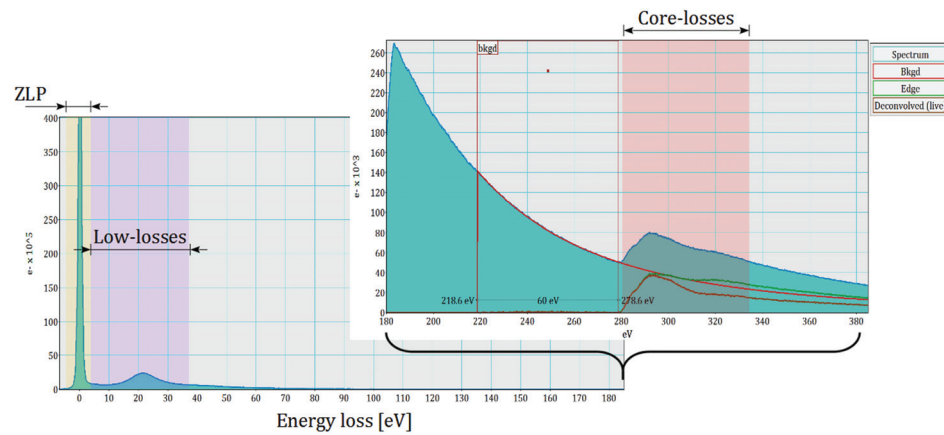


**Figure 2.4** – EELS spectrum recorded on a carbon containing sample. ZLP in orange shaded area, low-losses in purple and core-losses in red.



### 2.2.2 Magic angle conditions

In materials featuring an anisotropic electronic structure, EELS and EFTEM measurements can be severely affected by errors due to the difference in the components of the momentum transfer, parallel and perpendicular to the direction of motion of the electron. In addition, the electric field surrounding a fast-moving electron is not uniform but is in fact flattened and rather ellipsoidal than spherical. The combination of these two elements, the anisotropy of the target atoms electronic structure and the orientation of the sample in the TEM usually result in widely differing spectra if those are not recorded in a specific combination of convergence and collection semi-angles.

Figure 2.5 shows EELS spectra acquired at the boron nitride K-edge at a combination of convergence and collection semi-angles either below (Figure 2.5a) or above (Figure 2.5b) the magic angle conditions.

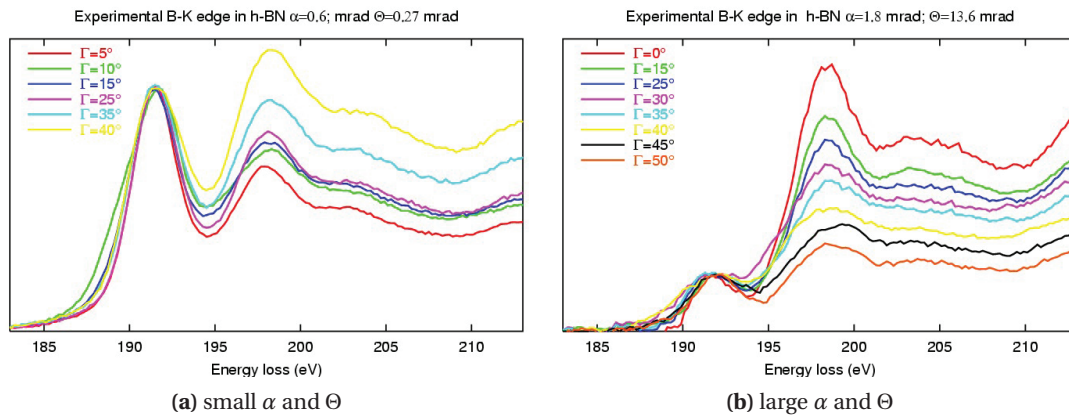


**Figure 2.5** – EELS spectra acquired at the boron K-edge of boron nitride samples at different tilt ( $\Gamma$ ) angles: small convergence  $\alpha$  and collection  $\Theta$  angles (a) and large convergence and collection angles (b). Graphs obtained from Prof. Hébert.

These spectra show well how significant anisotropy effects can be. The same phenomenon can be observed with graphite or pyrocarbon, because BN has a hexagonal lattice featuring an electronic structure very similar to that of graphite-like carbon. Any meaningful quantification of the peak areas relative to each other would be impossible in spectra such as the ones shown in Figure 2.5. The conditions in which these effects can be cancelled out through the choice of appropriate convergence and collection angle pairs are known as the *magic angle conditions*, shortened MAC.

To determine the MAC, one has to analyse the *double differential scattering cross-section* (DDSCS) in detail. The geometry used to analyse the transfer of momentum between the incoming electrons and the sample is shown in Figure 2.6. The fact that the incident electrons are losing energy means that the wave vector  $k$  is shortened by the interaction. The momentum transfer  $q$  is drawn on the right side of Figure 2.6. This vector is separated in its two components,  $q_{\perp}$  and  $q_{\parallel}$ , the momentum transfers perpendicular and parallel to the direction of travel of the incident electron. Since  $\theta \ll 1$ , the shortening of  $k$  is directly proportional to  $q_{\parallel}$ .

$$\vec{q} = \vec{k}_i - \vec{k}_f \quad (2.1)$$

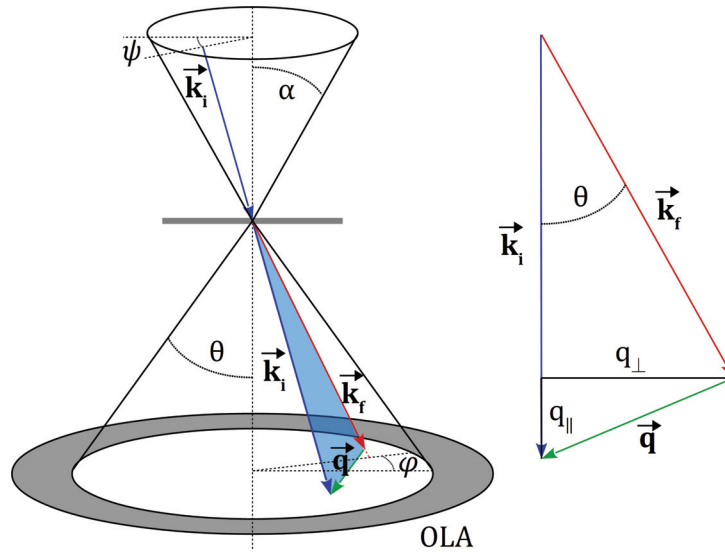


**Figure 2.6** – Schematic drawing of the scattering geometry (left) and enlarged representation of the momentum transfer (left). Based on a figure from [102].

The relationship between the convergence and collection semi-angles  $\alpha$  and  $\theta$  and the momentum transfer  $q$  is expressed in the DDSCS, i.e. the probability of the interaction at a given energy and angular condition. Since electrons accelerated at typical TEM voltages are moving at a significant portion of the speed of light  $c$ , a full or semi-relativistic treatment

of the inelastic scattering cross-section is necessary. The complete mathematical treatment can be found in references [102, 103]. The main results are presented here. Firstly, in its semi-relativistic limit, the DDSCS is expressed by Equation 2.2.

$$\frac{\partial^2 \sigma}{\partial E \partial \Omega} = \frac{4\gamma^2}{a_0^2 Q^2} \frac{k_f}{k_i} S(\mathbf{q}, E) \quad (2.2)$$

Where  $Q = q^2 - q_z^2 \beta^2$ ,  $a_0$  is the Bohr radius,  $\mathbf{k}_i$  and  $\mathbf{k}_f$  the wave vectors of the incident before and after scattering,  $\gamma$  the relativistic factor  $(1 - v_0^2/c^2)^{-1/2}$ ,  $\mathbf{q}' = \mathbf{q} - q_z \beta^2 \hat{\mathbf{z}}$  with  $\mathbf{q} = \mathbf{k}_f - \mathbf{k}_i$ ,  $\beta = v_0/c$  and  $S(\mathbf{q}, E)$  the dynamic form factor which contains information on the orientation of the sample. The z-axis is the direction of motion of the incoming electron. Based on the geometry shown in Figure 2.6, the momentum transfer at a given collection and illumination angles  $\Theta$  and  $\alpha_0$  is:

$$\mathbf{q} = \begin{pmatrix} k_i (\theta \cos \varphi - \alpha \cos \psi) \\ k_i (\theta \sin \varphi - \alpha \sin \psi) \\ k_i \theta_e \end{pmatrix} \quad (2.3)$$

With  $\theta_e$  the characteristic angle at which the energy loss  $\Delta E$  occurs. This angle is defined as the half width at half maximum of the Lorentzian distribution describing the energy loss as function of the scattering angle  $\theta_e$  and is equal to  $\Delta E / \gamma m_0 v^2$ . Inserting Equation 2.3 into the DDSCS introduced in Equation 2.2 lets one integrate it over the angles  $\phi$ ,  $\psi$ ,  $\alpha$  and  $\theta$ . This part of the treatment can be found in [102] and [103]. Additionally, the orientation of the sample relative to the laboratory system is introduced with a rotation matrix as a function of the tilt angles  $\Gamma$  and  $\Psi$ . The scattering cross-section can then be expressed in a given  $\Gamma$ ,  $\Phi$ ,  $\alpha_0$ ,  $\Theta$  and  $E$  interval. Thus, the quantity  $\Delta \sigma$  becomes a function of two integrals, noted  $a(\alpha_0, \Theta)$  and  $c(\alpha_0, \Theta)$ , which are functions of the convergence and collection angles and represent the scattering cross-section components parallel and perpendicular to the electron motion direction:

$$\begin{aligned} a(\alpha_0, \Theta) &= \frac{1}{\pi \bar{\alpha}_0} \int_0^{2\pi} d\psi \int_0^{\bar{\alpha}_0} \bar{\alpha} d\bar{\alpha} \int_0^{\bar{\Theta}} \frac{\bar{\theta}^2 + \bar{\alpha}^2 - 2\bar{\theta}\bar{\alpha} \cos \psi}{(\bar{\theta}^2 + \bar{\alpha}^2 - 2\bar{\theta}\bar{\alpha} \cos \phi + 1)} \bar{\theta} d\bar{\theta} \\ c(\alpha_0, \Theta) &= \frac{1}{\pi \gamma^2 \bar{\alpha}_0^2} \int_0^{2\pi} d\psi \int_0^{\bar{\alpha}_0} \bar{\alpha} d\bar{\alpha} \int_0^{\bar{\Theta}} \frac{1}{(\bar{\theta}^2 + \bar{\alpha}^2 - 2\bar{\theta}\bar{\alpha} \cos \phi + 1)} \bar{\theta} d\bar{\theta} \end{aligned} \quad (2.4)$$

These integrals have been scaled relative to the beam energy by the introduction of  $\gamma$  in the second integral as well as through a scaling of the angles:

$$\bar{\alpha}_0 = \frac{\gamma \alpha_0}{\theta_e} \quad \text{and} \quad \bar{\Theta} = \frac{\gamma \Theta}{\theta_e} \quad (2.5)$$

Both integrals  $a$  and  $c$  can be explicitly solved (see [102]) and the MAC can be determined by solving  $a = c$ , the traces of which are presented in Figure 2.7a. The conditions drawn on the right of the aforementioned figure are valid for the carbon K-edge specifically. A plot of the carbon K-edge characteristic angle  $\theta_e$  as well as the electron velocity is shown in Figure 2.8.

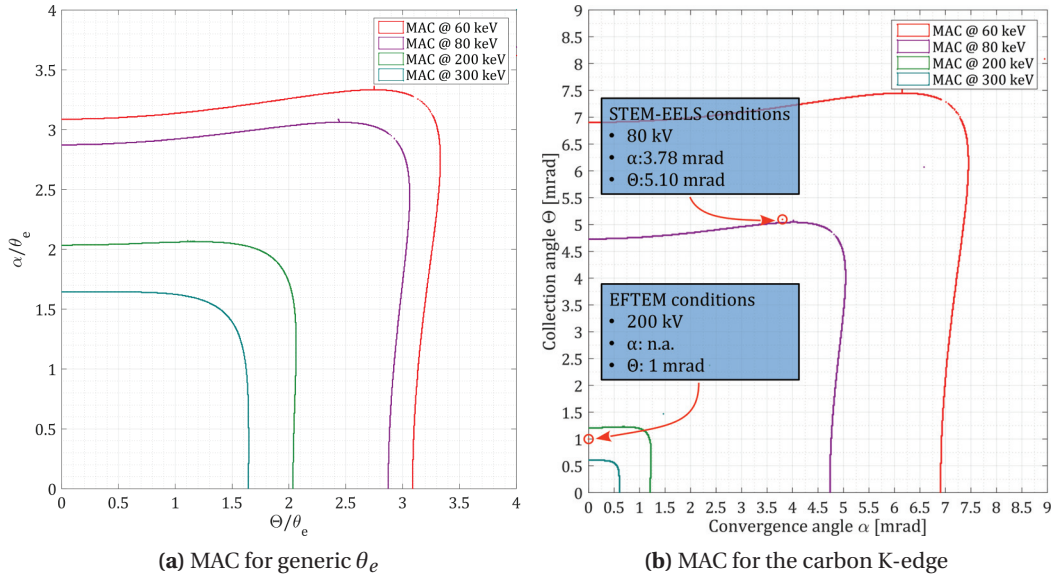


**Figure 2.7** – Trace of the MAC as a function of the inelastic scattering characteristic angle **(a)** and at the carbon K-edge **(b)** for a beam of 60, 80, 200 and 300 keV electrons. The circled location on the carbon MAC **(b)** correspond to the experimental conditions in which spectrum images were recorded in STEM-EELS at 80V kV, as well as EFTEM at 200 keV.

The MAC have been mapped for general STEM-EELS conditions with electron energies of 60, 80, 200 and 300 keV, since EFTEM maps were acquired both in EFTEM mode using a JEOL 2200FS at 200 kV and in STEM-EELS on a FEI Titan operated at 80 kV. As the latter can operate at the four corresponding tensions, the MAC were determined for each acceleration available. The relevant parameters used in the calculations are gathered in Table 2.1.

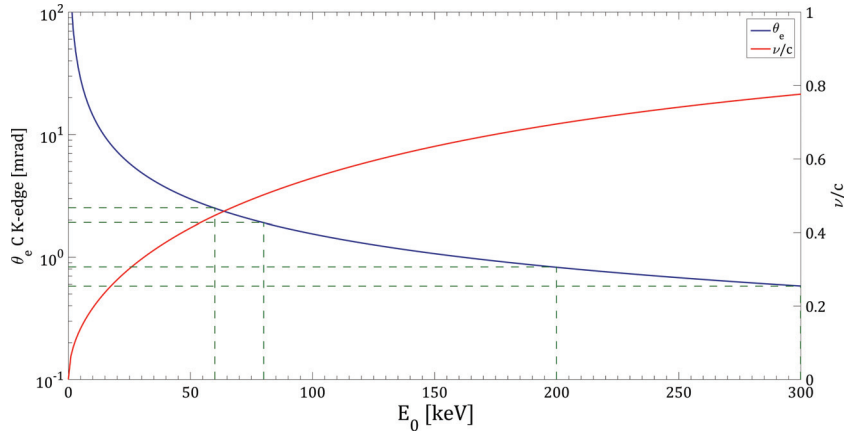


**Figure 2.8** – Carbon K-edge characteristic angle (blue) and electron velocity (red) as a function of the TEM acceleration voltage. The dashed green lines highlight  $\theta_e$  at the FEI Titan voltages (60, 80, 200 and 300 kV).

**Table 2.1** – Summary of the relevant parameters necessary to calculate the MAC at the acceleration voltages of the FEI Titan in STEM-EELS and JEOL 2200 FS in EFTEM ( $\Theta_{\text{MAC}} \parallel \text{beam}$ ), i.e. in TEM with a parallel illumination

$E_0$ [keV]	$v/c$	$\gamma$	$\theta_e$ [mrad]	$\Theta_{\text{MAC}} \parallel$ [mrad]	$\theta_B(002)$ [mrad]
60	0.4462	1.1174	2.498	6.902	7.42
80	0.5024	1.1566	1.9039	4.732	6.43
200	0.6953	1.3914	0.8262	1.209	4.07
300	0.7765	1.5871	0.5807	0.602	3.32

The last row of Table 2.1 gives the angle of the innermost diffraction ring of pyrolytic carbon, namely the reflections coming from the (002) graphitic planes. For the measurement to make sense, this must lie outside of the GIF entrance (STEM-EELS) or be cut-off by the objective lens aperture (EFTEM).

Figure 2.9 shows two spectra acquired with either no tilt (red spectrum) or at a very high tilt of 60 degrees, using a tomography holder on highly-oriented pyrolytic graphite (HOPG). These were acquired on a FEI Titan Themis at 80 kV, with a convergence angle of 3.78 mrad and a collection angle of 5.1 mrad<sup>3</sup>, conditions which are almost exactly on the trace of the MAC shown in Figure 2.7 b. These two spectra are practically identical, with minor differences, in part because when the sample is tilted at 60 degrees, the thickness through which the electrons travel is practically double that at no tilt. In addition to this, the resolution of the spectrum

<sup>3</sup>The actual perfect MAC would be at  $\Theta=5.03$  mrad, which cannot be achieved since the range of convergence angles is limited by the available camera lengths.

acquired without tilt seems to be better, meaning that the difference in height of the 284 eV dip could be explained by Gaussian broadening. Even though a Fourier ratio deconvolution is performed using simultaneously recorded low-loss spectra, minute differences such as those seen here can be expected.

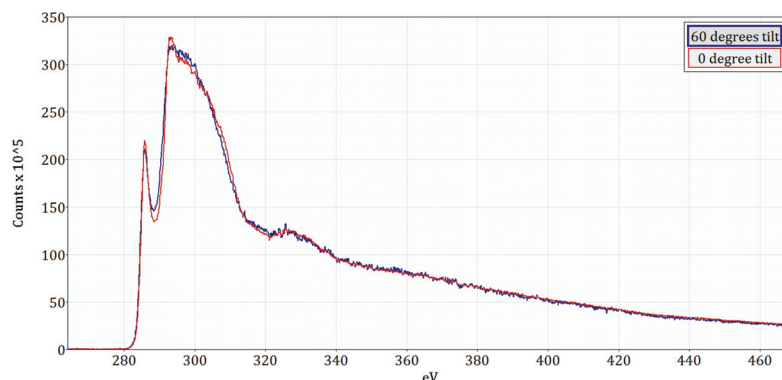


**Figure 2.9** – EELS spectra acquired on HOPG at magic angle conditions ( $\alpha=3.78$  mrad and  $\Theta=5.1$  mrad) at a tilt angle of zero and sixty degrees

### 2.2.3 Energy-filtered TEM

Energy-filtered transmission electron microscopy is a technique which is at the cross between normal imaging and spectroscopy. The first description of the underlying concept was presented in a paper by Jeanguillaume and Colliex [104], in which the authors discuss the merits of spectrum imaging in the frame of chemical mapping. The basic idea is to record subsequent micrographs using electrons that have inelastically lost a given amount of energy  $\Delta E$  over a range of energies large enough to encompass the absorption edge of the element one desires to analyse. By doing this, a data-cube in the spatial and energy space,  $x, y, E$  is recorded, in which each image is a slice of dimensions  $x, y, \Delta E$ . Thus, an EFTEM stack is made of a sequence of energy filtered images, in which the bright parts of the images are those where atoms are being ionised with exactly  $\pm 1/2 \Delta E$  eV.

Figure 2.10 shows a schematic representation of the aforementioned data-cube acquired at the PyC interphase of a SiC/SiC sample. The image on top is a slice taken at ionisation energies that are at the beginning of the peak corresponding to  $\sigma^*$  anti-bonding states. The spectrum on the right side of the figure is obtained by probing the energy axis at a specific location. Correspondingly, the highlighted part of the spectrum is the contribution from the image on the top. Notice the difference in contrast between the image picked out from the stack and the one on its surface. The first image is recorded at energy losses below the carbon K-edge: the interface appears completely dark since electrons passing through the PyC layer at this precise energy do not inelastically scatter with carbon atoms.

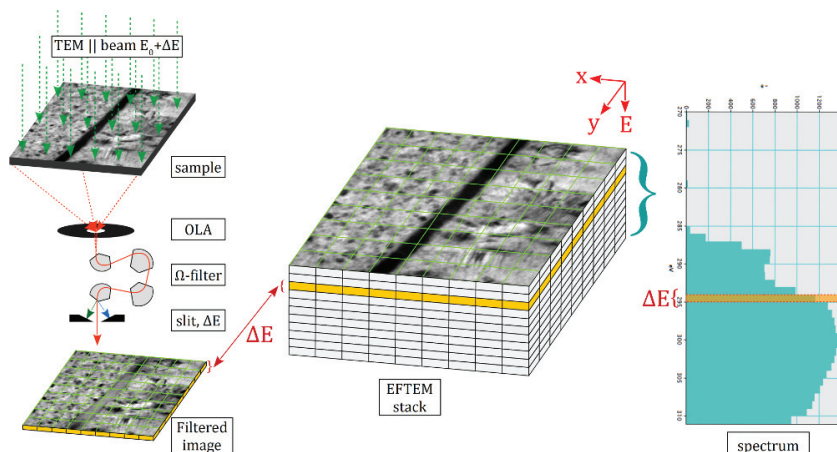


**Figure 2.10** – Schematic representation of an EFTEM data stack. Images or slices (orange) are acquired with a given energy step  $\Delta E$ . Absorption spectra over the acquisition energy range can be analysed pixel by pixel.

Alternatively to recording energy “slices” in EFTEM, a data cube such as the one shown in Figure 2.10 can be acquired pixel by pixel by recording full spectra in STEM. Both of these approaches to chemical analysis have their advantages and disadvantages, which are summarised in Table 2.2.

**Table 2.2** – Strengths and weaknesses of EFTEM and STEM EELS for chemical mapping purposes

	EFTEM	STEM-EELS
Probe area/statistics	⊕	⊖
Energy resolution	⊖	⊕
Acquisition time	⊕	⊕
Dose rate	⊕	⊖
Integrated dose	⊖	⊕

In this work, given the size of the investigated PyC interphases and the availability of the JEOL 2200FS, EFTEM was chosen as the primary method. However, because of technical issues discussed in section 2.4.2, STEM-EELS spectrum imaging has also been used at the end of the thesis. EFTEM was a quite sensible choice since the acquisition time for a stack with typical dimensions of 450 by 450 nm is about thirty to forty minutes.



### 2.2.4 Spectrum imaging

Electron spectroscopic imaging (ESI) is the analogue of EFTEM in scanning transmission electron microscopy (STEM-EELS). For a rather long time, the acquisition of ESI maps was lengthy compared to EFTEM. With recent data acquisition developments in modern microscopes, e.g. high speed scan generators and ultrafast spectrometers, this technique is now faster and more efficient than EFTEM on a “normal” TEM like a JEOL 2200FS. Though the recorded data stems from the same physical phenomena, STEM-EELS maps are drastically different on the numerical and qualitative end. A sketch of an ESI map acquisition is shown in Figure 2.11. Instead of recording energy filtered images which correspond to slices of the data cube, high resolution EELS spectra are recorded at each pixel. These correspond to “pillars” in the data cube.

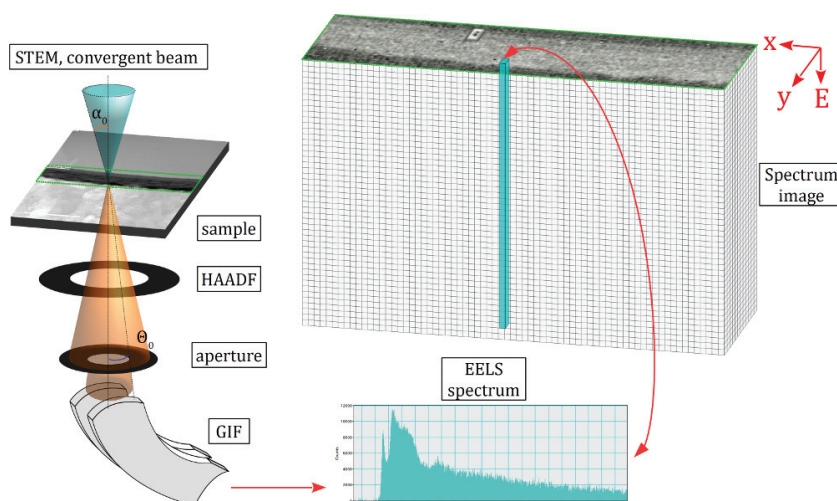


**Figure 2.11** – Schematic drawing of the acquisition of an ESI map. The converged electron beam is scanned over a ROI and high resolution EELS spectra are acquired at each pixel (260 to 470 eV with 0.1 eV dispersion here). The data cube is recorded one “pillar” at a time instead of slice-wise as is the case in EFTEM.

In terms of quality, ESI maps acquired on the Titan Themis have an energy resolution ten times higher than that of EFTEM stacks, whilst keeping a similar spatial resolution. The main difference is found in the size of the scanned areas: only the carbon interphases have been investigated. This makes sense since we are not interested in the Si-C bonds in the fibres and matrix. Additionally, the EFTEM maps acquired on the JEOL 2200FS have shown that the PyC interphases are rather homogeneous, thereby making the probing of very large areas unnecessary. In terms of acquisition time, recording an 50 by 150 pixels ESI over a 200 nm by 800 nm area takes about 15 minutes. Another major advantage of ESI over EFTEM is that the Titan Themis is equipped with a Gatan GIF Quantum ERS spectrometer. This new GIF has the highest energy resolution as well as the particularity of having dual channel recording abilities.



Thanks to this, both a low-loss and the core-loss spectra can be simultaneously acquired, thus enabling a pixel-wise deconvolution of multiple-scattering by the Fourier-ratio method<sup>4</sup>. However, this microscope could not be used from the very beginning as is the newest TEM at CIME and was brought in service in early 2016.

### 2.2.5 Thickness estimates: log-ratio

A useful application of electron energy-loss spectroscopy is the ability to get an estimate of the actual thickness of the TEM sample. This information is often required in order to determine elemental concentrations in both EDX and EELS. It also lets us know whether plural scattering has an impact on the spectrum. Finally, it has been used in this work to estimate the radiation damage levels achieved with the in-situ experiment carried out at the JANNuS facility.

The log-ratio method yields measurements of the sample thickness in terms of inelastic mean free path, i.e. in multiples of the average distance between two inelastic scattering events. By acquiring both a zero-loss<sup>5</sup> and a second image up to energy losses high enough so that the intensity reaches zero. The ratio between the thickness of the sample and the inelastic mean free path is given by Equation 2.6, which is derived from the Poisson statistics describing plural scattering [100]. Here  $I_t$  is the integral of the overall spectrum and  $I_0$  is that of the zero-loss peak shown in Figure 2.12.

$$\frac{t}{\lambda} = \ln \frac{I_t}{I_0} \quad (2.6)$$

---

<sup>4</sup>For details on this procedure, the book “Electron Energy-Loss Spectroscopy in the microscope” by Egerton [100] is highly recommended.

<sup>5</sup>Since this is done by using the smallest possible energy slit (1 eV), it actually qualifies as a low-loss rather than as a zero-loss image.

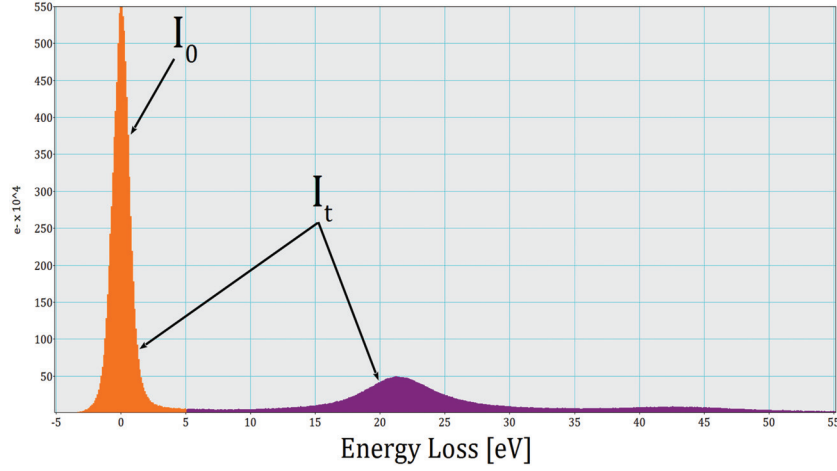


**Figure 2.12** – Integrals  $I_0$  and  $I_t$  used to compute the thickness of a TEM sample with the log-ratio technique. The energy range has been shortened for visibility purposes.

To convert a log-ratio map into an absolute thickness map such as the one featured in Figure 2.13, one needs to compute the inelastic mean free path  $\lambda$ . There are several models based on different sum rules accounting for the constraints that the spectrum intensity is subject to (e.g. Bethe and Kramers-Kronig sum rules). In this work, the log-ratio model proposed by Egerton and Cheng [105] is used to evaluate  $\lambda$  for 200 keV electrons going through carbon and silicon carbide. Equation 2.7 gives a parametrisation of  $\lambda$  as a function of the collection semi-angle  $\beta^6$ , the average energy loss per inelastic scattering event  $E_m$  and the energy of the incident electrons  $E_0$ . One should keep in mind that the mean-free-path calculated using Equation 2.7 has an error of about 10%, meaning that maps such as the one presented in Figure 2.13 give an idea about the thickness, but in no case do they yield exact measurements.

$$\lambda = \frac{106 \cdot F \frac{E_0}{E_m}}{\ln \frac{2\beta E_0}{E_m}} \quad (2.7)$$

<sup>6</sup>note that Egerton uses  $\beta$  for the collection semi-angle, whereas other authors use  $\Theta$

Here,  $F$  is a relativistic factor, and the material-dependent parameter  $E_m$  is a function of the atomic number of the species found in the sample. In the case of compounds such as SiC, one uses an effective atomic number  $Z_{eff}$ , calculated according to the Lenz model [106].

$$F = \frac{m_0 v^2}{2E_0} = \frac{1 + \frac{E_0}{1022 \text{ keV}}}{\left(1 + \frac{E_0}{511 \text{ keV}}\right)}, \quad E_m = 7.6 Z_{eff}^{0.36} \quad \text{and} \quad Z_{eff} = \frac{\sum_i f_i Z_i^{1.3}}{\sum_i f_i Z_i^{0.3}} \quad (2.8)$$

On the JEOL 2200FS used to record the thickness maps, the measurements were carried out with the second or fourth objective lens apertures inserted, which results in a  $\beta$  of 7.56 or 1 mrad, respectively. With this, the inelastic mean-free path of electrons is found to be around 170 nm in PyC and 145 nm in SiC.

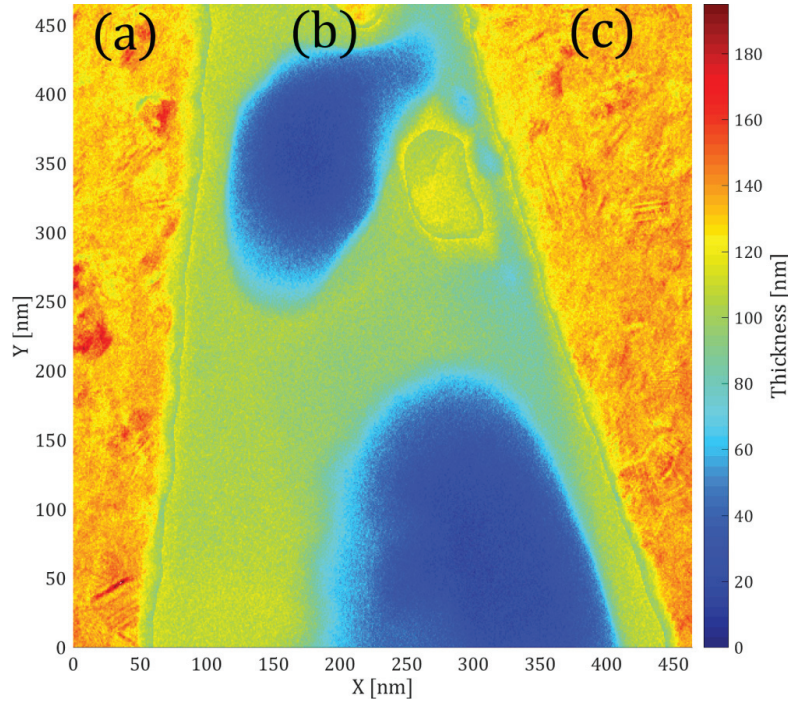


**Figure 2.13** –  $t/\lambda$  map converted to an absolute thickness map in nanometres acquired on a PyC interphase (a) between two SiC fibres (b) and (c)

The conversion of the  $t/\lambda$  maps into thickness maps as in Figure 2.13 is then a simple question of determining the PyC from the SiC areas on the image. The inhomogeneities seen in the silicon carbide are artefacts due to diffraction contrast; indeed, the OLA2 aperture does not cut off reflections from the SiC crystals. This is accomplished by creating masks using ImageJ and computing the thickness at each pixel with a MATLAB script.

## 2.2.6 Instrumentation

### In-column filters

From a technical standpoint, acquiring EFTEM stacks requires a means to filter out any electron, which have lost either more, or less than  $\Delta E$  electron volts, i.e. an imaging energy filter is needed. In a TEM, these systems are usually found in or after the column. Imaging energy filters belonging to the category of the *in-column filters* are commonly known from their brand name or that of their designers: for example, the Castaing-Henry, the Mandoline or the omega filters. Castaing and Henry were the first to develop such filters in the 1960s [107], implementing a magnetic prism with an electrostatic mirror. A schematic view of this type of filter is shown on Figure 2.14a. This design was limited to usages up to 80 kV because of the aforementioned mirror.

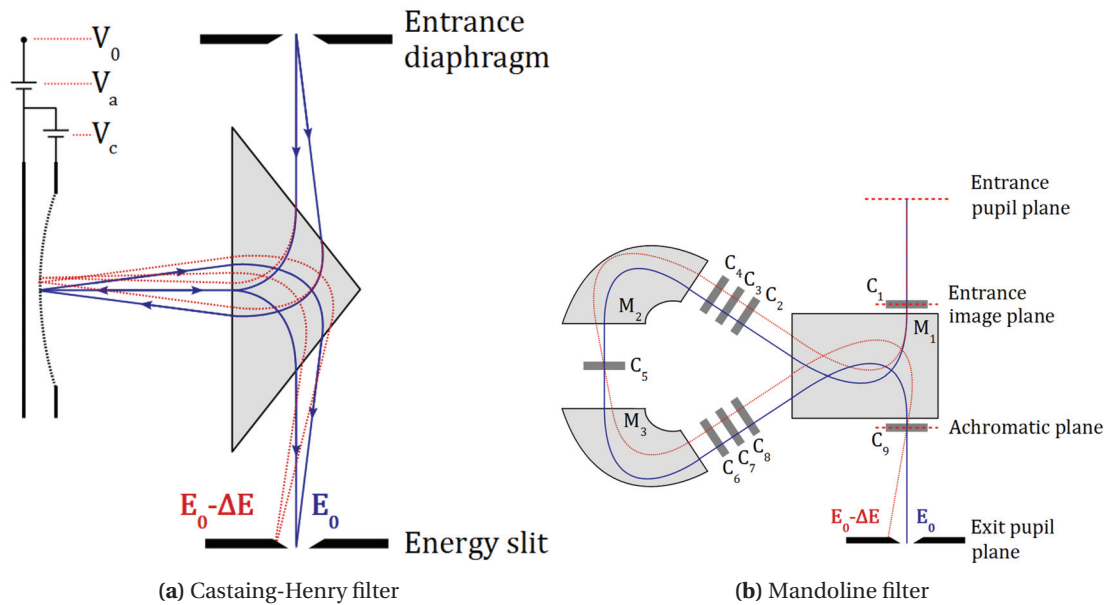


**Figure 2.14** – Ray diagrams of the Castaing-Henry (a) and Mandoline (b) in-column filters. Inspired from [107] and [108].

The operation of an in-column omega filter such as the one found on CIME's JEOL 2200FS is based on the tuning of the emission at the gun to a slightly higher energy than  $E_0$ . For each filtered image of the stack, the emission is tuned to  $E_0 + \Delta E$ , where  $\Delta E$  is the energy loss at which a frame will be recorded. Thanks to the magnetic filter, electrons having an energy loss  $\Delta E$ , arrive on the optical axis whilst others having either more, or less energy are further separated than before their entrance in the filter. Thus, the objective lens is tuned for  $E_0$  only, whilst it would have to be adjusted for each energy loss if one were not to operate in this manner. Here, the condenser lens is adjusted instead.

The ray diagram drawn in Figure 2.15 shows how the microscope is operated during the acquisition of EFTEM stacks. Firstly, a parallel beam of electrons having an energy of  $E_0 + \Delta E$  arrives on the sample, and an objective lens aperture with a diameter enabling a collection angle such that the MAC are fulfilled is inserted. The direct beam then enters the omega filter, and electrons having lost  $\Delta E$  through inelastic scattering with the sample atoms arrive on the TEM optical axis at the exit of filter. A slit of chosen width lets then electrons having now  $E_0 \pm \delta E$  into the lower parts of the microscope.

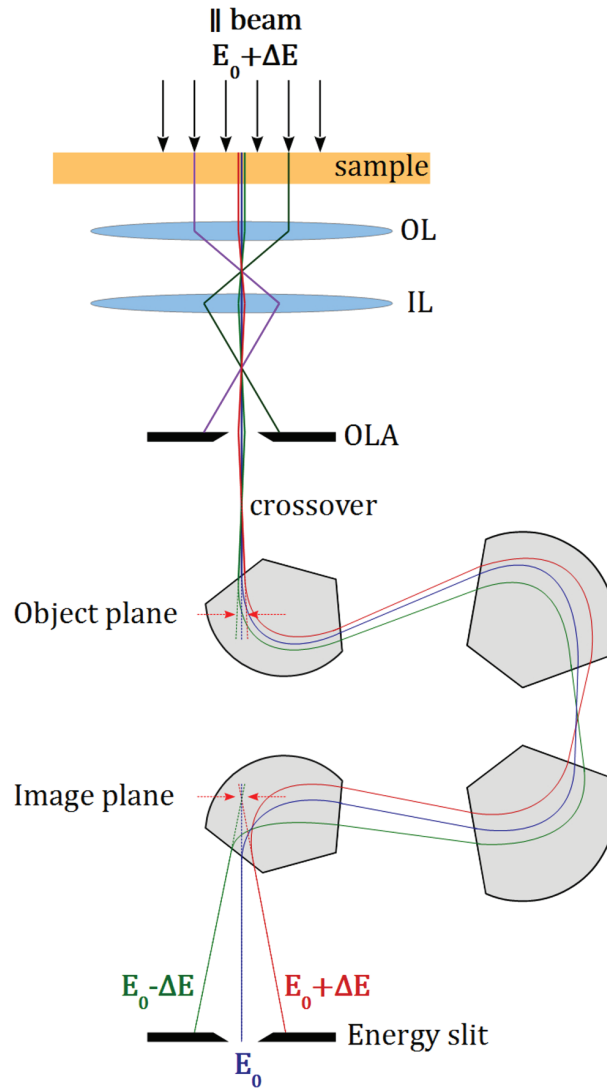


**Figure 2.15** – Ray diagram showing the path of electrons once they have been inelastically scattered by the atoms of the sample. OL=Objective Lens, IL=Intermediate Lens, OLA=Objective Lens Aperture. The energy filtering occurs in the  $\Omega$ -filter, enabling the selection of electrons having lost exactly  $\Delta E$  eV  $\pm \delta E$ , where  $\delta$  is the width of the energy slit. Sketch based on drawings from [99] and [109].

### Post Column filter (Gatan Image Filter)

As mentioned before, there is another option to in-column filters such as the three designs shown in previous sections. Indeed, the image filter can be placed at the end of the TEM, in which case we speak of a *post-column filter*. This design was pioneered by Krivanek et al. [110] in the 1990s, when they built the first post-column imaging filter for the company Gatan. A sketch showing the main components of a Gatan imaging filter (GIF) are shown in Figure 2.16.

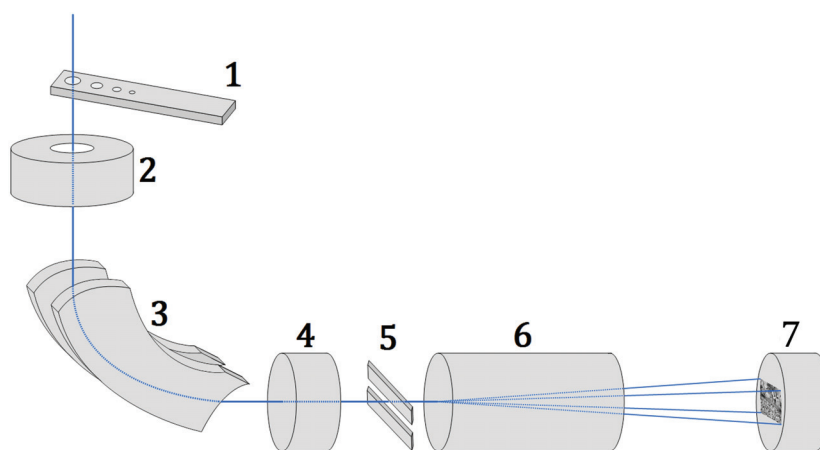


**Figure 2.16** – Sketch showing a side view of the main components found inside a GIF spectrometer. Based on sketches from [110]. 1) entrance apertures; 2) pre-prism focusing coils; 3) magnetic prism with a 90° bending angle; 4) spectrum magnifying quadrupoles; 5) energy-selecting slits; 6) imaging assembly consisting in a stack of quadru- and sextupoles; 7) CCD camera.

The operation principle of a post-column filter is similar to that of an in-column one such as the omega filter, with the difference of that it is placed at the very end of the TEM column. This is both an advantage and inconvenient of this design. Firstly, because of the position of the filter, the microscope has full magnification and camera length flexibility. Additionally, a GIF can be added to practically any TEM as an upgrade, which can be very interesting in terms of budget when the acquisition of a new microscope is considered.

## 2.3 Carbon hybridisation

Quantifying the hybridisation of carbon atoms found in a sample is a topic found throughout many carbon related research. Regardless of the many forms that carbon can take, be it amorphous, diamond or any of the many graphitising carbons, these allotropes can be identified from the type of orbitals that are binding the atoms together. Indeed, the K-edge absorption spectrum of diamond, graphite and amorphous carbon are very different from each other because of the types of bonds found in these allotropes.

### 2.3.1 Orbital theory

Electron orbitals are solutions to Schrödinger's equation, i.e. they describe density probabilities of electrons being in a specific configuration around an atomic nucleus. These solutions are characterised by several quantum numbers: the main,  $n$ , secondary,  $l$  and magnetic  $m_l$  quantum numbers, which correspond to energy levels, shapes ( $l = n - 1$ , noted  $s$ ,  $p$ ,  $d$  and  $f$ ) and the orbital's spatial orientation, respectively. The shapes of the electron orbitals  $s$ ,  $p$ ,  $d$  and  $f$  are easily found in many books as well as online. A carbon atom has six electrons which in their ground state are noted  $1s^2 2s^2 2p^2$ . Using an orbital diagram, this can be written down as shown in Figure 2.17.



**Figure 2.17** – Orbital diagram of the ground state of a carbon atom

Considering the limited number of electrons that a carbon atom has, as well as the fact that  $1s$  electrons do not participate in the formation of molecular orbitals, only the  $2s$  and  $2p$  orbitals are of relevance in this discussion. These are shown in Figure 2.18.

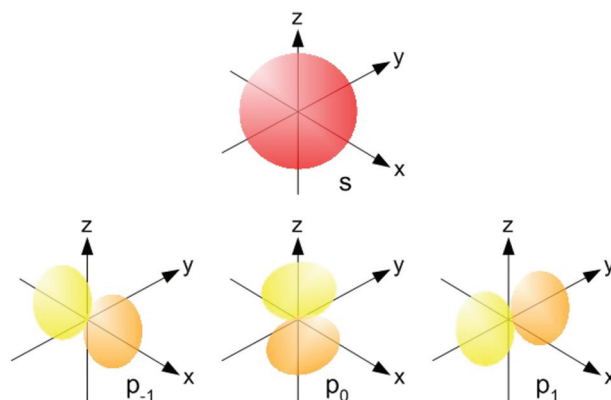


**Figure 2.18** –  $1s$ ,  $2p_x$ ,  $2p_y$  and  $2p_z$  electron orbitals. From [111].

There are different ways in which atoms can bind to one another. The metallic and ionic bonds are not relevant in this discussion. Indeed, carbon atoms bind to each other through covalent bonds, i.e. by sharing electrons in molecular orbitals. The binding of carbon atoms is described by the molecular orbitals  $sp$ ,  $sp^2$  and  $sp^3$ , which are linear combinations of either  $2s$  and  $2p$  orbitals. Their diagrams are shown in Figure 2.19.

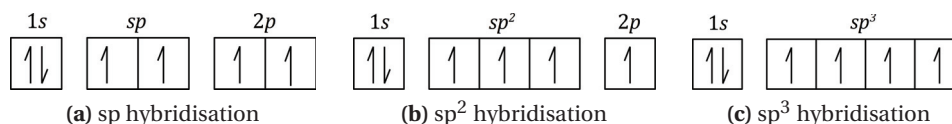


**Figure 2.19** – Orbital diagrams of the  $sp$ ,  $sp^2$  and  $sp^3$  molecular orbitals of hybridised carbon atoms

The promotion of electrons to higher energy orbitals can be energetically favourable since it increases the number of singly occupied orbitals from two  $2p$  to a combination of four orbitals; These can be used to form more bonds with other atoms. Mathematically speaking, the wave-functions of two atoms  $a$  and  $b$  can be combined in two ways, as in Equation 2.9.

$$\Psi = c_1\psi_1 + c_2\psi_2 \quad \text{and} \quad \Psi^* = c_1\psi_1 - c_2\psi_2 \quad (2.9)$$

$\Psi$  is known as the *bonding molecular orbital*, whereas  $\Psi^*$  is an *anti-bonding orbital*. The difference between these is whether the interaction between the atomic orbitals is in- or out of phase, i.e. constructive or destructive. Because of the constructive interaction of bonding orbitals, these have lower energy levels than the atomic orbitals used to form them. On the other hand, anti-bonding orbitals are made of higher energy states and tend to destabilise the bond. In the case of the  $sp$  and  $sp^2$  hybrids, the resulting orbitals have an in-plane symmetry called  $\sigma$ , thus their name of  $\sigma$  and  $\sigma^*$  orbitals. The geometry of  $sp^2$  orbitals is shown in Figure 2.20.

As it can be seen, the three  $\sigma$  ( $sp^2$ ) orbitals are all in the same plane, with a separation of  $120^\circ$  between each other, whilst the remaining  $2p$  orbital is out of plane, i.e. it is a  $2p_z$  orbital. This type of bonding is at the core of the hexagonal structure of graphite: the in-plane  $\sigma$  orbitals form tight bonds between the carbon atoms forming the graphene sheets, and the remaining  $2p_z$  orbitals combine to form  $\pi$  and  $\pi^*$  bands.

In a similar fashion,  $sp$  hybrids show two planar  $\sigma$  orbitals in line with one another, i.e. separated by  $180^\circ$  with two  $2p$  orbitals staying in the  $y$  and  $z$  planes. Lastly, the  $sp^3$  hybridisation results in the formation of four  $\sigma$  and  $\sigma^*$  orbitals. These are angled by  $109.5^\circ$



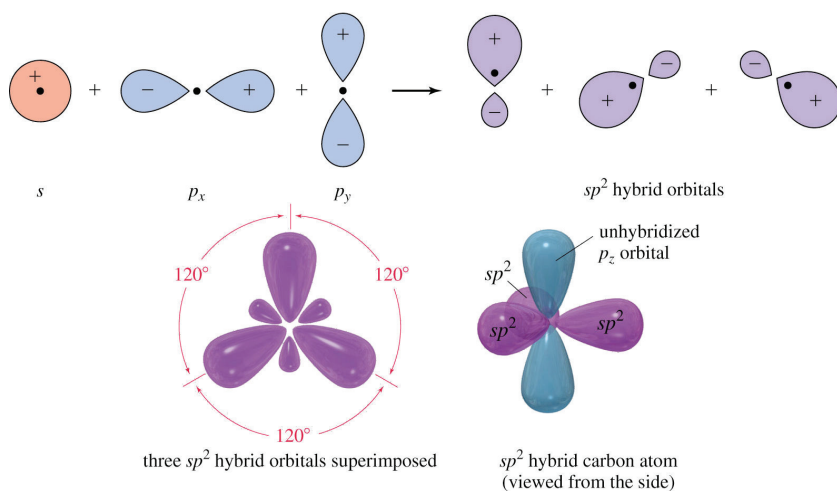


**Figure 2.20** – Drawing of the formation of  $sp^2$  orbitals [112]

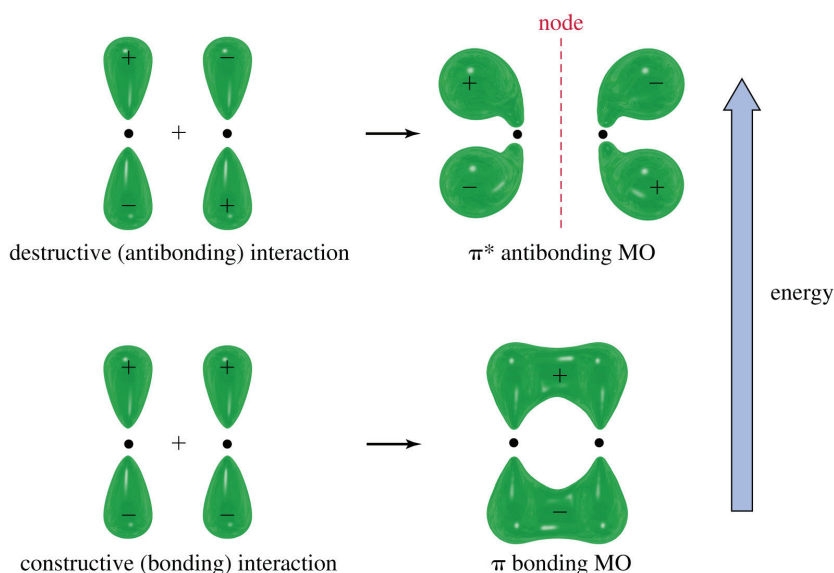


**Figure 2.21** – Drawing of the formation of  $\pi$  and  $\pi^*$  orbitals [112]

from each other and form a tetrahedron. Similarly to the geometry of the in-plane  $\sigma$  orbitals of graphite, the tetrahedral organisation of the  $sp^3$  orbitals is the reason behind the diamond structure, i.e. a FCC structure whose tetrahedral sites are filled.

Because of the difference in electronic structures discussed above, electrons excited to higher energy levels through inelastic scattering with the incident electrons will fill the available energy levels of the anti-bonding orbitals found in a given carbon allotrope. Since the  $\pi^*$  and  $\sigma^*$  orbitals have different characteristics and energy levels, the resulting energy loss of the incident electrons will be visible and can be used as a fingerprint of the carbon

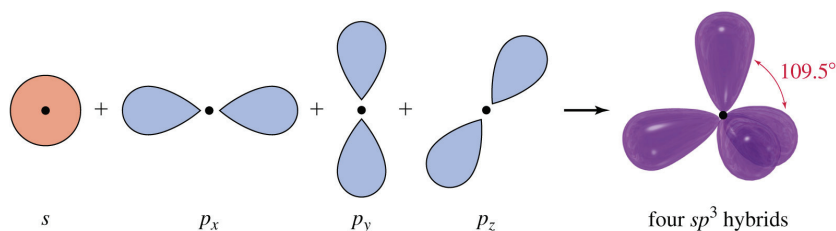


**Figure 2.22** – Drawing of the formation of  $sp^3$  orbitals [112]

hybridisation state in the EELS spectrum. Figure 2.23 shows the K-edge of diamond, graphite and amorphous carbon. We can see that the K-edge of diamond features a single peak around 294 eV, corresponding to the transition to the  $\sigma^*$  states, whilst graphite shows an additional narrower peak at 284 eV which is due to the filling of the  $\pi^*$  anti-bonding states. The case of amorphous carbon is between these two. Indeed, in this state, carbon features all three types of hybridisation, i.e.  $sp$ ,  $sp^2$  and  $sp^3$ , which results in a less featured absorption spectrum. The goal of both the EFTEM and ESI mappings performed in this work is to quantify the ratio between the  $\pi^*$  and  $\sigma^*$  peaks and to use this quantity, known as the *R-ratio*, to quantify the radiation-induced amorphisation of the PyC interphase, which can be identified by a reduction of the  $\pi^*$  peak intensity.

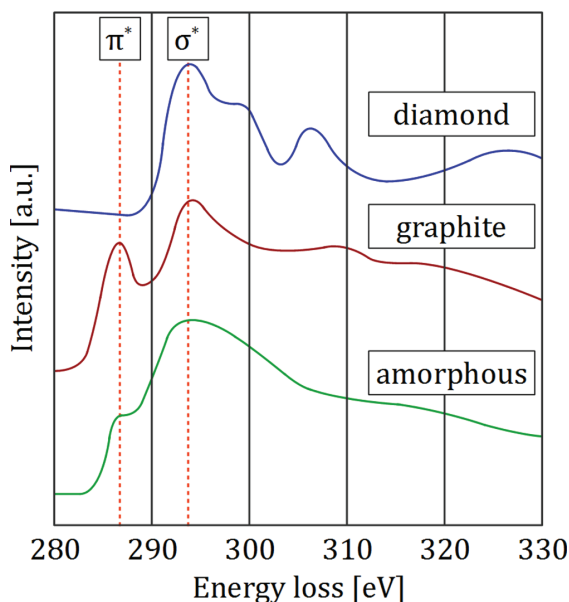


**Figure 2.23** – K-edge of the absorption spectrum of carbon recorded on the three main allotropes, diamond, graphite and amorphous carbon. Drawing based on a figure by Egerton [113].

### 2.3.2 $sp^2$ to $sp^3$ ratio quantification

There are different ways to approach the quantification of  $sp^2$  to  $sp^3$  hybridised carbon atoms. Two of these are based on integration of the spectra in specific energy ranges. The difference between them is that the *two-windows method* (TWM) [114, 115] uses a direct numerical integration over well-defined energy windows, whilst the *Gaussian and Lorentzian methods* focus on fitting the different peaks featured in the carbon K-edge. The fitting functions of the peaks are then integrated over appropriate energy ranges. Last, ab initio calculations also allow a spectrum to be computed based on first principles.

Regardless of which of the three techniques is used, using reference spectra so that upper and potentially lower bounds may be applied is necessary, if one is to compare a map to another. In this work HOPG, has been used for the upper limit of the  $sp^2/sp^3$  ratio. The spectra shown in Figure 2.24 and Figure 2.25 were all acquired on this reference material.

#### Gaussian and Lorentzian fitting

Both methods are based on the same principle: we know that at least three peaks are present in the carbon K-edge spectrum. As a matter of fact, all three peaks can be attributed to a specific type of carbon-carbon bond: a first rather narrow peak centred at about 286 eV, representing the  $C = C \pi^*$  anti-bonding states, a second peak at 292 eV, at the energy levels of the  $C - C \sigma^*$  states, and, finally, a broader peak at 298 eV due to the  $C = C \sigma^*$  states [116, 117, 118].

$$L(x) = x_0 + \sum_i \frac{2a_i}{\pi} \frac{\omega_i}{4(x - b_i)^2 + \omega_i^2} \quad (2.10)$$

$$G(x) = \sum_i a_i \exp - \left( \frac{x - b_i}{c_i} \right)^2 \quad (2.11)$$

As one can see in Figure 2.24, the fit is not perfect, with a dip around 288 eV between the first Gaussian ( $\pi^*$ ) and the other two ( $\sigma^*$ ). The corresponding peak of the residuals is given a potential explanation by Zhang [117], Bernier [119] and Mironov [118] by the presence of three possible features:

- Firstly, Bernier et al. [119] argue that the planar  $sp^2$  component of the  $\pi^*$  orbital is asymmetric, thus explaining that the corresponding peak is broadened towards higher energies.
- If present, C-H and C=O bonds feature  $\sigma^*$  centred around 287-289 eV, and  $\pi^*$  states at 288-289 eV, respectively.

- Lastly, fullerenes such as  $C_{60}$  and  $C_{70}$  feature a double peaked  $\pi^*$  components. These contain large amounts of pentagonal rings, which are also present in irradiated graphite, as shown in Figure 1.13 on page 49.

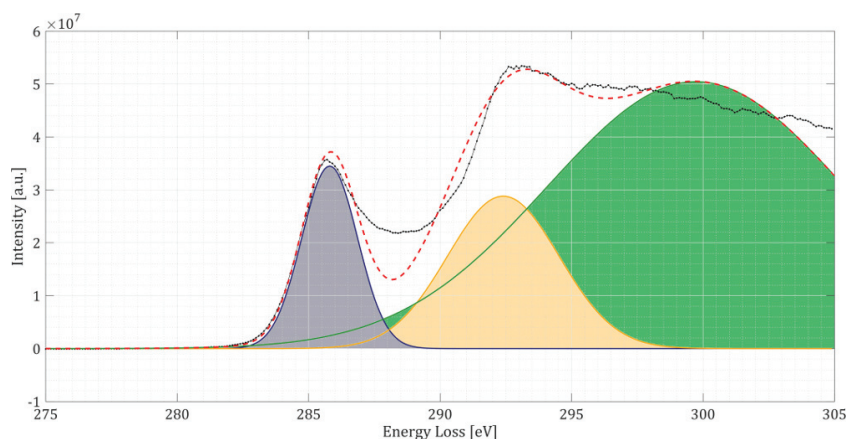


**Figure 2.24** – HOPG EELS spectrum analysed with the Gaussian fitting method. The three Gaussians represent different components of the total absorption spectrum: blue for the  $C=C \pi^*$ , orange for the  $C-C \sigma^*$  and green for the  $C=C \sigma^*$  contributions to the overall spectrum.

It has been decided not to include these additional peaks in the fitting routine because the presence of the aforementioned features would be difficult to prove. Although the presence of non-planar  $sp^2$  can be assumed with sufficient certainty, adding a fourth Gaussian adds more uncertainties to the overall data analysis, as it would introduce another three fit parameters with their respective confidence intervals.

### Two-windows method

With this technique, the ratio between carbon atoms hybridised either in  $sp^2$  and  $sp^3$  states is obtained via direct numerical integration of the EELS or EFTEM spectrum. A first integration range is centred on the  $\pi^*$  peak. The width of this window should be adjusted to include the low energy tails of the  $sp^2$  peak. Furthermore, it should stop at the local minimum between the  $\pi^*$  and  $\sigma^*$  peaks. Indeed, selecting a too large window for this part of the spectrum leads to errors, since  $sp^3$  contributions would then be included. The second window accounting for the  $sp^3$  hybrids is larger than the first. Here, the upper energy limit should be set before the onset of plural scattering oscillations. This approach has the advantage of being straight-forward and easy to implement, does not have fit parameters and can run very quickly. The orange and green areas shown in Figure 2.25 show the implementation of this technique on a reference HOPG spectrum.

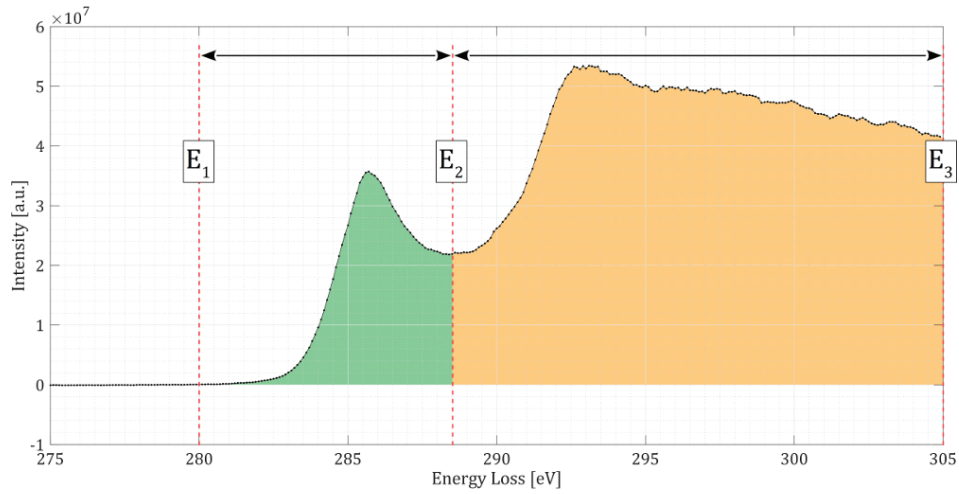


**Figure 2.25** – HOPG EELS spectrum analysed with the two-windows method. The green area accounts for  $sp^2$  hybridised atoms, whereas the orange surface represents the share of atoms in a  $sp^3$  state.

The robustness of this method can be contested because of its sensitivity to the location and width of the windows. Although the centre of the  $sp^2$  window is rather well defined, the definition of the point at which the  $sp^3$  window is set is more difficult. Nevertheless, the results obtained via this technique are consistent with the more time-consuming Gaussian fitting. Therefore, TWM has been used as the main method for the  $sp^2/sp^3$  quantification.

#### Ab-initio and density of state calculations

There is a last type of methods which can be used to calculate R-ratios based on theoretical calculations of the EELS spectrum of carbon. Performing a full spectrum computation can be done by calculating the density of states (DOS) from first principles (ab-initio [120]). Although the argument that these methods are more accurate than the TWM or Gaussian fitting can be made, they require intensive computations. Furthermore, the other two methods do yield satisfying results, as long as constraints on the parameters are well defined.

## 2.4 Experimental

### 2.4.1 EFTEM

The acquisition of all EFTEM stacks was carried out at EPFL on a JEOL 2200FS TEM. This microscope has a Schottky type field electron gun and is equipped with an omega in-column filter. To record EFTEM maps, the microscope must be aligned in a way such as to have a parallel beam on the sample with an objective aperture inserted, so that conditions as close to the MAC as possible are achieved. In addition to this, the emission is tuned by changing the voltage of the anodes A1 and A2 by a few hundreds of volts. As a rough guideline, one should aim at a beam current of around  $150\text{ }\mu\text{A}$ , which should result in a screen current of about  $500\text{ pA}\cdot\text{cm}^{-2}$ , at a magnification of about 30'000 times. Because the emission has been changed, a calibration of the in-column filter needs to be performed prior to any measurement. This is done by following the emission compensation routine in the calibration tab of the user interface of the energy filter. In these conditions, a parallel beam of  $1\text{ }\mu\text{m}$  diameter is obtained; a quick check to verify the microscope alignment before acquisition is to change focus. If everything has been done correctly, the beam diameter does not change in under- or over-focus.

The acquisition of EFTEM data cubes requires the acquisition of a dark reference after each of the energy-filtered images. This can be done by using the Smart EFTEM-SI plug-in developed by Watanabe [121]. This is particularly important to make sure that the recorded stacks are usable. Indeed, because of the drift of the dark references, a typical stack of 45 images, ranging from 270 to 315 eV losses, each acquired for 16 to 20 seconds, is often unusable if such precautions are not taken.

### 2.4.2 STEM-EELS

Due to technical difficulties with the Gatan Hyperscan camera of the JEOL 2200FS, EFTEM measurements became practically impossible after November 2015. Even after revision, the issues encountered when recording data stacks were not solved. After some further unsuccessful tries in April and May 2016, the decision of using the new Titan Themis microscope in STEM-EELS was taken. This allowed more flexibility in the measurement conditions. Based on the MAC traces shown in Figure 2.7, an acceleration voltage of 80 kV was selected, since this would allow rather large values of the convergence angle  $\Theta$ , making the MAC easier to reach than at 200 or 300 kV. Furthermore, the lower voltage is also advantageous in terms of beam damage, as 80 keV electrons are at the threshold where carbon atoms can be knocked from their lattice locations by the incident beam. This is particularly important in STEM, the whole beam being concentrated at a single location for short periods of time<sup>7</sup>.

---

<sup>7</sup>Typically 0.2 seconds in the case of the spectrum images presented in this work.

An issue that arose from the lower voltage is the increase in multiple scattering, due to the thickness of the samples. Since the TEM lamellae were prepared for observations at 200 kV, most samples had mean thicknesses between 100 and 150 nm, which is close to the mean free path of 80 keV electrons going through carbon  $\sim 127$  nm<sup>8</sup>. This problem is not as impactful as one would think, thanks to the new Gatan quantum ERS GIF, which features dual channel spectrum recording, thus allowing the simultaneous recording of both a core-loss and a low-loss spectrum. Using this additional data, multiple scattering can be corrected using the Fourier-ratio method. All of the spectrum images were acquired with a convergence angle of 3.78 mrad, a collection angle of 5.1 mrad<sup>9</sup> and an energy dispersion of 0.1 eV. The corresponding point on the MAC traces is circled in Figure 2.7b. The main difference between spectrum images and EFTEM stacks is found in the number of pixels recorded in a reasonable time. Most of the ESI feature around 150 by 50 pixels, whilst EFTEM stacks have a resolution of 256 by 256 pixels. Since the regions of interest are usually comparable in size, the pixel size of ESI stacks is larger than that of EFTEM data cubes.

### 2.4.3 JANNuS

Three days of beamtime were obtained at the JANNuS Orsay facility, between October 12<sup>th</sup> and 14<sup>th</sup>, 2015. The goal of this experiment was to use the unique equipment found at the Centre de Sciences Nucléaire et de Sciences de la Matière (CSNSM) to study ion irradiation effects whilst observing them in a TEM. What makes JANNuS special is the fact that a TEM is coupled with two ion beamlines, ARAMIS and IRMA, thus enabling in-situ TEM studies of radiation damage.

The first particle accelerator, ARAMIS, is a 2 MV tandem accelerator [123] which, in our case, was providing a beam of 1 MeV silicon ions. The second beamline is fed by 190 kV ion implanter called IRMA [124], and was used to obtain a 140 keV C<sup>+</sup> beam. It can produce a very wide range of ions with energies ranging from a few keVs to 570 keV. The third and, in this case, central part of the facility is the TECNAI G<sup>2</sup> 20 Twin TEM from FEI shown in Figure 2.26. This microscope has the particularity of having both beamlines arriving in the gap of the objective lens' pole piece. It is equipped with several analytical tools, out of which the post-column energy-filter GIF Tridiem from Gatan was used to acquire EELS spectra before and after the samples were exposed to the ion beam. During irradiations, images and movies were recorded using a Gatan ES500W camera. More details on the specifics of this TEM can be found on the website of the facility [92].

---

<sup>8</sup>this value is calculated using Equation 5.5, on page 297 of Egerton [122], and is valid for a beam set to be at the MAC for carbon, at 80 keV.

<sup>9</sup>This collection angle is obtained by working with a camera length of 115 mm.



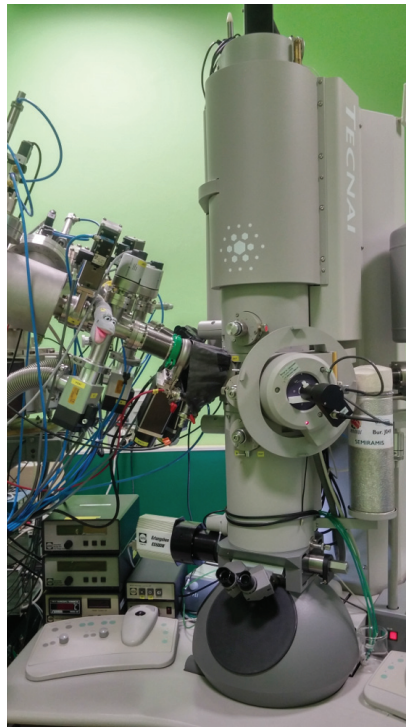


**Figure 2.26** – FEI's TECNAI G<sup>2</sup> 20 Twin with both ion beam line guides at JANNuS Orsay

The geometry of both ion beamlines and of the electron beam is somewhat particular. The three beams are in coincidence on the sample surface when the latter is tilted at  $\alpha = 22.5^\circ$  and  $\beta = -35^\circ$ . This combination of rather high tilt angles means that careful positioning of the sample in the holder is needed. Indeed, in cases where the sample is not in the right part of the double tilt holder, the sample might be shaded by the edge of the holder or out of the zone where all three beams meet. Figure 2.27 gives a schematic view of the discussed geometry.

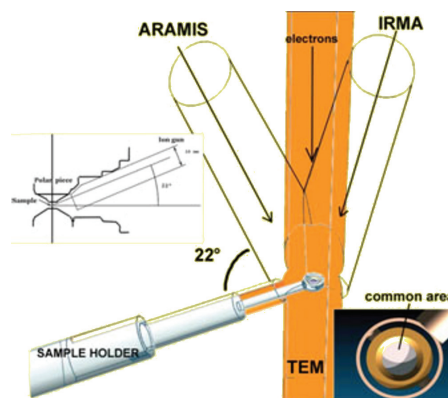


**Figure 2.27** – Schematic view of the geometry of the ion and electron beams coupling [92]



## 2.4. Experimental

A total of six samples were studied, five of which were prepared from the General Atomics/Westinghouse SiC/SiC clad sections and one from a piece of pristine material of the A034 sample which was irradiated with neutrons in 2009 in Petten. Due to technical difficulties, the first two samples, GA4 and GA1 were irradiated using Si<sup>+</sup> ions from ARAMIS only. Out of the four other TEM lamellae, one, GA7, was subjected to C<sup>+</sup> ions only. The reason for this single ion irradiation was to make sure that 140 keV C<sup>+</sup> ions were indeed reaching the sample surface whilst imaging it with 200 keV electrons, since ions are also influenced by the magnetic field of the objective lens.

The figures collected in Table 2.3 summarise the six in-situ irradiation, performed at the ambient.

**Table 2.3** – Details of the ion irradiations carried out at JANNuS Orsay, ion fluences in ions per square centimetre

Sample	140 keV C <sup>+</sup>	1 MeV Si <sup>+</sup>	# irradiations	dpa in PyC	dpa in SiC
GA1	-	1.680E <sup>15</sup>	2	1.32E <sup>-1</sup> ± 2.8E <sup>-3</sup>	2.20E <sup>-2</sup> ± 7.9E <sup>-3</sup>
GA4	-	9.100E <sup>14</sup>	2	4.33E <sup>-2</sup> ± 2.9E <sup>-3</sup>	7.00E <sup>-2</sup> ± 7.7E <sup>-4</sup>
GA6	7.040E <sup>14</sup>	1.420E <sup>15</sup>	2	8.86E <sup>-2</sup> ± 6.5E <sup>-3</sup>	1.49E <sup>-1</sup> ± 2.1E <sup>-2</sup>
GA7	1.628E <sup>15</sup>	-	4	1.00E <sup>-2</sup> ± 1.6E <sup>-3</sup>	2.67E <sup>-2</sup> ± 4.7E <sup>-4</sup>
GA9	7.226E <sup>14</sup>	1.445E <sup>15</sup>	2	9.00E <sup>-2</sup> ± 2.0E <sup>-3</sup>	1.48E <sup>-1</sup> ± 1.2E <sup>-3</sup>
A034	2.830E <sup>15</sup>	5.600E <sup>15</sup>	4	3.65E <sup>-1</sup> ± 1.8E <sup>-3</sup>	5.65E <sup>-1</sup> ± 3.0E <sup>-2</sup>

These parameters are converted into dpa, on the basis of simulations performed using SRIM [26].

The samples were filmed during the irradiations in bright field conditions. Diffraction patterns, as well as additional images and EELS spectra were recorded between the successive irradiations. EFTEM was not carried out because the conditions in which the measurements would have been performed were too far off from the MAC.

### 2.5 Data processing

The amount of processing required to extract useful information from an EFTEM stack is substantial. Firstly, although CIME's JEOL 2200FS, used to acquire all of the data cubes, is very stable<sup>10</sup>, spatial drift is always present during a twenty to forty minutes acquisition of about forty images. To correct this, a drift correction algorithm developed by Schaffer et al. [125] and implemented in Gatan Digital Micrograph (DM) is used to align the images of the data cubes. The working principles of this method are discussed in section 2.5.1. The second processing step is necessary to help with the usually low signal to noise ratio characteristic to EFTEM image series. To improve the quality of the previously aligned image series, another Digital Micrograph routine [126] is used. This stage of the processing is based on the multivariate statistical analysis (MSA) of the data and is discussed in section 2.5.2. After this, the background has to be removed from the spectra; the power law background removal in DM is very efficient at this. At this point, one should always make sure that a large enough energy range has been recorded prior to the ionisation edge to ensure a stable and consistent removal of the background.

After these steps, the data is ready for further analysis, namely the quantification of the  $sp^2/sp^3$  ratio at each pixel of the data cube via spectral analysis. A Matlab code has been developed to this end, using either of the quantification methods presented before. The principle of this analysis follows this scheme:

- preparation of the data. The EFTEM stacks are fed to the program as text files whose resolution, pixel size ( $n,m$ ) and the number of images  $k$  in the series have to be given in an input file. The data is then separated in cells of appropriate sizes ( $k, n, m$ );
- extraction of the spectra at each of the ( $n, m$ ) pixels;
- application of a mask to identify the PyC areas from the surrounding SiC fibres and matrix. One typically uses an image of the rotation factors obtained via spectral rotation or of the spectral factors computed through spatial rotations. These two processes are part of the MSA and addressed in section 2.5.2. This step is crucial since only the spectra of appropriate compositions can be analysed with the TWM, or the Gaussian method. Indeed, a triple Gaussian function parametrised for carbon-carbon bonds simply cannot be fitted on the absorption edge of a carbon-silicon bond. The TWM method would basically work, but the result would not make any sense;
- application of the Gaussian or TWM spectral analysis for the spectra found at the right locations according to the mask;

---

<sup>10</sup>This TEM, like all of the microscopes at CIME, is located in the basement of EPFL's MXC building.

- computation of the R-ratio at the analysed pixel. Reference values acquired on HOPG are used as a normalisation upper-bound for the ratio;
- the computed R-ratio map is saved in a matrix. This allows the user to get a 2D map of the ratio, which can be laid over a TEM micrograph to present the results.

### 2.5.1 Drift correction

The drift correction algorithm used in this work calculates the statistically determined spatial drift (SDSD) and has been developed by Schaffer et al. [125]. Like any other drift correction or image alignment algorithm, its goal is to determine the shift vectors of each individual image of an image series such as an EFTEM stack. What makes this algorithm particularly efficient and robust is the incorporation of a statistical treatment of the data. This particularity has the advantage of not needing a user defined reference image to which the other images are compared. This is very useful in EFTEM image series where in addition to spatial drift, contrast inversions due to the excitation of absorption edges add another difficulty to the drift correction.

The first step of this program is to apply digital filters to facilitate the stack registration and subsequent determination of the shift vectors. At first, a heavy low-pass filter is applied to reduce the influence of the noise. A contour-filter is then used on the images to reduce the influence of issues such as the aforementioned contrast inversions and to make the second processing step possible. The user can choose between the Sobel and Frei&Chen contour filters [125], depending on the type of features found in the images.

Secondly, the cross-correlation of the images in the reciprocal space is calculated by fast Fourier transform. This step is the reason why contour filters need to be applied. Indeed, the cross-correlation technique is based on the assumption that the content of the images is practically identical, i.e. that the only differences are the result of spatial drift. The particularity of Schaffer's program starts at this point. The core of the statistical treatment begins by calculating the cross-correlation of all possible image pairs from the data cube. The maximum of the cross-correlation peak is taken as an indication of the quality of the shift vectors. These are then either kept or discarded, depending on whether these values are above or below a given limit. In a second part of the treatment, the best possible reference image is found, and new drift vectors of all other images relative to this one are re-evaluated. Lastly, the average of the shift vectors, along with the corresponding standard deviations, are calculated, and the stack is aligned.

### 2.5.2 Multivariate statistical analysis

The second step of data processing aims at reducing the noisiness of the data through a multivariate statistical analysis, more precisely via a *principal component analysis* (PCA). In addition to this, one part of this processing yields composition maps, thus making the identification of PyC from SiC areas possible at the next stage of the image analysis.

Multivariate statistical methods such as the PCA yield less noisy information thanks to reduction of the dimensionality of the original data. Only the basic outline of the method as well as the points one must be particularly careful about are discussed here. For more information, the paper by G. Lucas et al. [126] and the user manual of CIME's PCA algorithm [127] implemented in DM are recommended.

Firstly, the data is organised in a matrix  $\mathbf{D}$  of dimensions  $(m \times n)$ . The columns  $m$  account for the pixels of the image, or more precisely, for all voxels, in the case of an EFTEM data cube. The  $n$  rows of the matrix represent the energy channels of the corresponding spectra.

#### PCA decomposition

The first step of the PCA consists in determining the principal components of the data. This is done by finding linear combination of variables maximizing the variance of the data in terms of least squares. The calculated variance is removed, and the algorithm keeps iterating this procedure, thus finding higher order components until the remaining variance is negligible. Mathematically, this translates in a factorisation of the matrix  $\mathbf{D}$  into  $\mathbf{D} = \mathbf{T}\mathbf{P}^T$ , where  $\mathbf{T}$  and  $\mathbf{P}$  are known as the score and loadings matrices. The product  $\mathbf{T}^T\mathbf{T}$  is a diagonal matrix whose elements are the eigenvalues of score and loading vectors combinations, i.e. pairs of voxels/energy channels. These are related to the amount of data variance explained by the corresponding component.

At this point, the user should carefully choose a subset of  $p$  components ( $p \ll n$ ), typically those having the highest eigenvalues, to account for the variance of the data in the best possible manner. The data can then be reconstructed with a new basis of vectors as  $\mathbf{D} \sim \tilde{\mathbf{D}} = \tilde{\mathbf{T}}\tilde{\mathbf{P}}^T$ , whose dimensions have been reduced to  $(m \times p)$  and  $(n \times p)$ , respectively. This stage of the PCA is a very sensitive one, since selecting too few components results means that meaningful information is discarded, thereby falsifying the data. However, choosing a larger subset might result in no net gain in data quality.

In actual cases, one practically never fully decomposes the matrix  $\mathbf{D}$  at once, but usually determines no more than 40 eigenvalues, as a full diagonalisation would be extremely inefficient in terms of computing time. Therefore, the matrix is separated in two orthonormal matrices  $\mathbf{U}$  and  $\mathbf{V}$  as well as in a diagonal matrix  $\Sigma$  to process it by the singular value

decomposition method (SVD) (see Lucas et al. [126] for further details). A measure of the quality of a subset of components selected for a reconstruction is given by the *relative sum of the squared residuals* (RSSR):

$$RSSR = \left( \frac{\sum_{i=1}^m \sum_{j=1}^n (\tilde{d}_{ij} - d_{ij})^2}{\sum_{i=1}^m \sum_{j=1}^n d_{ij}^2} \right)^2 \quad (2.12)$$

The closer to zero this quantity is, the less information is lost from the original data. Nevertheless, a RSSR value of zero would mean that the PCA yields no net improvement, since the reconstructed data would be identical to the original one. The goal of the PCA is to reduce the noise of the data whilst losing as few information as possible.

### Vector rotations

The interest of the aforementioned SVD method is that  $\mathbf{U}$  and  $\mathbf{V}$  are the eigenvectors of  $\mathbf{D}\mathbf{D}^T$  and  $\mathbf{D}^T\mathbf{D}$ . Orthogonal or oblique rotations can be performed either in the spectral or in spatial domains. The spectral factors obtained by rotations in the spectral domain are particularly useful for the next step of the analysis, as they yield abundance maps of the different species or spectral contributors found in the images. These are further processed using Fiji [128] to produce masks which are used to identify carbon atoms bond to each other from the ones bound to silicon in silicon carbide areas.



## **3 Thermal conductivity measurements**

The apparatus designed and built to measure the thermal conductivity of cladding tube sections in the present work is presented here. Design, drawing, mounting and implementation was done over the last three years; technical help was necessary for the electronic parts of the rig, as well as for the programming of the controlling unit. The centrepiece of this chapter is the theoretical model based on radiosity calculations according to Gebhart's method. This allows the determination of the radiant heat exchange by measuring the temperature at six locations in the apparatus. Lastly, the general experimental procedure is described.

### 3.1 Thermal conductivity measurement methods

Measuring the thermal conductivity of a material is a task which can be carried out in many ways. There are two main categories of thermal characterisation methods: steady state or transient measurements. Examples of steady state techniques are the hot-plate, the direct heating (also known as Kohlrausch) and the radial heat flow methods. On the other hand, the laser flash [129], the modulated differential scanning calorimetry [130] and the hot strip methods are all based on transient phenomena [131]. Regardless of the type of method, all techniques are based on geometries or configurations in which the heat equation can be solved:

$$\frac{\partial T}{\partial t} - \alpha \nabla^2 T = 0 \quad (3.1)$$

Whilst the differential form of the heat equation shown in Equation 3.1 is the most widely used, it is based on the assumption that the thermal diffusivity of the material  $\alpha$  is independent of position. In cases where this is not true, the thermal conductivity cannot be extracted from the second differential operator, and Equation 3.2 is used:

$$\rho C_p(\vec{r}) \frac{\partial T}{\partial t} - \nabla [k(\vec{r}, T) \nabla T] = 0 \quad (3.2)$$

Where  $\rho$ ,  $C_p$  and  $k$  are the mass density, the heat capacity and the thermal conductivity of the material.

Except for the radial heat flow and direct heating methods, these techniques require rather small and usually flat samples, such as platelets or millimetre-sized discs. Though any of these methods can be used to characterise the thermal conductivity of most materials, shape effects and highly anisotropic materials generally present an issue.

### 3.2 Radial heat flow method

#### 3.2.1 Basics

The radial heat flow has been chosen as the preferred technique for all the measurements carried out in the present thesis. The main motivation behind this choice is the potential of this method in tackling the difficulties presented by silicon carbide-based composite tubes. Indeed, because of the architecture of the composite material, the thermal conductivity of a tubular



sample is highly anisotropic. Additionally, due to the complexity of the multilayered structure and of the manufacturing process, many defects such as inhomogeneously distributed fibres and porosity have an influence on the radial conductivity. Therefore, the actual conductivity of a clad cannot be deduced from measurements taken on the individual components and must be measured on real tubes. Finally, the high aspect ratio of the tubes is expected to have an impact: the samples studied in this work have aspect ratios ranging from 7 to 20. Though relatively high, these aspect ratios are still far from that of an actual fuel rod, where it would be close to 1000.

The theoretical background behind the determination of the thermal conductivity of tubular samples using a radial heat flow setup is rather simple. This work is based on the implementation of Fourier's law of heat conduction in a radial system.

$$\dot{q}'' = -k \frac{dT}{dr} \quad (3.3)$$

As previously introduced, the temperature gradient is the physical phenomenon measured in the present experiment. This implies that one only needs to determine the heat flux  $\dot{q}''$  and to divide it by the measured gradient to assess the thermal conductivity of a material.

Though seemingly very simple, assessing the heat flowing through the sample in an accurate way is in fact difficult since many factors have to be accounted for. The sketch presented in Figure 3.1 outlines the simplified geometry considered in this discussion. The system is reduced to its most prominent components, namely the heating rod, the sample and the vacuum chamber. The quantity we want to measure and model is the transverse thermal conductivity.

The experimental apparatus is built as a fully axis-symmetric device. Thermocouples are attached at the mid-height and top of the heating wire, inner (middle and top positions) and outer surfaces of the sample, at the top of the electrical connection cylinder, as well as on the inner surface of the vacuum chamber. Heating occurs via Joule heating within the heating element, a long and thin graphite rod.

The measurements are carried out in vacuum to avoid oxidation. This also guarantees that the heat transfer is only radiative, i.e. convection can be neglected. In addition to this, the inner surface of the vacuum chamber has been coloured in black with a carbon-based paint to allow a better control of its emissivity.

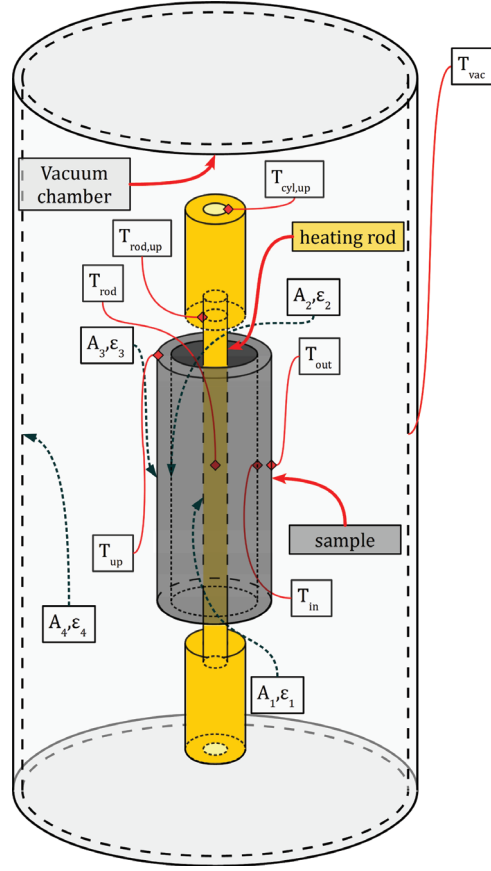


**Figure 3.1** – Simplified geometry of the experimental setup. The four surfaces shown here are split into six because of the axial temperature profile along the heating rod. The heating rod and its two holding graphite cylinders are shown in yellow, the sample is the hollow cylinder in the centre and the vacuum chamber surrounds the assembly. Figure 3.6 shows the subdivision of the surface  $A_1$  into three separate parts.

### 3.2.2 Heat equation

To extract the desired material property from the experimental data, one needs to solve the heat equation within the sample. After a sufficiently long hold time, a steady state is reached, meaning that the temperature gradient in the sample wall attains a constant value whilst other parts of the apparatus such as the vacuum can still heat up slightly – an effect that can be neglected because of its limited magnitude. Further details on the quasi-static temperature of the sample will be discussed later. Furthermore, the angular and axial components of the heat flux can be set to zero. This assumption is only true close enough to the sample mid-height, i.e. where the gradient is measured. Indeed, if one is to consider a slice in the  $r - z$  reference frame, the temperature field is described by orthogonal functions, more specifically by Fourier series [132].

### Radial temperature profile

The geometry considered in the following analysis is represented on Figure 3.2. The sketch on the left shows the geometry in which the heat equation is solved, whereas the profiles on the right give a schematic representation of these solutions in the heating rod and through the sample wall.

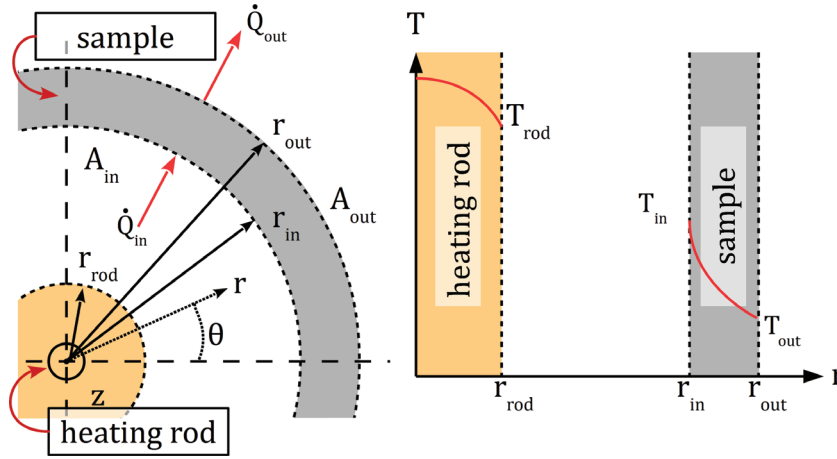


**Figure 3.2** – Sketch showing the geometry in which the heat equation is solved to determine the thermal conductivity (left) and temperature profiles in the heating rod and across the sample wall (right)

With these considerations, the heat equation is reduced to:

$$\frac{1}{r} \left[ \frac{d}{dr} r \left( \frac{dT}{dr} \right) \right] = 0 \quad (3.4)$$

which yields the following general solution:

$$T(r) = \frac{C_1}{\ln r} + C_2 \quad (3.5)$$

where  $C_1$  and  $C_2$  are integration constants, determined using Dirichlet boundary conditions at both surfaces of the tube,  $T(r = r_{in}) = T_{in}$  and  $T(r = r_{out}) = T_{out}$ :

$$C_1 = \frac{T_{in} - T_{out}}{\ln(r_{out}/r_{in})} \quad \text{and} \quad C_2 = T_{in} - \frac{T_{in} - T_{out}}{\ln(r_{out}/r_{in})} \ln r_{in} \quad (3.6)$$

Hence, the temperature field is given by:

$$T(r) = T_{\text{in}} + \frac{\ln(r/r_{\text{in}})}{\ln(r_{\text{out}}/r_{\text{in}})} (T_{\text{out}} - T_{\text{in}}) \quad (3.7)$$

Introducing the latter in Equation 3.3 yields the following expression for the through-thickness thermal conductivity:

$$k = -\frac{1}{T_{\text{in}} - T_{\text{out}}} \frac{\dot{Q}_{\text{in}}}{2\pi h} \ln\left(\frac{r_{\text{out}}}{r_{\text{in}}}\right) \quad (3.8)$$

#### Axial temperature profile

Though knowledge of the axial temperature profile is not required to calculate the equation defining the radial thermal conductivity, it is necessary to determine the heat flow rate at each of the surfaces of the apparatus. Based on experimental data, we know that significant losses occur along the length of the samples. This is explained as follows: the pair of surfaces composed of the inside of the sample and the heating wire form a *cavity*. The difference between the measurement points at the top and middle of the heating element can reach magnitudes of more than 600°C<sup>1</sup>. This effect must be taken into account so that the correct heat fluxes can be determined.

From a theoretical standpoint, the axial component of the temperature profile should be described by Bessel-type functions. However, analytically determining these with the boundary conditions at hand (radiative heat fluxes) would be extremely difficult, if not impossible. Indeed, solving this problem would involve Neumann boundary conditions, which are proportional to  $T^4$ , yielding a partial differential equation of the form  $ay'' + by' = y^4$  at the sample surfaces. To circumvent this difficulty, FEM simulations helped providing numerical solutions to the heat equation.

---

<sup>1</sup>As an example, a temperature of 432°C has been measured at the top of the heating element, whilst it reached 1050°C at its mid-height.

### Finite elements modelling

Finite element simulations have been carried out using ElmerFEM [133], thus yielding heat maps such as the one presented in Figure 3.3. Using case specific simulations, one can extract the axial-profile from the FEM results. These simulations are performed using the built-in heat equation solver, in a two-dimensional slice in the  $rz$  reference frame, as seen in the top half of Figure 3.3. The boundary conditions are an external temperature of 25°C, as well as a volumetric heat source calculated from the experimental results. Based on this, as well as on the temperatures measured at the extremity and middle of the sample, one can evaluate a fit using Fourier series such as Equation 3.9.

$$T(z) = a_0 + \sum_i a_i \cos(i\omega z) + b_i \sin(i\omega z) \quad (3.9)$$

This example illustrates why the temperatures of the sample and heating element cannot be assumed to be uniform. Since radiosity calculations are carried out with a single surface temperature, this means that the average of the three profiles shown in Figure 3.3 has to be determined.

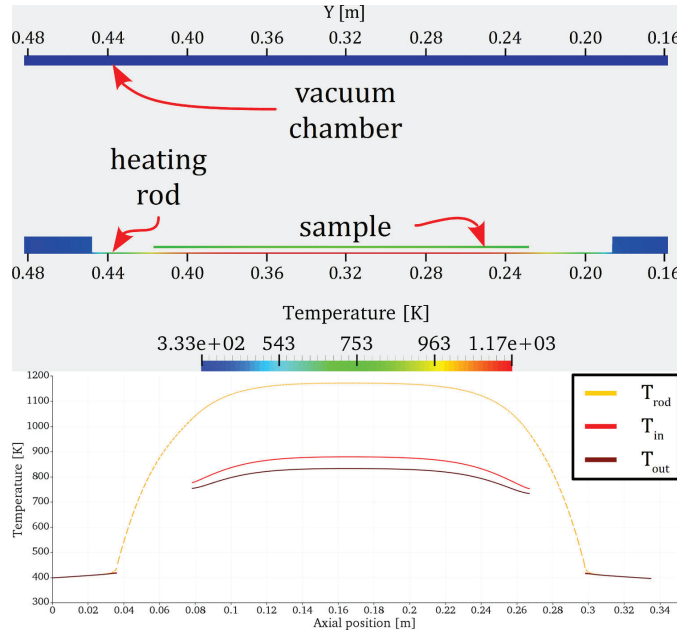


**Figure 3.3** – FEM heat map output showing the axial temperature gradients along both the sample and heating wire surfaces. The upper blue area is the vacuum chamber wall, the blue blocks on the left and right sides of the heat map are the graphite cylindrical holders seen in Figure 3.1, the thin green area represents a sample, and the red rod is the heating element. The profiles on the lower half of the figure are taken along the  $y$  axis of the relevant surfaces.

Using a Fourier series fit with four sine and cosine terms yields an accurate enough approximation of the orthogonal function describing the temperature field [132]. To obtain this, one needs to use some properties of the Fourier series fitting routines implemented in Matlab, i.e. that a  $n$  components Fourier-series fit requires at least  $2n + 2$  data points to be defined. Based on the FEM simulations, the relative temperature of the sample can be known for a few specific points, such as 10, 20, 40, 60, 80 and 90 percent of the sample length. These points are semi-empirical, and represent inflexion points of the curves seen in Figure 3.3. Extrapolating these additional points, the whole profile can be obtained and averaged.

The case of the heating element is a bit more complicated since the axial temperature profile is the result of two superposed Bessel functions. An additional measurement point is needed at the top of the rod, so that it can be characterised. The temperature profile can then be fitted with the previously discussed Fourier series.

### 3.3 Radiosity

The central part of this discussion deals with the determination of the amount of heat flowing across the sample wall. To do this, the incoming and outgoing heat fluxes must be calculated at both the inner and outer surfaces of the sample. Since the heat transfer occurs solely through thermal radiation, a measurement of the temperature surfaces is not sufficient. Indeed, radiative heat exchange depends strongly on the geometry of the experimental apparatus as well as on the surface characteristics of the sample, heating body and those of any other surface involved in the exchange of energy.

Gebhart [134] laid out a formalism based on the analysis of the amount of energy absorbed at surfaces forming an enclosure in which radiant heat transfer occurs. This analytical scheme, mostly known as the radiosity method, is particularly well suited for analysing such cases. The radiosity of an arbitrary surface noted  $J_e$  is the radiant heat flux  $\Phi_e$  leaving the aforementioned surface per unit area.

$$J_e = \frac{d\Phi_e}{dA} = J_{e,em} + J_{e,r} + J_{e,tr} \quad (3.10)$$

with

- $\Phi_e$ , the radiant flux leaving the surface;
- $J_{e,em}$ , the emitted part of the radiant flux, also known as the radiant exitance of the surface:  $J_{e,em} = \varepsilon \sigma T^4$ ;

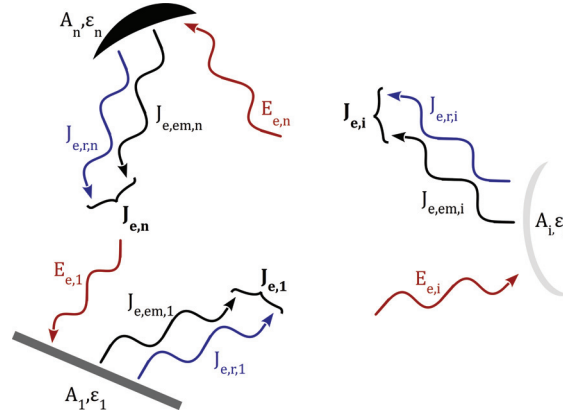


**Figure 3.4** – Set of three arbitrary surfaces exchanging heat via thermal radiation

- $J_{e,r}$ , the reflected component of the radiosity of any of the surfaces;
- $J_{e,tr}$ , the transmitted component of the surface's radiosity, which is zero for the surface of opaque bodies.

This discussion of Gebhart's formalism is based on the complete demonstration found in Howell, Mengüç and Siegel [135]. The goal of the analysis is to determine the factors  $\Gamma_{ij}$ , which account for the fraction of the energy emitted from a surface  $A_i$  that reaches another surface  $A_j$ , and is absorbed there. These factors include all possible paths that the energy could take to reach  $A_j$ , meaning that even though both surfaces do not “see” each other, a non-zero fraction of the energy emitted by  $A_i$  could reach and be absorbed at the surface  $j$  through multiple reflections against the other surfaces forming the enclosure. Hence, the quantity  $\Gamma_{ij} A_i \epsilon_i \sigma T_i^4$  is the fraction of the energy emitted by  $A_i$  and absorbed by  $A_j$ . The energy balance at the surface  $j$  can be expressed as:

$$\dot{Q}_j = A_j \epsilon_j \sigma T_j^4 - \sum_{i=1}^N \Gamma_{ij} A_i \epsilon_i \sigma T_i^4 \quad (3.11)$$

To determine the factors  $\Gamma_{ij}$ , one expands the right-hand side of Equation 3.11. The surface  $A_i$  emits a total amount of energy  $E_i = A_i \epsilon_i \sigma T_i^4$ , out of this quantity,  $\epsilon_j F_{ij} A_i \epsilon_i \sigma T_i^4$ , where  $F_{ij}$  is the view factor between  $A_i$  and  $A_j$ ; these geometry dependent factors are further discussed in section 3.3.1. The fractions of  $E_i$  reaching any of the other surfaces  $A_n$  and which is then

### Chapter 3. Thermal conductivity measurements

reflected is  $\rho_n F_{in} E_i$ , where  $\rho_n$  is the absorptance of the surface  $n^2$ . Out of this amount of reflected energy, a fraction  $\Gamma_{nj}$  will reach  $A_j$  and be absorbed there. Thus, one can develop the fraction  $\Gamma_{ij} E_i$  into the expression given in Equation 3.12.

$$\Gamma_{ij} E_i = E_i \left( \varepsilon_j F_{ij} + \sum_{k=1}^N F_{ik} \rho_k \Gamma_{kj} \right) \quad (3.12)$$

At this point, the emitted energy  $E_i$  can be left out the expression, and one can arrange the terms in the following way:

$$F_{ij} \varepsilon_j = \Gamma_{ij} - \sum_{k=1}^N F_{ik} \rho_k \Gamma_{kj} \quad (3.13)$$

Generalising this to the  $N$  surfaces forming the enclosure yields the following set of  $N$  equations:

$$\begin{cases} (1 - \rho_1 F_{11}) \Gamma_{1j} & \cdots & -F_{1N} \rho_N \Gamma_{Nj} & = & F_{1j} \varepsilon_j \\ \vdots & \ddots & \vdots & & \vdots \\ -F_{N1} \rho_1 \Gamma_{1j} & \cdots & (1 - \rho_N F_{NN}) \Gamma_{Nj} & = & F_{Nj} \varepsilon_j \end{cases} \quad (3.14)$$

This equation system is solved for each of the  $\Gamma_{ij}$ , and further expanding on the  $j$  indices yields then the complete solution for the so-called *Gebhart factors matrix*.

$$\overbrace{\begin{pmatrix} 1 - \rho_1 F_{11} & \cdots & -\rho_N F_{1N} \\ \vdots & \ddots & \vdots \\ -\rho_1 F_{N1} & \cdots & 1 - \rho_N F_{NN} \end{pmatrix}}^{\mathbf{M}} \overbrace{\begin{pmatrix} 1 - \rho_1 F_{11} & \cdots & -\rho_N F_{1N} \\ \vdots & \ddots & \vdots \\ -\rho_1 F_{N1} & \cdots & 1 - \rho_N F_{NN} \end{pmatrix}}^{\mathbf{\Gamma}} = \overbrace{\begin{pmatrix} 1 - \rho_1 F_{11} & \cdots & -\rho_N F_{1N} \\ \vdots & \ddots & \vdots \\ -\rho_1 F_{N1} & \cdots & 1 - \rho_N F_{NN} \end{pmatrix}}^{\mathbf{F}} \quad (3.15)$$

<sup>2</sup>This is equal to  $1 - \varepsilon$  in the case of diffuse grey surfaces.



The Gebhart matrix is obtained through the inversion of  $\mathbf{M}$ , yielding  $\Gamma = \mathbf{M}^{-1}\mathbf{F}$ . The Gebhart factors share some properties with the view factors presented later<sup>3</sup>. The sum rule is also valid, since all the emitted energy has to be absorbed by the surfaces of the enclosure. In addition to this rule, the reciprocity theorem applies, as the factors  $\Gamma_{ij}$  are built upon the view factor themselves. Equation 3.16 shows these two properties in written form.

$$\sum_{j=1}^N \Gamma_{ij} = 1 \quad \text{and} \quad \varepsilon_i A_i \Gamma_{ij} = \varepsilon_j A_j \Gamma_{ji} \quad (3.16)$$

Using these two relationships in the energy balance from Equation 3.11 yields the following expression for any surface  $i$ .

$$\dot{Q}_i = A_i \varepsilon_i \sigma T_i^4 \sum_{j=1}^N \Gamma_{ij} - \sum_{j=1}^N \Gamma_{ij} A_i \varepsilon_i \sigma T_j^4 = A_i \varepsilon_i \sum_{j=1}^N \Gamma_{ij} \sigma (T_i^4 - T_j^4) \quad (3.17)$$

In the case of the experimental rig built for this study, the simplified geometry contains six bodies, which surfaces exchange heat through thermal radiation. Hence, the system is simplified to a six by six matrix equation. However, as a first step towards a solution, the view factors need to be calculated.

#### 3.3.1 View factors

A view factor is a geometrical function used to characterise the heat transfer between two bodies. Thus, the amount of radiation leaving a body and reaching another is proportional to  $F_{12}$ . The mathematical definition for any pair of two surfaces is given by Equation 3.18.

$$F_{12} = \frac{1}{A_1} \int_{A_1} \int_{A_2} \frac{\cos \theta_1 \cos \theta_2}{\pi s^2} dA_1 dA_2 \quad (3.18)$$

where  $\theta_1$  and  $\theta_2$  are the angles between the normals of the surfaces  $A_1$  and  $A_2$ , and,  $s$  is the direct line linking them, as shown in Figure 3.5.

In addition to the mathematical definition of the view factors themselves, there are three fundamental and extremely useful properties that are always true.

<sup>3</sup>Equations 3.20, 3.19 and 3.21 to be precise.

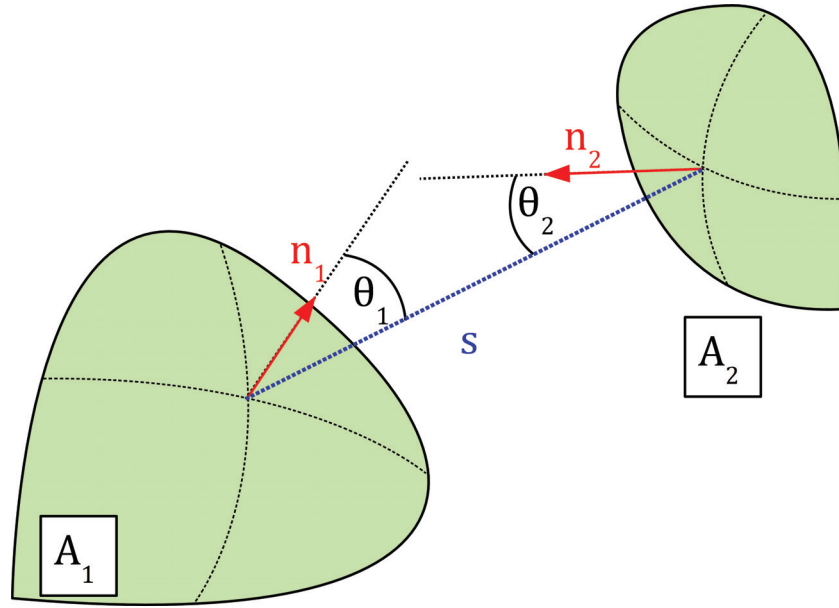


**Figure 3.5** – Arbitrary pair of surfaces  $A_1$  and  $A_2$  separated by a distance  $s$ , and normals  $n_1$  and  $n_2$  angled at  $\theta_1$  and  $\theta_2$  relative to the aforementioned line  $s$

- the sum of all view factors originating from any surface equals one. This follows directly from the conservation of energy. Indeed, there cannot be more, or less, energy coming out of a surface than what is emitted.

$$\sum_j F_{ij} = 1 \quad (3.19)$$

- The view factor of a surface to itself depends on its curvature.

$$F_{ii} \begin{cases} = 0 & \text{if } A_i \text{ is convex or flat} \\ > 0 & \text{if } A_i \text{ is concave} \end{cases} \quad (3.20)$$

- The reciprocity theorem can be used to determine  $F_{ji}$  if  $F_{ij}$  is known.

$$A_i F_{ij} = A_j F_{ji} \quad (3.21)$$

### View factors describing the experimental apparatus

As previously mentioned, the geometry of the experimental apparatus can be simplified to a sub-set of six surfaces. The sketch presented on Figure 3.6 shows a 2D view in the  $rz$  plane, in cylindrical coordinates. It shall be noticed that the flanges of the vacuum chamber are not considered. The reason behind this simplification is that, given the aforementioned aspect ratio of the sample, a large fraction of the thermal radiation goes directly from the heating element to the sample. Once back reflections with the vacuum chamber are considered, only a negligible amount of energy is unaccounted, whereby justifying this simplified geometry.

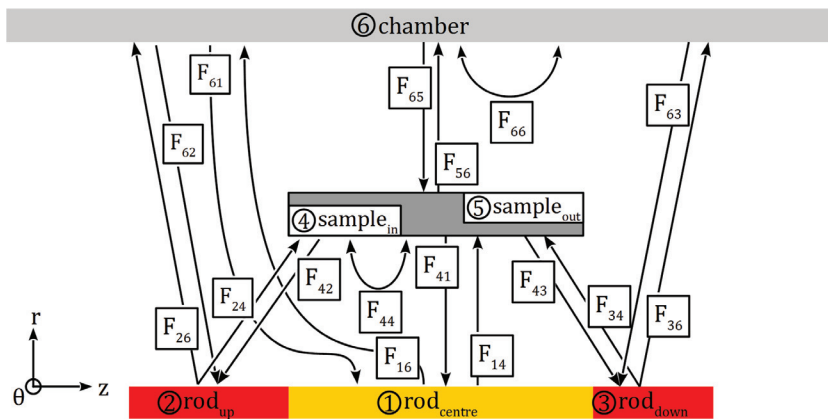


**Figure 3.6** – 2D view of the experimental apparatus used to determine the thermal radiation heat exchange

Out of the thirty-six possible view factors, only half of them are non-zero. These are all presented in Figure 3.6. The reasons for which eighteen view factors are zero are listed below.

- A large number of view factors are equal to zero because their respective pairs of surfaces have no direct line of sight. These are coloured in blue in Table 3.1.
- Another four factors, coloured in orange, are zero because they are from convex surfaces to themselves.

Although a view factor is equal to zero, it does not necessarily mean that no thermal radiation can be exchanged between the pair of surfaces. It only means that no direct exchange occurs; heat can however be exchanged via multiple reflections, since we are dealing with diffuse grey bodies.

### Chapter 3. Thermal conductivity measurements

Some of the view factors collected in Table 3.1, coloured in light grey, can be calculated with well-defined equations, namely  $F_{41}$  using Equation 3.24,  $F_{44}$  with Equation 3.26,  $F_{26}$ ,  $F_{36}$  and  $F_{56}$  with Equation 3.27 as well as the sum  $F_{14} + F_{24} + F_{34}$  using Equation 3.22. For all the other non-zero view factors, either the sum rule (dark grey) or the reciprocity theorem (white) are used.

**Table 3.1** – Summary of the view factors implicated in the radiosity calculations determining the heat fluxes between the heating rod, the sample and the vacuum chamber. Surface indices are the same as the ones used in Figure 3.6. The colour code is the following: light grey  $\equiv$  equation from literature, dark grey  $\equiv$  sum rule, white  $\equiv$  reciprocity, blue  $\equiv$  no line of sight and orange  $\equiv$  flat or convex surfaces.

$i \setminus j$	$F_{i,1}$	$F_{i,2}$	$F_{i,3}$	$F_{i,4}$	$F_{i,5}$	$F_{i,6}$
$F_{1,j}$	0	0	0	$F_{14}$	0	$F_{16}$
$F_{2,j}$	0	0	0	$F_{24}$	0	$F_{26}$
$F_{3,j}$	0	0	0	$F_{34}$	0	$F_{36}$
$F_{4,j}$	$F_{41}$	$F_{42}$	$F_{43}$	$F_{44}$	0	$F_{46}$
$F_{5,j}$	0	0	0	0	0	$F_{56}$
$F_{6,j}$	$F_{61}$	$F_{62}$	$F_{63}$	$F_{64}$	$F_{65}$	$F_{66}$

#### Heating rod to sample

Describing the radiant heat transfer between the heating rod and the sample is done by using two view factors. The first geometrical configuration considered is that of the whole heating rod exchanging heat with the sample, noted  $F_{14,\text{tot}}$ , which is equal to the sum of  $F_{14}$ ,  $F_{24}$  and  $F_{34}$ . This situation is sketched in Figure 3.7. The reason for using this specific view factor is that there is no direct equation describing the view factors between the colder parts of the heating rod and the sample. Therefore, the difference between this view factor and the one describing the situation of the hotter central part of the rod and the sample,  $F_{14}$ , is equal to the sum of  $F_{24}$  and  $F_{34}$ .

This first situation is that of a centred full cylinder inserted within a shorter hollow cylinder, with the smaller full cylinder emerging on both ends of the shorter hollow body, the solution of which can be found in Rea [136].

$$F_{14,\text{tot}} = \frac{Y}{L} + \frac{X}{L} F_X + \frac{Z}{L} F_Z - \frac{X+Y}{L} F_{X+Y} - \frac{Y+Z}{L} F_{Y+Z} \quad (3.22)$$

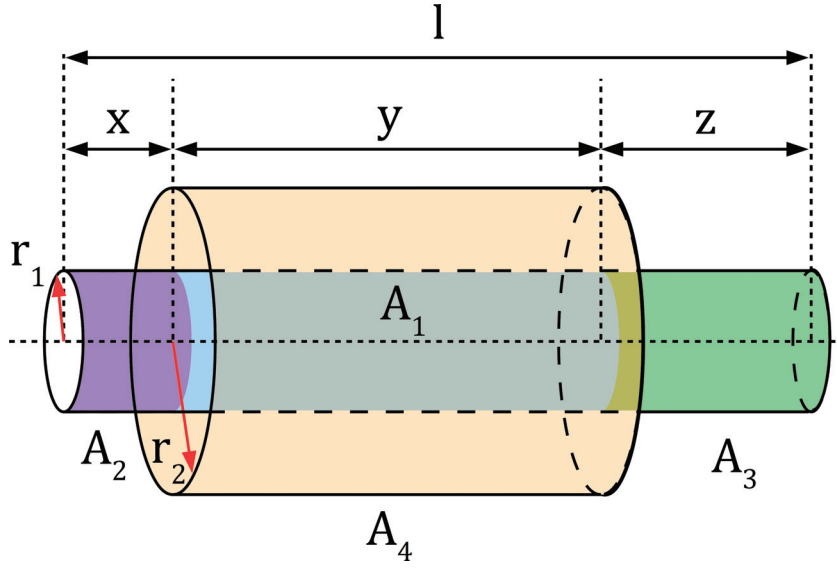


**Figure 3.7** – Geometry between the full length of the heating rod and the sample, used to calculate  $F_{14,\text{tot}}$ . The blue surface accounts for the hotter part of the heating rod  $A_1$ , the purple and green surfaces represent its colder parts  $A_2$  and  $A_3$  and the orange surface is the inner surface of the sample  $A_4$ .

with

$$F_{\xi} = \frac{B_{\xi}}{8R\xi} + \frac{1}{2\pi} \left\{ \cos^{-1} \left( \frac{A_{\xi}}{B_{\xi}} \right) - \frac{1}{2\xi} \left[ \frac{(A_{\xi} + 2)^2}{R^2} - 4 \right]^{1/2} \cos^{-1} \left( \frac{A_{\xi}R}{B_{\xi}} \right) - \frac{A_{\xi}}{2\xi R} \sin^{-1} R \right\} \quad (3.23)$$

where  $\xi = X, Z, X + Y$  or  $Y + Z$  are defined as follows:

$$X = \frac{x}{r_2}, \quad Y = \frac{y}{r_2}, \quad Z = \frac{z}{r_2}, \quad L = \frac{l}{r_2}, \quad R = \frac{r_1}{r_2}, \quad A_{\xi} = \xi^2 + R^2 - 1 \text{ and } B_{\xi} = \xi^2 - R^2 + 1$$

Next, comes the case of the view factor between the central part of the heating wire and the inner surface of the sample,  $F_{14}$ . In this case, two coaxial cylinders of equal length are considered. The situation is sketched in Figure 3.8.

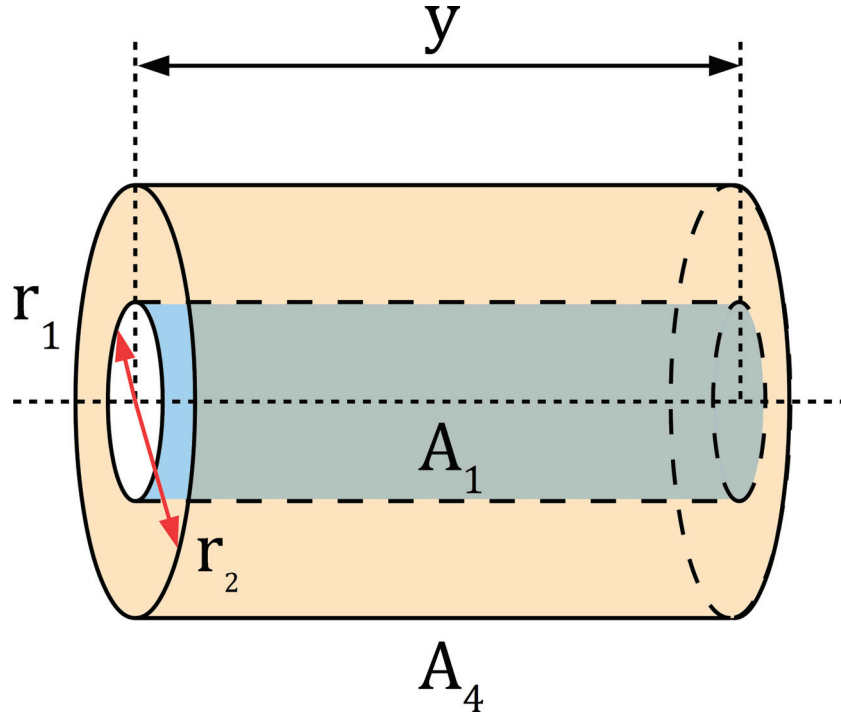


**Figure 3.8** – Geometry used to determine the view factor between the hot part of the heating rod and the sample

Solutions of the reciprocal problem,  $F_{41}$  have been published by Leuenberger and Person as well as Hamilton and Morgan [137, 138]. In these papers, the exchange from the outer to the inner cylinder is analytically solved, yielding Equation 3.24.

$$F_{41} = \frac{1}{\pi R_2} \left\{ \begin{array}{l} \frac{1}{2} (R_2^2 - R_1^2 - 1) \cos^{-1} \left( \frac{R_1}{R_2} \right) + \pi R_1 - \frac{\pi}{2} AB \\ -2R_1 \tan^{-1} (R_2^2 - R_1^2)^{1/2} + [(1 + A^2)(1 + B^2)]^{1/2} \\ \tan^{-1} \left[ \frac{(1 + A^2)B}{(1 + B^2)A} \right]^{1/2} \end{array} \right\} \quad (3.24)$$

where  $R_1$  and  $R_2$  are the aspect ratios of both cylinders, and the parameters  $A$  and  $B$  are the sum and difference of the aspect ratios.

$$R_1 = \frac{r_1}{y}, \quad R_2 = \frac{r_2}{y}, \quad A = R_1 + R_2 \text{ and } B = R_2 - R_1$$

$F_{14}$  is then obtained using the reciprocity theorem presented in Equation 3.21.

### Cold top and bottom parts

Continuing onto the colder parts of the heating rod, whereby a cylinder on top of another is considered with a separation  $d$  was solved by Rea [136]. This situation is sketched in Figure 3.9.

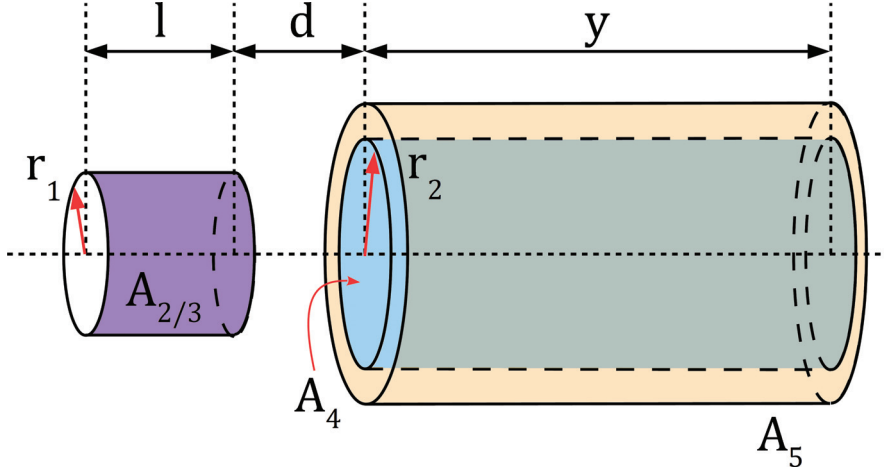


**Figure 3.9** – Geometry between the cold parts  $A_{2/3}$  (purple) of the heating elements and the inner surface of the sample  $A_4$  (in blue). The orange surface  $A_5$  is the outer area of the sample.

These two view factors are calculated using Equation 3.25, in the limit of  $d \rightarrow 0$

$$F_{14/34} = \frac{L+D}{L} F_{L+D} + \frac{Y+D}{L} F_{Y+D} - \frac{D}{L} F_D - \frac{L+D+Y}{L} F_{L+D+Y} \quad (3.25)$$

Here, the  $F_\xi$  are given by Equation 3.23, with the addition of  $D = d/r_2$ .

### Inner surface of the sample to itself

An exact solution also exists for the geometry shown in Figure 3.10. This case is similar to the one used to calculate  $F_{41}$ . Solutions to the double integral describing the view factor have been published by several authors [137, 138, 139].

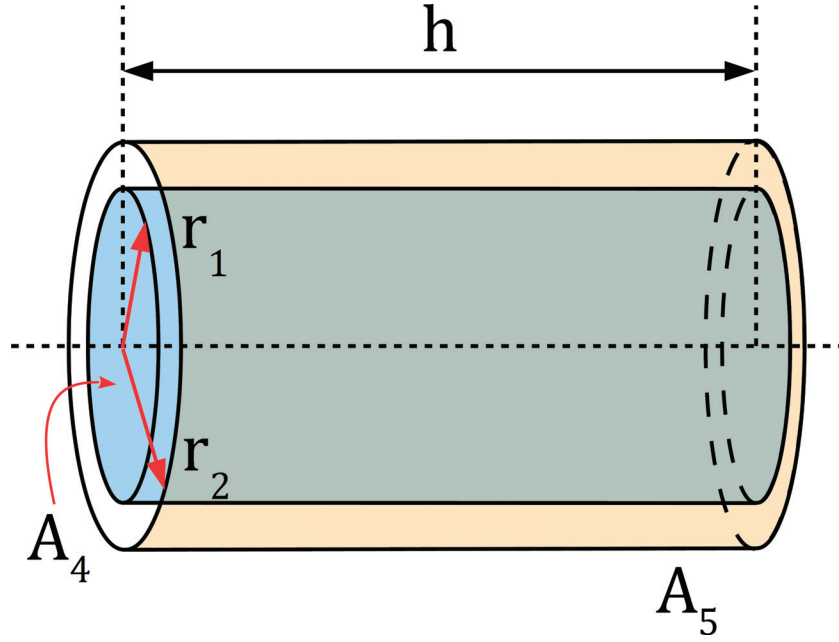


**Figure 3.10** – View factor of the inner surface of the sample  $A_4$  (in blue) with itself

$$F_{44} = \frac{1}{\pi R_1} \left\{ \begin{array}{l} \pi (R_2 - R_1) + \cos^{-1} \left( \frac{R_1}{R_2} \right) \\ - (1 + 4R_2^2)^{1/2} \tan^{-1} \frac{[(1 + 4R_2^2)(R_2^2 - R_1^2)]^{1/2}}{R_1} \\ + 2R_1 \tan^{-1} \left[ 2(R_2^2 - R_1^2)^{1/2} \right] \end{array} \right\} \quad (3.26)$$

With  $R_1 = r_1/h$  and  $R_2 = r_2/h$ . This view factor could also be deduced from the sum rule. Nevertheless, it is interesting to compute it in order to validate the assumption made to calculate the view factors between the colder parts of the heating word and the sample,  $F_{24}$  and  $F_{34}$ .



### Sample to vacuum chamber

The last cases for which view factors can be calculated directly are those of the heat transfer between the sample and the inner wall of the vacuum chamber, as well as between both cold parts of the heating rod and the chamber wall. The situation is that of a short cylinder fully enclosed within another larger coaxial cylinder. The sketch on Figure 3.11 gives an overview of the geometrical parameters used to calculate this view factor.

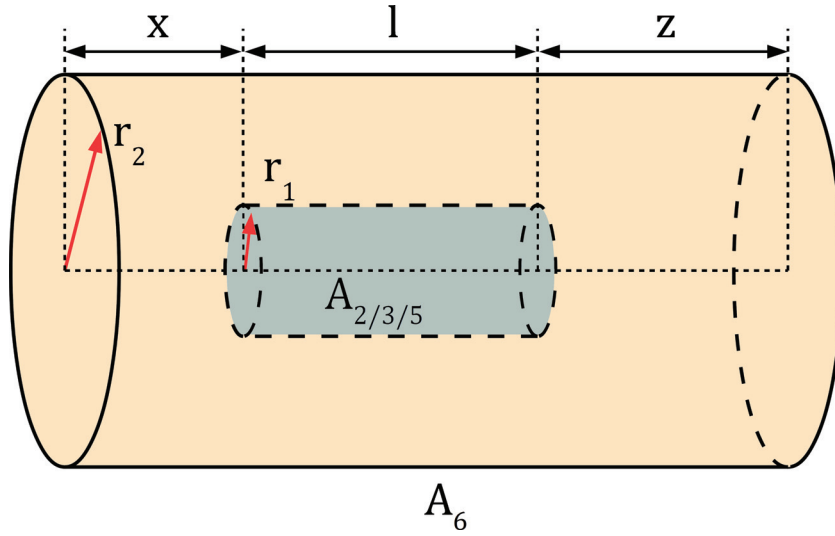


**Figure 3.11** – Geometry between the outer surface of the sample and the vacuum chamber, and between the cold parts of the heater and the chamber walls

The view factors,  $F_{26}$ ,  $F_{36}$  and  $F_{56}$ , are given by:

$$F_{i6} = 1 + \frac{X}{L} F_X + \frac{Z}{L} F_Z - \frac{L+X}{L} F_{L+X} - \frac{L+Z}{L} F_{L+Z}, \quad i = 2, 3, 5 \quad (3.27)$$

where  $X$ ,  $Z$ ,  $R$  and  $L$  are case specific length scales:

$$X = \frac{x}{r_2}, \quad Z = \frac{z}{r_2}, \quad R = \frac{r_1}{r_2} \text{ and } L = \frac{l}{r_2}$$

With the same functions  $F_\xi$ ,  $\xi = X, Z, L+X$  or  $L+Z$  as the ones used to calculate the previous view factors.

### 3.3.2 Effect of thermocouples

An additional point that needs clarifying is the potential effect of the gluing points of the thermocouples on the temperature measurement. Here, the question is whether the temperature recorded with the thermocouples is representative of that of the sample. Indeed, the thermocouples are attached to the sample by a graphite-based high temperature adhesive.

Depending on the thickness of the layer of glue applied during the preparation of the experiments, an error might be introduced. In this regard, the geometry of the sample and of the thermocouples attached to it is rather simple and can be represented as a series of thermal resistances. A view in the  $xz$  plane is shown in Figure 3.13.

The engineering concept of thermal resistance is not a material property per se; it does have relevance in the case of a piece or slab of material. It is the proportionality constant linking the temperature drop or increase across a piece of material, when a given heat flux is applied to it. The sketch displayed in Figure 3.12 shows a piece of material of dimensions  $x$ ,  $y$  and  $t$  and a thermal conductivity  $k$ . The temperature difference between the sides of the slab normal to the heat flux  $\dot{q}''$  are linked by the expression given in Equation 3.28.

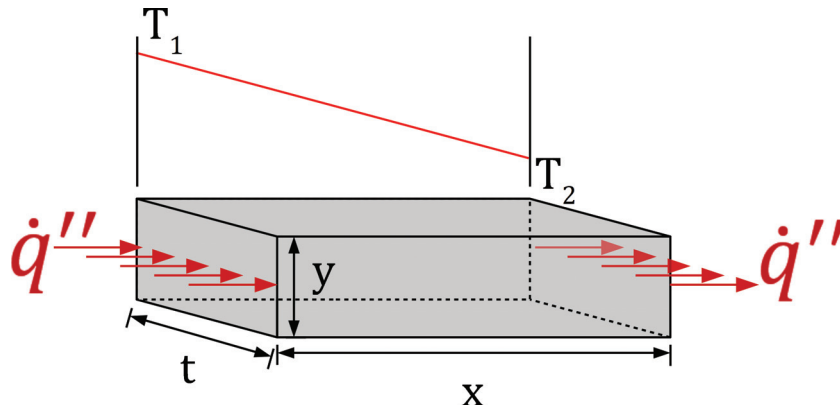


**Figure 3.12** – Temperature drop across a slab of material due to its thermal resistance  $R$ , in  $\text{K}\cdot\text{W}^{-1}$  against a heat flux  $\dot{q}''$ . The slab cross-sectional area is  $A = xy$  and its thickness is  $t$ .

$$\dot{q}'' = \frac{1}{A} \frac{T_1 - T_2}{R} \quad \text{with} \quad R = \frac{t}{k \cdot A} \quad (3.28)$$

Based on this equation, the temperature gradient across any of the components shown in Figure 3.13 can be calculated.

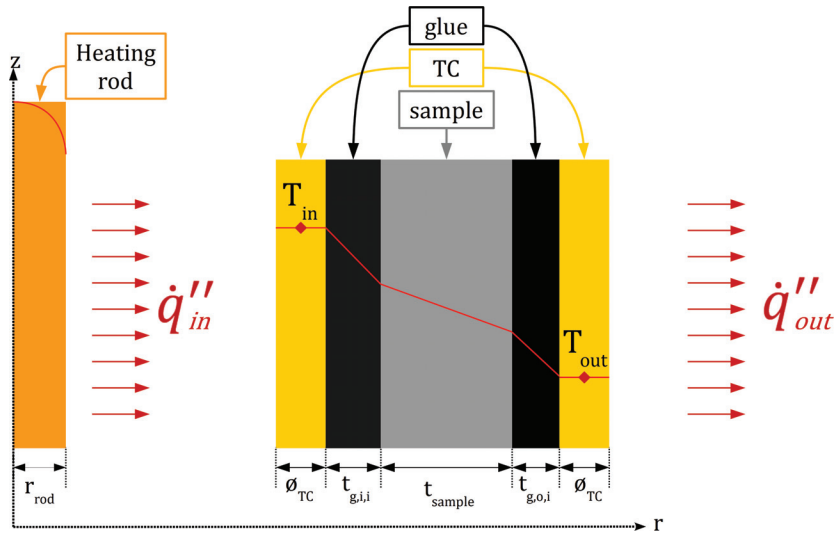


**Figure 3.13** – Sketch showing the temperature profile across the sample-glue-thermocouples system. Note that the thicknesses of the gluing points can be different.

Using the relationship given in Equation 3.28, the temperature drop through the graphite adhesive can be determined. Assuming that both the temperature and heat flux are continuous at the thermocouple/glue interface (Dirichlet and Neumann boundary conditions), one can determine the temperature at the glue/sample interfaces shown in Figure 3.13.

$$T_{s,in} = T_{TC,in} - \frac{\dot{q}''_{in} t_{g,in}}{k_g} \quad T_{s,out} = T_{TC,out} + \frac{\dot{q}''_{out} t_{g,out}}{k_g} \quad (3.29)$$

The effect of the glue on the measurement is rather negligible for a simple reason. Although the thermal conductivity of the glue itself is not very high – about  $5 \text{ W} \cdot \text{m}^{-1} \cdot \text{K}^{-1}$  –, the fact that the amount of applied glue is very small, in the order of 50 to 200  $\mu\text{m}$  at most, means that even though the heat flux can reach values in the tens of thousands of watt per square metre, only a sub-degree drop occurs there<sup>4</sup>.

<sup>4</sup>Note that a significant temperature difference is observed in case where the inner thermocouple is not properly glued. In such occurrences, the only solution is to stop the measurement, glue the thermocouple again and resume the experiment.

### 3.4 Experimental

#### 3.4.1 Experimental apparatus

The experimental apparatus designed and built for this project has been made, as much as possible, from simple and easily obtainable parts. Aside from the custom-made vacuum chamber (70 cm high, 20 cm diameter), four ceramic discs making the central part of the holding system and two hollow cylindrical graphite connectors, all parts are either commercially available or can be manufactured by any well-equipped workshop.

The overall system is held by three M12 bars of 60 cm, which are held by a basket system attached to the upper flange of the vacuum chamber. Two of the aforementioned ceramic discs (made out of  $Y_2O_3$  stabilised  $ZrO_2$ ) are placed at an appropriate height at a distance of 30 cm from one another. Two similar ceramic discs are symmetrically set between the other two. Their spacing corresponds to the length of the measured sample. These two discs have three wound drill holes to hold the sample at its extremities with M6 screws. All four discs are made of a ceramic, as they are in contact with the electrical system; this warrants the use of an insulator. Would they be made of a metal, the whole chamber would enter in contact with the circuit, what would be very dangerous, considering that the apparatus is operated at currents up to 60 Amps and 15 Volts.

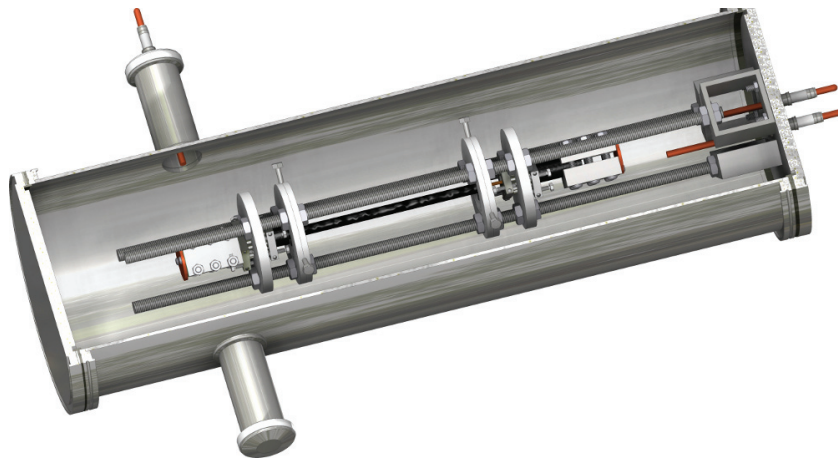


**Figure 3.14** – 3D view of the experimental apparatus designed with Autodesk Inventor. The vacuum chamber is 70 cm long and has a diameter of 20 cm.

Electrical current is brought in and out of the chamber using W-HV15S-CE-CU64 current feedthroughs bought from Baruvac. These are large copper rods (6 mm diameter) made to carry currents up to 180 Amps at fairly high voltages. Flexible steel braids are used to link the feedthroughs to large pieces of steel holding a 7 cm long hollow cylinder made of graphite, with an outer diameter of 1.9 cm and an inner diameter of exactly 3.18 mm, so that it can act as

a connector with the heating element. The heating body is a rod of isomolded graphite bought from the Graphitestores company. It has a length of 30.48 cm and a diameter of 3.18 mm. A CAD 3D render of the actual apparatus is shown in Figure 3.14.

#### 3.4.2 Thermocouple positioning and gluing

Positioning and gluing the thermocouples at precise locations on the surfaces of the samples proved to be a much bigger challenge than initially expected. Due to the difficulties that come from working in a thermal radiation mode, the introduction of any additional body such as expansion and contraction rings to hold the thermocouples was rapidly ruled out. Furthermore, no welding is possible, since ceramic tubes are being measured. This led to the decision to use high temperature adhesives for the attachment of the thermocouples to the surface.

Several adhesives were tried before a suitable one could be found. Several products from Cerambond were considered, such as  $\text{Al}_2\text{O}_3$ -, steel-, nickel-,  $\text{ZrO}_2$  and SiC-based adhesives. These consistently failed, most probably because of differential thermal expansion coefficients and because some would simply not adhere to SiC. Finally, Cédric Sauder from CEA advised to try a carbon-based adhesive from Ucar, which he used to glue SiC pieces together. This product was found to adhere to both type K thermocouples and the SiC sample and has been used with some success. Indeed, even with the right glue, the success rate of the gluing procedure was well below 50%, mainly because of the difficulty of gluing a thermocouple with a diameter of 250  $\mu\text{m}$  ten centimetres inside a tube having an inner diameter of 7.5 to 8.5 mm.

#### 3.4.3 Experimental procedure

A typical TC measurement experiment takes between four and six days. As introduced before, steady state methods are much slower than transient techniques. The reason for the long experimental procedure is that the temperature of the heating element is slowly increased and held for about three to five hours to ensure that all temperatures are fairly stable before it is raised further. Most measurements have been carried out with 32 temperature steps, ranging from 50 to 850°C on the heating element. The resulting sample temperatures depend on the radius and length of the latter, since radiant heat transfer depends on the view factors between the different surfaces considered in the theoretical model.

Figure 3.15 shows the various temperatures measured during an experimental run carried out on a sandwich cladding tube from CEA. One can see from the temperature curves that this method clearly decouples the axial and radial components of the thermal conductivity of the composite. Whilst the temperature gradient across the sample wall reaches figures of several

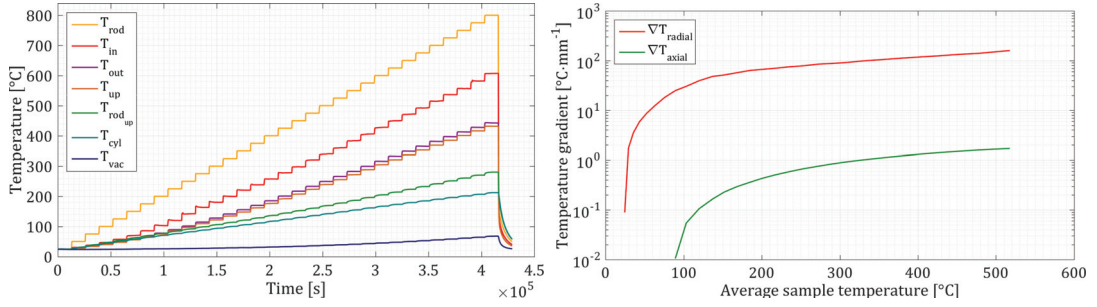


**Figure 3.15** – Example of a TC measurement carried out on a CEA sandwich sample (a) and resulting radial and axial temperature gradients in  $^{\circ}\text{C}\cdot\text{mm}^{-1}$  (b). A total of 17 temperatures were measured for 2 hours. Note that the measured temperatures are plotted against time whilst the gradients are plotted against the average sample temperature.

tens of degree per millimetre, the axial gradient measured with the difference between  $T_{\text{out}}$  and  $T_{\text{up}}$  is about two orders of magnitude smaller, giving a clear indication towards the much higher axial thermal conductivity. This topic is further discussed in the next chapters.

The 95<sup>th</sup> percentile of the temperatures of each of the six measurement points shown in Figure 3.15 are taken as the temperature at which equilibrium is reached. This is done for each of the measurement steps. This high percentile is preferred over the average temperature since it is much less sensitive to instabilities from the power supply as well as to the sharp increases at the beginning of each step, i.e. to remove outliers. This “cleaning” of the data is necessary for the radiosity calculations, as the surfaces must have a single temperature to compute the radiant heat rates. In addition to this, the axial temperature profile is accounted for by computing it with help of the aforementioned Fourier series functions given by Equation 3.9. The average of these is then used as the actual inner and outer sample temperatures as well as those of the cold and hot parts of the heating rod.

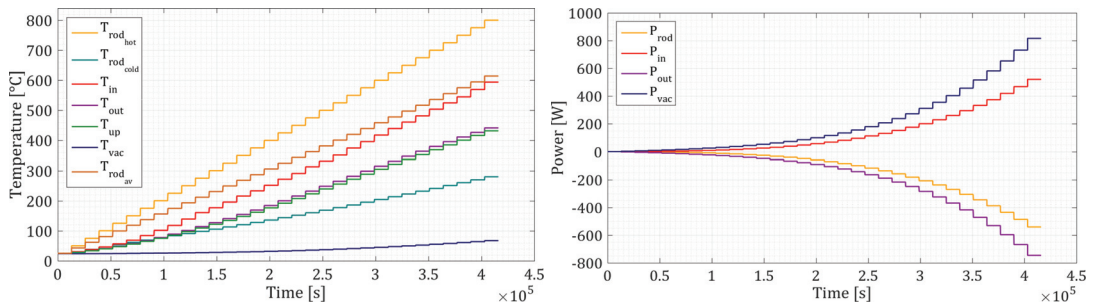


**Figure 3.16** – 95<sup>th</sup> percentile temperatures over the measurement steps (a) and power dissipated and absorbed at the relevant surfaces of the apparatus (b). Both quantities are plotted against measurement time.

## 4 Modelling

The present chapter of this thesis is focused on the modelling activities involved in this work. The theoretical models used to assess the effects of microstructural radiation-induced changes on the effective thermal conductivity are discussed. An effective medium approach known as the *Markworth* model has been followed and is presented here. This type of model can be effectively used to describe the impact of interphase changes on the overall properties of the composite.

### 4.1 Introduction

Modelling the transverse conductivity of actual composite cladding tubes involves many steps. First, the overall architecture of the studied clad has to be considered. Indeed, the “sandwich” approach taken by CEA is significantly different from the duplex and triplex concepts used by General Atomics and Westinghouse. Even a tube made only of SiC/SiC needs to be treated as a multicomponent system because of the heterogeneities found between successive tows of fibres. The case of multilayered composite tubes is a classical one; its discussion is presented in the next section.

### 4.2 Conductivity of a composite tube

To determine the actual thermal conductivity of the prototype fuel pins, we need to work with thermal resistances. The concept of interfacial thermal resistances was developed by Kapitza [140] and has since then become a fundamental concept in thermal analysis. From the solution of the heat equation, the radial temperature distribution across a hollow cylinder heated from the inside is given by Equation 3.7 on page 98. The geometry sketched in Figure 4.1 shows the situation at hand. The circumferential and axial components of the temperature distribution can be ignored close to the mid-height of the tubes, a simplification which holds true for the radial heat flow measurements since the thermocouples are attached at this exact location. The solution is repeated here for readability purposes.

$$T(r) = T_{\text{in}} + \frac{\ln(r/r_{\text{in}})}{\ln(r_{\text{out}}/r_{\text{in}})} (T_{\text{out}} - T_{\text{in}})$$

Combining this solution with the definition of the heat flux yields

$$q = \frac{2\pi kL}{\ln\left(\frac{r_{\text{in}}}{r_{\text{out}}}\right)} (T_{\text{in}} - T_{\text{out}}) \equiv \frac{\Delta T}{R} \rightarrow R = \frac{\ln\left(\frac{r_{\text{out}}}{r_{\text{in}}}\right)}{2\pi kL} \quad (4.1)$$

Equation 4.1 is the exact definition of the thermal losses due to a thermal resistance, meaning that a hollow cylinder acts as a barrier against heat flow  $q$  with a strength  $R$ .



## 4.2. Conductivity of a composite tube

When dealing with a combination of different layers and/or materials, thermal resistances are combined the same way as electrical ones, i.e. following Kirchhoff laws presented in Equation 4.2. This is valid as far as the said layers are in parallel to one another.

$$R_{\perp} = \sum_i R_i \text{ and } R_{\parallel} = \left( \sum_i \frac{1}{R_i} \right)^{-1} \quad (4.2)$$

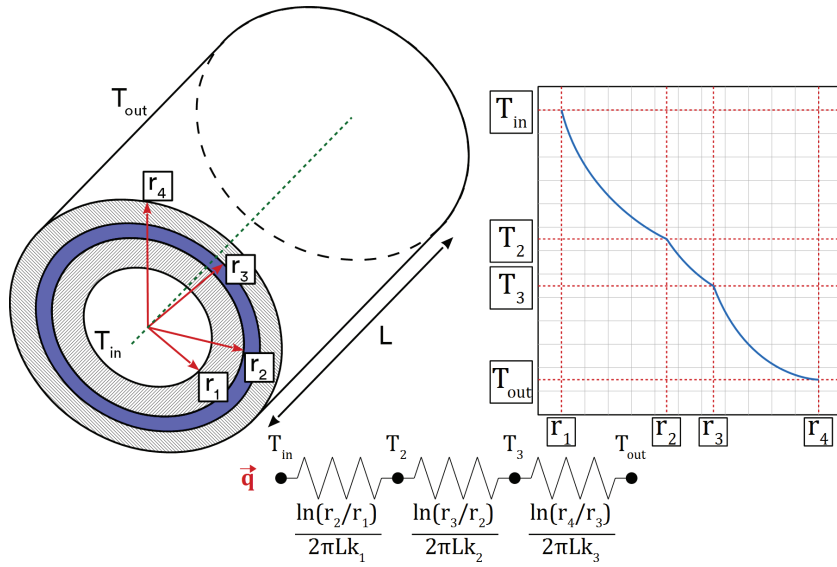


**Figure 4.1** – Sketch of a multilayered composite tube with the resulting network of thermal resistances as well as the general shape of the temperature profile, when it is heated from the inside

In a composite hollow tube heated from the inside, the thermal resistances of the layers are all normal to the radial heat flow, and the system is basically a series circuit, as shown on the bottom part of Figure 4.1. Thus, the thermal resistance of the whole tube is:

$$R_{tot} = \sum_{i=1}^N \frac{\ln\left(\frac{r_{i+1}}{r_i}\right)}{2\pi k l} \quad (4.3)$$

Using this expression, one can extract an expression for the equivalent thermal conductivity of a composite cylinder made of  $N$  layers, given by Equation 4.4.

$$k_{eq} = \frac{\prod_{i=1}^N k_i \ln\left(\frac{r_N}{r_1}\right)}{\sum_{i=1}^N \left[ \prod_{j \neq i}^N k_j \ln\left(\frac{r_{i+1}}{r_i}\right) \right]} \quad (4.4)$$

With these considerations, the calculation of the equivalent conductivity of the various types of prototype cladding tubes is straightforward. A Matlab code has been written to easily compute this.

### 4.3 Modelling of the effective conductivity of SiC/SiC layers

The previous section dealt with the thermal conductivity of composite tubes made of several concentric layers. However, the tube is composite not only at the scale of its constituting layers, but also within some of the layers themselves. Indeed, the layers made of SiC/SiC require further analytical treatment to obtain a thorough model.

As far as the modelling of the effective thermal conductivity of a composite material is concerned, several techniques, three of which can be considered as the main “families”, are available. Finite elements modelling [141, 142] is reliable at capturing the dependence of thermal conductivity on macroscopic defects such as porosity or debonding. FEM has the potential to yield accurate numerical predictions, providing that the right resources and sufficient computing power and time are available.

Alternatively, a computational scheme named after Eshelby, Mori and Tanaka (EMTA approach) [143] can be used to model the effective thermal conductivity of heterogeneous materials. This technique uses schemes developed by Eshelby [144] as well as by Mori and Tanaka [145] to model the stress fields in a matrix containing inclusions. Hiroshi and Minoru [146] showed that this approach can be used to solve the heat conduction in composite materials. This is done by replacing the stiffness tensor  $C_{ijkl}$  by a thermal conductivity tensor  $K_{ij}$ , the stress  $\sigma_{ij}$  by the heat flux  $q_i$ , and the strain  $\varepsilon_{ij}$  by the temperature  $T_i$ . EMTA computations follow a multi-scale approach, whereby a unidirectional composite containing aligned fibres, with or without interphase, is considered in a first step. Secondly, a homogenisation step is carried out in order to obtain the properties of *equivalent fibres*, meaning that interfacial conductance effects are included at this point. Lastly, the actual properties of the composite are obtained through a fibre orientation averaging.

The third modelling approach discussed in this thesis is known as *effective medium* models. This type of models has been selected for the present doctoral work for the following reasons. Firstly, analytical expressions can be obtained through this approach, and contrarily to FEM, it does not require resources (time, software and computing power) that were not available in the frame of this work. Furthermore, the less complex mathematical treatment allows adjustments of the model, such as the inclusion of porosity, radiation damage and debonding, more easily than EMTA schemes.

#### 4.3.1 Effective medium models

The effective medium approach encompasses a broad family of models where the composite is considered as a continuous, stationary medium, with a unique thermal conductivity depending on the individual conductivities of its different phases. Progelhof et al. [147] presented a thorough review of this type of model, within the field of polymer-based composites of solid-solid or solid-gas compositions. The suitability for modelling the effective thermal conductivity of SiC/SiC of some of these has been discussed by Youngblood et al. [148, 149].

According to the literature, two models stand out; both are cylinder-based schemes, based on either two or three concentric cylinders. The Hasselmann-Johnson model [150] is based on a two-cylinders approach, whilst the Markworth [151] model includes a third cylinder to overcome some limitation of the former modelling scheme. In either case, a central cylinder accounts for a fibre to which a larger outwardly placed cylinder of matrix is attributed to the unit cell per the volume fractions of the composite. The Hasselmann-Johnson model includes the effect of fibre/matrix interphases by introducing an interfacial thermal conductance term  $h_c$  that acts as a finite thermal barrier, i.e. introduces a temperature gap at the interface. This model shows weaknesses in the modelling of medium to high fibre-content composites. Indeed, it requires the radius of the matrix volume ( $b$ ) allocated to each fibre to be much larger than their radius ( $a$ ). Another requirement, is that the ratio between the matrix thermal conductivity and the product of the fibre radius with the interfacial conductance must be close to zero:  $k_m/ah_c \sim 0$ . The first of these two conditions is in no case satisfied by the SiC/SiC found in the composite tubes. Furthermore, the second requirement would probably not be met either, since the interfacial gap conduction would be given by the thermal conductivity of PyC, leading to a non-zero ratio.

To overcome the interface limitations of a two-cylinders approach, Markworth [151] proposed a similar modelling idea in which an additional cylinder is introduced between the ones representing the fibre and the matrix. This model suits our needs well, since the conductivity

of the interphase can be adjusted, meaning that radiation-induced amorphisation of the PyC interlayer can be included. Moreover, the three cylinders approach is appropriate for medium to high fibre volume fractions.

### 4.3.2 Three cylinders model

The paper by Markworth [151] considers unidirectional (UD) composites to which a transverse temperature gradient is applied and in which matrix to fibre debonding is seen as a coating with a given thickness and thermal conductivity. This situation is similar to the one of SiC/SiC cladding, where the fibres are coated with pyrolytic carbon and the heat flux goes from the inside to the outside of the fuel pin. Furthermore, the material is a quasi-UD composite in the radial direction, since the fibre tows are woven in the axial and circumferential directions of the tube.

The starting points of the analysis are the following:

- SiC fibres with a diameter  $2a$  are considered homogeneously distributed;
- a PyC layer of thickness  $w$  is deposited on the surface of the fibres;
- a given volume of matrix can be attributed to each fibre as a concentric cylinder with a diameter  $2b$  according to the fibre volume fraction  $V_f$ ;
- the volume fraction of fibres is  $V_f = \left(\frac{a}{b}\right)^2$ ;
- a temperature gradient  $(\nabla T \ 0 \ 0)$  is applied on the composite, i.e. the actual cladding tubes are heated from the inside;

The schematic views presented in Figure 4.2 show the aforementioned geometry in 3D (4.2a) and in 2D (4.2b). The 3D view is evidently not realistically scaled; however, it gives a clear view of the geometry, in which the composite is modelled.

In this situation, the temperature distribution in the composite follows the following Equation [98]:

$$T_i = A_i + \left( \frac{B_i}{\rho} + C_i \rho \right) \cos \theta \quad (4.5)$$

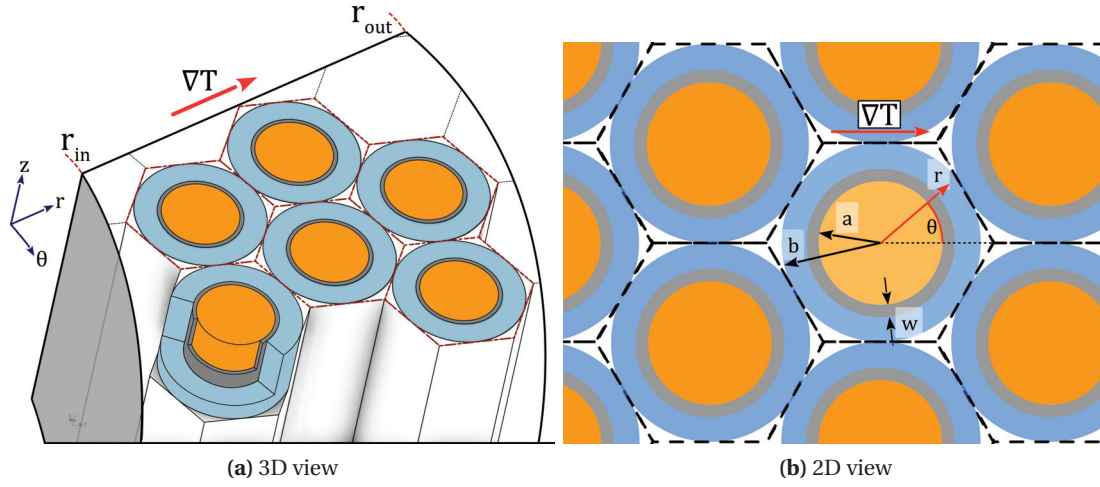


**Figure 4.2** – Schematic view of the SiC/SiC composite structure, with fibres (orange), interphase layer (grey) and matrix (blue)

The different phases of the composite are identified with the subscripts 1 to 4, 1 representing the effective medium, i.e. the composite material as a whole, 2, the amount of matrix attributed to each fibre according to the volume fraction of fibres  $V_f$ , 3, the PyC interphase and 4, the fibres themselves. Since we can choose an arbitrary temperature scale,  $A_1$  can be set to zero. In addition to this, continuity at the interfaces requires that  $A_i = 0$ ,  $i > 1$ . Moreover, the effective medium “1” is continuous from the point of view of a fibre, which means that  $B_1$  equals zero. Also, the temperature at the centre of any fibre is finite, meaning that  $B_4$  is also zero. Last, the temperature in the effective medium is simply proportional to the gradient applied on the composite, i.e.  $C_1 = \nabla T$ .

As a result of these considerations, the following equations can be written to describe the temperature fields in the various phases.

$$T_i = \begin{cases} \nabla T \cdot r \cdot \cos \theta & i = 1 \\ \left( \frac{B_i}{r} + C_i \cdot r \right) \cdot \cos \theta & 1 < i < 4 \\ C_i \cdot r \cdot \cos \theta & i = 4 \end{cases} \quad (4.6)$$

To solve this set of equations, Neumann and Dirichlet boundary conditions are applied at each of the domain interfaces:

- $T_i = T_{i+1}$  at  $r = a, a + w, b$

$$\bullet \quad k_i \left( \frac{dT_i}{dr} \right)_{r=a, a+w, b} = k_{i+1} \left( \frac{dT_{i+1}}{dr} \right)_{r=a, a+w, b}$$

Doing this, an overdetermined system of six equations and five unknowns is obtained:

$$\begin{aligned} r = b : & \begin{cases} \nabla T = \frac{B_2}{b^2} + C_2 \\ k_1 \nabla T = k_2 \left( C_2 - \frac{B_2}{b^2} \right) \end{cases} \\ r = a + w : & \begin{cases} \frac{B_2}{(a+w)^2} + C_2 = \frac{B_3}{(a+w)^2} + C_3 \\ k_2 \left( C_2 - \frac{B_2}{(a+w)^2} \right) = k_3 \left( C_3 - \frac{B_3}{(a+w)^2} \right) \end{cases} \\ r = a : & \begin{cases} \frac{B_3}{a^2} + C_3 = C_4 \\ k_3 \left( C_3 - \frac{B_3}{a^2} \right) = k_4 C_4 \end{cases} \end{aligned}$$

Solving this set of equations yields unique solutions for the first four constants,  $B_2$ ,  $C_2$ ,  $B_3$  and  $C_3$ . However,  $C_4$  must fulfil two different equalities since the system is overdetermined.

$$C_4 = \frac{B_3}{a^2} + C_3 = \frac{k_3}{k_4} \left( C_3 - \frac{B_3}{a^2} \right) \quad (4.7)$$

Using the equality in Equation 4.7 and inserting the solution for  $B_3$  yields an equality from which  $k_1$  can be extracted.

$$\begin{aligned} & \frac{1}{2k_2k_3} \left[ \left( \frac{a+w}{a} \right)^2 (k_1k_2 + k_2^2 - k_1k_3 - k_2k_3) + \left( \frac{b}{a} \right)^2 (k_1k_2 - k_2^2 + k_1k_3 - k_2k_3) \right] \\ + & \frac{1}{2k_3} \left\{ k_2 \left[ \frac{k_1+k_2}{k_2} - \left( \frac{b}{a+w} \right)^2 \frac{k_2-k_1}{k_2} \right] + k_3 \left[ \frac{k_1+k_2}{k_2} \left( \frac{b}{a+w} \right)^2 \frac{k_2-k_1}{k_2} \right] \right\} \\ = & \frac{k_3}{k_4} \left\{ \frac{1}{2k_3} \left\{ k_2 \left[ \frac{k_1+k_2}{k_2} - \left( \frac{b}{a+w} \right)^2 \frac{k_2-k_1}{k_2} \right] + k_3 \left[ \frac{k_1+k_2}{k_2} \left( \frac{b}{a+w} \right)^2 \frac{k_2-k_1}{k_2} \right] \right\} \right. \\ - & \left. \frac{1}{2k_2k_3} \left[ \left( \frac{a+w}{a} \right)^2 (k_1k_2 + k_2^2 - k_1k_3 - k_2k_3) + \left( \frac{b}{a} \right)^2 (k_1k_2 - k_2^2 + k_1k_3 - k_2k_3) \right] \right\} \end{aligned}$$

After some algebra, and with the following definitions:

- $\mu = \left(\frac{a+w}{a}\right)^2$
- $\lambda = \left(\frac{b}{a}\right)^2$
- $R_m = \frac{k_3}{k_2}$
- $R_f = \frac{k_3}{k_4}$

The expression given in Equation 4.8 is obtained for the effective thermal conductivity  $k_1$ , written  $k_{\text{eff}}$  from this point forward.

$$k_{\text{eff}} = k_m \frac{(1 - R_f) \left[ 1 - \frac{1}{\mu V_f} + R_m \left( 1 + \frac{1}{\mu V_f} \right) \right] - (1 + R_f) \left[ \mu (1 - R_m) - \frac{1 + R_m}{V_f} \right]}{(1 + R_f) \left[ \mu (1 - R_m) + \frac{1 + R_m}{V_f} \right] - (1 - R_f) \left[ 1 + \frac{1}{\mu V_f} + R_m \left( 1 - \frac{1}{\mu V_f} \right) \right]} \quad (4.8)$$

#### 4.3.3 Effect of porosity

The theoretical basis of our understanding of the effect of porosity on the thermal conductivity of materials is based on Maxwell's studies on the electrical conductivity of mixed materials [152]. His approach was then later adapted to model the thermal conductivity of porous materials.

The simplest type of model defines the effective thermal conductivity with expressions following Equation 4.9, in which  $k_s$  is the conductivity of the fully dense solid,  $v_p$  is the porosity,  $b$  is an exponent introduced in some models used to better fit experimental data, and  $k_p$  is the thermal conductivity of the pores themselves. A commonly used exponent is  $b = 3$ , a case called the *percolation* model.

$$k = k_s (1 - v_p)^b + v_p^b k_p \quad (4.9)$$

In the simplest approach, known as the parallel relation,  $k_p$  is ignored and  $b = 1$  thence yields a linear relationship between effective thermal conductivity and porosity. As Smith et al. [153] point out, that this approach is often satisfactory at  $v_p < 15\%$ . In the range of intermediate porosities  $15\% < v < 65\%$ , the connectivity of the porosity needs to be accounted for, and more complicated models, such as Landauer's [154] (Equation 4.10), percolation or the Maxwell-Eucken's (Equation 4.11), are better suited to tackle the aforementioned effect. Finally, at very

high porosities, the three previous models are not particularly well suited, since the way in which the solid part of the material is considered would not have a physical meaning anymore. In such cases, the Hashin-Shtrikman model can account for the situation at hand. There, the solid is modelled as hollow shells touching each other. It is however not of relevance here, since the average porosity of SiC/SiC tubes does not reach more than 20 to 45%.

$$k = \frac{1}{4} \left\{ k_p (3v_p - 1) + k_s (2 - 3v_p) + \left\{ [k_p (3v_p - 1) + k_s (2 - 3v_p)]^2 + 8k_s k_p \right\}^{1/2} \right\} \quad (4.10)$$

$$k = k_s \frac{k_p + 2k_s + 2v_p (k_p - k_s)}{k_p + 2k_s - v_p (k_p - k_s)} \quad (4.11)$$

Figure 4.3 shows three plots featuring curves of the four aforementioned models, with three cases,  $k_s/k_p = 1000, 100$  &  $10$ . The percolation model features a stronger porosity effect than any of the other three, except for the Landauer at  $v_p > 65\%$ , which is the upper limit from where it should not be used anymore.

For the samples studied in this work, the Landauer model is the most appropriate, as shown by Smith et al. [153]. Indeed, these authors have shown that from  $v > 15\%$ , porosity begins to be connected, i.e. a network of open porosity appears. Out of the four most common models, that of Landauer is the best at predicting heat transport in ceramics with  $15\% < v_p < 65\%$ : The percolation model diverges too strongly, whilst the parallel and Maxwell-Eucken approaches underestimate the effect of connected open porosity. These findings are supported with measurements carried out on  $\text{Al}_2\text{O}_3$  and  $\text{ZrO}_2$  ceramics with different porosities [153].

The thermal conductivity within the pores of a material has two components, a convective term accounting for heat transport by gas molecules trapped in closed porosity and a second contribution due to thermal radiation. The latter is a topic further detailed in the discussion of the thesis results.



### 4.3. Modelling of the effective conductivity of SiC/SiC layers

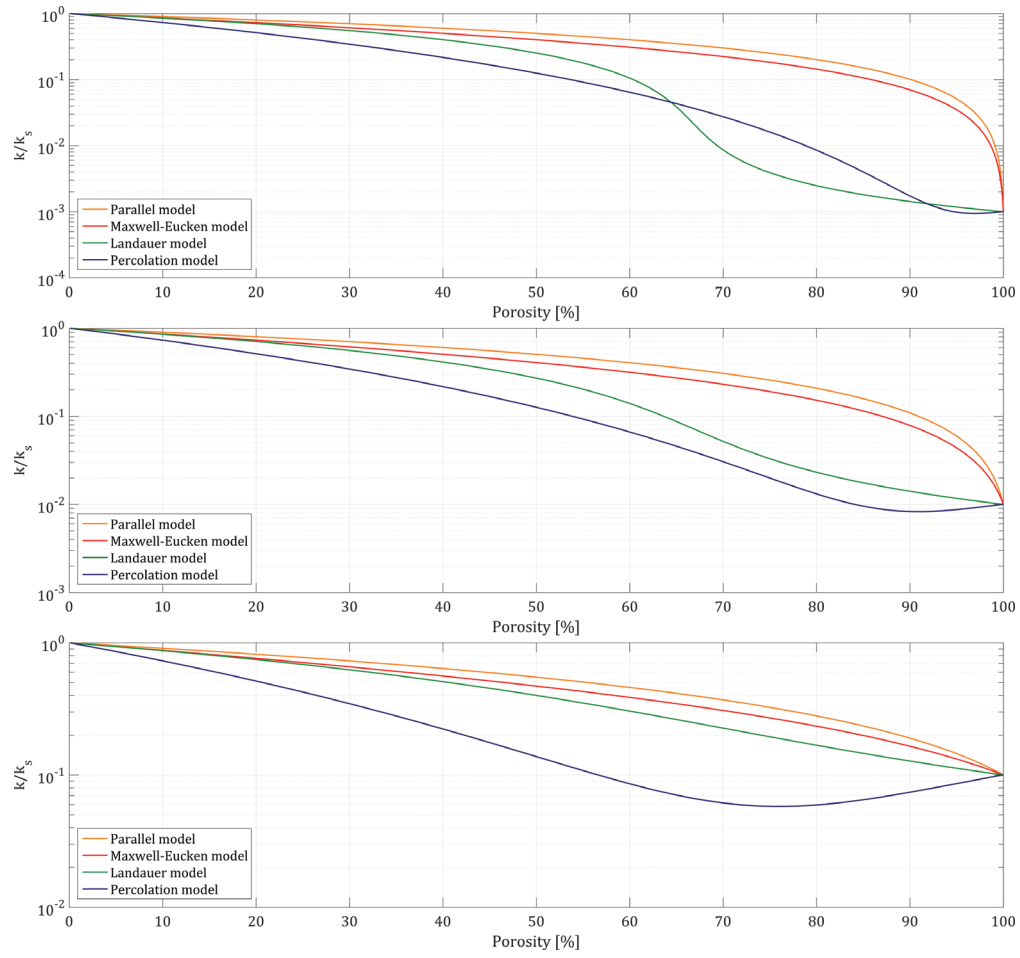


**Figure 4.3** – Effect of porosity on thermal conductivity according to the parallel ( $b = 1$ ), percolation ( $b = 3$ ), Landauer and Maxwell-Eucken models. Ratio of  $k_s/k_p$  ranging from 1000, 100 and down to 10 (top to bottom).



## 5 Results and discussion

This final chapter presents the results linked to the three main parts of the work introduced in the previous chapters. Firstly, electron microscopy results are presented. This starts with the discussion of microstructural features observed during the in-situ irradiations at JANNuS, following with the results of the quantitative analysis of EFTEM and ESI data. The results of thermal conductivity measurements are then analysed and interpreted. Lastly, the modelling approach introduced in chapter 4 is used to link both experimental parts of the work, and the consequences of these findings on fuel assemblies are discussed.

## 5.1 Electron microscopy

### 5.1.1 JANNuS results

Six FIB lamellae were used for the in-situ work at the JANNuS facility. For technical reasons, not all irradiations were performed with the same ions. In addition, due to the low mass and energy of the  $C^+$  ions, there was a doubt whether 140 keV  $C^+$  could reach the sample. Therefore, the sample GA6 was implanted with  $Si^+$  and  $C^+$ , but with the objective lens (OL) switched off, what does not allow imaging during the irradiation. Subsequently, GA7 was irradiated with  $C^+$  only but with the OL switched on, thereby confirming that damage did occur, i.e. that carbon ions reached the lamella. Finally, the last two lamellae were irradiated with both ions species, and the OL switched on.

#### Dose determination

The level of damage achieved in the TEM lamellae irradiated during the in-situ experiment depends on several parameters such as the beam energy, ion species and the thickness of the samples as well as their composition.

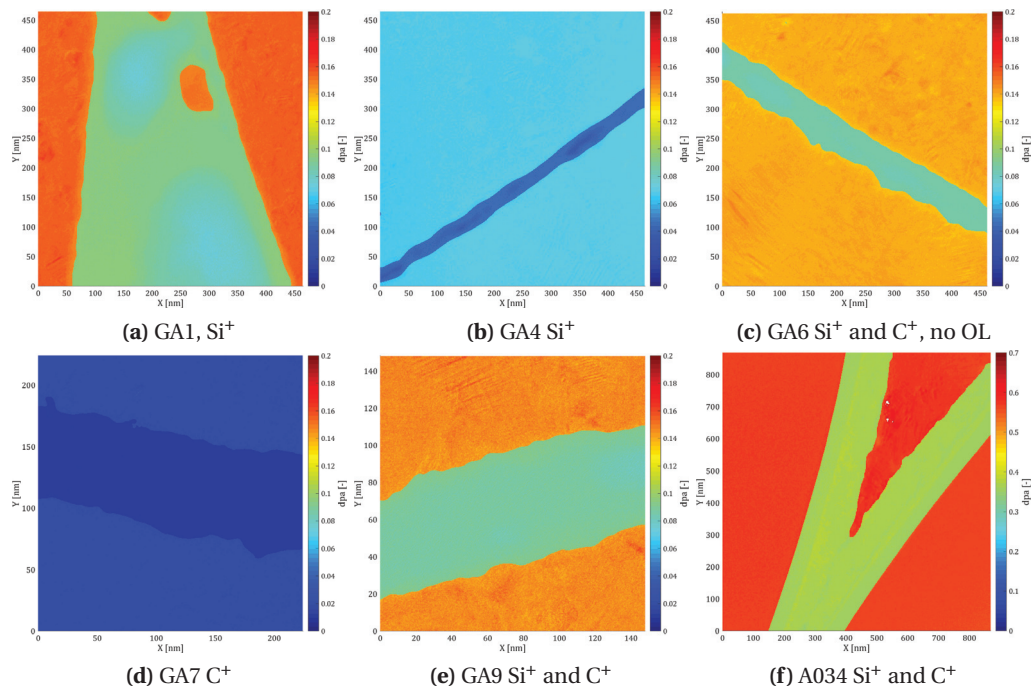


**Figure 5.1** – dpa maps obtained by integrating SRIM damage profiles onto thickness maps. Note that the colour scale of the sixth image (5.1f) is different from the other five.

The procedure behind the damage calculation is based on four SRIM calculations using 2 MeV  $\text{Si}^+$  and 140 keV  $\text{C}^+$  ions in either silicon carbide or pyrolytic carbon, up to a depth of 250 nm<sup>1</sup>. These profiles are then numerically integrated pixel wise and scaled with the actual fluences obtained in Orsay to obtain a dpa map.

### Width increase and SiC amorphisation

A total of six samples were irradiated during the in-situ campaign at JANNuS Orsay<sup>2</sup>. The main results observed on-site were a significant increase of the width of the PyC interphases and a partial, to total, amorphisation of the SiC matrix and fibres.

All the samples featured a widening of the interlayer. Whilst most samples showed moderate width increases, the sample GA1-1 featured an increase of about 200%, starting at ~37 nm and growing up to 116 nm after an irradiation of 0.13 dpa using 1 MeV  $\text{Si}^+$  ions. In all cases, the width increase can be explained by the formation of additional graphitic domains, either between pre-existing ones within the PyC layer, or at the SiC/PyC interface. In the aforementioned case of extreme increase, one can see in Figure 5.2 that this particular sample had a large area where the CVI deposition of the matrix failed, as it seems to have been filled by amorphous carbon at an earlier stage. The large area of amorphous carbon seen between the two fibres might have acted as a reservoir of carbon atoms available to fuel the significant growth of the PyC layer. This would explain how an apparently constrained PyC interphase grew as much as what Koike reported about unconstrained HOPG [79].

### Sample GA1

This sample was irradiated on the first day of the in-situ experiment at JANNuS. It could be irradiated with  $\text{Si}^+$  ions only because the IRMA accelerator providing the  $\text{C}^+$  ions kept discharging. Several features are visible in the image sequence displayed in Figure 5.2. The overall number of small grains showing stacking faults is decreasing as soon as the irradiation begins. This sample being one the first to be irradiated, diffraction patterns were unfortunately not acquired throughout the sequence. Though this decrease is most likely accompanied by an amorphisation of silicon carbide, there is no direct proof for this sample.

---

<sup>1</sup>  $n > 10^6$  ions, i.e.  $\Delta \text{dpa} < 0.1\%$

<sup>2</sup> see Table 2.3 for irradiation details

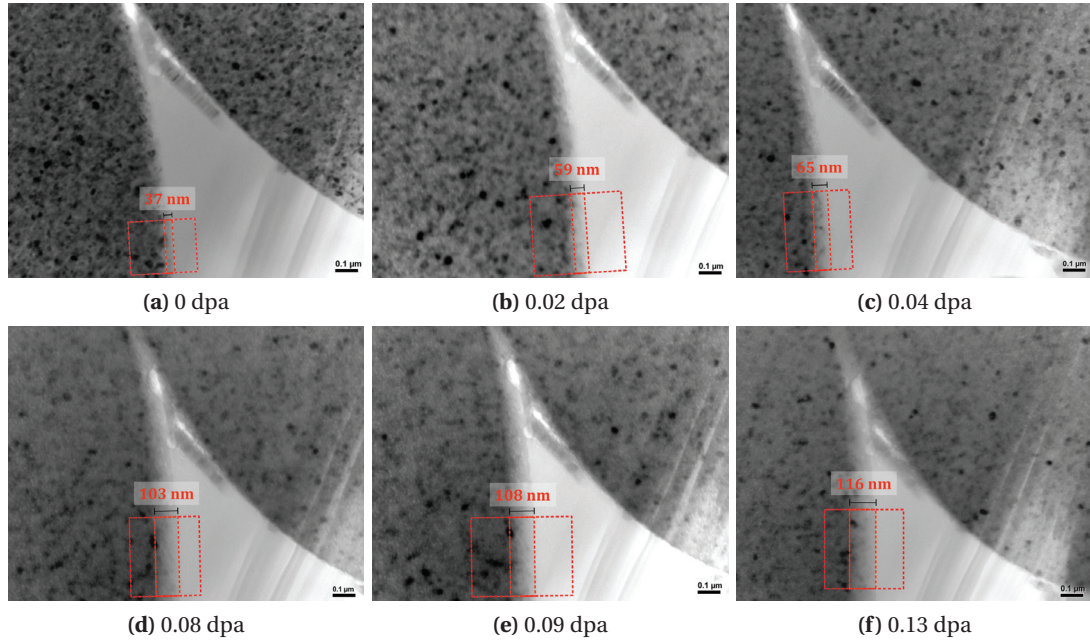


**Figure 5.2** – TEM bright field images recorded before and during irradiation with 1 MeV Si<sup>+</sup> ions of the GA1 sample. Damage levels – 0 to 0.13 dpa – are valid for the PyC interlayer.

In addition, the sequence shows a very significant increase of the width of the PyC interlayer. It grew from about 37 nm up to ~116 nm, which equates to an increase of  $\sim 213 \pm 3.15\%$ , i.e. more than thrice the growth of the other samples. This discrepancy can be explained by the fact that the PyC interphase of this sample is not constrained by a SiC matrix. As a matter of fact, the large light area between both fibres is made of amorphous carbon. This happened during the fabrication of the tube itself, possibly during the densification by CVI at which point this area was not reached by all of the reactants. Because of this large "reservoir" of carbon, the growth of the PyC layer could go unchecked, by both adding new graphitic planes on top of the existing ones as well as by buckling of the planes evidenced by an increase of non-planar sp<sup>2</sup> hybrids.

Using thickness maps acquired on the samples before and after the in-situ experiment at JANNuS, the third dimension of the PyC interphase can be measured. Hence, a volumetric swelling can be calculated. Based on the averages of several maps such as the ones featured in Figure 5.3, a thickness reduction of  $\sim 7.9 \pm 0.76\%$  has been measured on this particular sample. When brought together with the width increase evidenced in Figure 5.2, a volumetric increase of  $\sim 190 \pm 13\%$  is calculated. Since this is calculated as a relative change, the inherent error of 10% on any  $t/\lambda$  measurement can be ignored. Indeed, given the fact that the measurements

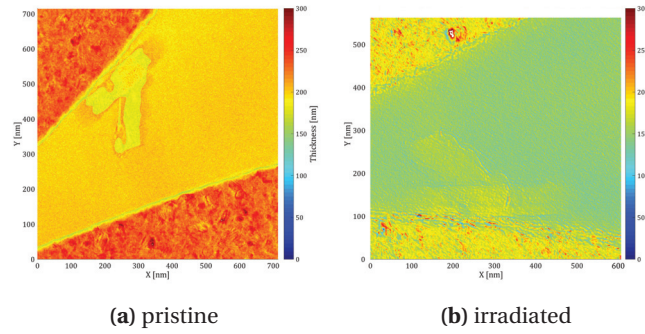


**Figure 5.3** – Thickness maps of the sample GA1 before and after irradiation

are carried out in the same conditions, the  $F$  factor in Equation 2.7, which is the main source of error, cancels out. As discussed before, this sample is a special case, since the carbon layer is not constrained between the fibres and the matrix of the composite. Therefore, this very large growth is more of an oddity than a trend one could expect to see in SiC/SiC. Nevertheless, such largely inhomogeneous areas would better be avoided at the manufacturing stage, since they would be very detrimental to both the thermal and mechanical properties of the composite.

### Sample GA4

This sample experienced a low irradiation dose of  $\text{Si}^+$  ions, more specifically 0.043 dpa. No changes in the width of the PyC are visible in this sequence. This might be an indication that such a modification does not occur at doses below 0.05 dpa. However, other samples, namely GA6, GA7 and GA9, featured increases in their width at these low damage levels. This could be linked to the fact that these three lamellae were irradiated with either silicon and carbon ions (6 & 9) or  $\text{C}^+$  only (7), and not  $\text{Si}^+$  only.

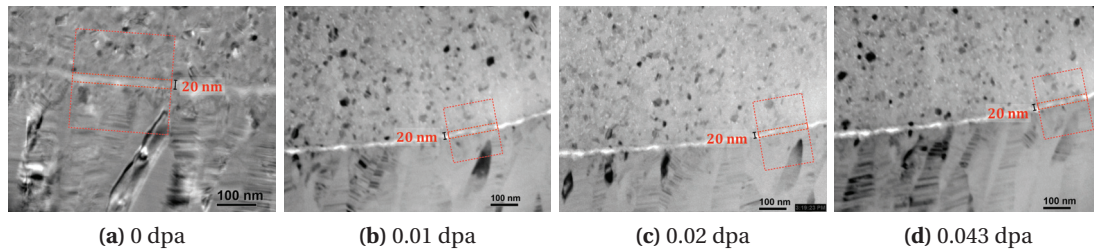


**Figure 5.4** – TEM bright field images recorded before and during an irradiation with 1 MeV  $\text{Si}^+$  of the GA4 sample. Damage levels – 0 to 0.043 dpa – for the PyC interlayer.

Similarly to the width measurements, no significant difference in thickness can be evidenced from the  $t/\lambda$  maps.



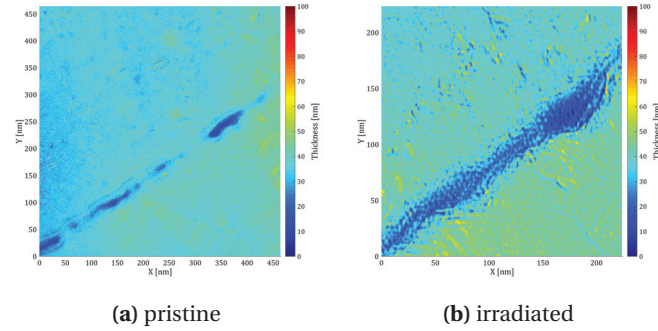


**Figure 5.5** – Thickness maps of the sample GA4 before and after irradiation

Though no dimensional changes are visible in Figure 5.4, subtle diffraction contrast changes are visible in the larger grains of the matrix, as seen in the bottom half of the images. This is an indication that the silicon carbide crystals are very sensitive to the increase of point defect density when their mobility is limited, as is the case in these room temperature in-situ experiments.

### Sample GA6

The next two samples, GA6 and GA9, were both irradiated with Si and C ions for about half an hour, what yielded around 0.09 dpa in the PyC layer. In the first of the aforementioned samples, little changes occurred in the SiC fibre, whereas the matrix does show some changes in contrast as a result of its amorphisation<sup>3</sup>. Similarly to the other samples, the annealing of stacking faults in the large grains of the matrix has an earlier onset than in the finer-grained fibres.

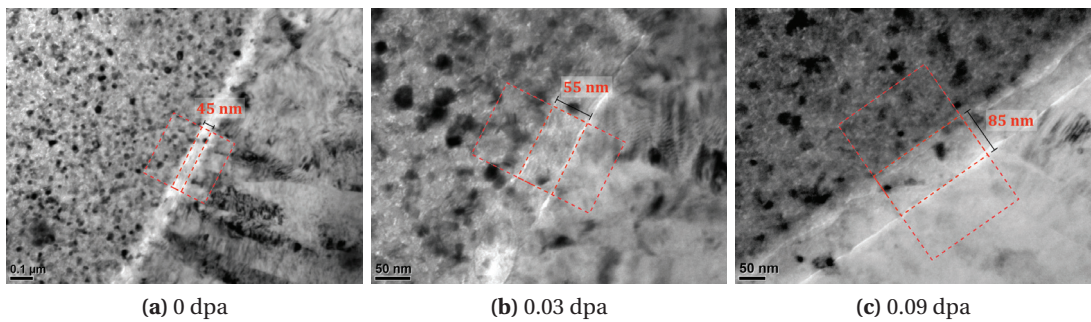


**Figure 5.6** – TEM bright field images recorded before and during an irradiation with 1 MeV Si<sup>+</sup> and C<sup>+</sup> ions of the GA6 sample. Damage levels, – 0 to 0.09 dpa – for the PyC interlayer.

<sup>3</sup>Diffraction patterns acquired on this sample would show changes similar to those visible in the diffraction patterns displayed in the image sequence of Figure 5.8.



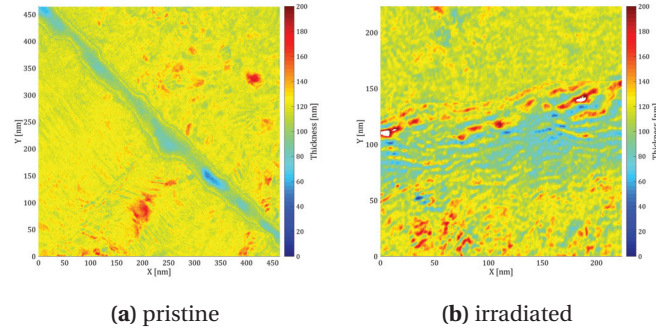


**Figure 5.7** – Thickness maps of the sample GA6 before and after irradiation

Although the overall damage is low, only – 0.1 dpa – the PyC interlayer shows dimensional changes at 0.03 dpa already. The total layer width goes from 45 to 85 nm. This is accompanied by a thickness reduction of  $26.7 \pm 1.05\%$ . This can then be extrapolated to a volumetric increase of  $53.3 \pm 9.1\%$ .

### Sample GA9

As mentioned above, this sample experienced the same irradiation conditions as GA6. In this case, we realised that diffraction patterns should have been recorded between the irradiations. As one can see in the patterns shown in Figures 5.8b and 5.8c, the crystallinity of the matrix is already significantly reduced at a dose of 0.09 dpa.

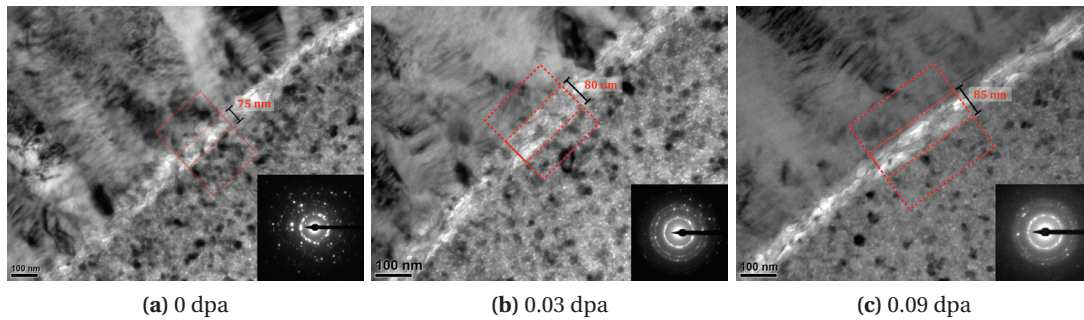


**Figure 5.8** – TEM bright field images recorded before and during irradiation with 1 MeV  $\text{Si}^+$  and 140 keV  $\text{C}^+$  ions of the GA9 sample. Damage levels, – 0 to 0.09 dpa – for the PyC interlayer.

Even if the irradiation dose and the dose rate are almost identical to those applied to GA6, the width of the interphase increases to a lesser degree in this sample. This could be due to a better adhesion between the three phases involved, resulting in the carbon being more constrained

than in the other cases. This would however be difficult – if possible at all – to ascertain and should rather be considered as a reminder that radiation damage mechanisms are seldom homogeneous.

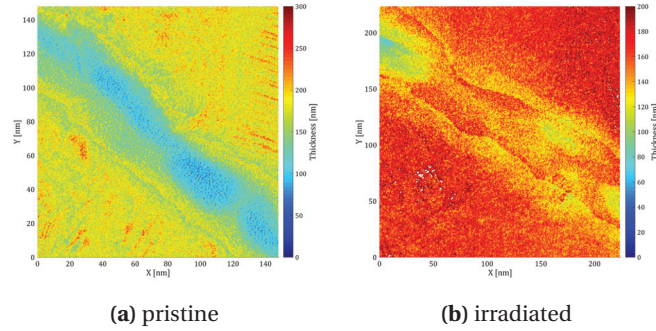


**Figure 5.9** – Thickness maps of the sample GA9 before and after irradiation

In addition to the lesser increase in width of the PyC interlayer, this sample also features an increase in its thickness of  $6.04 \pm 0.25\%$ , seen in Figure 5.9. This is further discussed at the end of the present section.

### Sample GA7

This TEM lamella was irradiated for 102 minutes with  $C^+$  ions only. This specific irradiation was performed this way in order to verify that low energy carbon ions did indeed hit the lamella and were not deflected by the 2 T magnetic field of the objective lens.

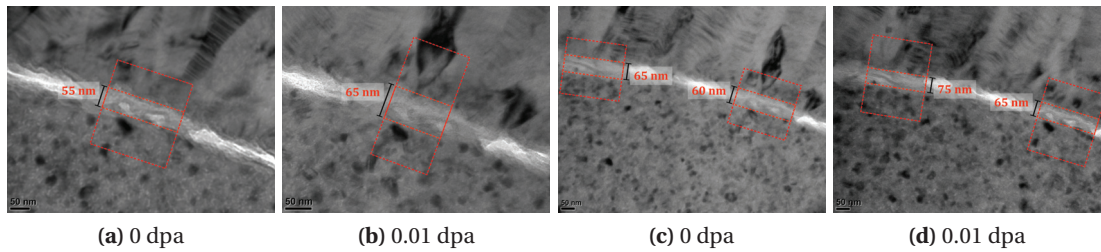


**Figure 5.10** – TEM bright field images recorded before and during an irradiation with 140 keV  $C^+$  ions of the GA7 sample. Damage levels, – 0 to 0.01 dpa – for the PyC interlayer.

The image sequence in Figure 5.10 shows similar features to what is displayed in Figure 5.8, with a slight growth of the pyrocarbon. The total increase is also about 10 nm, though it was achieved with little damage. This is due to the lower energy deposition rate of the  $C^+$  compared to the  $Si^+$  ions.

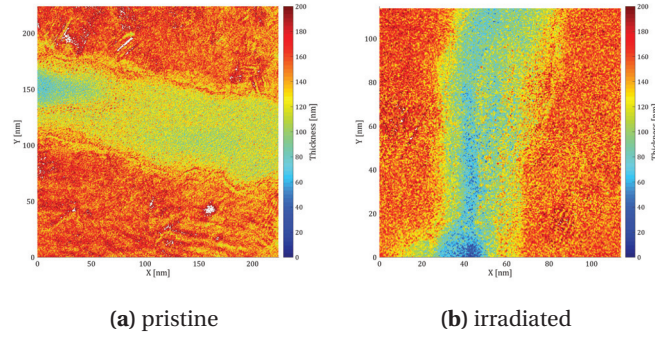


**Figure 5.11** – Thickness maps of the sample GA7 before and after irradiation

Similarly to the GA9 lamella, this sample also features an increase in thickness, though to a larger extent. Based on the  $t/\lambda$  measurements shown in Figure 5.11, a  $\Delta t/t_0 \sim 12.4 \pm 0.8\%$  is measured.

### Sample A034

This sample extracted from the platelet obtained from CNRS-SNECMA was irradiated with both silicon and carbon ions on the last of the three days at JANNuS. It was the last lamella available; therefore, a much longer irradiation was achieved, reaching 0.36 dpa in PyC. As one can see in the image sequence shown in Figure 5.12, the silicon carbide matrix is almost fully amorphised after 0.16 dpa (49 minutes of irradiation). Indeed, the diffraction pattern overlaid in Figure 5.12c features only four faint diffraction spots; these fully disappear at 0.26 dpa, possibly earlier, given the rate at which those disappear in the first two micrographs.

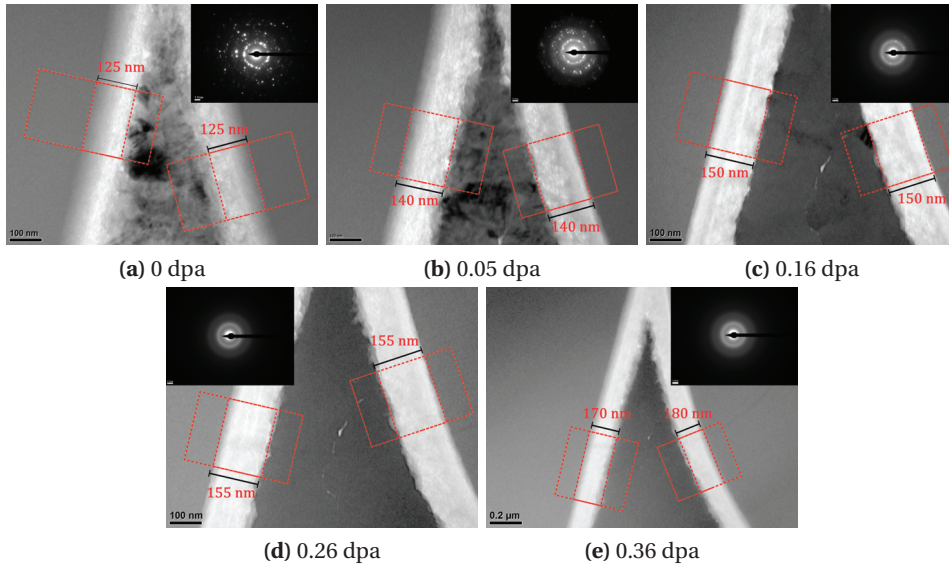


**Figure 5.12** – TEM bright field images recorded before irradiation and during an irradiation with 1 MeV Si<sup>+</sup> and 140 keV C<sup>+</sup> ions. Damage levels, – 0 to 0.36 dpa – for the PyC interlayer.

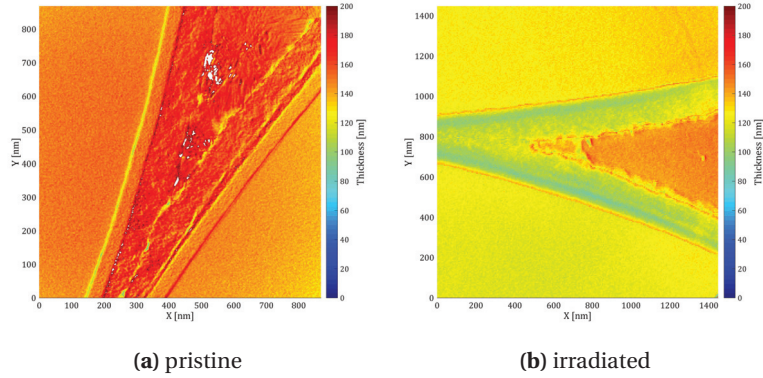
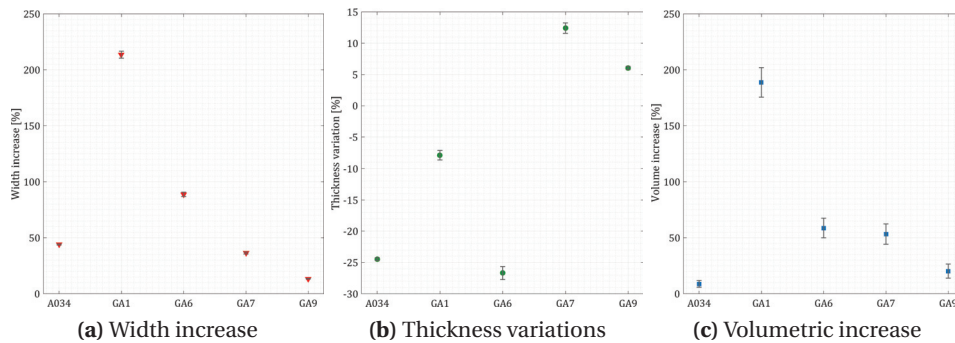


**Figure 5.13** – Thickness maps of the sample A034 before and after irradiation

Lastly, this sample shows large changes in the width of its carbon interphase. Starting at about 125 nm, it grows by  $44.0 \pm 0.5\%$ , reaching  $\sim 180$  nm. Combining this with the maps shown in Figure 5.13, a volume increase of  $\sim 8.8 \pm 3.1\%$  is calculated; the width increases by  $44 \pm 0.5\%$  and the thickness decrease by  $\sim 24.5 \pm 0.2\%$ .

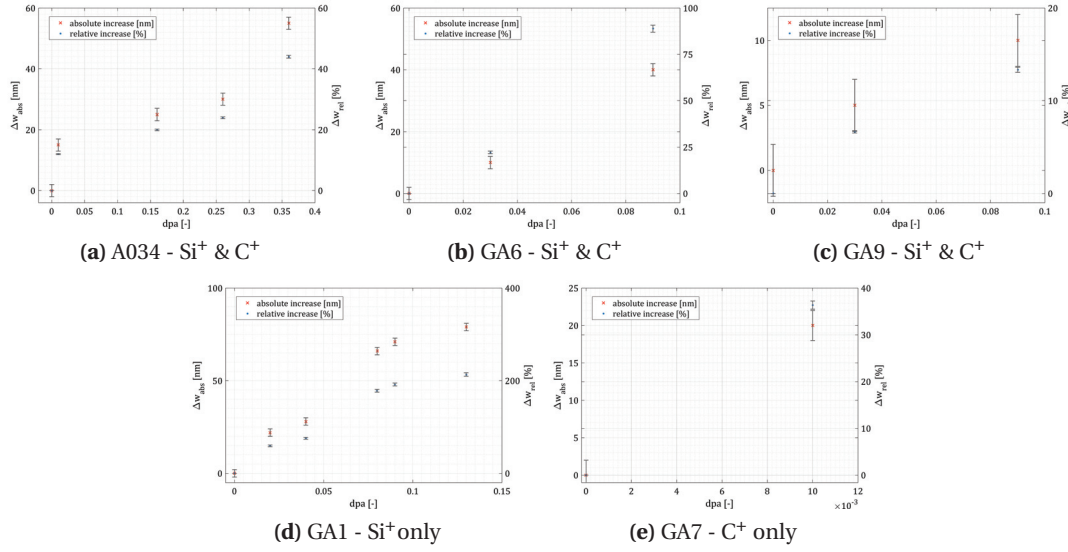
Overall, all the samples, save for the GA4 lamella, show dimensional changes of their PyC interphases. These samples are fully comparable to one another: A034 is made with effectively amorphous Nicalon fibres, and a wide PyC interphase whilst the GA lamellae feature thinner PyC interlayers of about 40 nm and both their matrices and fibres are highly crystalline. Out of the five samples from this batch of SiC/SiC, GA1 is an oddity since it does not contain any matrix.

Figure 5.14 shows the variations of the width and thickness of the PyC interphases, as well as the resulting volumetric swelling. The large spread of the error bars seen in Figures 5.14c is due to the large uncertainties coming with log-ratio thickness measurements.



**Figure 5.14** – Changes of the width, thickness and volume of the PyC interphases irradiated at JANNuS





**Figure 5.15** – Detailed width increases measured on the JANNuS samples

Interestingly enough, although their respective thickness and width changes differ, the lamellae 6, 7 and 9 all show a similar volumetric change. Indeed, the sample GA6 features a thinning of  $\sim 26.7 \pm 3.7\%$  of its interphase, whereas the samples 7 and 9 featured a slight increase in their thicknesses. On the other hand, the width increase of sample 6 is more pronounced than that of the other two.

The proposed reason for the dimensional changes observed is a combination of the buckling of the graphitic planes with the growth of additional planes, as well as the nucleation of amorphous pockets. These phenomena increase the average spacing along the c-axis, with the build-up of strain in the layer. The reduction of thickness seen in the A034, GA1 and GA6 lamellae can then be explained by a contraction in the basal planes direction caused by Poisson's stresses. In the other two cases, where the thickness increases, the planes might warp, and thus overlap, thereby making the interphase thicker. In addition, this also gives an explanation to the lesser width increase seen in the GA7 and GA9 samples. Lastly, sputtering is not likely to be responsible for these dimensional changes. The beams hit the sample at a  $22.5^\circ$ , and based on the SRIM calculations, no significant amounts have been sputtered during the in-situ experiments. The plots shown in Figure 5.15 shows the absolute and relative width increases of five samples featured in Figure 5.14. These increases are plotted as a function of the dpa and grouped according to the type of irradiation experienced by the samples. This sorting of the data does not highlight an actual trend. Indeed, although the lamellae A034, GA6 and GA9 saw the same type of irradiation, the difference being in the duration, neither the absolute, nor the relative width increases seem to correlate.

### 5.1.2 EFTEM and STEM-EELS

The quantitative analysis of the EFTEM and ESI stacks has brought to light the following results. First of all, irradiations, be it with ions or neutrons, result in a reduction of the  $sp^2$  to  $sp^3$  ratio. As one can see in Figures 5.16b, 5.16c, 5.21b and 5.23b, the distribution of the R-ratio is much wider after irradiation than before. This trend is clear in both sample types investigated in this work. Pristine PyC interphases have rather narrow distributions of  $\pi^*$  to  $\sigma^*$  ratios, with medians lying near 95 to 97% of graphitic character. Ion irradiations result in large distributions, visible in the heterogeneity of the R-ratio maps shown in Figures 5.18 and 5.22. Comparatively to neutron irradiated PyC, the effect of  $C^+$  and  $Si^+$  irradiations is much more pronounced. Indeed, the lamellae used for the in-situ experiments at JANNuS only experienced damage in the range of 0.03 to 0.46 dpa at room temperature, whilst neutron irradiated samples reached 0.66 to 1.92 dpa at much higher temperatures. The differences are due to the irradiation conditions; high dose rate and low temperature in the first case, and low dose rate at high temperature in the second case. Further investigations would be required, to allow a better understanding of the mechanisms involved in the amorphisation of PyC.

The  $sp^2$  to  $sp^3$  ratios shown here are on a zero to one scale, meaning that the ratios are capped at the value corresponding to pure graphite, whilst the lower limit is equivalent to the electronic structure of diamond, i.e. pure  $sp^3$ . Measurements have also been carried out on Lacey carbon grids, with the idea of using these as a reference for the lower limit of the R-ratio. This approach has not been successful, since some ion irradiated samples are showing ratios below that of the amorphous carbon reference. The reason for this surprising outcome is probably found in the very large type of amorphous carbons. Ferrari et al. [155] and Lascovich et al. [156] have reported measurements of the  $sp^2$  to  $sp^3$  ratios of various amorphous carbons using grazing-angle X-ray reflectivity, EELS, X-ray photoelectron spectroscopy (XPS) and X-ray excited Auger electron spectroscopy (XAES). In these papers, R-ratios ranging between 0.2 and 0.9 have been reported. Therefore, it is not guaranteed that Lacey carbon films can be considered as a good reference for amorphous carbon. Hence, the ratio measurements have been normalised on the upper end only, and their lowest value would be that of purely  $sp^3$  hybridised carbon, i.e. diamond. All of the quantified maps, as well as the corresponding EFTEM or HAADF images are in the Appendix B. Nevertheless, if Lacey carbon was to be taken as an amorphous carbon reference, the median of the boxplots featured in Figures 5.18, 5.16c, 5.21b and 5.23b would express an amorphisation of 60 to 70%.

## A034

The series of boxplots presented in Figure 5.16 show the most complete set of data at hand. The pristine lamellae are close to pure graphite, with a median ratio of about 95% of that of HOPG, and the percentiles  $q_{25}$  and  $q_{75}$  spreading over a range of 92.5 to 97.5%, i.e. narrowly and homogeneously distributed ratios, as shown in Figure 5.17.

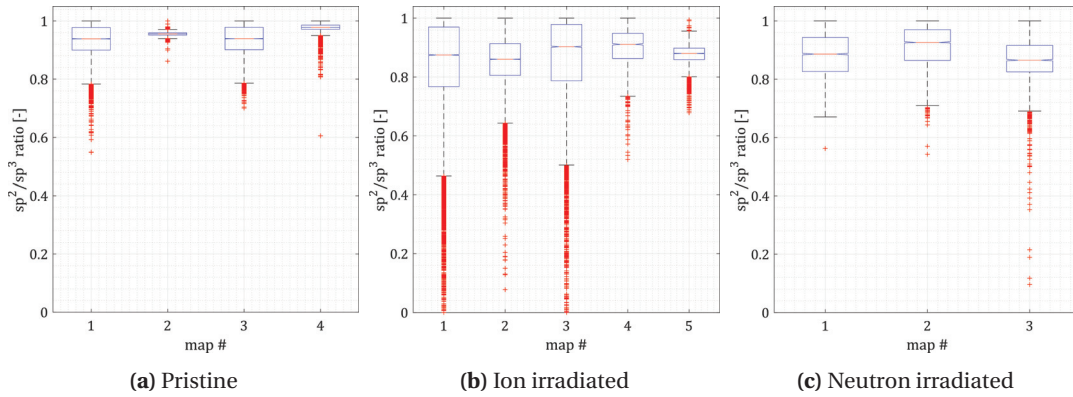


**Figure 5.16** –  $sp^2/sp^3$  distributions measured on pristine, ion- and neutron irradiated A034 samples. The boxplots feature the median of the distributions (red line), and the blue boxes include half of the observations, i.e. they spread over  $q_{75}$ - $q_{25}$ . The bars above and below the boxes are the 5<sup>th</sup> and 95<sup>th</sup> percentiles, whilst outliers are represented as red "plus" signs.

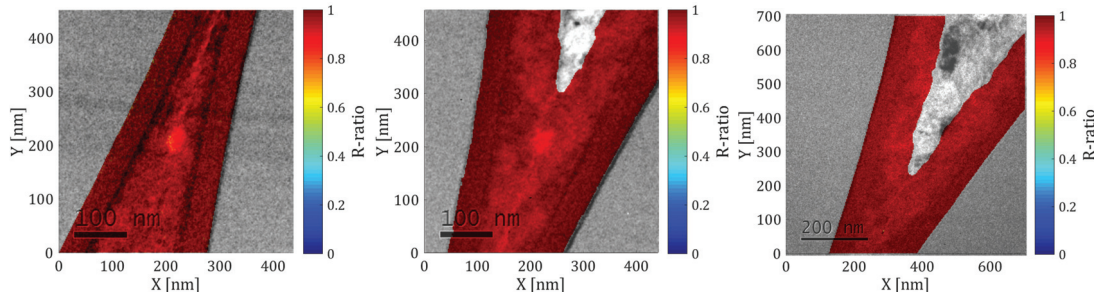


**Figure 5.17** – R-ratio maps calculated with the TWM method overlaid on EFTEM images acquired on pristine A034

After the in-situ ion irradiation, the medians are dropping to about 90% of the HOPG reference. Whilst these values are not too far from the pristine ones, the breadth of the distributions is much more considerable. Indeed, half of the distributions are found in an interval ranging from the same maxima as before irradiation, down to a R-ratio only 80% of the HOPG reference. As one can see in Figure 5.16b, ion irradiated PyC samples feature many outliers, whose  $sp^2/sp^3$

ratios are nearing zero, i.e. regions where  $\pi$ -bonds have been practically fully destroyed by the irradiation. These samples also feature a rather high inhomogeneity in their ratios, as can be seen in Figure 5.18.

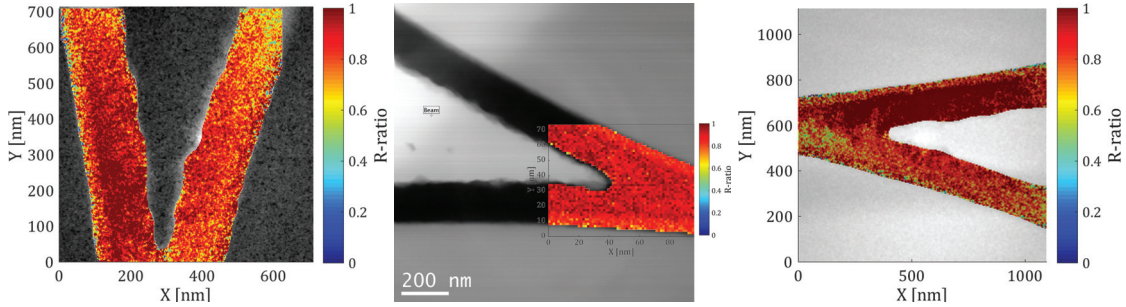


**Figure 5.18** – R-ratio maps calculated with the TWM method overlaid on EFTEM and HAADF images acquired on ion irradiated A034

Lastly, neutron irradiated PyC also shows a reduction of its graphitic character. As a matter of fact, the ratio distributions shown in Figure 5.16c have a larger spread, ranging between 0.82 and 0.95, with medians in the range of  $\sim 0.92$ . The width of these distributions is less than what is observed in ion irradiated PyC, as well as less heterogeneous. Compared to neutron irradiated H1-4, these interphases are less amorphised. This is probably due to the much higher irradiation temperature experienced by these sample: about 800°C, versus temperatures close to the ambient at MITR<sup>4</sup>.

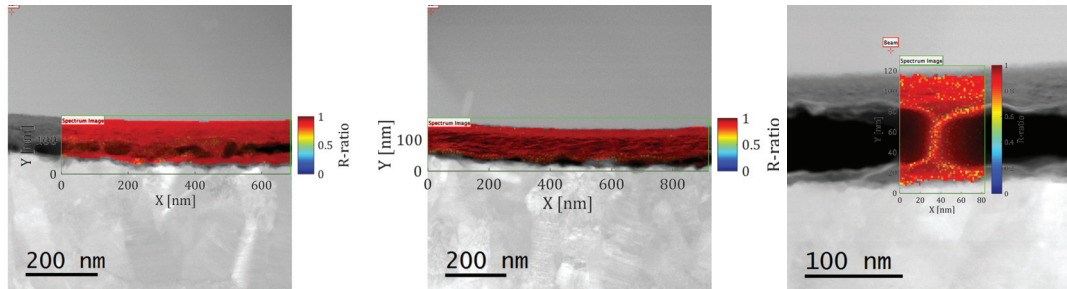


**Figure 5.19** – R-ratio maps calculated with the TWM method overlaid on HAADF images acquired on neutron irradiated A034

<sup>4</sup>MITR is the research reactor at MIT.



### GA samples

Similarly to the PyC interlayer found in A034, the interphases observed in lamellae extracted from the GA prototypes feature narrow distributions close to that of pure graphite in its pristine state. Figure 5.20 shows a series of R-ratio maps overlaid on EFTEM images acquired before irradiation.

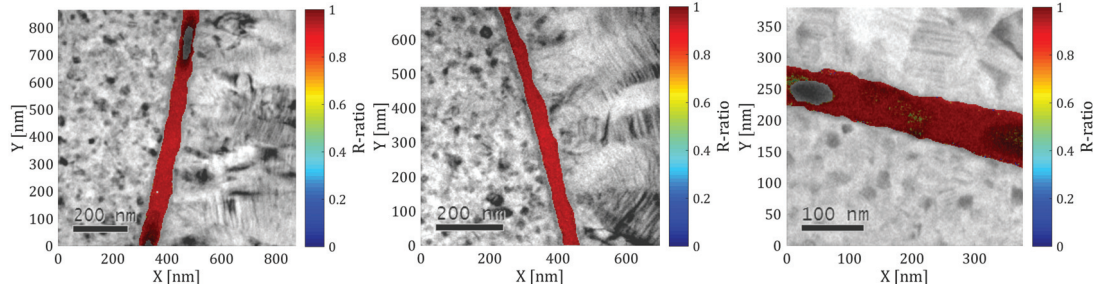


**Figure 5.20** – R-ratio maps calculated with the TWM method overlaid on EFTEM images acquired on pristine GA SiC/SiC

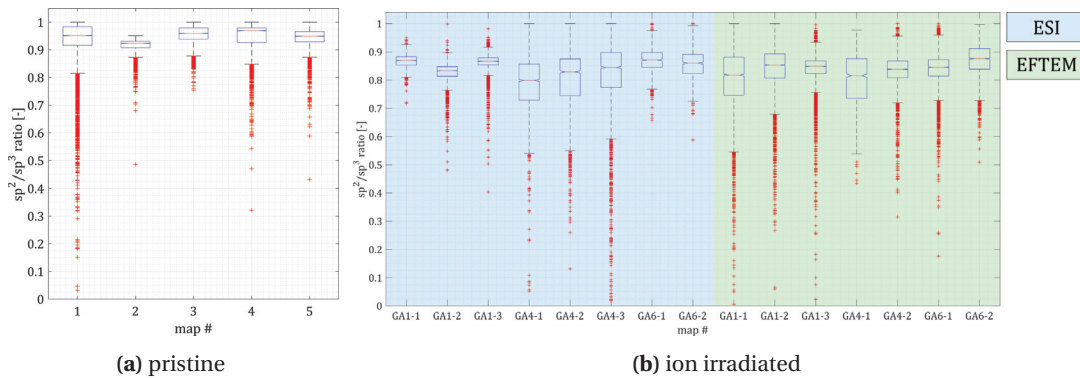


**Figure 5.21** – R-ratio maps calculated with the TWM method overlaid on EFTEM images acquired on pristine A034

The distribution of the ratios shown in Figure 5.20 are presented in Figure 5.21a. These are rather narrow and homogeneous, with a nonetheless fair number of outliers.

The situation becomes significantly different after ion irradiation. The distributions shown in Figure 5.21b show that the measured locations feature a PyC less graphitic than before. Similarly to the case of ion irradiated A034, the distributions are rather large, showing that interphases damaged by ions are more heterogeneous than neutron irradiated samples. In all these cases, the ratios are consistently lower than before irradiation, meaning that one could expect to see a low heat transfer rate across these pyrocarbon layers.

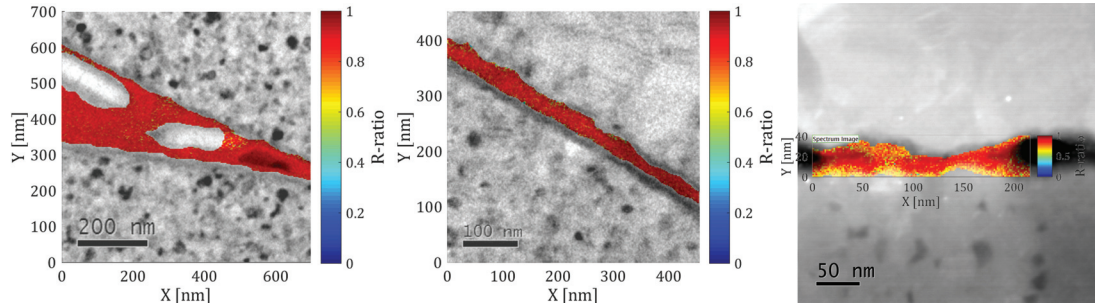


**Figure 5.22** – R-ratio maps calculated with the TWM method overlaid on EFTEM and HAADF images acquired on ion irradiated GA SiC/SiC

#### H1-4

The neutron irradiated H1-4 samples presented in Figure 5.23 show results similar to those of the A034 neutron irradiated samples. This is true in the sense that the distributions are quite symmetric and narrow. The degree of amorphisation is however larger in these interphases. The medians of the normalised ratios are around 0.85, with a spread, i.e. a FWHM, of 0.02. There are a few outliers showing values closer to pure graphite. These are however of little statistical relevance, since they are outside of the  $q_{95}$ - $q_5$  interval.

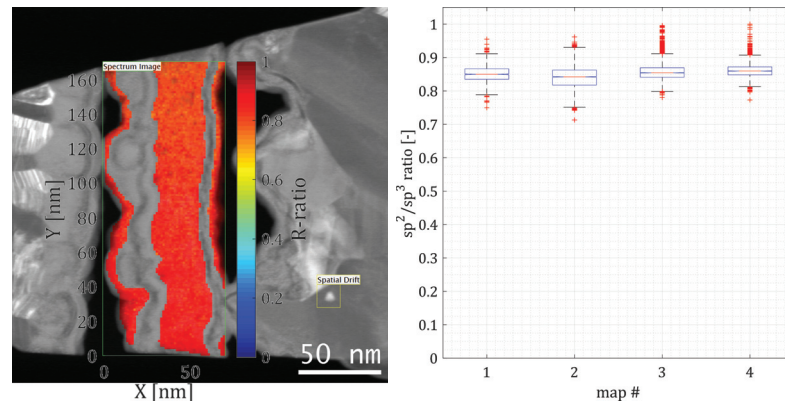


**Figure 5.23** – Map and boxplot of the R-ratio calculated with the TWM method overlaid on an HAADF image acquired on neutron irradiated H1-4 SiC/SiC

Compared to neutron irradiated A034, these samples show a more pronounced shift towards amorphisation. This is explained by the much lesser mobility of point defects at the irradiation temperature of H1-4 – about 50 to 100°C. Indeed, although it has seen a third of the damage – 0.66 and 1.92 dpa, respectively – point defects are much less mobile at these low temperature, whereas A034 was irradiated at 798°C.

## 5.2 Thermal conductivity

### 5.2.1 Steel tube measurement

The theoretical model of the experiment as well as the overall experimental procedure needed validating. To this end, a large stainless steel (316L) tube has been prepared by the PSI workshop in a similar way to the one used to prepare SiC/SiC tubes, with the only difference being that instead of being glued, the thermocouples were welded on the sample surface. Three type K thermocouples were placed at the mid-height of the sample on both the inner and outer surfaces of the tube, whilst a third thermocouple was attached to the extremity of the tube length on its outer surface. This tube had to be rather large because of the difficulty of welding a thermocouple on its inner surface.

**Table 5.1** – Dimensions of the 316L tube used to validate the heat transfer model

Steel grade	Length [mm]	Inner diameter [mm]	Outer diameter [mm]
316L	200	38.4	42.4

This reference sample has then been measured at temperatures ranging from 25 to 250°C. At a first glance, it immediately appears that the thermal conductivity of this large hollow cylinder is much higher than that of the SiC/SiC tubes measured in this work. The reason for choosing a reference made of stainless steel was that 316L is a widely available, well documented material and could easily be obtained at PSI. Furthermore, it is easily machined, and thermocouples can be welded without much difficulty. Thermal conductivity values for SiC/SiC composites found in the literature are close to that of 316L [45, 10], making it a good calibration sample. The fact that the thermal conductivity of SiC/SiC tubes with complex multilayered architectures are so low is an unexpected result of this work.

As previously mentioned, the thermal conductivity of 316L and its dependence on temperature are well-known and can be fitted with Equation 5.1, with T in Kelvin [157].

$$6.321 + 0.09147 \cdot T^{0.7631} \quad (5.1)$$

Figure 5.24 shows the measured thermal conductivity of 316L against sample temperature (crosses with error bars) as well as the reference data from Ho et al. [157]. The experimental curve displayed above shows that the radial heat flow method is not appropriate to measure the

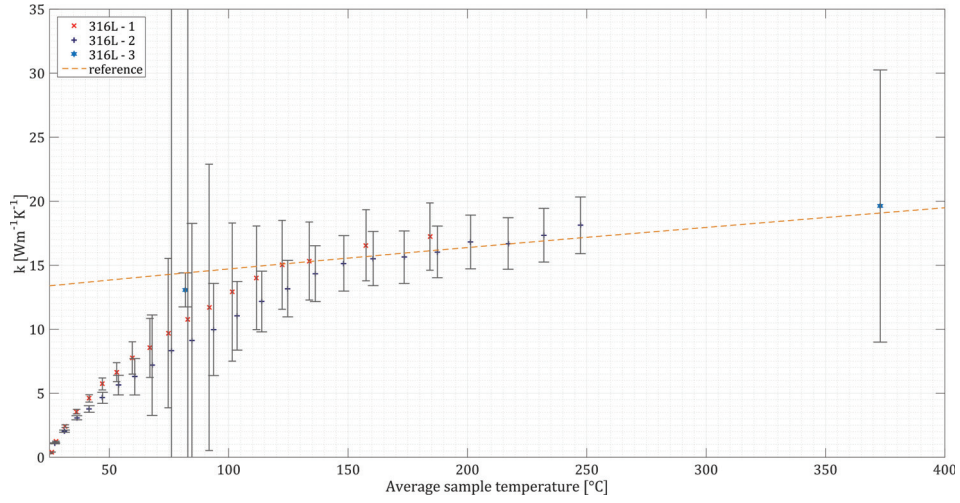


**Figure 5.24** – Thermal conductivity 316L stainless steel against temperature. Dashed line after Ho et al. [157], experimental data from three measurement using the radial heat flow method.

thermal conductivity of conductive materials at temperatures below 150°C. Indeed, the radiant energy of the vacuum chamber itself exceeds that of the heating element at low temperature. As the sample approaches 100°C, the energy coming from the heating element and from the sample become large enough to compensate that of the chamber being at room temperature. In addition to this, if the material has a conductivity similar to that of 316L, the temperature gradients become so small that the uncertainties are too large.

### 5.2.2 SiC/SiC tubes

All the experimental curves featured in the following plots have been recorded for around a week and correspond to a sample. This long procedure is necessary to reach thermal equilibrium during the experiments. The error bars featured on the plots account for uncertainties on the geometrical parameters influencing the thermal conductivity measurement. Among others, this includes geometrical uncertainties, such as the position of the sample within the vacuum chamber, the heating, as well as the sample and vacuum chamber dimensions. Additionally, systematic errors come from the thermocouples themselves, further increasing the magnitude of the errors. Lastly, the emissivities of the sample, heating rod and vacuum chamber cannot be taken as certain. Mathematically speaking, the error  $\Delta k/k$  is obtained by

applying the variance equation on the whole mathematical treatment presented in chapter 3. For this, Equation 5.2 is applied on each of the view factors and propagated on the Gebhart matrix, heat flows and, finally, on the conductivity itself.

$$\frac{\Delta k}{k} = \sqrt{\sum_i^n \left( \frac{\Delta x_i}{x_i} \right)^2 \left( \frac{\partial k(x_1, \dots, x_n)}{\partial x_i} \right)^2} \quad (5.2)$$

The variables  $x_i = r_i, l_i, \varepsilon_i, T_i$  are considered independent on each other, i.e. it is assumed that they are not correlated. This simplification is necessary for the propagation to be feasible. Indeed, using first order derivatives only yields a function of more than 2000 pages. The exact uncertainties considered for the various parameters are depended on the measured quantities. Sample and heating rod dimensions  $r_{in}$ ,  $r_{out}$ ,  $r_{rod}$  and  $h$  where measured with a digital calliper, i.e. with a  $\pm 10 \mu\text{m}$  accuracy. The position of the sample within the vacuum chamber where measured with a manual calliper, meaning that a  $\pm 50 \mu\text{m}$  uncertainty is considered. The temperatures, save for that of the heating rod, are measured with type K thermocouples. Those have an uncertainty of  $\pm \max(2.2^\circ\text{C}, 0.75\%T)$ , whilst the type R thermocouples used on the heating rod are more accurate, with a  $\pm \max(1.5^\circ\text{C}, 0.25\%T)$  uncertainty. Lastly, the emissivities of the surfaces are a large source of error, and have been considered with a  $\pm 0.1$  uncertainty. As one might notice, the error between individual samples can vary in a significant manner. This is particularly true in the case of the more conductive samples seen in Figures 5.28 and 5.29. The reason why this occurs is that the more conductive a sample is, the smaller the gradient is, resulting in larger error bars in these cases. In addition to this, the heat fluxes are proportional to  $T^4$ , which increases the error as the measurement temperature increases.

### CEA samples

Although the various types of samples obtained from CEA have been introduced in section 1.5, these are explained again in the present section. *SiC/SiC* tubes are clads with no Ta liner, whereas *sandwich* and *pre-damaged* tubes do contain a Ta liner.

Overall, these samples feature a very poor conductivity, showing the behaviour expected from insulating materials, with conductivities ranging between  $0.1$  and  $1 \text{ W}\cdot\text{m}^{-1}\cdot\text{K}^{-1}$ , rather than that of nuclear cladding. The most conductive of the CEA samples are those in which no liner is found. Even in these samples, macrostructural defaults, such as pores of several hundreds



of micrometres and not well-connected domains of varying fibre volume fractions, result in a poor heat transfer. The conductivity of sandwich tubes is further degraded by the very poor adhesion of the inner SiC layers to the Ta liner. This single feature results in a practically complete loss of heat transfer across the tube. Lastly, because of cracking at their outer Ta/SiC interfaces, pre-damaged tubes, i.e. cladding sections strained to 0.1, 0.3 and 0.5%, show an even lower thermal conductivity.

Considering that these samples are rather similar to most of the composites studied in the literature, the conductivities measured here are surprisingly low. Indeed, Katoh et. al [45] collected a large amount of data on composites made with CVI densified HNLS fibres, with values ranging between 8 and 15  $\text{W}\cdot\text{m}^{-1}\cdot\text{K}^{-1}$ . The thermal conductivity curves presented in Figures 5.25, 5.26 and 5.27 are the results of repeated measurements on the samples presented in Table 1.4 (page 56). As one can see, the data is rather scattered, particularly in the case of the pre-damaged samples. In this instance, a tube strained to 0.2% shows a higher conductivity than the other measured tubes. This scatter of the data is a result of the high inhomogeneity of the composites. In the aforementioned figures, SEM micrographs show cross-sectional views of the respective sample types. These tubes are nowhere near being homogeneous, featuring extensive pores of several hundreds of micrometres. Because of these large macrostructural defects, the thermal conductivity of the multilayered tubes is not homogeneous either. Thus, the different samples and location of the thermocouples lead to different results.

### SiC/SiC tubes

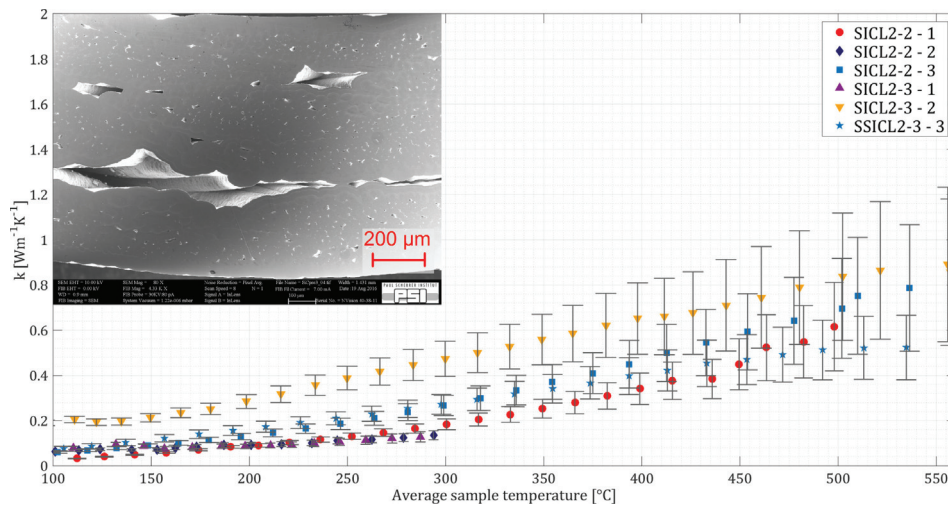


**Figure 5.25** – Measured thermal conductivity of CEA SiC/SiC tubes. The SEM image on the left-hand side of the image shows a representative view of the cross-section of these samples.

### Sandwich tubes

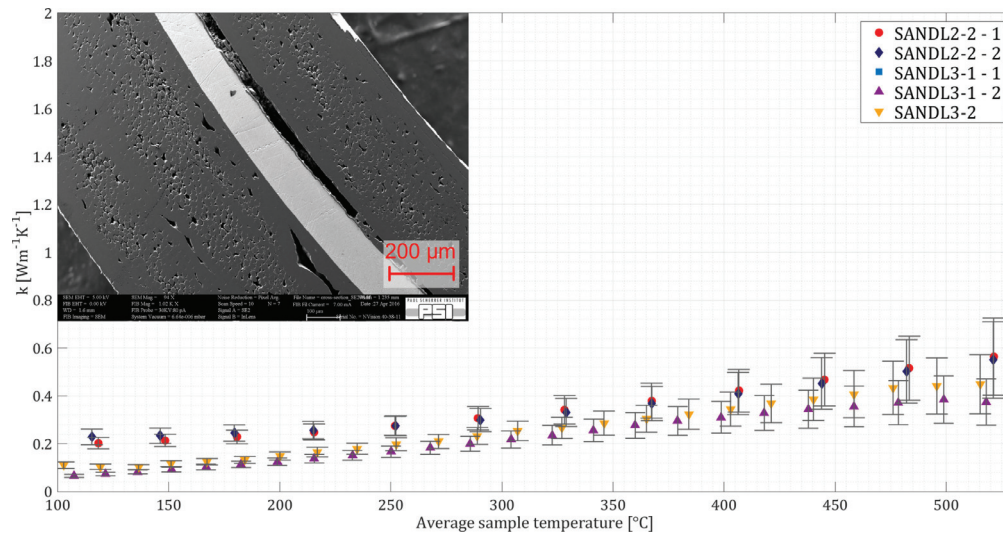


**Figure 5.26** – Measured thermal conductivity of CEA sandwich tubes. The SEM image on the left-hand side of the image shows a representative view of the cross-section of these samples.

### Pre-damaged tubes

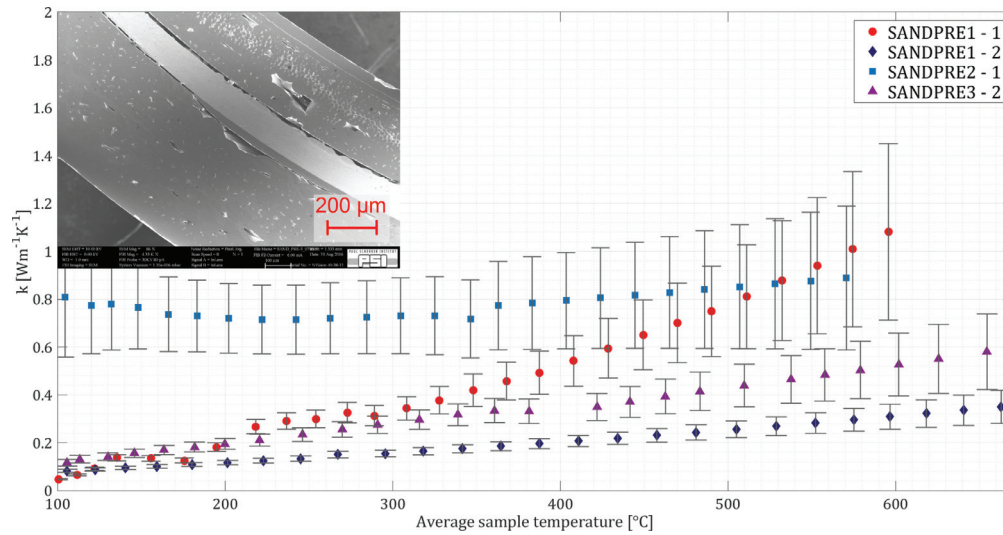


**Figure 5.27** – Measured thermal conductivity of CEA pre-damaged sandwich tubes. The SEM image on the left-hand side of the image shows a representative view of the cross-section of these samples.

### GA sample

The GA samples feature better conductivities than the CEA claddings. These tubes feature less complicated structures, consisting in a thick SiC monolith, on top of which layers of SiC/SiC composite are put. Lastly, thin monolithic SiC is also present as the outermost layer. The absence of a metallic liner significantly helps the heat transfer. Furthermore, even though the SiC/SiC layers also contain large pores, these are not as extensive as in the CEA samples. This results in conductivities scaling between 0.5 and  $\sim 4 \text{ W}\cdot\text{m}^{-1}\cdot\text{K}^{-1}$ . Similarly to the CEA samples, the measurements presented in Figure 5.28 also show a significant scatter. The thermal conductivity of the GA1 tube ranges from 1.2 to  $\sim 4 \text{ W}\cdot\text{m}^{-1}\cdot\text{K}^{-1}$ . Again, this is due to the inhomogeneity of the SiC/SiC composites, which results in a large scatter in the data, depending on the measurement location on the sample.

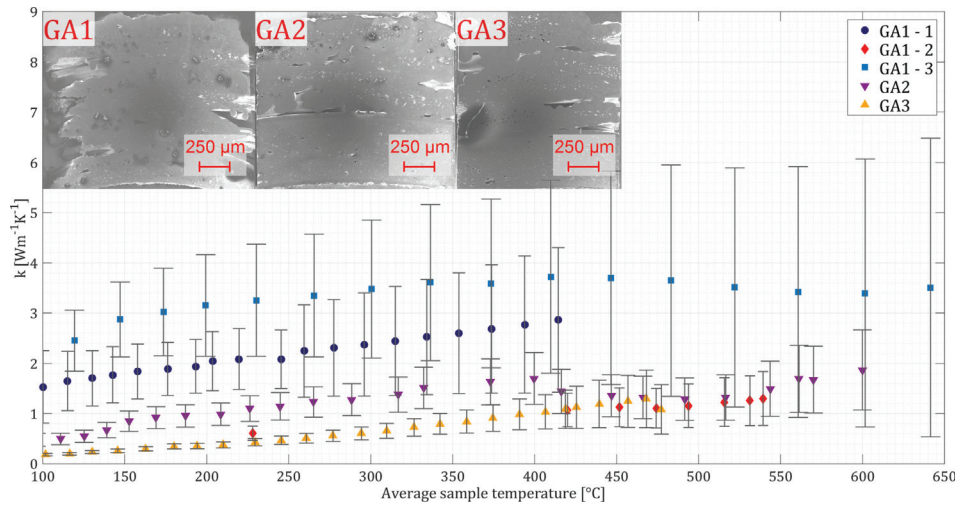


**Figure 5.28** – Measured thermal conductivity of pristine GA/Westinghouse SiC/SiC tubes. The SEM images on the left-hand side of the image shows a representative view of the cross-section of these samples.

The results of the measurements carried out on the neutron irradiated cladding sections obtained from GA/Westinghouse are presented in Figure 5.29. Unfortunately, the neutron irradiated samples H1-4, 10-2 and F4-5 are not comparable to the pristine ones, and sections of pristine material coming from the same production batch could not be obtained. These sections are quite dissimilar to the GA1, -2 and -3 tubes with thinner walls, and overall smaller diameters. 10-2 and F4-5 show almost no thermal conductivity, with about  $0.5 \text{ W}\cdot\text{m}^{-1}\cdot\text{K}^{-1}$  throughout the temperature measurement range. This translates in gradients of more than  $200^\circ\text{C}\cdot\text{mm}^{-1}$  at sample average temperatures of about  $500^\circ\text{C}$ . This can be attributed to the same reasons as the ones discussed for pristine samples, with the addition of radiation-induced



## 5.2. Thermal conductivity

conductivity loss at the PyC interphase and, more importantly, to a thermal conductivity loss in the matrix and fibres. The last of the three neutron irradiated samples, H1-4, shows a better behaviour, with a conductivity of about  $4 \text{ W}\cdot\text{m}^{-1}\cdot\text{K}^{-1}$  at temperatures ranging from the ambient up to  $400^\circ\text{C}$ . The conductivity shows then a decrease, down to about  $1.5 \text{ W}\cdot\text{m}^{-1}\cdot\text{K}^{-1}$ , before it rises again once the sample reaches temperatures beyond  $700^\circ\text{C}$ . This behaviour might be explained on the basis of the structure of this tube. The inner monolith found in the tube is much denser than those found in the other samples. Furthermore, the interface between the monolith and the outwardly placed SiC/SiC is good, with no significant structural defects such as the ones seen in CEA tubes. Additionally to this, this composite is manufactured with Sylramic-iBN instead of HNLS fibres. This particular fibre is more than twice as conductive as HNLS, with a thermal conductivity of more than  $46 \text{ W}\cdot\text{m}^{-1}\cdot\text{K}^{-1}$  [33], against the  $18 \text{ W}\cdot\text{m}^{-1}\cdot\text{K}^{-1}$  of HNLS. The combination of both these points could explain why the conductivity of this sample exhibits a behaviour closer to literature data, i.e. conductivities ranging between 8 and 25 [45], see Table 1.1, page 35. Following the same trend as the other samples, the conductivity of this tube also increases at higher temperatures, an effect due to radiation thermal conductivity within the SiC/SiC layers.

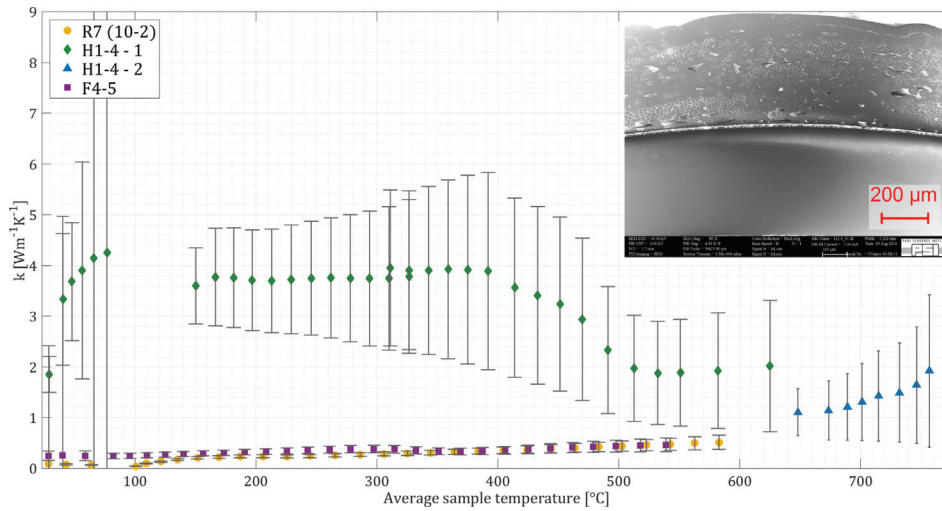


**Figure 5.29** – Measured thermal conductivity of neutron irradiated GA/Westinghouse SiC/SiC tubes. The SEM image on the left-hand side of the image shows a representative view of the cross-section of these samples.

### 5.2.3 Discussion

The general trend observed in the experimental data is unexpected for two reasons. Firstly, the overall observed values are much lower than what could be expected based on commonly available literature measurements, namely 8 to 15 W·m<sup>-1</sup>·K<sup>-1</sup>. Secondly, the thermal conductivity of most of the measured tubes features an increase with temperature. The precise point at which this occurs depends on the samples, with the least conductive tubes featuring it the earliest.

The first point has been quite worrisome, since it brought significant doubt on the experimental method. These measurements being the first to be carried out on the actual geometry of cladding tubes, no references are available for comparison. Since the validity of the heat transfer model was verified and validated using a stainless steel reference, part of our worries could be alleviated. The question is why these measurements are so very different than usual laser flash data. This topic is discussed in section 5.2.4. The previous paragraphs have hinted at the fact that the complex architecture of the claddings being the main culprit of the low thermal conductivity of the assemblies. This is further evidenced in section 5.3, where the modelling aspects of the tubes are discussed.

The reason behind the second point – the increase of thermal conductivity with increasing sample temperature – follows directly from the rather high and large porosity of the tubes. The thermal conductivity being extremely low due to the structure of the composite tubes, heat transport through the diffusion and scattering of infrared photons becomes noticeable. This phenomenon of radiative heat transport is addressed in section 5.2.5.

### 5.2.4 Comparison with laser flash

Two essential differences between the present radial heat flow measurements and laser flash experiments have to be discussed to understand the overall thermal behaviour measured in the prototype claddings. Firstly, data currently available from the literature is always measured on small discs or platelets, as this sample geometry is a requirement for the laser flash method. In addition to this geometrical difference, the majority of published data [158, 45, 10, 17] has been acquired on flat platelets made of SiC/SiC only, i.e. the actual multilayered structures such as the ones studied in this work have not seen much investigation yet. The second significant difference between a measurement performed using a radial heat flow and a laser flash apparatus is the directionality of the measurement or lack thereof, respectively. In the case of a steady state technique like the one used in this work, sufficient time is needed for a

thermal equilibrium to be reached. In these conditions, the axial and radial components of the temperature field can be decoupled at the measurement point, thereby yielding an output directly linked to the radial thermal conductivity of hollow tubular samples.

In the case of transient techniques, few papers are dealing with the measurement of anisotropic materials. Jeon et al. [159] published a theoretical model for photothermal deflection, whereas McMasters [160] recently discussed an analytical treatment to account for anisotropy in laser flash measurements. The thermal conductivity of a "simple" anisotropic material with three conductivities  $k_{xx}$ ,  $k_{yy}$  and  $k_{zz}$  aligned along their respective axis can be represented as an ellipsoid parametrised by Equation 5.3.

$$\frac{r^2 \cos^2 \phi \sin^2 \theta}{a^2} + \frac{r^2 \sin^2 \phi \sin^2 \theta}{b^2} + \frac{r^2 \cos^2 \theta}{c^2} = R^2 \quad (5.3)$$

The semi-axes of this ellipse are equal to  $1/\sqrt{k_i}$ , as represented in Figure 5.30. Additionally, the "radius"  $R$  is the effective thermal conductivity  $k_{\text{eff}}$ .

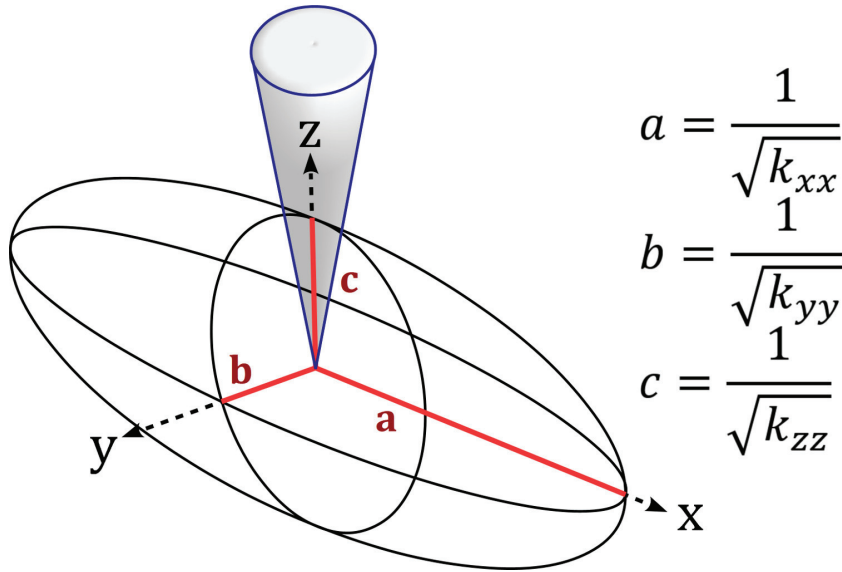


**Figure 5.30** – Representation surface of the thermal conductivity of an anisotropic material. The cone on top of the ellipse represents the "probe" used to measure  $k_{\text{eff}}$  along an arbitrary direction.

Jeon et al. [159] have shown that the temperature profile of the sample surface shows significant changes when  $k_i \neq k_j$ . More specifically, they showed that the heat flux is not parallel to the temperature gradient, apart from the semi-axes directions.

## Chapter 5. Results and discussion

In the case of the radial heat apparatus designed for this thesis, the temperature gradient across the sample wall is measured in a purely radial direction. Given the architecture of SiC/SiC samples, the representation surface of  $k_{\text{eff}}$  is aligned with its shortest semi-axes parallel to the sample radius. Hence, one can assume that the components  $k_i$ ,  $i = 1, 3$  are decoupled from one another, or that the cone in which the measurement is performed is very narrow.

The in-plane thermal conductivity of SiC/SiC also varies with respect to the heat flux direction, relative to the orientation of the fibres. This will not be addressed here, since the present discussion is focused on the through-thickness heat transport. Therefore, the semi-axes  $a$  and  $b$  of the ellipsoid are assumed to be equal. In this case, the ellipsoid becomes a flattened sphere, simplifying the analysis. Indeed, in this geometry, the situation can be brought in two dimensions, using Equation 5.4.

$$k_{\text{eff}} = k_{\parallel} \cos \phi + k_{\perp} \sin \phi \quad (5.4)$$

The curve featured in Figure 5.31 can then be calculated, and the effective thermal conductivity one would measure as a function of the semi-angle of a cone aligned along the radial direction can be estimated.

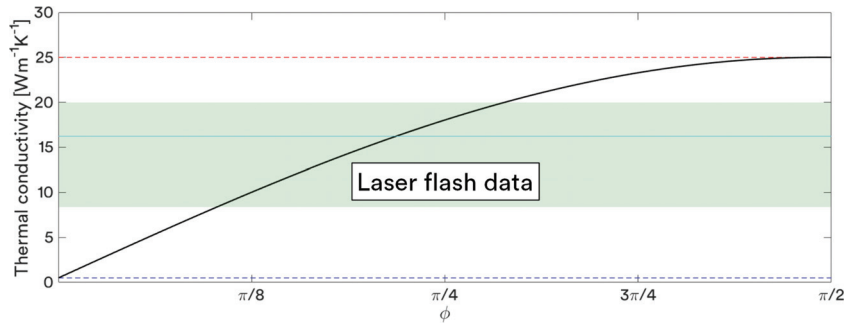


**Figure 5.31** – 2D view of the effective thermal conductivity of a composite with  $k_{xx} = k_{yy}$

Here, the in-plane conductivity  $k_{xx}$  has been renamed  $k_{\parallel}$ , and  $k_{zz} = k_{\perp}$ . It can be concluded that the values obtained for the effective thermal conductivity of a highly anisotropic composite like SiC/SiC depends on the measurement method as well as on the ability of the said method to separate the components of  $k_{\text{eff}}$ ,  $k_{\parallel}$  and  $k_{\perp}$ . The conductivity values commonly reported for SiC/SiC platelets, i.e. pure composite material, would be found in the green area of the

chart, i.e. values between 8 and 20-25 W·m<sup>-1</sup>·K<sup>-1</sup> [17, 10, 158, 45]. This indicates that these conductivities are an average over a measurement cone with a solid angle which projection ranges from 15 to 60°.

### 5.2.5 Radiative thermal conductivity

In materials featuring optical properties or porosity levels allowing infrared photons to diffuse, the energy they carry can contribute to the overall thermal conductivity of the material. This share is usually not seen in dense conductive materials since its magnitude rarely exceeds a few mW·m<sup>-1</sup>·K<sup>-1</sup> to W·m<sup>-1</sup>·K<sup>-1</sup>. However, measurements and discussion of this phenomenon are widely addressed in the literature discussing thermal insulation and porous materials [161]. Since the composite tubes measured in this work can effectively be considered as thermal insulators rather than as conductors, the radiative thermal conductivity<sup>5</sup> of SiC/SiC must be discussed to explain the experimental results.

The same basic principles of the kinetic theory of gases previously introduced (page 6) apply to photons as well. Thus, the extent to which photons can carry heat in a frequency interval  $\omega$  is given by Equation 5.5.

$$\kappa_{\omega} = \frac{1}{3} C_{\omega} v \lambda_{\omega} \quad (5.5)$$

Where  $C_{\omega}$  is the specific energy carried by photons in a frequency range  $d\omega$ ,  $v$  is the velocity of photons, which is simply given by  $c/n$ , with  $c$  the speed of light,  $n$  the refractive index, and lastly,  $\lambda_{\omega}$  is the mean free path of the photons in the aforementioned frequency range. Since complete theoretical treatment of the radiative thermal conductivity of ceramics can be found in a paper by Flynn [162], only the most relevant steps are discussed here.

Firstly, the total radiant energy emitted in the medium is given by the well-known Stefan-Boltzmann law:

$$E_{\omega} = \epsilon_{\omega} n^2 \sigma T^4 \text{ and } E_{\text{tot}} = n^2 \sigma T^4 \quad (5.6)$$

---

<sup>5</sup>The radiation thermal conductivity is often called *porosity thermal conductivity*, since pores are usually the main contributors to this heat transport mechanism.

## Chapter 5. Results and discussion

---

Equation 5.6 is not in its usual form: the term  $n^2$  is the squared refractive index of the medium, which is usually not written since it is by definition equal to one in vacuum. One can demonstrate that the energy carried by phonons in the interval  $d\omega$  is given by Equation 5.7.

$$C_\omega = \frac{4n}{c} \frac{dE_\omega}{dt} d\omega \quad (5.7)$$

Lastly, the mean free path of photons at a given frequency is  $1/\beta_\omega$ , where  $\beta_\omega$  is the extinction coefficient. Putting all these terms together in Equation 5.5 and integrating over all frequencies yields the expression displayed in Equation 5.8 for  $k_{\text{rad}}$ .

$$k_{\text{rad}} = \frac{1}{3} \cdot \frac{4n}{c} \cdot \frac{c}{n} \cdot \frac{1}{\beta_R} \cdot \frac{dE}{dt} = \frac{16n^2\sigma T^3}{3\beta_R} \quad (5.8)$$

Here,  $\beta_R$  is the Rosseland mean extinction coefficient, which we cannot precisely evaluate in the case of the tubular samples studied in this work. The various contributions to the overall extinction can however be discussed. Generally speaking, the mean free path of photons can be described by the following relationship.

$$\lambda = \left( \frac{1}{\lambda_a} + \frac{1}{\lambda_s} + \frac{1}{\lambda_b} \right) \quad (5.9)$$

Where the subscripts stand for absorption, scattering and boundary effects.

### Optical properties of silicon carbide

This discussion also applies to SiC/SiC composite tubes. Indeed, the structure of the composite clad allows both forward scattering against porosity and fibres and photonic transport. Since all these effects strongly depend on the photon wavelength, one must first determine in which regime the transport is likely to occur. The wavelength, at which thermal radiation peaks, is given by Wien's displacement law, given in Equation 5.10.

$$\lambda_{\max} = \frac{b}{T}, \text{ with } b = 2.898 \cdot 10^{-3} \text{ m} \cdot \text{K} \quad (5.10)$$

The values of  $\lambda_{\max}$  for a typical measurement range are plotted in Figure 5.32 (blue curve). Here, one can see that depending on the temperature of the sample, thermal radiation peaks between 2 and 10  $\mu\text{m}$ , which corresponds to the thermal infrared.

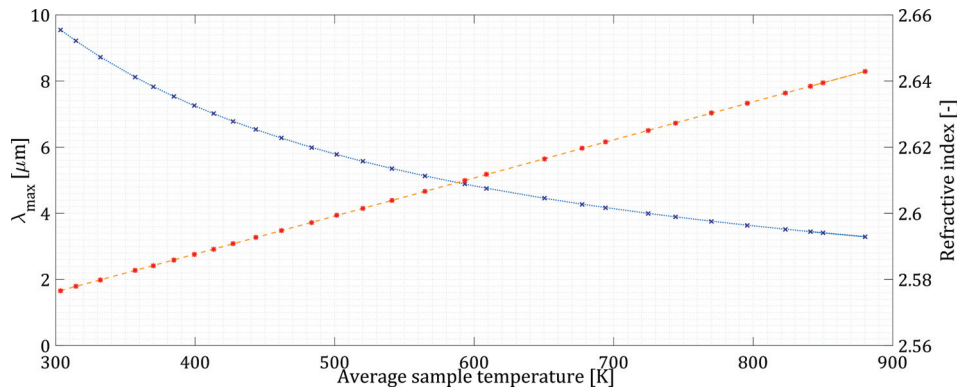


**Figure 5.32** – Wavelength of the thermal radiation emission peak calculated with Equation 5.10 (blue) and refractive index of SiC as a function of the average temperature of the sample (red). Based on data from [163].

Two optical properties are required to assess the magnitude of radiation thermal conductivity given by Equation 5.8: the refractive index  $n$  and the total absorption  $\beta_R$ .

## Chapter 5. Results and discussion

The limited availability of reliable optical data on the appropriate wavelength range makes the evaluation of the expression above difficult. Tropf et al. [163] have published refractive index data recorded in the infrared range. A temperature/wavelength dependent fit, giving the refractive index of optical 3C SiC at long wavelength, is presented in this paper and is given in Equation 5.11.

$$n = \left( 1 + S_0 + \frac{S_1}{\nu_1^2} \nu^2 + \frac{S_2 \nu_2^2}{\nu_2^2 - \nu^2} \right)^{1/2} \quad (5.11)$$

Here,  $\nu$  is the wavenumber of the peak emission in  $\text{cm}^{-1}$ , and the fit parameters are given in Table 5.2. The second curve plotted in Figure 5.32 shows the result of this fit as a function of the sample temperature in Kelvin.

**Table 5.2** – Fit parameters for the wavelength and temperature dependent refractive index of SiC in the infrared region. T in Kelvin.

Parameter	Expression
$1 + S_0$	$6.44669 + 1.76331 \cdot 10^{-4} T$
$S_1/\nu_1^2$	$1.45 \cdot 10^{-9}$
$S_2 \nu_2^2$	$1.88536 \cdot 10^6 + 51.3412 \cdot T$
$\nu_2^2$	$8.07274 \cdot 10^5 - 56.65 \cdot T$

The second optical property necessary to determine the radiative thermal conductivity of a sample is the absorption coefficient of SiC in the same range of wavelengths. Data on this quantity is even scarcer, even though a few astrophysics papers discuss this optical property of SiC because of its presence in carbon stars. A complete dataset published by Hoffmeister et al. [164] is available online, the plot of which is shown in Figure 5.33.

One shall note that these properties are those of pure SiC crystals, hence differences should be expected as far as both the matrix and fibres of SiC/SiC are concerned. The most significant effect of the composite microstructure will be on the absorption coefficient, which should be higher than for pure optical quality silicon carbide.



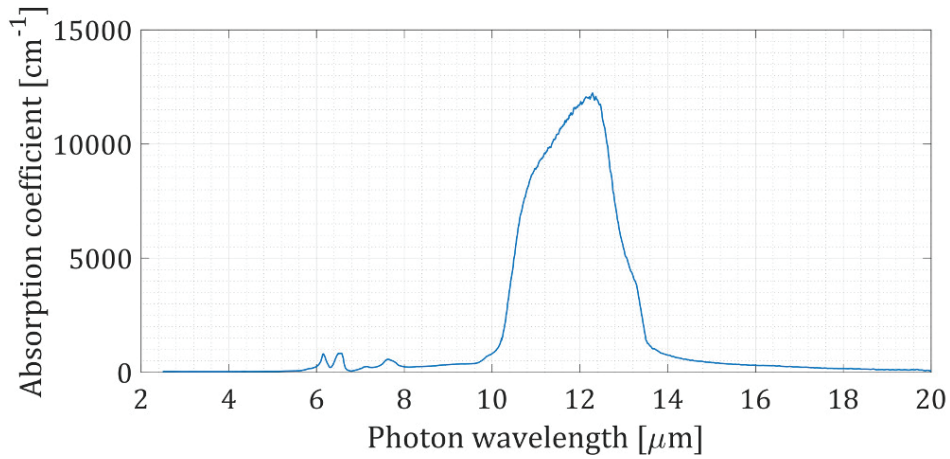


**Figure 5.33** – SiC absorption coefficient in the infrared range as a function of the photon wavelength [164]

### Photon scattering in SiC/SiC composites

In addition to the photon diffusion which is dictated by the optical properties of silicon carbide, scattering is also contributing to the photonic heat transport. Photons are known to scatter in three regimes; Rayleigh, Mie and geometrical scattering, the first two of which are schematically represented in Figure 5.34. To determine in which scattering regime events are likely to occur, one uses the dimensionless particle size  $x$  defined in Equation 5.12.

$$x = \frac{2\pi r}{\lambda} \quad (5.12)$$

- Rayleigh scattering<sup>6</sup> occurs when the wavelength of the photons is much larger than the scattering objects, i.e. when  $x \ll 1$ . In this case, the scattering cross-section is proportional to  $d^6/\lambda^4$ .
- In cases where the scattering object has a size parameter similar to the photon wavelength, Rayleigh's model breaks down. This scattering regime is described by Mie's theory<sup>7</sup>.

<sup>6</sup>The most visible occurrence of Rayleigh scattering is the blue colour of the sky, which is due to the scattering of photons against gas molecules and small particles of the atmosphere.

<sup>7</sup>Mie scattering is responsible for the white colour of clouds. It is due to the size of water droplets and ice crystals whose particle size parameter has values ranging over the whole visible light spectrum wavelength.

- When objects are much larger than the wavelength, geometrical optics, i.e. ray-tracing diagrams are used to describe how such large objects “scatter” light.

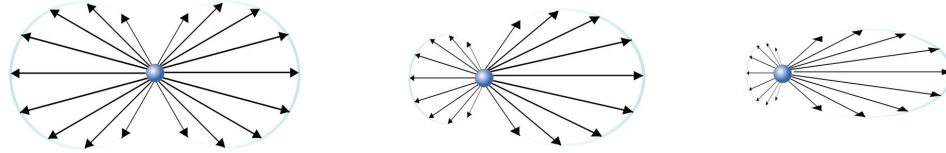


**Figure 5.34** – Rayleigh (left) and Mie scattering against small (centre,  $x \sim 1$ ) and large (right,  $x \sim 10$ ) particles. From [165].

There are three types of “particles” which scatter thermal radiation in a SiC/SiC composite. Firstly, the fibres are often surrounded by porosity and open structures which can be seen as scattering objects along the radius of the tube. The second and third types of “particles” are pores: the studied composites feature a bimodal porosity size distribution, with both very small pores featuring sizes in the hundreds of nanometres, and larger openings with sizes comparable to a fibre diameter and above. Determining the actual magnitude of the various scattering coefficients is not achievable in the present work and would be beyond this scope of the study. It is however important to note that this contribution to the thermal conductivity is seen in all the tubular samples and has not been reported before, most probably because these are, to date the only measurements, carried out on actual prototype tubes in this geometry.

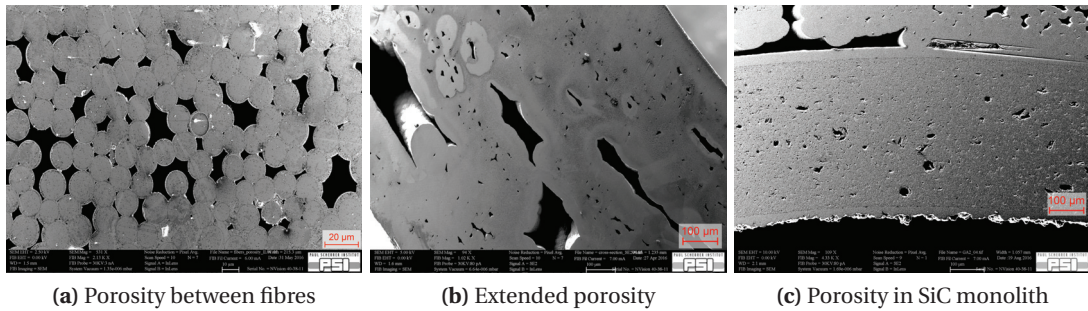


**Figure 5.35** – Types of porosities found in SiC/SiC composite tubes: small scale porosity between individual fibres **(a)**, large extended pores **(b)** and small pores within SiC monolith of GA/Westinghouse samples **(c)**

The graph displayed in Figure 5.36 shows the aforementioned parameter  $x$  plotted against the photon wavelength. The first set of data shows  $x$  for large porosity and SiC fibres, i.e. a “particle” diameter of 8 to 12  $\mu\text{m}$ , whereas the second dataset accounts for the size parameter of small scale pores with a diameter ranging between 100 and 500 nm. On the basis of this information, we can assume that practically all of the scattering will occur in the Mie regime. The strong

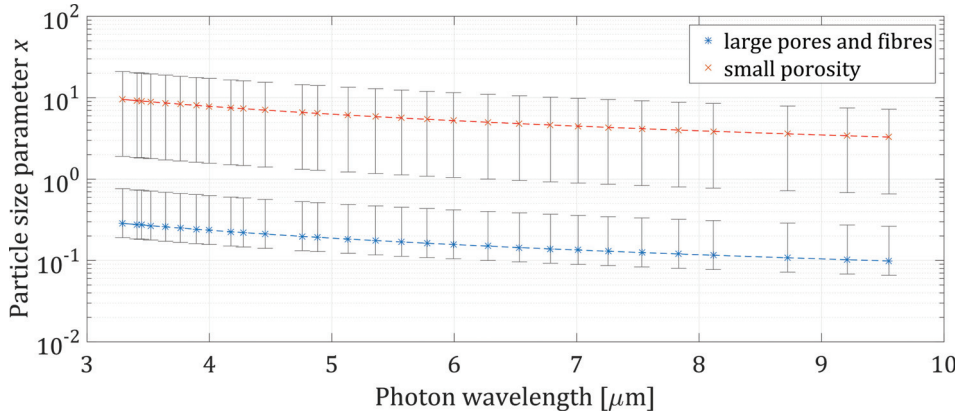


**Figure 5.36** – Dimensionless size parameter  $x$  as a function of the thermal radiation wavelength for small porosity ( $\varnothing = 100$  to  $500\text{nm}$ ), large pores and fibres ( $\varnothing = 8$  to  $12\mu\text{m}$ )

directionality of this type of scattering is supporting the fact that the thermal conductivity of the SiC/SiC prototypes feature a large contribution of radiant heat transport through the scattering of infrared photons against both large and small cavities as well as against SiC fibres.

As a side note, one might keep in mind that gaseous conductivity might also occur, depending on the environment in which the tubes would be used <sup>8</sup>. Assuming that this contribution is rather negligible in the present case as well as in LWR conditions seems reasonable. Indeed, except for closed porosity where the cavities are filled with unreacted CVI gases, the open porosity is empty. In a LWR, these would contain either water or helium from the cladding interior. A good introduction to this problem in porous ceramics can be found in Flynn [162]. The main result presented by the author is an estimation of the conductivity of the gases found in the pores.

$$k_g = \frac{f k_b}{6S} \left( \frac{3RT}{M} \right) \quad (5.13)$$

Equation 5.13 defines the gas conductivity as a function of the degrees of freedom of its molecules  $f$ , its molecular weight  $M$  and the cross-sectional area of its molecules  $S$ .

<sup>8</sup>This might become a noticeable contribution to the overall conductivity in a GFR or VHTR.

## 5.3 Modelling

### 5.3.1 SiC/SiC thermal conductivity

This last part of the discussion brings together the observation made at the microstructural level with the experimental data from thermal conductivity measurements.

By combining both the Landauer porosity model and the Markworth continuous medium approach, the loss of thermal conductivity following a full or partial amorphisation of the PyC interphase, accounted for with an interlayer conductivity of 1 to  $10 \text{ W}\cdot\text{m}^{-1}\cdot\text{K}^{-1}$ , are calculated using Equation 4.8. Figure 5.37 shows the data resulting from such calculations for different porosity levels typically encountered in SiC/SiC composites.

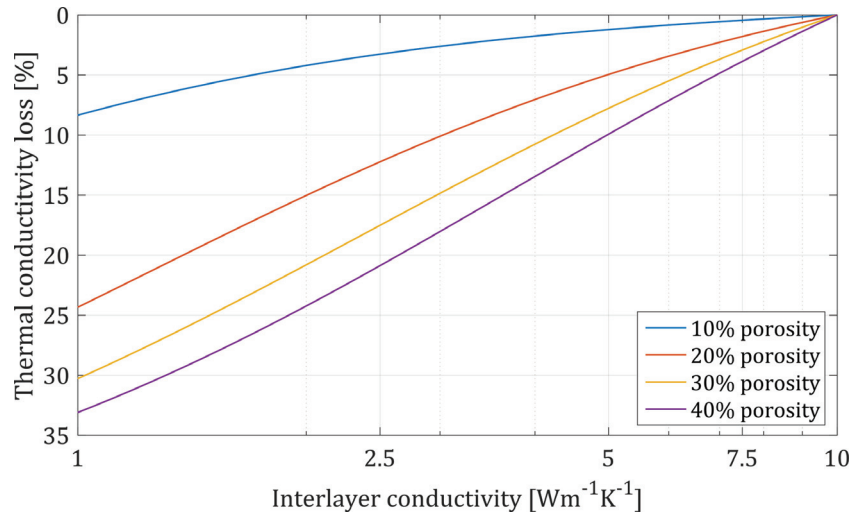


**Figure 5.37** – Effective thermal conductivity of a SiC/SiC composite with varying matrix porosity and interlayer thermal conductivity

The limits to the interlayer thermal conductivity are taken from Figure 1.12 (page 47). Amorphous carbon has a TC of about  $1 \text{ W}\cdot\text{m}^{-1}\cdot\text{K}^{-1}$ , whilst that of pyrolytic carbon is slightly below  $10 \text{ W}\cdot\text{m}^{-1}\cdot\text{K}^{-1}$  in the cross-plane direction.

As one can see, a full amorphisation of the PyC interphase would lead to a thermal conductivity loss of 10 to 35%, depending on the total porosity. The typical range of porosities in CVI SiC matrices is between 10 and 25% in average, with locally much higher porosities of 40 to 50%. Note that these results hold for a material in which the pores are insulators compared to the

matrix. This effect would likely be mitigated at elevated temperatures, since amorphous carbon becomes slightly more conductive at elevated temperatures, whereas the c-axis conductivity of PyC decreases with rising temperature.

### 5.3.2 Application to an actual case

The thermal conductivity data featured in section 5.2.2, can be explained by combining the three models considered in our modelling approach. This gives insight on the reasons why almost all the samples measured in this work are such poor conductors. To continue the discussion, we will consider the case of the CEA sandwich cladding tubes, the conductivity curves of which are shown in Figure 5.38.

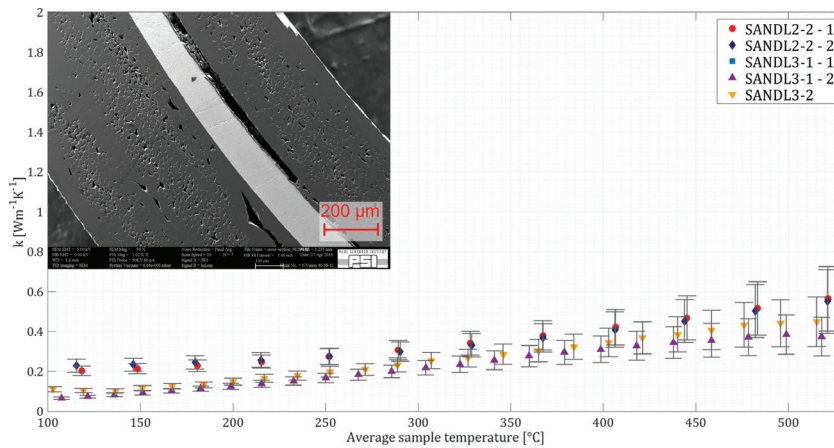


**Figure 5.38** – Measured thermal conductivity of CEA sandwich tubes

A typical view of the cross-section of these samples is shown in Figure 5.39a. Tackling the question of the thermal conductivity of the SiC/SiC layers by using Equation 4.4 and combining it with the aforementioned Landauer/Markworth approaches allows one to determine the actual conductivity of the multilayer system.

Considering the measured temperatures as well as the conductivities of the layers calculated according to our modified Markworth model, a temperature profile such as the one featured in Figure 5.39b can be calculated. This shows the profile across the 1 mm wall of the tube, with the seven layers identified in the SEM image shown in Figure 5.39a.

The profile displayed in Figure 5.39b evidences that layers with a poor adhesion to one another, such as the ceramic/tantalum interface result in a quasi-total insulation. Inspecting the cross-section, we see that this layer has a contact area with the tantalum of only 10 to



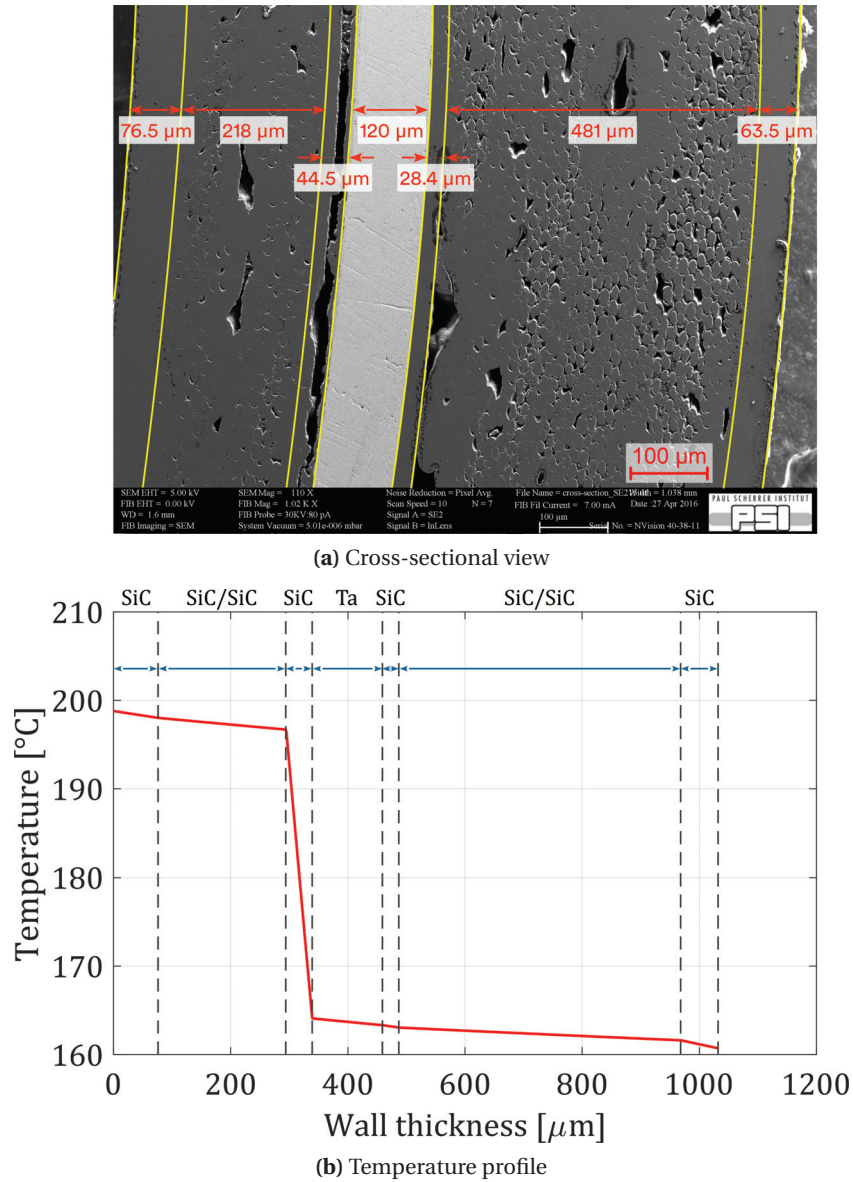


**Figure 5.39** – SEM image showing the microstructure of the cross-section of a CEA cladding tube section (a) and associated temperature profile across the wall of the multilayered sandwich cladding (b)

20%. Hence, the tube equivalent thermal conductivity is about  $0.33 \text{ W}\cdot\text{m}^{-1}\cdot\text{K}^{-1}$ . Though the overall porosity of the cladding tube is about 20%, the innermost and outermost layers are made of monolithic SiC, whose density can be considered practically equal to the theoretical  $3.125 \text{ g}\cdot\text{cm}^{-3}$ . Considering this as well as the fact that the metal liner is a purely dense component with a density of  $16.5 \text{ g}\cdot\text{cm}^{-3}$ , the porosity of the SiC matrix in the SiC/SiC layers is closer to 45%.

### 5.4 Effect of cladding conductivity on fuel temperature

The results presented in this chapter raise concerns about the question of the safety of operations if fuel cladding much less conductive than Zry were to be employed. In fact, the temperature at the centre of the fuel pellets, known as the *fuel centre-line temperature*, is one of many parameters upon which stringent safety limits have to be imposed. Currently, almost all nuclear reactors are fuelled with uranium oxide,  $\text{UO}_2$ , or with MOX, a mixture of uranium and plutonium oxides. These ceramics have very high melting points (2850 and 2750°C for  $\text{UO}_2$  and MOX, respectively). To ensure that the fuel does not melt during operational transients, a hard limit has been set by the NRC on the peak cladding temperature. This limit has been defined for Zry claddings, which oxidise exothermically at  $\sim 980^\circ\text{C}$  and above. Furthermore, the rate of this reaction significantly increases at temperature beyond  $1205^\circ\text{C}$ <sup>9</sup>. This last section discusses the impact of low conductivity claddings on the fuel centre-line temperature.

#### 5.4.1 Thermal analysis of a fuel element

A nuclear element is an ensemble comprising fuel pellets, a helium filled gap and the cladding itself. The gap between the fuel and the cladding ensures two functions: it gives space for the fuel to expand, following the significant temperatures and microstructural changes it experienced during operations and allows a free volume to accommodate the fission gases. The gap is filled with helium because of the excellent thermal conductivity of this gas. In terms of physical dimensions, it is about 50  $\mu\text{m}$  wide and pressurised at 15.2 bar. The analysis is done for a *European Pressurised Reactor* (EPR), designed by Areva<sup>10</sup>

Figure 5.40 shows the cross-sectional view of a fuel element. Typical fuel pellets have a diameter of 8.19 mm and are about 13.5 mm high. Analysing this system in steady state is rather straight-forward, since the heat equation is solved in the radial direction only. The only difference with the case presented in section 3 is that the fuel is a full cylinder with an internal heat source.

The volumetric power generation of fuel pellet can be deduced from the number of fuel elements found in a reactor with a given thermal power. The relevant parameters necessary for this operation are given in Table 5.3.

---

<sup>9</sup>This limit was defined by the NRC at 2200°F [8].

<sup>10</sup>This reactor was selected because of the availability of technical data.

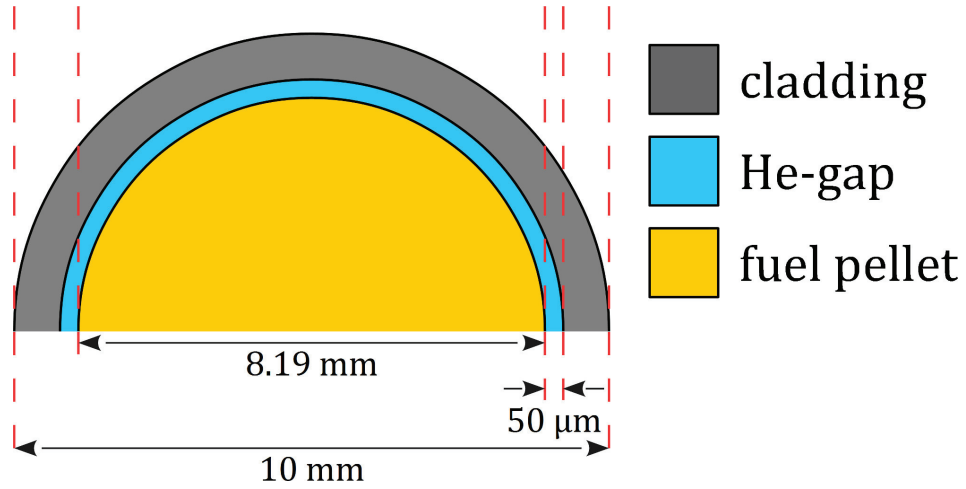


**Figure 5.40** – Cross-section view of a fuel element

**Table 5.3** – EPR parameters required to analyse the radial temperature distribution of a fuel element. Data obtained from the US NRC [166] and Skrzypek et al. [167].

Power [MW <sub>th</sub> ]	# assemblies	rods per assembly	pitch
4'590	241	17 × 17	12.6
rod diameter [mm]	flow rate [m·s <sup>-1</sup> ]	$\bar{T}_{\text{cool}}$ [°C]	$\dot{q}'_{\text{max}}$ [kW·m <sup>-1</sup> ]
9.5	5	314	44.62

The complete thermal analysis goes through the determination of the radial temperature distributions in four domains, the pellet, the He-gap, the cladding and the coolant-cladding interface layer. The full discussion of this subject can be found in R. Othman's master thesis [168].

### Fuel pellet

Within the fuel pellet, the temperature profile follows Equation 5.14, the solution of the heat stationary heat equation with a volumetric source.

$$T(r) = T_0 - \frac{r^2}{4k_f} \dot{q}''' \quad (5.14)$$



#### 5.4. Effect of cladding conductivity on fuel temperature

Where  $T_0$  is the fuel centerline temperature,  $k_f$  is the thermal conductivity of the fuel and  $\dot{q}'''$  is the volumetric heat source. The temperature difference across the fuel pellet radius (assuming a constant  $k_f$ ) is then simply given by:

$$\Delta T_{\text{fuel}} = \dot{q}''' \frac{r_f^2}{4k_f} \underbrace{\dot{q}' = \pi r_f^2 \dot{q}'''}_{=} \frac{\dot{q}'}{4\pi k_f}$$

#### Gas gap

From the aforementioned reference, the temperature drop across the gap is given by:

$$\Delta T_{\text{gap}} = \frac{\dot{q}'}{2\pi r_f h_{\text{gap}}}$$

This requires a more extended development than what is presented by Othman [168]. Indeed, the heat transfer coefficient across the gap should include radiant heat exchange in addition to heat transfer by the gas. This issue is well described by No [169], yielding Equation 5.15:

$$h_{\text{gap}} = \frac{k_{\text{gas}}}{t_{\text{gap}}} + \frac{\sigma}{\frac{1}{\epsilon_{\text{fuel}}(T)} + \frac{1}{\epsilon_{\text{clad}}} - 1} \frac{T_{\text{fuel}}^4 - T_{\text{clad}}^4}{T_{\text{fuel}} - T_{\text{clad}}} \quad (5.15)$$

Here,  $T_{\text{fuel}}$  and  $T_{\text{clad}}$  are the temperature of the fuel and cladding at their outer and inner surfaces, respectively. No [169] gives temperature correlations for both  $\epsilon_{\text{fuel}}$  and  $k_{\text{gas}}$ .

#### Cladding

The case of the cladding was already discussed in chapter 3. The temperature distribution is given again here with Equation 5.16

$$T(r) = T_{\text{in}} + \frac{\ln(r/r_{\text{in}})}{\ln(r_{\text{out}}/r_{\text{in}})} (T_{\text{out}} - T_{\text{in}}) \quad (5.16)$$

### Coolant

A few concepts of thermohydraulics should be considered at first. The heat transfer coefficient between a substrate and flowing water  $h_{\text{wall}}$  is linked to the Nusselt [170] number and the hydraulic diameter of the flow channel:

$$h_{\text{wall}} = \frac{k}{D_h} \text{Nu} \quad (5.17)$$

In Equation 5.17,  $D_h$  is the *hydraulic diameter* of the flow channel, and  $k$  is the thermal conductivity of water.  $D_h$  is a common concept in fluid dynamics, whereby complex flow channels can be seen as cylinders [171]. It is defined as:

$$D_h = \frac{4A}{P} \quad (5.18)$$

Here,  $A$  is the cross-sectional area, and  $P$  is the wetted perimeter. Considering the flow channel geometry sketched in Figure 5.41, one can calculate  $D_h$  for this specific case:

$$D_h = \frac{4(p^2 - \pi r_f^2)}{2\pi r_c}$$

The Nusselt number is a function of the Prandtl and Reynolds numbers of the fluid. The Dittus-Boelter relationship is often used to link these three dimensionless numbers.

$$\text{Nu} = 0.023 \cdot \text{Re}^{0.8} \text{Pr}^{0.4} \text{ with } \quad \text{Pr} = \frac{c_p \mu}{k} \quad \text{Re} = \frac{\rho \mathbf{v} D_h}{\mu}$$

Several thermophysical parameters of water at 300°C are needed to compute these numbers.  $\mu$  is the dynamic viscosity,  $\rho$  the density and  $\mathbf{v}$  the fluid mean velocity of the cooling water. An online article by Pradmuditya [172] gives a good overview of the necessary parameters

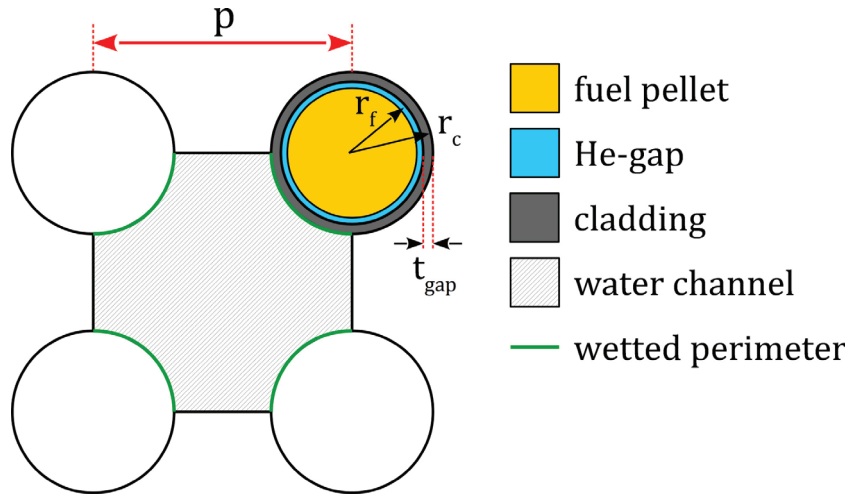


**Figure 5.41** – Drawing of a flow channel in a fuel assembly

**Table 5.4** – Thermophysical properties of 300°C water at 155 bar

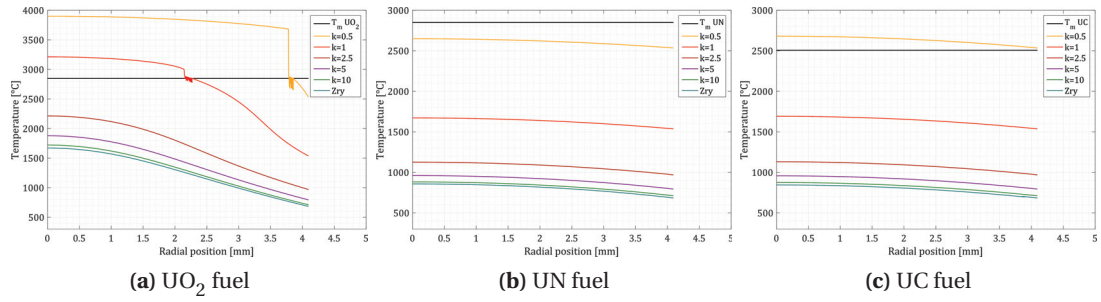
$\rho$ [kg·m <sup>-3</sup> ]	$c_p$ [kJ·kg <sup>-1</sup> ·K <sup>-1</sup> ]	$\mu$ [Pa·s]	$k$ [W·m <sup>-1</sup> ·K <sup>-1</sup> ]	Pr	Re	Nu
720.4	5.587	2.925E <sup>-5</sup>	0.556	0.2942	7.2417E <sup>5</sup>	717.04

calculated with Xsteam, with the appropriate fit functions. Thanks to this resource, the properties displayed in Table 5.4 have been calculated. Using this data yields a heat transfer coefficient of  $6.087 \cdot 10^4 \text{ W} \cdot \text{m}^{-2} \cdot \text{K}^{-1}$ .

### 5.4.2 Fuel pellet temperature profiles

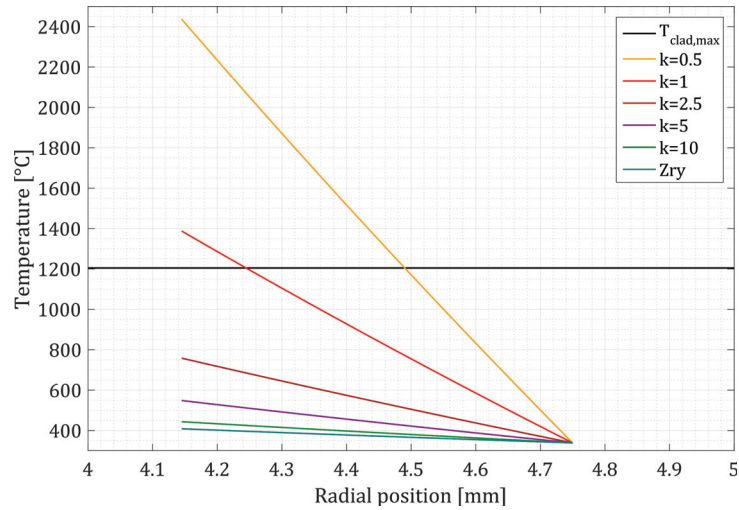
On the basis of the points mentioned above, a Matlab routine has been coded to calculate the temperature profile. The temperature dependence of the fuel thermal conductivity has been included, using data from Carbajo [34] for  $\text{UO}_2$  and an IAEA publication [173] for UN and UC properties. These calculations are inwardly iterated with respect to the radius, so that the temperature profiles are corrected with regard to the temperature dependence of the fuel thermal conductivity.

Figure 5.42 shows the results of the computations mentioned above. To be conservative in the estimation of the impact of low conductivity claddings, all of these have been performed with the peak linear heat rate, i.e. the highest operational power generation foreseen by Areva. The inflexion of the curves displayed in Figure 5.42a is due to the increase of the thermal conductivity of  $\text{UO}_2$  at temperatures beyond 1500°C. As the temperature further increases, the fuel becomes more conductive, inflecting the temperature profile. In addition, the fuel melts



**Figure 5.42** – Fuel temperature profiles calculated for  $\text{UO}_2$ , UN and UC pellets. Six different conductivities have been computed, from 0.5 to  $10 \text{ W} \cdot \text{m}^{-1} \cdot \text{K}^{-1}$ , as well as for Zry.

at  $2850^\circ\text{C}$ , at which point the computation switches to the thermal conductivity of molten  $\text{UO}_2$ . Uranium carbide would also melt in the extreme case of  $k = 0.5$ . However, since data for molten UC is not available and the model does not switch to another conductivity. This has been included for the sake of completeness, although a fuel melt is likely to lead to failure of the assembly during subsequent cooling. The fusion of the  $\text{UO}_2$  fuel is the reason for the instabilities of the fuel temperature profile with the lowest cladding thermal conductivity. Lastly, the temperature profiles across the cladding are shown in Figure 5.43. As one can see, the peak cladding temperature exceeds the aforementioned  $1205^\circ\text{C}$  limit, at which point the melting of the fuel is expected.



**Figure 5.43** – Temperature profiles across claddings with different conductivities

Based on these results, the combination of  $\text{UO}_2$  fuel and poorly conducting claddings would be very unsafe. The SiC/SiC cladding tubes such as most of the ones investigated in this work feature an increasing conductivity thanks to photonic heat transport. In operating conditions,

#### 5.4. Effect of cladding conductivity on fuel temperature

the average temperature of the clad is about 450°C. At these temperatures, CEA clads are not conductive enough for their use to be considered. The GA/Westinghouse tubes would however be in the range of  $2 \text{ W}\cdot\text{m}^{-1}\cdot\text{K}^{-1}$ , a conductivity already high enough to avoid melting. However, the safety margins would be much too tight and the conductivity should be higher. The profiles shown in Figure 5.44 show the complete calculation for a cladding with  $k = 5 \text{ W}\cdot\text{m}^{-1}\cdot\text{K}^{-1}$ .

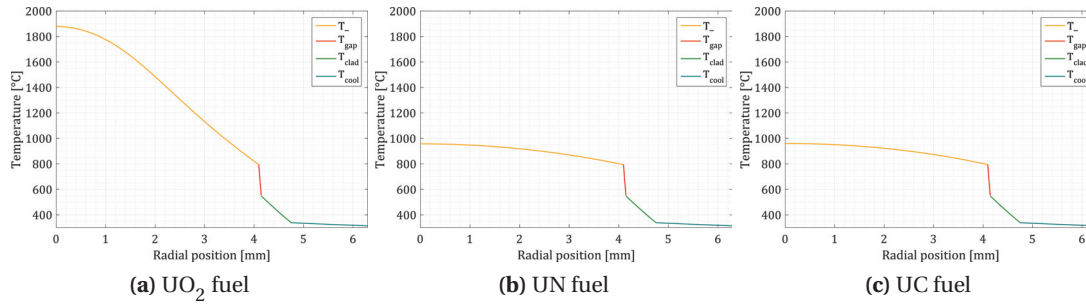


**Figure 5.44** – Temperature profiles from the fuel pellet to the coolant calculated for  $\text{UO}_2$ , UN and UC pellets. All three profiles are calculated with a cladding thermal conductivity of  $5 \text{ W}\cdot\text{m}^{-1}\cdot\text{K}^{-1}$

If combined with other types of fuels, the low thermal conductivity of the cladding is not an issue anymore. Indeed, both UC and UN are significantly better conductors than uranium oxide, resulting in practically flat temperature profiles across the pellet. This illustrates well the reason why a large portion of ATF activities are focused on the development of nitride, carbide or silicide fuels. Nevertheless, the high inhomogeneity of the cladding properties is a cause for concern. The aforementioned target of a homogeneous conductivity of at least  $5 \text{ W}\cdot\text{m}^{-1}\cdot\text{K}^{-1}$  is probably a realistic, and achievable development goal; this could be attained by focusing on the adhesion of the tightness layers and SiC/SiC. Additionally, improving the densification process, either by exploring F-CVI, P-CVI (see page 43) or by successfully scaling the NITE process from the laboratory up to the industrial scale.



## Conclusion and perspectives

The overall methodology followed in the present thesis was successful at giving new insights on the thermal conductivity of prototype nuclear cladding based on a highly anisotropic silicon carbide-based CMCs, with a focus on the role of the pyrolytic carbon interphases emphasis linking the fibres to the matrix. The main result of this work is an unexpected one: the through-thickness thermal conductivity of most SiC/SiC cladding prototypes is extremely poor, mainly because of the too numerous interfaces between the many layers found in these complex multilayered tubes. Although this type of architecture is a technical necessity, dictated by the need for gas and water tightness of the fuel pin, further effort is necessary from the manufacturers if such claddings are to be used in operating nuclear power plants. Out of the whole set of samples, only two, H1-4 and GA1, featured a conductivity approaching 2 to 4  $\text{W}\cdot\text{m}^{-1}\cdot\text{K}^{-1}$ , at which point a cladding is conductive enough to avoid the melting of  $\text{UO}_2$  fuel. Another major issue which needs to be solved is the high inhomogeneity of the SiC/SiC composite tubes: measurements carried out on identical samples have shown conductivities varying by a factor of four or more, depending on the measurement location. In terms of power plant operations, this would mean that the fuel temperature could not be controlled as efficiently as it currently is. Hot-spots would be found along the whole length of the core, as well as in the circumference of the cladding. This might open the possibility for local *departure from nucleate boiling* (DNB), which could be detrimental to the plant operation, in terms of safety, neutronics and economics. Indeed, the fuel burnup could not be near the homogeneities currently achieved with Zry: at local hotspots, DNB would lead to local boiling, hence to local reactivity variation through the water void coefficient, thereby making the control of the reactor neutronics more difficult than it needs to be.

These new results were obtained by performing measurement with a radial heat flow apparatus developed in the first stages of this PhD work. This experimental device was built to be as modular as possible whilst operating in vacuum, so that heat transfer would be purely radiant. In our current state of knowledge, these are the first thermal conductivity measurements

## Conclusion and perspectives

---

carried out on the actual geometry of cladding tubes. Indeed, most of the data available from the literature is obtained from transient photothermal techniques. Based on the results presented here, it seems that these techniques often do not address the actual radial conductivity of SiC/SiC, but rather a mixture of both the planar and axial components. Moreover, the real geometry, with all the challenges it involves, is not taken into account in diffusivity measurements. This is where the relevance of the apparatus built for this work shines. Even though steady state methods have become much less prominent since the invention of laser flash by Parker [129], this implementation has shown that they should not be discarded yet. Nevertheless, the versatility of photothermal deflection or laser flash makes these techniques necessary in the first development steps of a technical material like SiC/SiC cladding. Another advantage of the device developed for this project is its modularity; samples with lengths ranging from 35 mm to 200 mm have been characterised. In terms of external diameters, the composite tubes were in the range of 9.78 to 11.63 mm, with wall thicknesses between 1 and 1.5 mm. The 316L stainless steel reference was even larger, with a diameter of 42.4 and a 2 mm thick wall. The main reason for modularity is the fact that the samples are made of a technical material, currently in assessment for future use in power plants. Therefore, the experimental plan had to accommodate limitations and restrictions coming from the suppliers' side. Thus, although it has been shown that PyC does become partly amorphous after irradiation with either ions or neutrons, the impact of this effect on the overall conductivity of SiC/SiC tubes could not be brought to light, and thus can only be modelled.

An issue seen in all of the studied cases is the large scatter in the measured thermal conductivity. This behaviour is due to the highly inhomogeneous micro- and macrostructures of the tubes, specifically in their cross-section. In many places, the composite exhibits extended porosity of hundreds of micrometres; at these locations, the material shows almost no conductivity. This is where a weakness of the experimental apparatus makes itself clear. The location and distribution of the aforementioned production defaults are quite random, meaning that the depending on the position of the thermocouples, different results are obtained. If more data could be obtained, more might be said about the inhomogeneity of the effective thermal conductivity. This was however not possible in the present work, since typical measurements require more than a week; due to the time necessary to design, build, test and finally validate the experimental setup, most samples could be measured only once or twice. In addition to this, the difficulty coming from the need to glue the thermocouples to the samples made the measurement rate rather low.



In most cases, the unexpectedly low thermal conductivities found in the available prototypes featured a non-negligible amount of photonic heat transport. This heat conduction mechanism is specific to porous and IR semi-transparent materials. Moreover, it often has too small a magnitude to be noticeable, compared to the phononic and electronic contribution to the total thermal conductivity – this is in part the case for two samples, GA1 and H14. However, it is present in the majority of the studied prototypes and acts as the primary means of heat transfer as soon as temperature reaches about 300°C. The physical mechanisms involved in this transport process are mainly the forward scattering of IR-photons, as well as partial diffusion of the photons within the SC itself. Out of these two phenomena, the former is likely the main contributor to photonic conduction. Indeed, the CVI SiC matrix is highly porous – about 35% in average –, with pore sizes in the tens to hundreds of  $\mu\text{m}$ . Additionally to these large pores, fibres are often seen with almost no matrix attached to them, making them the equivalent of "particles", and thus features against which infrared radiation scatters – examples of these features are shown in Figure 5.35 (page 160). The non-dimensional particle size diameters, which can be attributed to these micro- to macrostructural features are between 0.5 and  $\sim 50$ . In this range, light scattering is described by the Mie theory, which is the key to the increase of thermal conductivity with temperature. In this regime, if the dimensionless particle size diameter is of the same order of magnitude, or larger, than the wavelength of photons, scattering is primarily occurring in the forward direction. Given the sizes of the aforementioned structural defaults, this phenomenon is the core reason why IR photons contribute to the conductivity of the tubes.

Electron microscopy was the second pillar of this work. EFTEM and spectrum imaging in STEM-EELS were carried out to enable a detailed analysis of the carbon K-edge of the PyC interphases. Since these measurements were performed in magic angle conditions, the magnitude of the  $\pi^*$  peak, relative to that of the  $\sigma^*$  peak, could be performed on the spectral data. Doing this, a reduction of the amount of  $\text{sp}^2$  to  $\text{sp}^3$  hybridised carbon atoms, synonymous to a partial amorphisation of the originally graphite-like interlayer, was evidenced. This has consequences on both the thermal and mechanical properties of these crucial interlayers. In fact, the thermal conductivity of an amorphised PyC layer would barely be a tenth of that of a pristine graphite-like PyC interphase. As a result, a SiC/SiC composite, whose interphases are amorphous, would see a loss of up to 35% in its effective thermal conductivity. The conductivity would of course be further degraded by the thermal defect resistance [17, 11, 45] of the SiC fibres and matrix. The case of the H1-4 sample would be an example of such a phenomenon. However, since no pristine material could be obtained, the defect resistance could not be determined in this case. Nevertheless, this composite would be sufficiently

## Conclusion and perspectives

---

conductive to avoid a fuel melt if it were to be used in its current state. Additionally to these spectroscopic investigations, an in-situ irradiation experiment was carried out at the JANNuS in Orsay. The aim of these experiments was to focus our attention on the PyC interphases, as well as to obtain additional samples of irradiated material. Overall, this experiment proved successful: samples featured an amorphisation of their SiC fibres and matrices – due to the low irradiation temperature – the dimensional changes discussed in section 5.1.1 and a decrease in their graphitic nature. They could be compared to neutron irradiated samples, showing that much care should be taken when interpreting data from ion irradiations. Indeed, although the overarching trend shows a reduction of the  $sp^2/sp^3$  ratio, ion irradiated PyC features distributions of this ratio, which tend to be wider, and many more outliers than neutron irradiated PyC. This is explained by several factors; firstly, the rate at which ion irradiated samples are damaged is more than four orders of magnitude higher than in neutron irradiations. This is a well-known effect, which often translates in the onset of many radiation-induced effects to lower temperatures [21]. Secondly, the amount and the way in which energy is deposited in the case of an ion irradiation is significantly different than that of exposure to neutrons. Whilst neutrons can shed up to 15.4% of their energy in a single collision with a carbon atom, ions will deposit their energy in a continuous manner until the Bragg peak, where the remaining energy is deposited at once. Whilst the energy deposited by a single fission neutron might reach much higher values than 140 keV  $C^+$  or 2 MeV  $Si^+$  ions, the samples studied here mostly experienced collisions with rather low energy neutrons. Indeed, whilst the neutron spectrum of MITR is slightly harder than that of a LWR, it is rather similar nonetheless. Since the samples irradiated in this test reactor did not contain fuel, most of the neutrons that collided with C atoms within the samples had to have been at least partially moderated, i.e. their energies were a few tens of keV at most. Therefore, the  $sp^2/sp^3$  ratios measured on the H1-4 lamellae are higher than those of ion irradiated PyC, since the ions have been able to deposit more energy, thus being potentially more damaging, hence the lower ratios and larger distributions. The same cannot be said of neutron irradiated A034, since HFR has an epithermal neutron spectrum, i.e. more energetic neutrons are present. The reason for which the R-ratio of these samples is also higher than those of the ion irradiated lamellae is probably found in the irradiation temperature. HFR operates at much higher temperatures than MITR, in the present case, the samples were irradiated at 796°C [90]. As a reminder, in operations, Zry cladding has an average temperature of about 500°C. At an elevated temperature like that of HFR, one can expect to see a significant recombination of point defects, leading to a at least partial recovery of the damage. This is supported by the fact that the SiC matrix of these samples is still highly crystalline, even though the sample was irradiated to 2 dpa.

The modelling part of the work binds both experimental parts. SiC/SiC composites have been studied both at the microstructural scale, whereby the response to radiation damage of the PyC interphases has been addressed, as well as at the macro-scale, by measuring the thermal conductivity of SiC/SiC prototype clads. Through continuous medium modelling, the effect of a PyC amorphisation on the effective thermal conductivity of SiC/SiC composites has been discussed. As a matter of fact, modelling the composite tubes as a multilayered stack of thermal resistances yields results in agreement with the radial heat flow measurements. The aforementioned loss of conductivity which does ensue could not be identified with the available samples. To do this, one would need to either have strong ties with the industry or on-site manufacturing capabilities. In such a case, samples could be prepared with pure SiC/SiC layers, i.e. without tightness-ensuring layers like Ta liners or SiC monoliths. Doing this, one could then move on to a systematic study using high energy ions or neutrons. Alternatively, thermoreflectance could be used in a SEM [174, 175]. The issue here is that the width of the PyC interphases is often very close to the resolution of this technique – tens of nanometres. Lastly, a complete analysis of the steady state temperature profiles of a fuel pin, including a fuel pellet, the helium gas gap, the cladding and the turbulent layer of the coolant has been performed. As a result, we can affirm that claddings with conductivities of  $1 \text{ W}\cdot\text{m}^{-1}\cdot\text{K}^{-1}$  or less would lead to fuel melting and cannot be considered. Moreover, if the clad does not have a radial conductivity of at least  $4 \text{ W}\cdot\text{m}^{-1}\cdot\text{K}^{-1}$ , the fuel centreline temperature exceeds  $2000^\circ\text{C}$ , which does not leave much of a safety net for operational or accidental transients. A potential alternative discussed in section 5.3 is the use of other fuels, such as uranium carbide or nitride, which are much more conductive than uranium dioxide.

## Perspectives

### Planar to non-planar $\text{sp}^2$ quantification

A potential direction for future work could be the detailed analysis of the 280 to 290 eV energy range of the carbon K-edge. The quantification of both EFTEM and ESI maps has evidenced that, although changes do occur in the PyC interphase, amorphisation does not suffice to explain the extent of the changes. In many cases, the integral of the intensity attributed to the filling  $\pi^*$  states does not seem to significantly change after irradiation. In some cases, this spectral feature is showing more of a broadening than a real reduction of its magnitude. Zhang [117] and Bernier [119] have hypothesised that the dip seen in the spectrum fit shown

in Figure 2.24 can be explained by the presence of non-planar  $sp^2$ . With the addition of a fourth narrow Gaussian constrained at  $\sim 288$  eV, this part of the spectrum can be fitted and quantified. Figure 7 shows the corresponding fit performed on a HOPG reference.

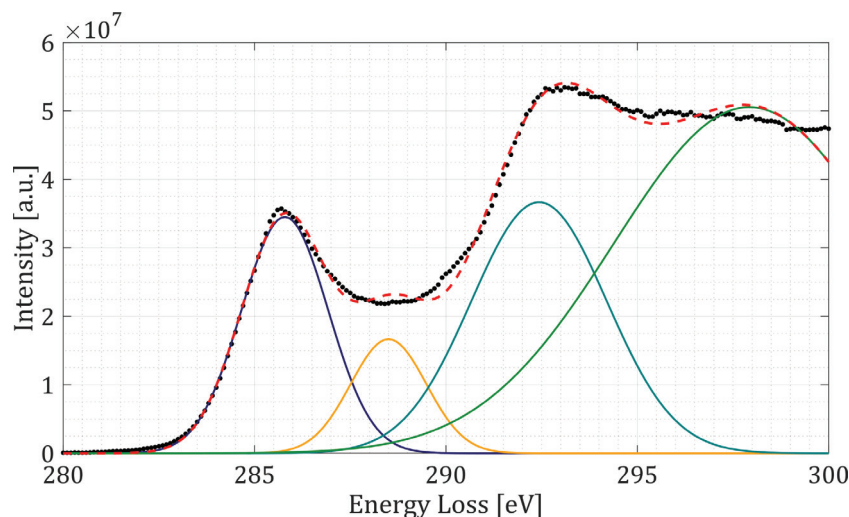


**Figure 7** – Carbon K-edge absorption spectrum fitted with four Gaussians

Carrying out this type of detailed analysis of the spectra in combination with HRTEM might provide additional insights on the radiation mechanisms occurring in PyC interphases. In addition to this, further in-situ experiments would enable a deeper understanding of the radiation-induced amorphisation of PyC. Putting a special emphasis on such activities, obtaining a week of beam-time at JANNuS is not unthinkable. Furthermore, the overall cost of such experiments is not outrageous, if access is obtained through an academic institution. Another option for in-situ TEM irradiation experiments is the forthcoming MIAMI II facility at the university of Huddersfield [176]. Currently in construction this installation will have irradiation capabilities like those of JANNuS, with the advantage of a new Hitachi H9500 TEM, equipped new high-end devices. Performing more of these experiments, one could address the questions of temperature, as well as dose, and/or dose rate effects, on the behaviour of PyC interphase under irradiation. Lastly, one could also put irradiate a reference sample made of HOPG, to determine a baseline to the  $sp^2$  to  $sp^3$  ratio.

### Improvements to the TC apparatus

The experimental method used in the present thesis proved to be difficult to implement, as well as time-consuming. An issue arising from the use of thermal radiation as the only heating mechanism is the significant systematic errors coming from the radiosity analysis. Indeed,

to determine the Gebhart matrix, one needs to calculate eighteen view factors. Although the relative errors on the nine dimensions required to calculate these functions can be limited, the degree to which they propagate through calculations leading to an equation yielding the heat flow rates is significant. In addition to this, good data for total emissivities are elusive quantities. Few applicable references can be found, and one should actually measure these for the whole temperature range to reduce uncertainties. An alternative design, which could be promising in both the aspects of simplicity as well as time consumption would be the construction of a gas loop. The sample would be set as a part of the piping system of the loop. One could then add a shroud outside of the sample. Its function would be to surround the sample, thereby acting as insulation along the length, as well as to keep the gas in the system. In terms of heat carrier, helium would be the best choice, as it is one of the most conductive gases, is not too expensive and is inert, meaning that oxidation issues would also be avoided. The apparatus would work as a heat loop, where helium is heated up to a given temperature by a heater or a heat exchanger system. By measuring the temperature at both the inlet and outlet of the sample length, the amount of heat lost along the sample length could be determined, thus giving a starting point for the determination of the radial heat flow. Such an apparatus would need a collaboration with thermohydraulics experts, so that a heat transfer model for the sample walls could be determined. With such a system, thermocouples could be held in position with a mechanical system such as expansion rings, allowing the use of more thermocouples for better statistics, as well as avoiding the use of high temperature adhesives. Since the experimental zone would be the length of the sample only, radiant heat transfer would be a formality. Indeed, the sample would only "see" itself and the outer shroud, which could be made of graphite, and be as flush with the sample as possible. In this case, the radiosity analysis would be simple, with only two decoupled pairs of surfaces, which view factors would be equal to one. Additionally, with such a system, the temperature of the sample could be measured at several axial and circumferential positions, hence providing a better accuracy as well as better statistics.



# **Appendices**





# A Thickness maps

## A.1 GA1

### A.1.1 Unirradiated material

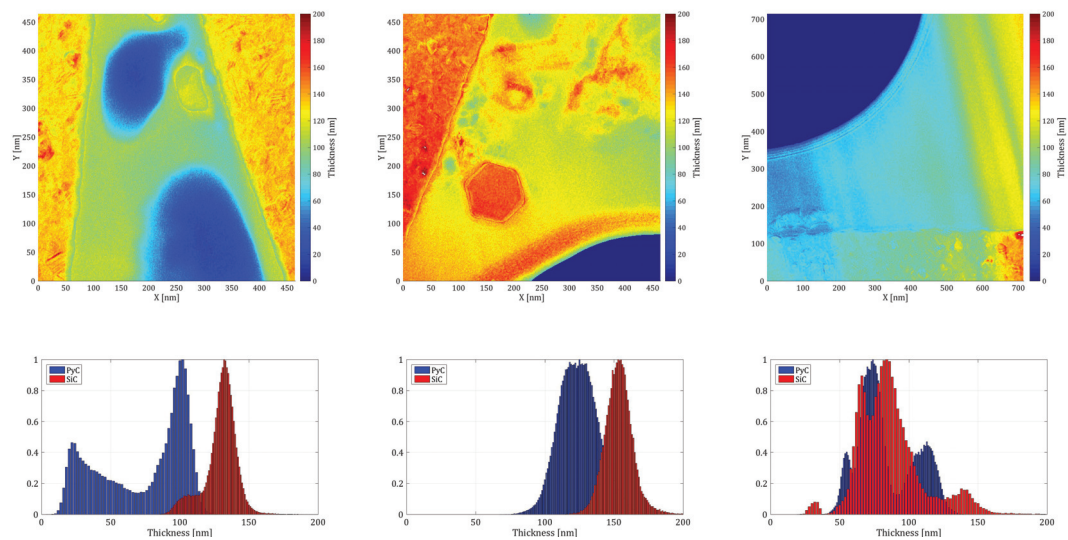


**Figure A.1** – Thickness maps and histograms of the unirradiated GA1 lamella

## Appendix A. Thickness maps

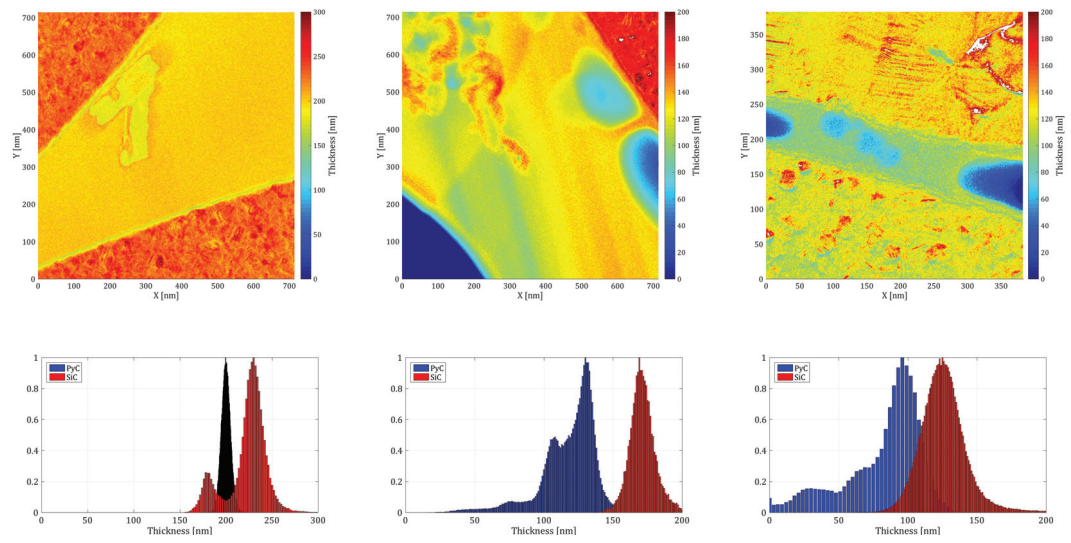


**Figure A.2** – Thickness maps and histograms of the unirradiated GA1 lamella

## A.1.2 Irradiated material

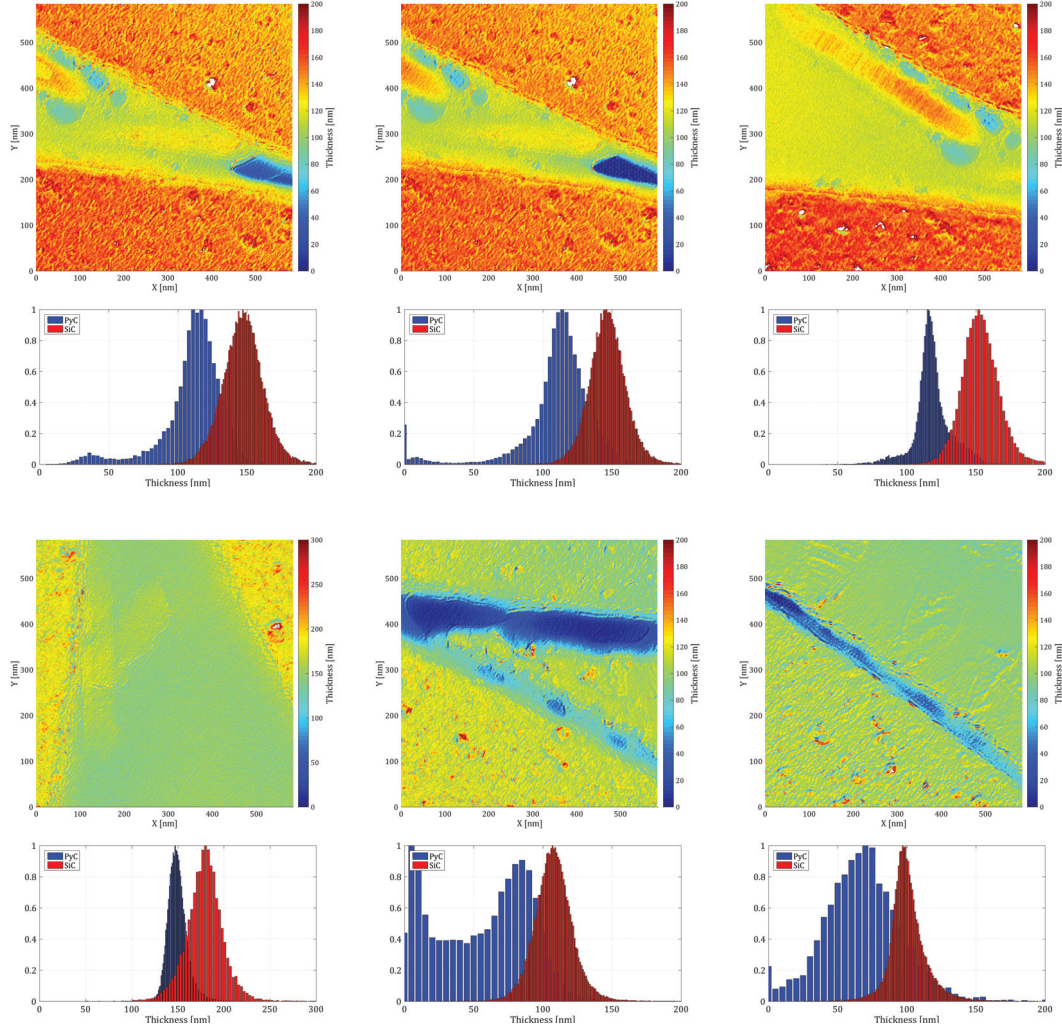


**Figure A.3** – Thickness maps and histograms of the ion irradiated GA1 lamella

## Appendix A. Thickness maps

### A.2 GA4

#### A.2.1 Unirradiated material

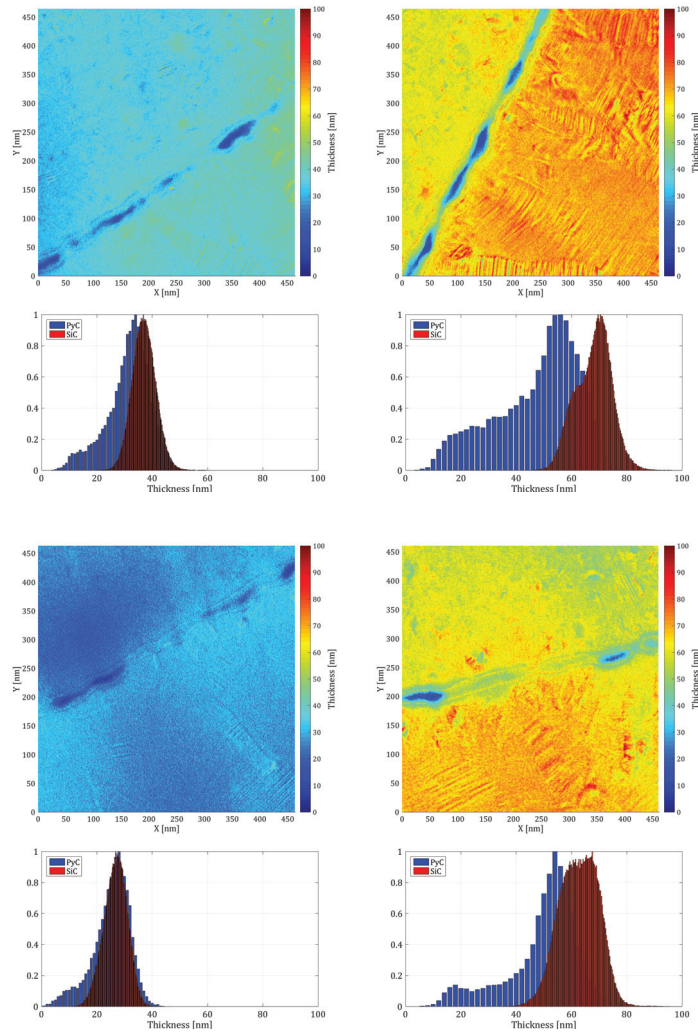


**Figure A.4** – Thickness maps and histograms of the unirradiated GA4 lamella

## A.2.2 Irradiated material

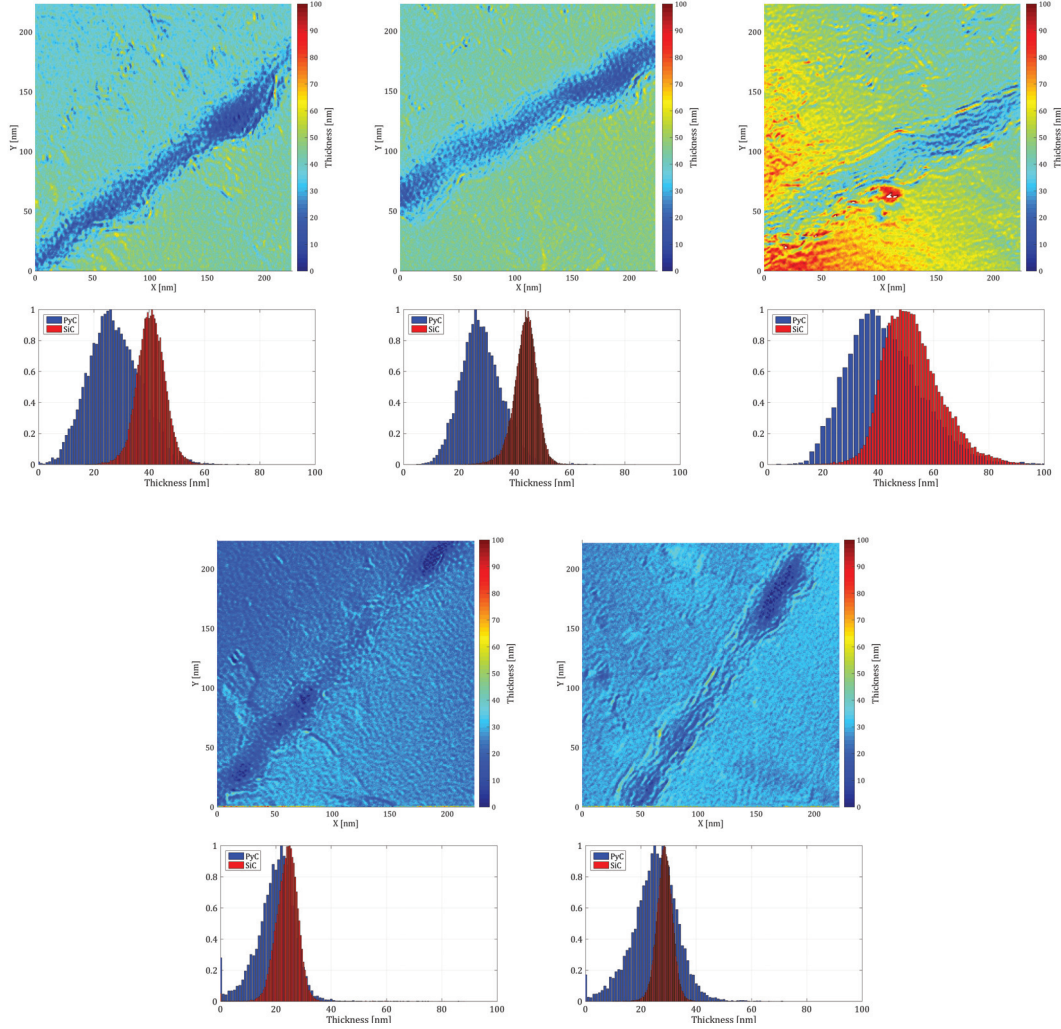
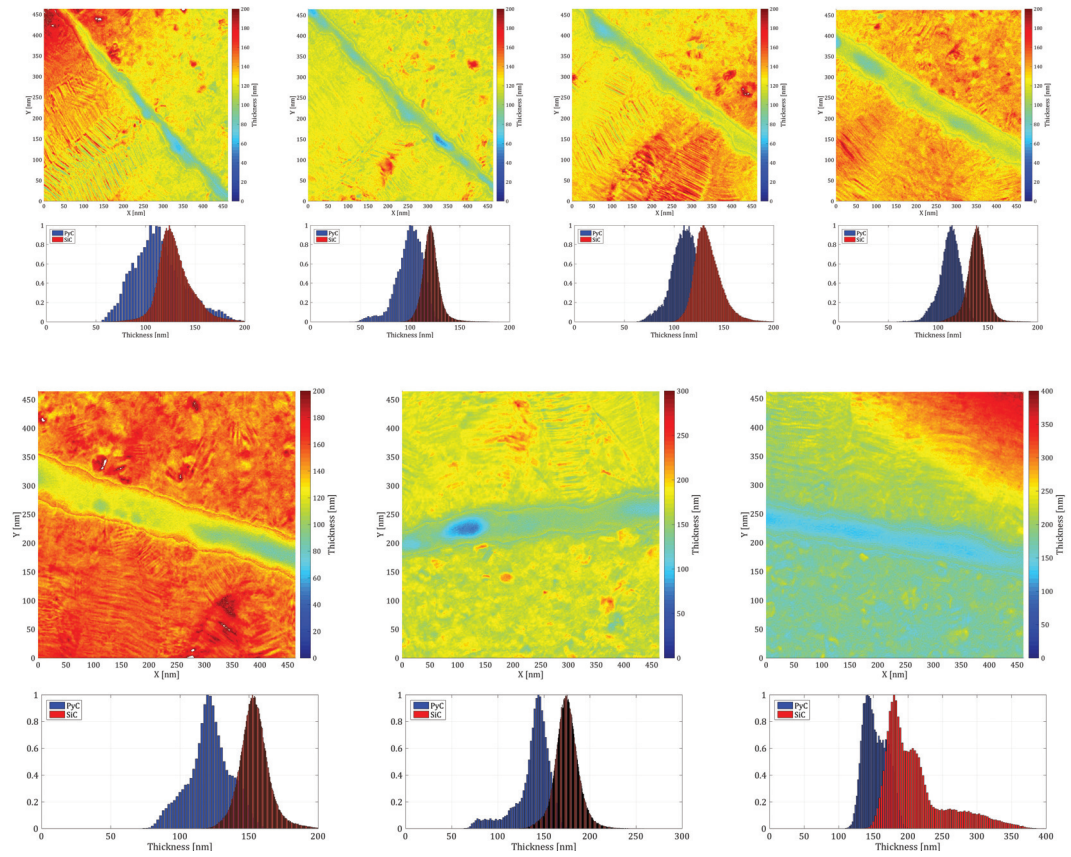


Figure A.5 – Thickness maps and histograms of the ion irradiated GA4 lamella



## A.3 GA6

### A.3.1 Unirradiated material



**Figure A.6** – Thickness maps and histograms of the unirradiated GA6 lamella

## A.3.2 Irradiated material

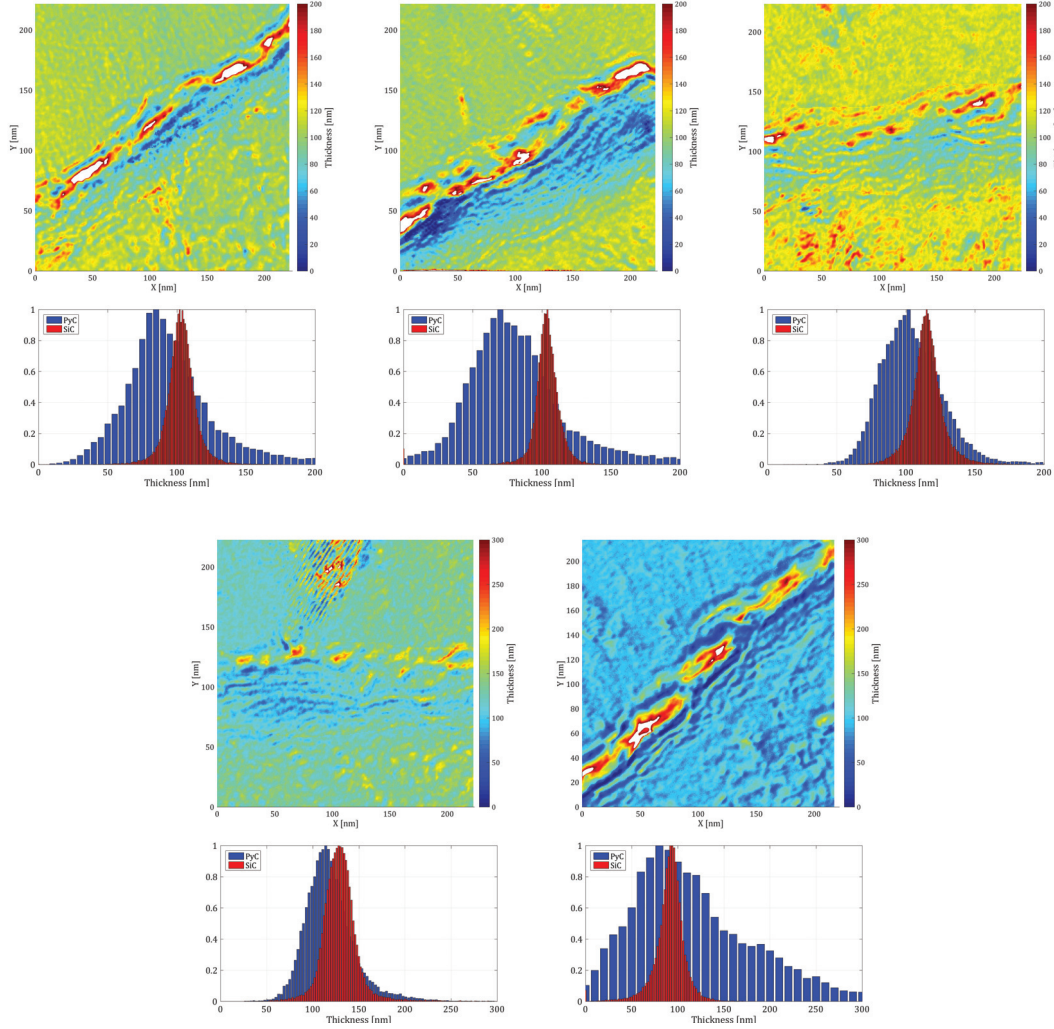
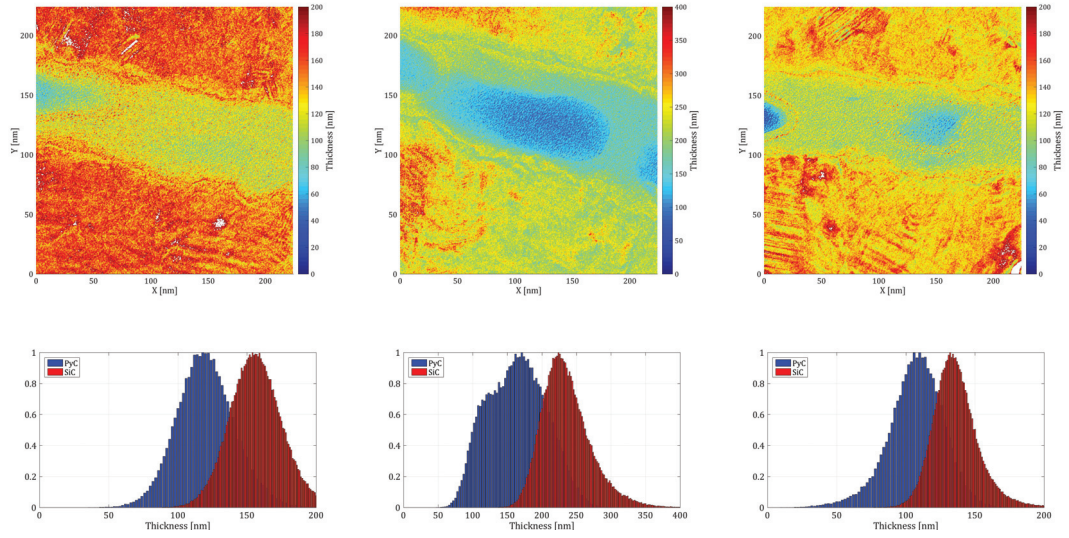


Figure A.7 – Thickness maps and histograms of the ion irradiated GA6 lamella

### A.4 GA7

#### A.4.1 Unirradiated material



**Figure A.8** – Thickness maps and histograms of the unirradiated GA7 lamella



## A.4.2 Irradiated material

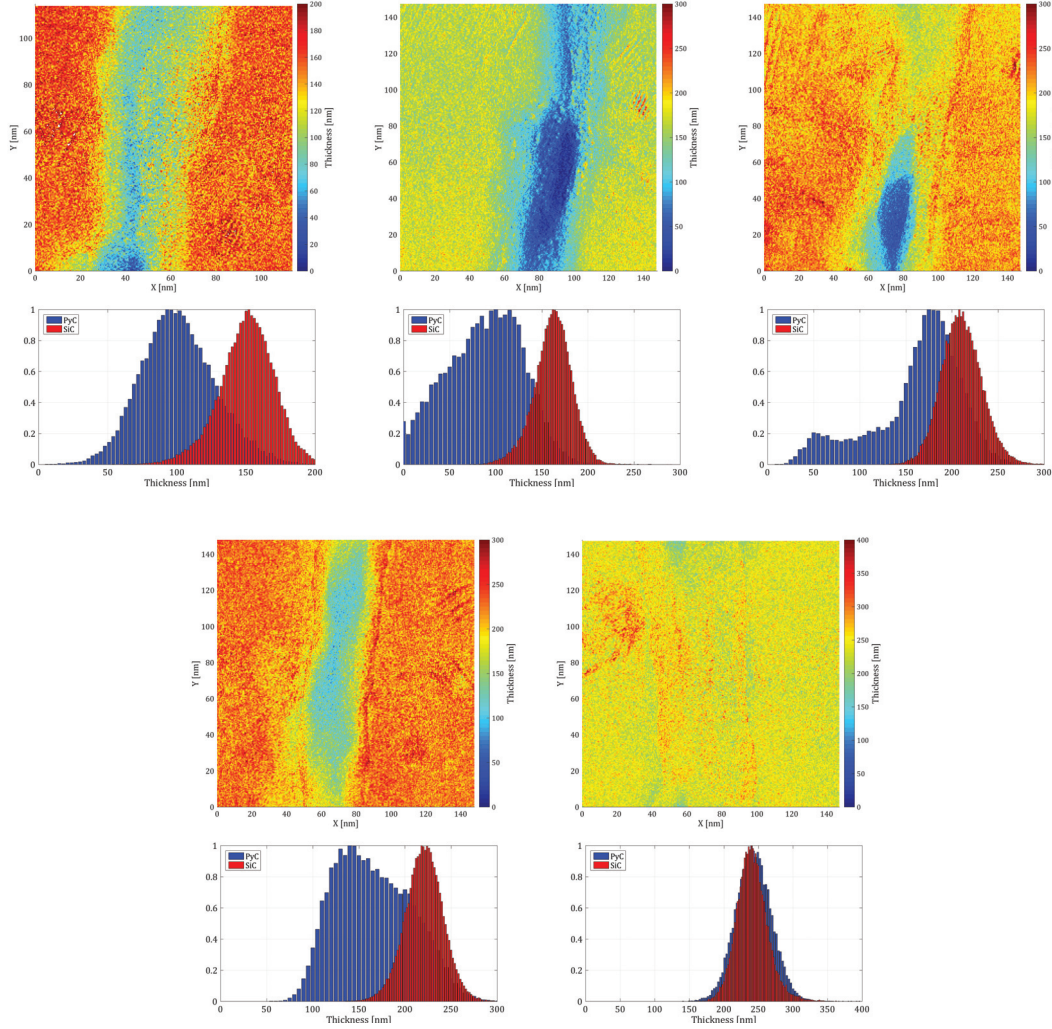
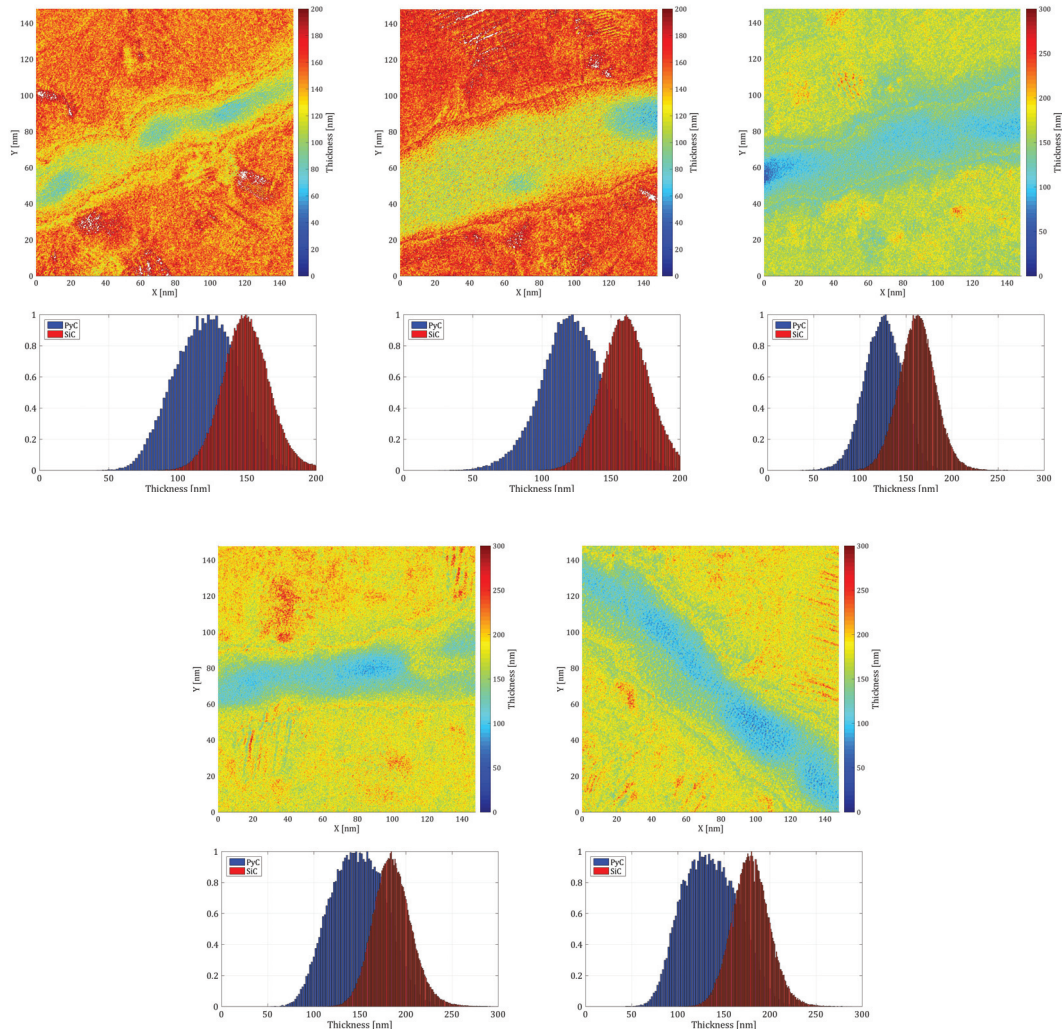


Figure A.9 – Thickness maps and histograms of the ion irradiated GA7 lamella

### A.5 GA9

#### A.5.1 Unirradiated material



**Figure A.10** – Thickness maps and histograms of the unirradiated GA9 lamella

## A.5.2 Irradiated material

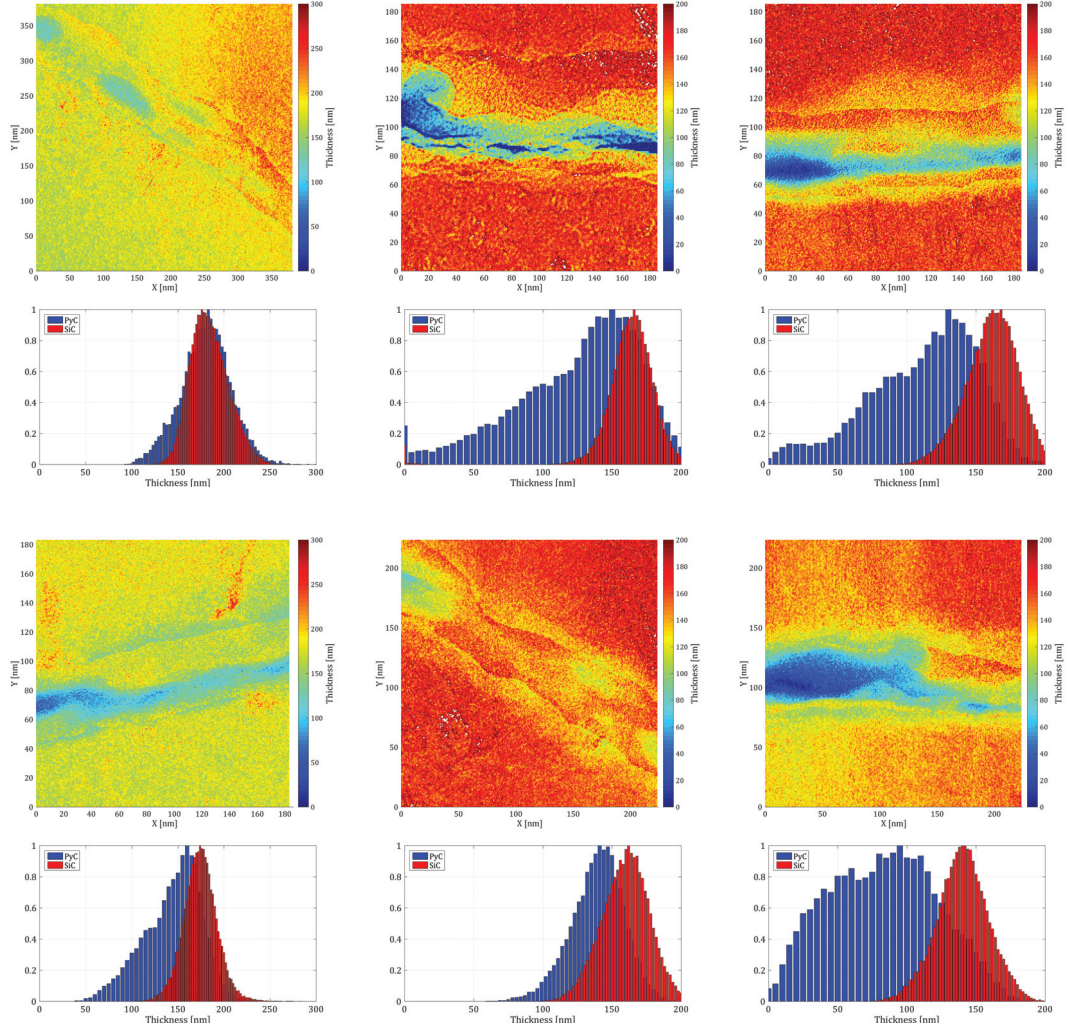
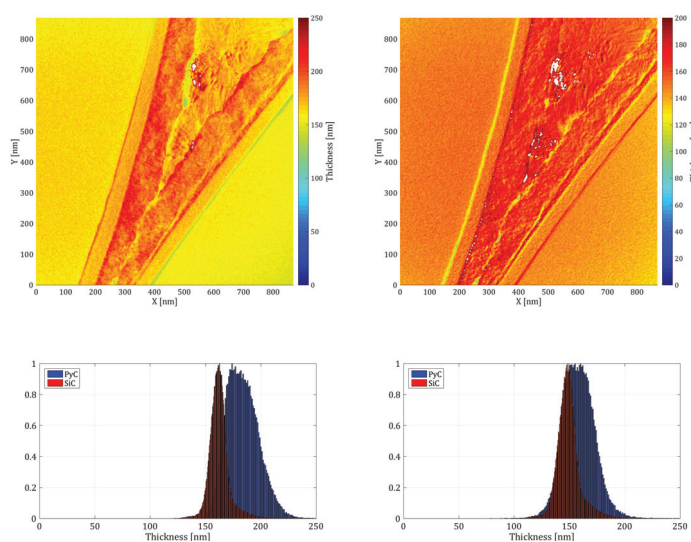


Figure A.11 – Thickness maps and histograms of the ion irradiated GA9 lamella

### A.6 A034

#### A.6.1 Unirradiated material



**Figure A.12** – Thickness maps and histograms of the unirradiated A034 lamella



## A.6.2 Irradiated material

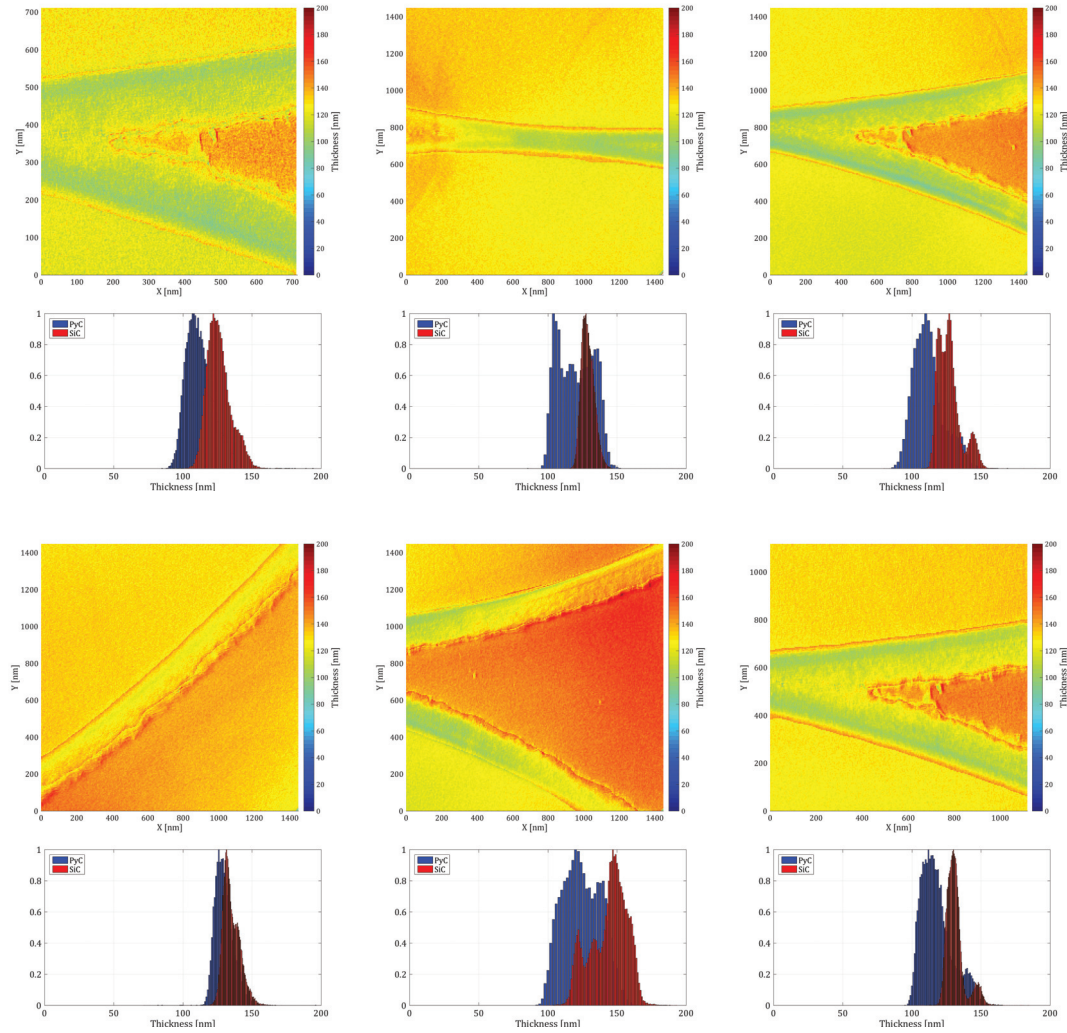


Figure A.13 – Thickness maps and histograms of the irradiated A034 lamella



## B EFTEM and STEM-EELS maps

### B.1 References

#### B.1.1 HOPG

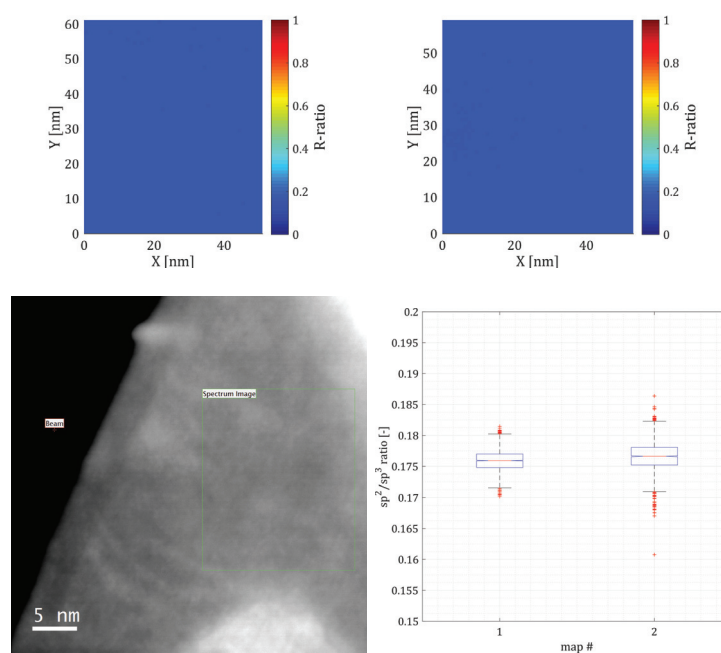


**Figure B.1** – ESI quantified maps of the HOPG reference with the corresponding boxplot and a HAADF overview

### B.1.2 Lacey carbon

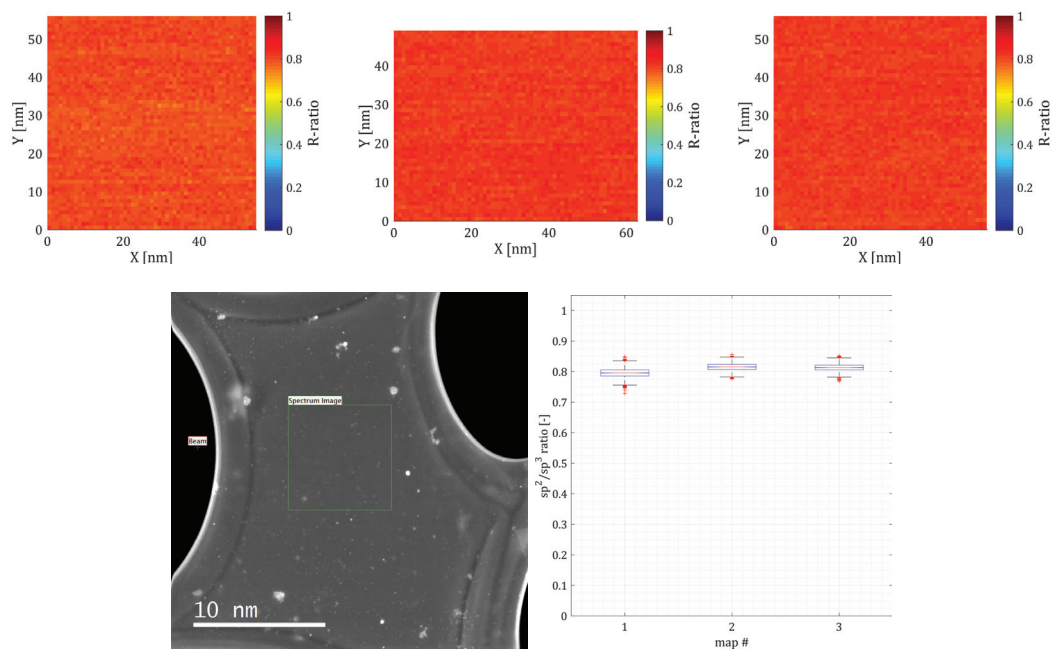


**Figure B.2** – ESI quantified maps of the Lacey carbon reference with the corresponding boxplot and a HAADF overview



## B.2 A034

### B.2.1 Unirradiated material

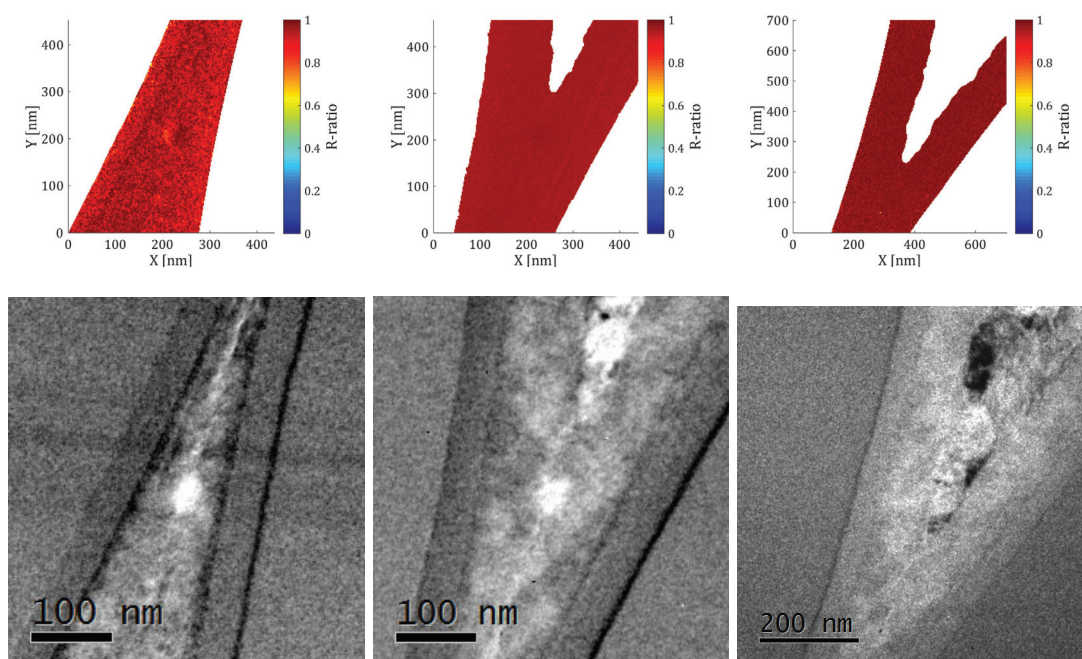


**Figure B.3** – EFTEM and ESI quantified maps of unirradiated A034 with their respective survey views

### B.2.2 Ion irradiated material

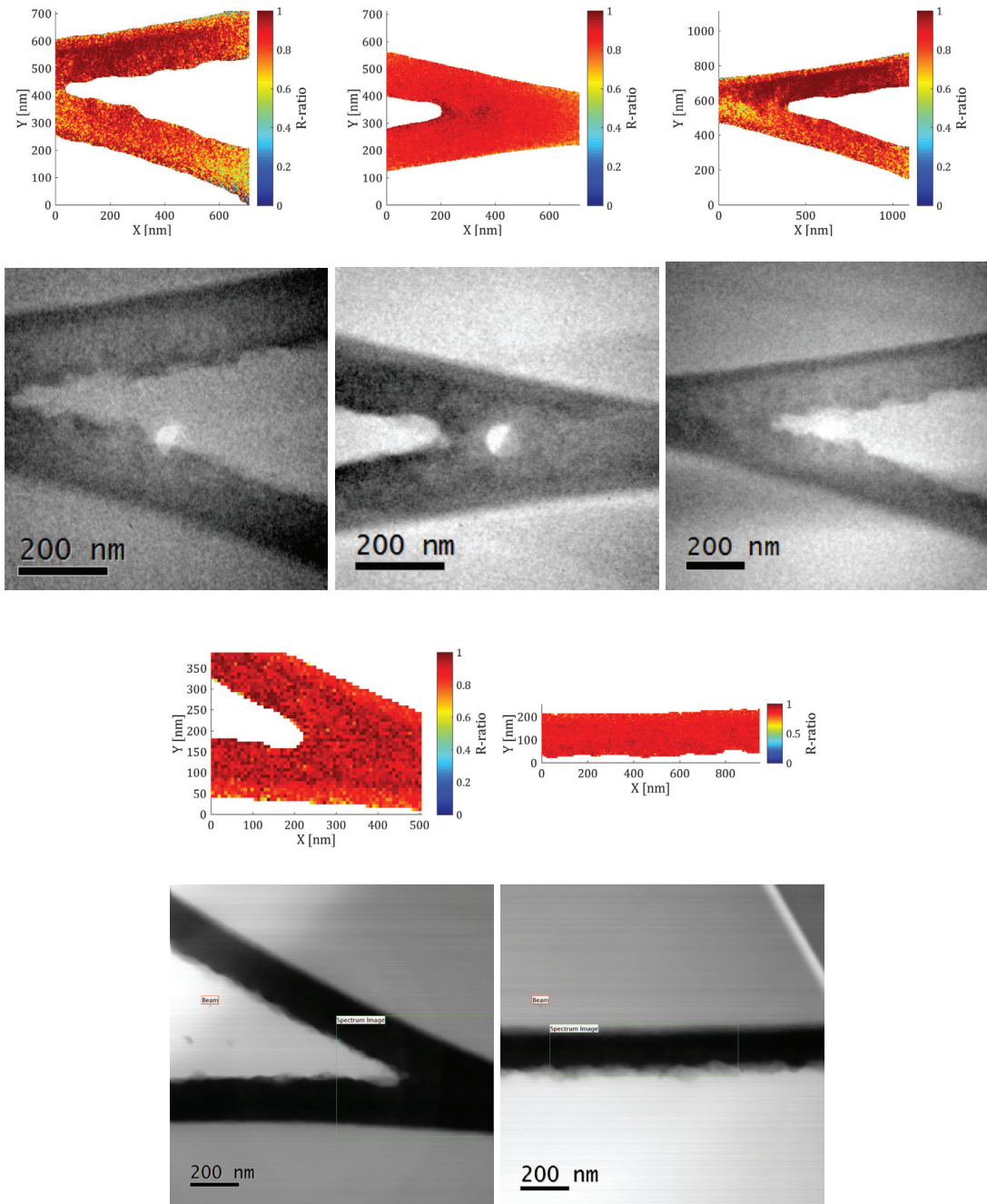


**Figure B.4** – EFTEM and ESI quantified maps of ion irradiated A034 with their respective survey views

### B.2.3 Neutron irradiated material

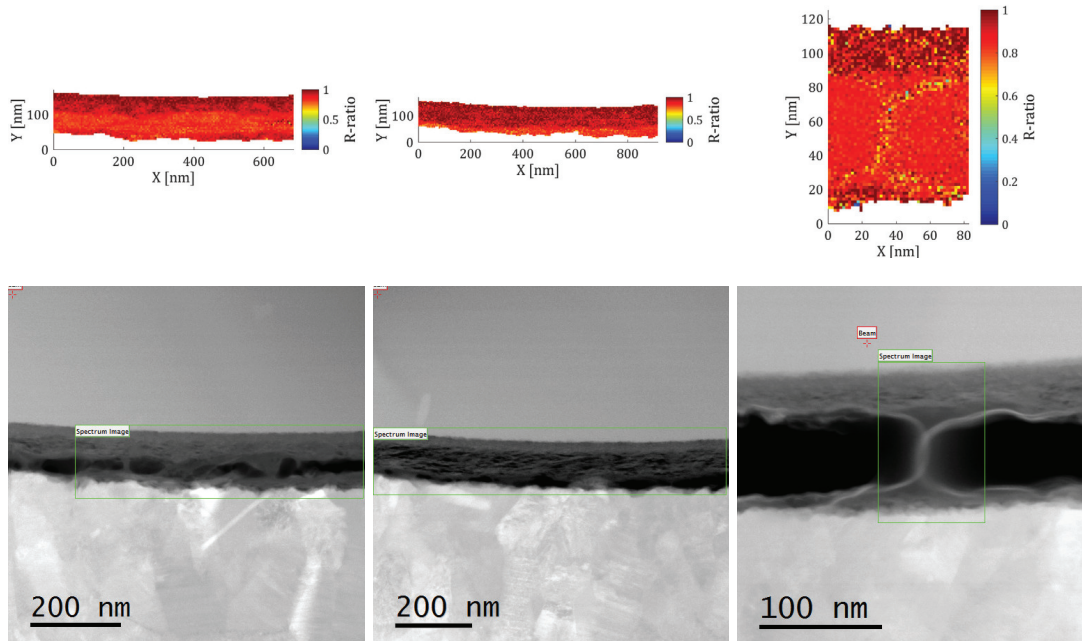


**Figure B.5** – EFTEM and ESI quantified maps of neutron irradiated A034 with their respective survey views





## B.3 GA

### B.3.1 Unirradiated material

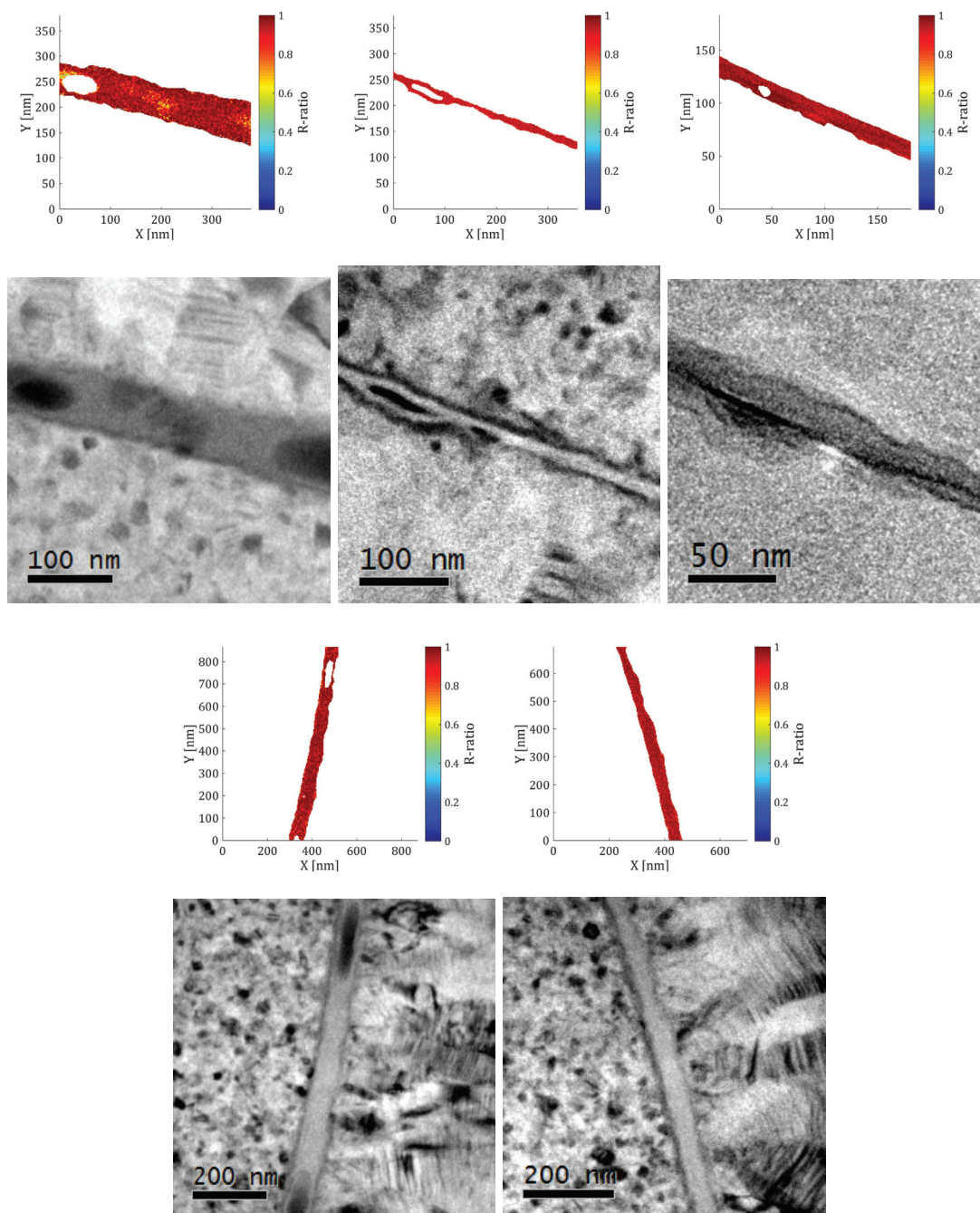


**Figure B.6** – EFTEM and ESI quantified maps of unirradiated GA lamellae with their respective survey views

### B.3.2 Ion irradiated material

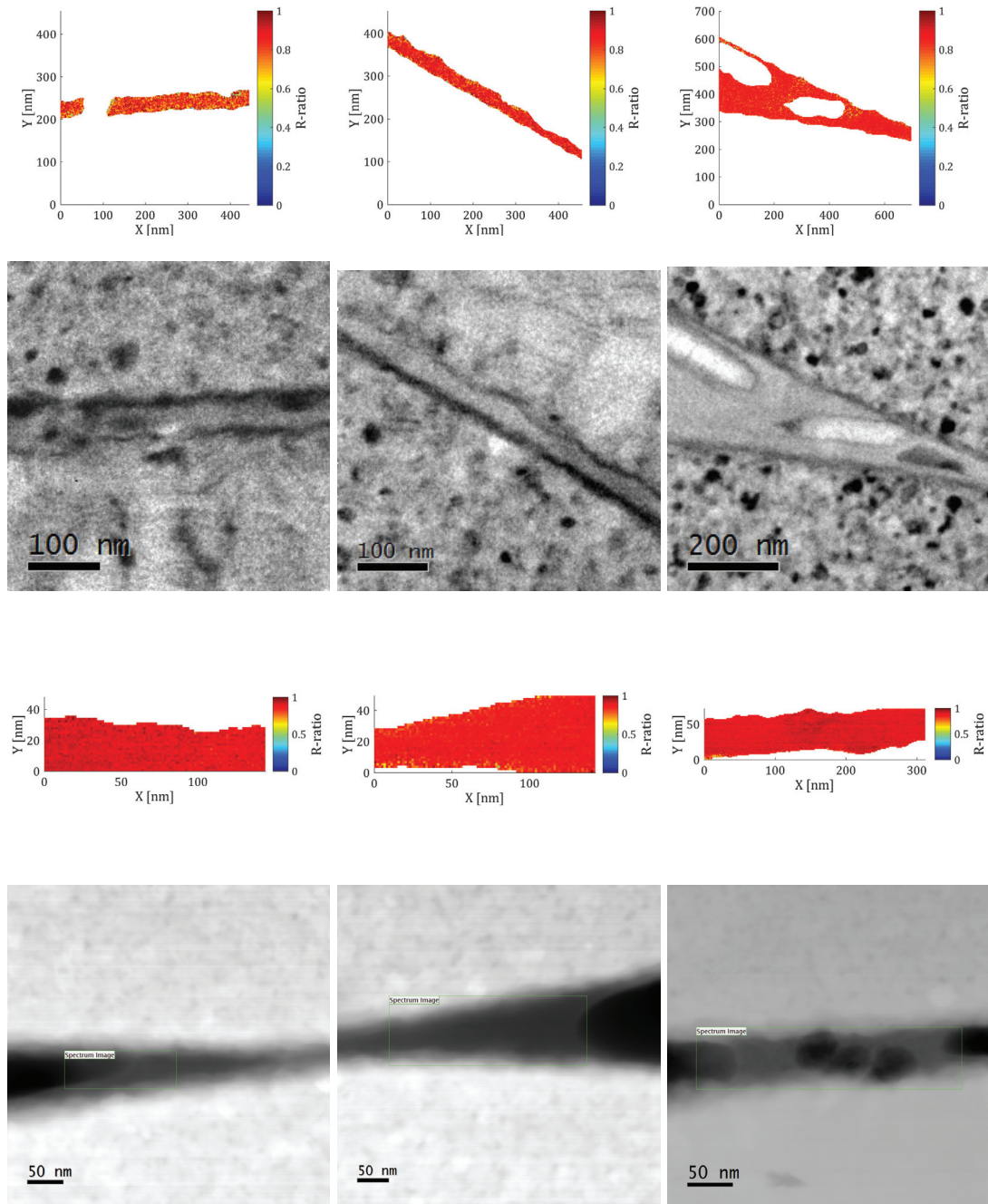


**Figure B.7** – EFTEM quantified maps of ion irradiated GA lamellae with their respective survey views

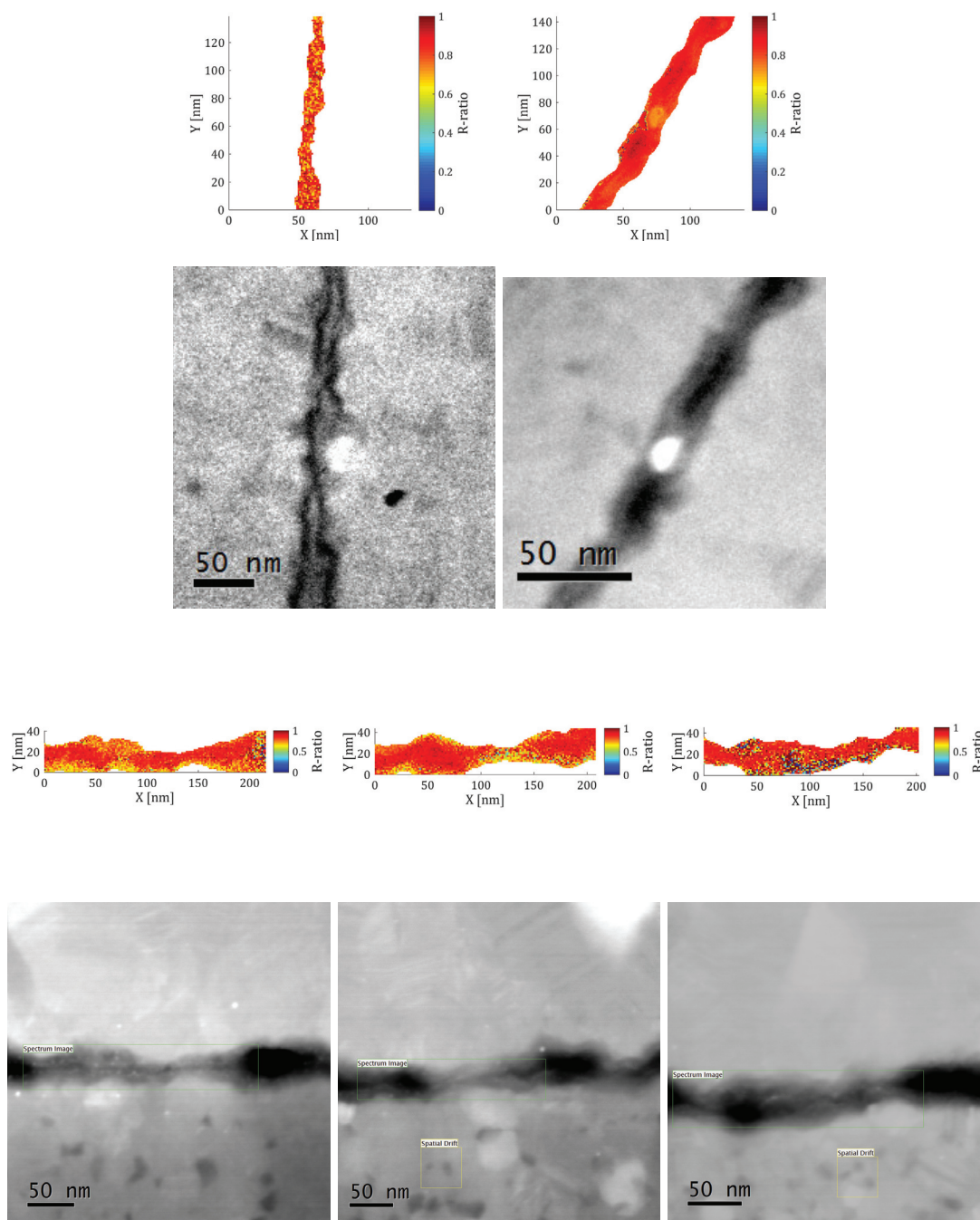


**Figure B.8** – EFTEM and ESI quantified maps of ion irradiated GA lamellae with their respective survey views



## Appendix B. EFTEM and STEM-EELS maps

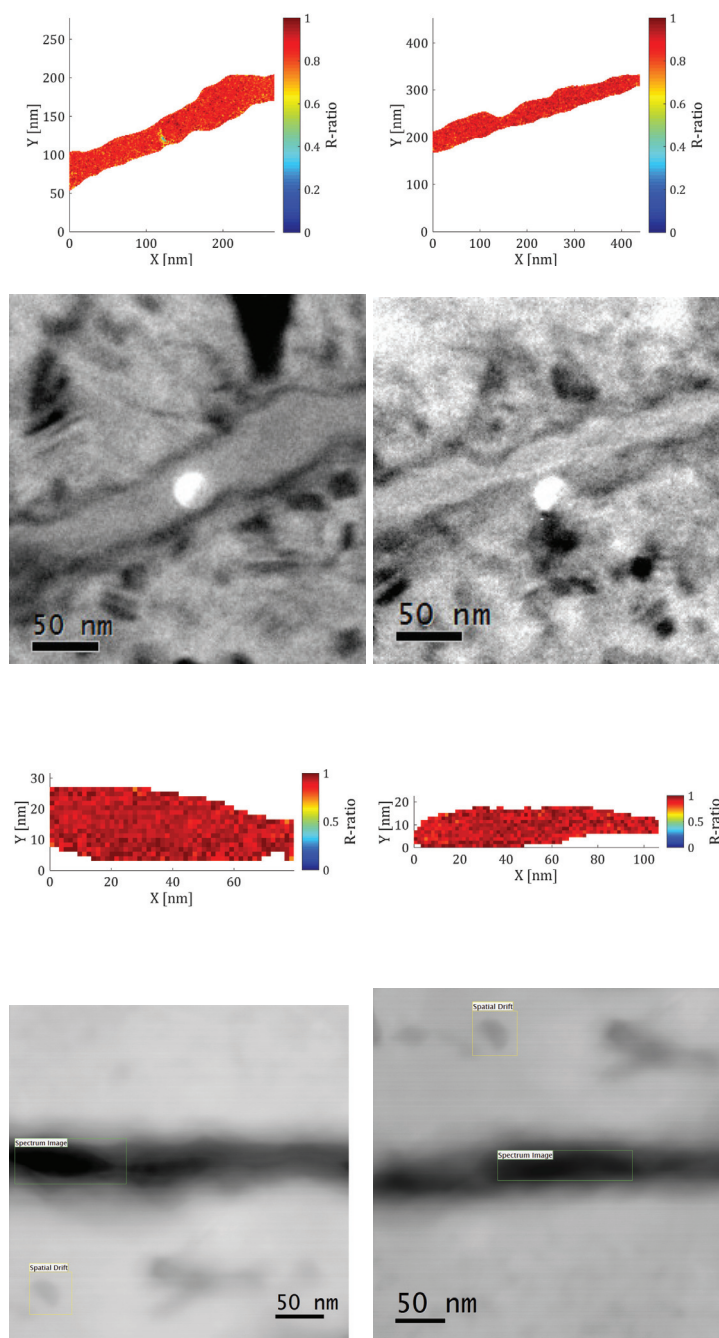


**Figure B.9** – EFTEM and ESI quantified maps of neutron irradiated A034 with their respective survey views



## B.4 H1-4

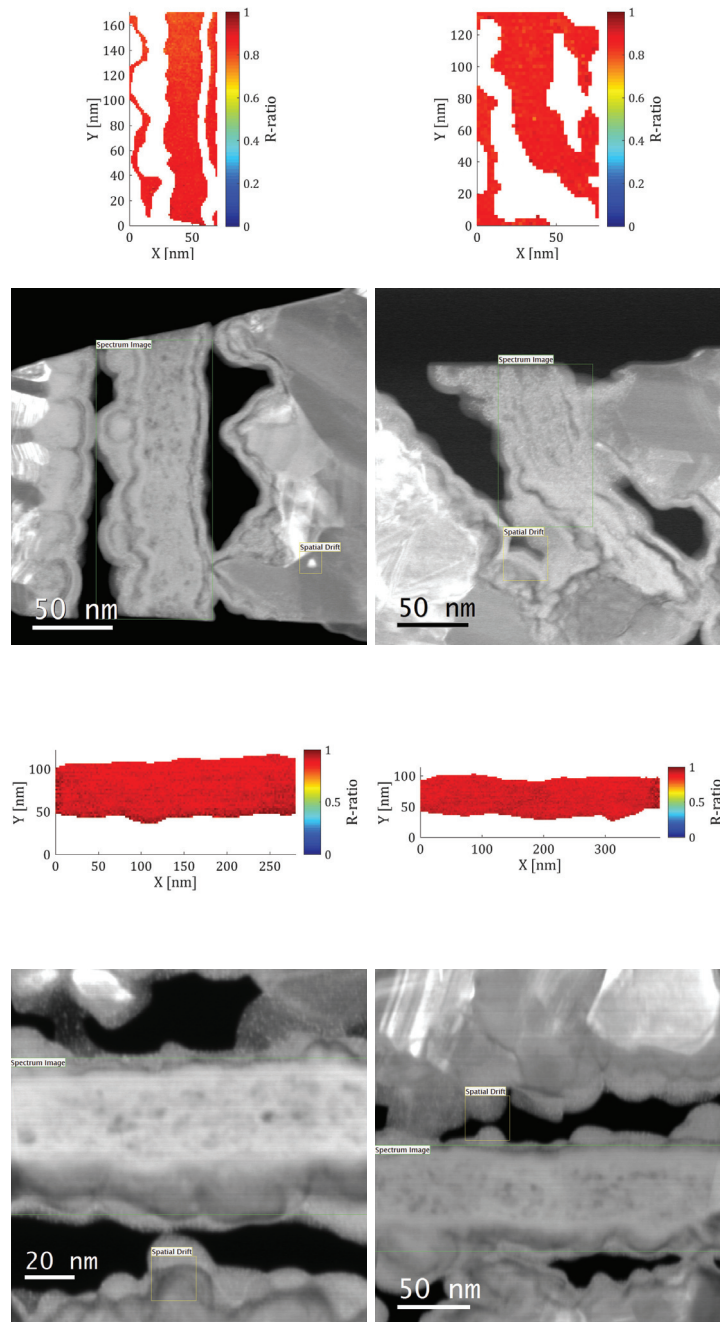


**Figure B.10** – EFTEM and ESI quantified maps of neutron irradiated H1-4 lamellae with their respective survey views



# Bibliography

- [1] IEA. *World Energy Outlook 2015*. World Energy Outlook. OECD Publishing, Nov. 10, 2015. ISBN: 978-92-64-24365-1 978-92-64-24366-8. URL: [http://www.oecd-ilibrary.org/energy/world-energy-outlook-2015\\_weo-2015-en](http://www.oecd-ilibrary.org/energy/world-energy-outlook-2015_weo-2015-en) (visited on 07/24/2016).
- [2] *Electricity*. URL: <http://www.iea.org/topics/electricity/> (visited on 07/24/2016).
- [3] *Fifth Assessment Report - Synthesis Report*. Synthesis Report IPCC, 2014. Intergovernmental Panel on Climate Change, 2014, p. 151. URL: <https://www.ipcc.ch/report/ar5/syr/> (visited on 07/24/2016).
- [4] Stefan Hirschberg et al. "Severe Accidents in the Energy Sector: Comparative Perspective". In: *Journal of Hazardous Materials* 111 (1-3 July 2004), pp. 57–65. ISSN: 03043894. DOI: 10.1016/j.jhazmat.2004.02.009. URL: <http://linkinghub.elsevier.com/retrieve/pii/S030438940400086X> (visited on 07/24/2016).
- [5] *GIF Portal - Home - Public*. URL: [https://www.gen-4.org/gif/jcms/c\\_9260/public](https://www.gen-4.org/gif/jcms/c_9260/public) (visited on 04/03/2014).
- [6] *GIF Portal - Very-High-Temperature Reactor (VHTR)*. URL: [https://www.gen-4.org/gif/jcms/c\\_42153/very-high-temperature-reactor-vhtr](https://www.gen-4.org/gif/jcms/c_42153/very-high-temperature-reactor-vhtr) (visited on 06/12/2016).
- [7] *GIF Portal - Gas-Cooled Fast Reactor (GFR)*. URL: [https://www.gen-4.org/gif/jcms/c\\_42148/gas-cooled-fast-reactor-gfr](https://www.gen-4.org/gif/jcms/c_42148/gas-cooled-fast-reactor-gfr) (visited on 06/12/2016).
- [8] NRC. *NRC: 10 CFR 50.46 Acceptance Criteria for Emergency Core Cooling Systems for Light-Water Nuclear Power Reactors*. URL: <http://www.nrc.gov/reading-rm/doc-collections/cfr/part050/part050-0046.html> (visited on 08/12/2016).
- [9] Jean Baptiste Joseph Fourier. *Théorie analytique de la chaleur*. In collab. with New York Public Library. Chez Firmin Didot, père et fils ..., 1822. 638 pp. URL: <http://archive.org/details/thorieanalytiqu00fourgoog> (visited on 04/07/2016).

## Bibliography

---

- [10] Lance L. Snead et al. “Handbook of SiC Properties for Fuel Performance Modeling”. In: *Journal of Nuclear Materials*. Nuclear Fuels and Structural Materials I Proceedings of the First Symposium on Nuclear Fuels and Structural Materials for Next Generation Nuclear Reactors 371 (1–3 Sept. 15, 2007), pp. 329–377. ISSN: 0022-3115. DOI: 10.1016/j.jnucmat.2007.05.016. URL: <http://www.sciencedirect.com/science/article/pii/S0022311507007623> (visited on 04/20/2016).
- [11] L.L. Snead, Y. Katoh, and T. Nozawa. “Radiation Effects in SiC and SiC–SiC”. In: *Comprehensive Nuclear Materials*. Elsevier, 2012, pp. 215–240. ISBN: 978-0-08-056033-5. URL: <http://linkinghub.elsevier.com/retrieve/pii/B9780080560335000938> (visited on 05/28/2016).
- [12] *Dulong–Petit Law*. In: *Wikipedia, the Free Encyclopedia*. Page Version ID: 696680987. Dec. 24, 2015. URL: [https://en.wikipedia.org/w/index.php?title=Dulong%E2%80%93Petit\\_law&oldid=696680987](https://en.wikipedia.org/w/index.php?title=Dulong%E2%80%93Petit_law&oldid=696680987) (visited on 05/28/2016).
- [13] *Heat Capacity*. In: *Wikipedia, the Free Encyclopedia*. Page Version ID: 721512622. May 22, 2016. URL: [https://en.wikipedia.org/w/index.php?title=Heat\\_capacity&oldid=721512622](https://en.wikipedia.org/w/index.php?title=Heat_capacity&oldid=721512622) (visited on 05/28/2016).
- [14] *Debye Model*. In: *Wikipedia, the Free Encyclopedia*. Page Version ID: 721514794. May 22, 2016. URL: [https://en.wikipedia.org/w/index.php?title=Debye\\_model&oldid=721514794](https://en.wikipedia.org/w/index.php?title=Debye_model&oldid=721514794) (visited on 05/28/2016).
- [15] Charles Kittel. *Wiley: Introduction to Solid State Physics, 8th Edition - Charles Kittel*. 8th. Wiley, 2004. URL: <http://eu.wiley.com/WileyCDA/WileyTitle/productCd-EHEP000803.html> (visited on 04/24/2016).
- [16] *Phonon Scattering*. In: *Wikipedia, the Free Encyclopedia*. Page Version ID: 698623183. Jan. 7, 2016. URL: [https://en.wikipedia.org/w/index.php?title=Phonon\\_scattering&oldid=698623183](https://en.wikipedia.org/w/index.php?title=Phonon_scattering&oldid=698623183) (visited on 05/28/2016).
- [17] L. L. Snead, S. J. Zinkle, and D. P. White. “Thermal Conductivity Degradation of Ceramic Materials due to Low Temperature, Low Dose Neutron Irradiation”. In: *Journal of Nuclear Materials* 340 (2–3 Apr. 15, 2005), pp. 187–202. ISSN: 0022-3115. DOI: 10.1016/j.jnucmat.2004.11.009. URL: <http://www.sciencedirect.com/science/article/pii/S0022311504010001> (visited on 04/03/2014).
- [18] P. G. Klemens. “Phonon Scattering and Thermal Resistance due to Grain Boundaries”. In: *International Journal of Thermophysics* 15.6 (Nov. 1994), pp. 1345–1351. ISSN: 0195-928X, 1572-9567. DOI: 10.1007/BF01458842. URL: <http://link.springer.com/10.1007/BF01458842> (visited on 05/28/2016).

- 
- [19] C. T. Walker and R. O. Pohl. "Phonon Scattering by Point Defects". In: *Physical Review* 131.4 (Aug. 15, 1963), pp. 1433–1442. ISSN: 0031-899X. DOI: 10.1103/PhysRev.131.1433. URL: <http://link.aps.org/doi/10.1103/PhysRev.131.1433> (visited on 05/28/2016).
- [20] Ja Sprague and David Kramer, eds. *Effects of Radiation on Structural Materials*. 100 Barr Harbor Drive, PO Box C700, West Conshohocken, PA 19428-2959: ASTM International, Jan. 1, 1979. ISBN: 978-0-8031-0327-6. URL: <http://www.astm.org/doiLink.cgi?STP683-EB> (visited on 05/29/2016).
- [21] ASTM. *Standard Practice for Neutron Radiation Damage Simulation by Charged-Particle Irradiation*. URL: <http://compass.astm.org/download/E521.21210.pdf> (visited on 04/23/2016).
- [22] Gary S. Was. *Fundamentals of Radiation Materials Science*. Berlin, Heidelberg: Springer Berlin Heidelberg, 2007. ISBN: 978-3-540-49471-3. URL: <http://link.springer.com/10.1007/978-3-540-49472-0> (visited on 07/10/2016).
- [23] Peter Sigmund, ed. *Stopping of Heavy Ions*. Vol. 204. Springer Tracts in Modern Physics. Berlin, Heidelberg: Springer Berlin Heidelberg, 2004. ISBN: 978-3-540-22273-6 978-3-540-44471-8. URL: <http://link.springer.com/10.1007/b98483> (visited on 07/10/2016).
- [24] James Ziegler. *SRIM - The Stopping and Range of Ions in Matter*. May 2, 2015. 398 pp.
- [25] Michael Nastasi and James W. Mayer. *Ion Implantation and Synthesis of Materials*. Berlin, Heidelberg: Springer Berlin Heidelberg, 2006. ISBN: 978-3-540-23674-0 978-3-540-45298-0. URL: <http://link.springer.com/10.1007/978-3-540-45298-0> (visited on 07/10/2016).
- [26] James F. Ziegler, M. D. Ziegler, and J. P. Biersack. "SRIM – The Stopping and Range of Ions in Matter (2010)". In: *Nuclear Instruments and Methods in Physics Research Section B: Beam Interactions with Materials and Atoms*. 19th International Conference on Ion Beam Analysis 268 (11–12 June 2010), pp. 1818–1823. ISSN: 0168-583X. DOI: 10.1016/j.nimb.2010.02.091. URL: <http://www.sciencedirect.com/science/article/pii/S0168583X10001862> (visited on 04/24/2016).
- [27] B. Cox. "Pellet-Clad Interaction (PCI) Failures of Zirconium Alloy Fuel Cladding — A Review". In: *Journal of Nuclear Materials* 172.3 (Aug. 1990), pp. 249–292. ISSN: 00223115. DOI: 10.1016/0022-3115(90)90282-R. URL: <http://linkinghub.elsevier.com/retrieve/pii/002231159090282R> (visited on 06/12/2016).
- [28] Ron Adamson et al. *IZNA-6 Special Topic Report: Pellet-Cladding Interaction (PIC and PCMI)*. Ron Adamson, Oct. 2006.

## Bibliography

---

- [29] *Silicon Carbide*. In: *Wikipedia, the Free Encyclopedia*. Page Version ID: 715410504. Apr. 15, 2016. URL: [https://en.wikipedia.org/w/index.php?title=Silicon\\_carbide&oldid=715410504](https://en.wikipedia.org/w/index.php?title=Silicon_carbide&oldid=715410504) (visited on 04/17/2016).
- [30] J. Lamon. "2.12 - Properties and Characteristics of SiC and SiC/SiC Composites". In: *Comprehensive Nuclear Materials*. Ed. by Rudy J.M. Konings. Oxford: Elsevier, 2012, pp. 323–338. ISBN: 978-0-08-056033-5. URL: <http://www.sciencedirect.com/science/article/pii/B9780080560335000227> (visited on 11/28/2012).
- [31] You Zhou et al. "Development of High-Thermal-Conductivity Silicon Nitride Ceramics". In: *Journal of Asian Ceramic Societies* 3.3 (Sept. 2015), pp. 221–229. ISSN: 21870764. DOI: 10.1016/j.jascr.2015.03.003. URL: <http://linkinghub.elsevier.com/retrieve/pii/S2187076415000214> (visited on 07/12/2016).
- [32] Yu Goldberg, M.E. Levinshtein, and S.L. Rumyantsev. "Silicon Carbide (SiC)". In: *Properties of Advanced Semiconductor Materials: GaN, AlN, InN, BN, SiC, SiGe*. Ed. by M.E. Levinshtein, S.L. Rumyantsev, and M.S. Shur. John Wiley & Sons, Inc. New York: Wiley, Jan. 2001, pp. 93–148. URL: <http://eu.wiley.com/WileyCDA/WileyTitle/productCd-0471358274.html> (visited on 07/10/2016).
- [33] James A. DiCarlo and Hee-Mann Yun. "Non-Oxide (Silicon Carbide) Fibers". In: *Handbook of Ceramic Composites*. Ed. by Narottam P. Bansal. Springer US, 2005, pp. 33–52. ISBN: 978-1-4020-8133-0 978-0-387-23986-6. DOI: 10.1007/0-387-23986-3\_2. URL: [http://link.springer.com/chapter/10.1007/0-387-23986-3\\_2](http://link.springer.com/chapter/10.1007/0-387-23986-3_2) (visited on 04/11/2016).
- [34] J J Carbajo. *Thermophysical Properties of MOX and UO2 Fuels Including the Effects of Irradiation*. ORNL/TM-2000/351, 777671. Jan. 11, 2001. URL: <http://www.osti.gov/servlets/purl/777671/> (visited on 07/12/2016).
- [35] J.T. White et al. "Thermophysical Properties of USi to 1673 K". In: *Journal of Nuclear Materials* 471 (Apr. 2016), pp. 129–135. ISSN: 00223115. DOI: 10.1016/j.jnucmat.2016.01.013. URL: <http://linkinghub.elsevier.com/retrieve/pii/S0022311516300125> (visited on 07/12/2016).
- [36] J.T. White et al. "Thermophysical Properties of U3Si to 1150K". In: *Journal of Nuclear Materials* 452 (1-3 Sept. 2014), pp. 304–310. ISSN: 00223115. DOI: 10.1016/j.jnucmat.2014.05.037. URL: <http://linkinghub.elsevier.com/retrieve/pii/S0022311514003043> (visited on 07/12/2016).

- [37] J.T. White et al. "Thermophysical Properties of U<sub>3</sub>Si<sub>2</sub> to 1773K". In: *Journal of Nuclear Materials* 464 (Sept. 2015), pp. 275–280. ISSN: 00223115. DOI: 10.1016/j.jnucmat.2015.04.031. URL: <http://linkinghub.elsevier.com/retrieve/pii/S002231151500241X> (visited on 07/12/2016).
- [38] J.T. White et al. "Thermophysical Properties of U<sub>3</sub>Si<sub>5</sub> to 1773K". In: *Journal of Nuclear Materials* 456 (Jan. 2015), pp. 442–448. ISSN: 00223115. DOI: 10.1016/j.jnucmat.2014.10.021. URL: <http://linkinghub.elsevier.com/retrieve/pii/S0022311514007053> (visited on 07/12/2016).
- [39] H.D. Lewis and J.F. Kerrisk. *Electrical and Thermal Transport Properties of Uranium and Plutonium Carbides*. LA-6096, 7276665. Sept. 1, 1976. URL: <http://www.osti.gov/servlets/purl/7276665-0Bok7n/> (visited on 07/12/2016).
- [40] Steven B. Ross, Mohamed S. El-Genk, and R.Bruce Matthews. "Thermal Conductivity Correlation for Uranium Nitride Fuel between 10 and 1923 K". In: *Journal of Nuclear Materials* 151.3 (Feb. 1988), pp. 318–326. ISSN: 00223115. DOI: 10.1016/0022-3115(88)90026-8. URL: <http://linkinghub.elsevier.com/retrieve/pii/0022311588900268> (visited on 07/12/2016).
- [41] Alexander A. Balandin. "Thermal Properties of Graphene and Nanostructured Carbon Materials". In: *Nature Materials* 10.8 (Aug. 2011), pp. 569–581. ISSN: 1476-1122. DOI: 10.1038/nmat3064. URL: <http://www.nature.com/nmat/journal/v10/n8/full/nmat3064.html> (visited on 03/31/2016).
- [42] *Online Materials Information Resource - MatWeb*. URL: <http://www.matweb.com/> (visited on 07/12/2016).
- [43] M. E. Sawan, Y. Katoh, and L. L. Snead. "Transmutation of Silicon Carbide in Fusion Nuclear Environment". In: *Journal of Nuclear Materials*. FIFTEENTH INTERNATIONAL CONFERENCE ON FUSION REACTOR MATERIALS 442 (1–3, Supplement 1 Nov. 2013), S370–S375. ISSN: 0022-3115. DOI: 10.1016/j.jnucmat.2012.11.018. URL: <http://www.sciencedirect.com/science/article/pii/S0022311512006046> (visited on 04/03/2014).
- [44] C.-H. Chen and W.J. Weber. "In-Situ TEM Characterization of Helium Bubble Evolution in Nano-Engineered SiC under Kr<sup>2+</sup> Irradiation". WOTWISI-4. GIF sur yvette, France, Mar. 17, 2016. URL: [http://wotwisi4.in2p3.fr/IMG/pdf/oralwotwisi-4\\_weber.pdf](http://wotwisi4.in2p3.fr/IMG/pdf/oralwotwisi-4_weber.pdf) (visited on 05/30/2016).



## Bibliography

---

- [45] Yutai Katoh et al. "Continuous SiC Fiber, CVI SiC Matrix Composites for Nuclear Applications: Properties and Irradiation Effects". In: *Journal of Nuclear Materials* 448 (1–3 May 2014), pp. 448–476. ISSN: 0022-3115. DOI: 10.1016/j.jnucmat.2013.06.040. URL: <http://www.sciencedirect.com/science/article/pii/S0022311513008647> (visited on 04/24/2016).
- [46] Konstantinos G. Dassios and Costas Galiotis. "Direct Measurement of Fiber Bridging in Notched Glass-Ceramic-Matrix Composites". In: *Journal of Materials Research* 21 (05 May 2006), pp. 1150–1160. ISSN: 2044-5326. DOI: 10.1557/jmr.2006.0132. URL: [http://journals.cambridge.org/article\\_S0884291400082649](http://journals.cambridge.org/article_S0884291400082649) (visited on 04/06/2016).
- [47] Akira Kohyama. "CMC for Nuclear Applications". In: *Ceramic Matrix Composites*. Ed. by -Ing Walter Krenkel. Wiley-VCH Verlag GmbH & Co. KGaA, 2008, pp. 353–384. ISBN: 978-3-527-62241-2. URL: <http://onlinelibrary.wiley.com/doi/10.1002/9783527622412.ch15/summary> (visited on 04/03/2014).
- [48] IAEA. *Thermophysical Properties Database of Materials for Light Water Reactors and Heavy Water Reactors*. TECDOC 1496. 2006. URL: <http://www-pub.iaea.org/books/IAEABooks/7489/Thermophysical-Properties-Database-of-Materials-for-Light-Water-Reactors-and-Heavy-Water-Reactors> (visited on 07/18/2016).
- [49] IAEA. *Applicability of the Leak Before Break Concept (Report of the IAEA Extrabudgetary Programme on the Safety of WWER-440 Model 230 Nuclear Power Plants) Status Report on a Generic Safety Issue*. TECDOC 710. International Atomic Energy Agency, 1993. URL: <http://www-pub.iaea.org/books/IAEABooks/972/Applicability-of-the-Leak-Before-Break-Concept-Report-of-the-IAEA-Extrabudgetary-Programme-on-the-Safety-of-WWER-440-Model-230-Nuclear-Power-Plants-Status-Report-on-a-Generic-Safety-Issue> (visited on 07/18/2016).
- [50] Granta Design. "Granta CES Edupack 2009 - 2: Material and Process Selection Charts". Cambridge University, Jan. 2009. URL: [http://www.mie.uth.gr/ekp\\_yliko/2\\_materials-charts-2009.pdf](http://www.mie.uth.gr/ekp_yliko/2_materials-charts-2009.pdf).
- [51] F. R. N. Nabarro. In: *Report of a Conference on Strength of Solids*. Bristol, UK: The Physical Society, London, 1947, pp. 75–90. URL: <https://www.jim.or.jp/journal/e/46/09/1951.html> (visited on 04/17/2016).
- [52] Conyers Herring. "Diffusional Viscosity of a Polycrystalline Solid". In: *Journal of Applied Physics* 21.5 (May 1, 1950), pp. 437–445. ISSN: 0021-8979, 1089-7550. DOI: 10.1063/1.1699681. URL: <http://scitation.aip.org/content/aip/journal/jap/21/5/10.1063/1.1699681> (visited on 04/17/2016).



- [53] R. L. Coble. "A Model for Boundary Diffusion Controlled Creep in Polycrystalline Materials". In: *Journal of Applied Physics* 34.6 (June 1, 1963), pp. 1679–1682. ISSN: 0021-8979, 1089-7550. DOI: 10.1063/1.1702656. URL: <http://scitation.aip.org/content/aip/journal/jap/34/6/10.1063/1.1702656> (visited on 04/17/2016).
- [54] S. Yajima et al. "Development of High Tensile Strength Silicon Carbide Fibre Using an Organosilicon Polymer Precursor". In: *Nature* 273.5663 (June 15, 1978), pp. 525–527. DOI: 10.1038/273525a0. URL: <http://www.nature.com/nature/journal/v273/n5663/abs/273525a0.html> (visited on 04/17/2016).
- [55] Shuang Zhao et al. "Fabrication and Characterization of 2.5D and 3D SiCf/SiC Composites". In: *Fusion Engineering and Design* 88 (9-10 Oct. 2013), pp. 2453–2456. ISSN: 09203796. DOI: 10.1016/j.fusengdes.2013.04.002. URL: <http://linkinghub.elsevier.com/retrieve/pii/S0920379613003827> (visited on 05/29/2016).
- [56] *Innovative SiC/SiC Composite for Nuclear Applications Innovative SiC/SiC Composite for Nuclear Applications - epjconf\_MINOS2012\_01003.pdf*. URL: [http://www.epj-conferences.org/articles/epjconf/pdf/2013/12/epjconf\\_MINOS2012\\_01003.pdf](http://www.epj-conferences.org/articles/epjconf/pdf/2013/12/epjconf_MINOS2012_01003.pdf) (visited on 05/22/2016).
- [57] Jacques Lamon. "Chemical Vapor Infiltrated SiC/SiC Composites (CVI SiC/SiC)". In: *Handbook of Ceramic Composites*. Ed. by Narottam P. Bansal. Springer US, 2005, pp. 55–76. ISBN: 978-1-4020-8133-0 978-0-387-23986-6. DOI: 10.1007/0-387-23986-3\_3. URL: [http://link.springer.com/chapter/10.1007/0-387-23986-3\\_3](http://link.springer.com/chapter/10.1007/0-387-23986-3_3) (visited on 05/22/2016).
- [58] Akira Kohyama, Shaoming Dong, and Yutai Katoh. "Development of SiC/SiC Composites by Nano-Infiltration and Transient Eutectoid (NITE) Process". In: *26th Annual Conference on Composites, Advanced Ceramics, Materials, and Structures: A: Ceramic Engineering and Science Proceedings*. Ed. by Hua-Tay Lin and Mrityunjay Singh. John Wiley & Sons, Inc., 2002, pp. 311–318. ISBN: 978-0-470-29474-1. URL: <http://onlinelibrary.wiley.com/doi/10.1002/9780470294741.ch36/summary> (visited on 05/24/2016).
- [59] Kazuya Shimoda et al. "Densification Mechanism and Microstructural Evolution of SiC Matrix in Nite Process". In: *Ceramics in Nuclear and Alternative Energy Applications: Ceramic Engineering and Science Proceedings, Volume 27, Issue 5*. John Wiley & Sons, Inc., Mar. 26, 2008, pp. 19–27. ISBN: 978-0-470-29134-4. URL: <http://onlinelibrary.wiley.com/doi/10.1002/9780470291344.ch3/summary> (visited on 04/28/2016).

## Bibliography

---

- [60] Y Katoh et al. "SiC/SiC Composites through Transient Eutectic-Phase Route for Fusion Applications". In: *Journal of Nuclear Materials*. Proceedings of the 11th International Conference on Fusion Reactor Materials (ICFRM-11) 329–333, Part A (Aug. 1, 2004), pp. 587–591. ISSN: 0022-3115. DOI: 10.1016/j.jnucmat.2004.04.157. URL: <http://www.sciencedirect.com/science/article/pii/S0022311504002703> (visited on 05/29/2016).
- [61] A. Kohyama et al. "SiC/SiC Composite for Fusion by NITE Process and Its Performance". In: *ResearchGate* (). URL: [https://www.researchgate.net/publication/228608920\\_SiCSiC\\_composite\\_for\\_fusion\\_by\\_NITE\\_process\\_and\\_its\\_performance](https://www.researchgate.net/publication/228608920_SiCSiC_composite_for_fusion_by_NITE_process_and_its_performance) (visited on 04/28/2016).
- [62] Sébastien Bertrand et al. "Hi-Nicalon/SiC Minicomposites with (Pyrocarbon/SiC)<sub>n</sub> Nanoscale Multilayered Interphases". In: *Journal of the American Ceramic Society* 82.9 (Sept. 1, 1999), pp. 2465–2473. ISSN: 1551-2916. DOI: 10.1111/j.1151-2916.1999.tb02105.x. URL: <http://onlinelibrary.wiley.com/doi/10.1111/j.1151-2916.1999.tb02105.x/abstract> (visited on 04/03/2014).
- [63] S. Bertrand et al. "TEM Structure of (PyC/SiC)<sub>n</sub> Multilayered Interphases in SiC/SiC Composites". In: *Journal of the European Ceramic Society* 20.1 (Jan. 2000), pp. 1–13. ISSN: 0955-2219. DOI: 10.1016/S0955-2219(99)00086-2. URL: <http://www.sciencedirect.com/science/article/pii/S0955221999000862> (visited on 04/03/2014).
- [64] T Taguchi et al. "Fabrication of Advanced SiC Fiber/F-CVI SiC Matrix Composites with SiC/C Multi-Layer Interphase". In: *Journal of Nuclear Materials* 329–333, Part A (Aug. 1, 2004), pp. 572–576. ISSN: 0022-3115. DOI: 10.1016/j.jnucmat.2004.04.120. URL: <http://www.sciencedirect.com/science/article/pii/S0022311504002673> (visited on 11/28/2012).
- [65] Haijiao Yu et al. "Properties of Carbon Nano-tubes–Cf/SiC Composite by Precursor Infiltration and Pyrolysis Process". In: *Materials & Design* 32.6 (June 2011), pp. 3516–3520. ISSN: 02613069. DOI: 10.1016/j.matdes.2011.02.038. URL: <http://linkinghub.elsevier.com/retrieve/pii/S0261306911001166> (visited on 05/29/2016).
- [66] T. Taguchi, Y. Hasegawa, and S. Shamoto. "Effect of Carbon Nanofiber Dispersion on the Properties of PIP-SiC/SiC Composites". In: *Journal of Nuclear Materials*. Proceedings of ICFRM-14 417 (1–3 Oct. 1, 2011), pp. 348–352. ISSN: 0022-3115. DOI: 10.1016/j.jnucmat.2010.12.078. URL: <http://www.sciencedirect.com/science/article/pii/S0022311510009001> (visited on 05/29/2016).

- [67] Agnès Oberlin. "Pyrocarbons". In: *Carbon* 40.1 (Jan. 2002), pp. 7–24. ISSN: 0008-6223. DOI: 10.1016/S0008-6223(01)00138-5. URL: <http://www.sciencedirect.com/science/article/pii/S0008622301001385> (visited on 05/19/2016).
- [68] *Pebble-Bed Reactor*. In: *Wikipedia, the Free Encyclopedia*. Page Version ID: 720057694. May 13, 2016. URL: [https://en.wikipedia.org/w/index.php?title=Pebble-bed\\_reactor&oldid=720057694](https://en.wikipedia.org/w/index.php?title=Pebble-bed_reactor&oldid=720057694) (visited on 05/22/2016).
- [69] *AVR Reactor*. In: *Wikipedia, the Free Encyclopedia*. Page Version ID: 720842017. May 18, 2016. URL: [https://en.wikipedia.org/w/index.php?title=AVR\\_reactor&oldid=720842017](https://en.wikipedia.org/w/index.php?title=AVR_reactor&oldid=720842017) (visited on 05/22/2016).
- [70] *TRISO Coated Fuel Particle | CenERgy Group*. URL: <http://eddiehonorato.wordpress.com/tag/triso-coated-fuel-particle/> (visited on 04/03/2014).
- [71] B Reznik and K. J Hüttinger. "On the Terminology for Pyrolytic Carbon". In: *Carbon* 40.4 (Apr. 2002), pp. 621–624. ISSN: 0008-6223. DOI: 10.1016/S0008-6223(01)00282-2. URL: <http://www.sciencedirect.com/science/article/pii/S0008622301002822> (visited on 05/22/2016).
- [72] J. -M. Leyssale et al. "Structural Features of Pyrocarbon Atomistic Models Constructed from Transmission Electron Microscopy Images". In: *Carbon* 50.12 (Oct. 2012), pp. 4388–4400. ISSN: 0008-6223. DOI: 10.1016/j.carbon.2012.05.015. URL: <http://www.sciencedirect.com/science/article/pii/S0008622312004435> (visited on 05/22/2016).
- [73] J. P. Da Costa et al. "Investigating Carbon Materials Nanostructure Using Image Orientation Statistics". In: *Carbon* 84 (Apr. 2015), pp. 160–173. ISSN: 0008-6223. DOI: 10.1016/j.carbon.2014.11.048. URL: <http://www.sciencedirect.com/science/article/pii/S0008622314011348> (visited on 05/22/2016).
- [74] B. Farbos et al. "Nanoscale Structure and Texture of Highly Anisotropic Pyrocarbons Revisited with Transmission Electron Microscopy, Image Processing, Neutron Diffraction and Atomistic Modeling". In: *Carbon* 80 (Dec. 2014), pp. 472–489. ISSN: 0008-6223. DOI: 10.1016/j.carbon.2014.08.087. URL: <http://www.sciencedirect.com/science/article/pii/S0008622314008276> (visited on 05/22/2016).
- [75] T. D. Burchell. "4.10 - Radiation Effects in Graphite A2 - Konings, Rudy J.M." In: *Comprehensive Nuclear Materials*. Oxford: Elsevier, 2012, pp. 299–324. ISBN: 978-0-08-056033-5. URL: <http://www.sciencedirect.com/science/article/pii/B9780080560335000914> (visited on 05/23/2016).

## Bibliography

---

- [76] Florian Banhart. "Irradiation Effects in Carbon Nanostructures". In: *Reports on Progress in Physics* 62.8 (Aug. 1, 1999), pp. 1181–1221. ISSN: 0034-4885, 1361-6633. DOI: 10.1088/0034-4885/62/8/201. URL: <http://stacks.iop.org/0034-4885/62/i=8/a=201?key=crossref.59dc06970256651c592563e84070dc05> (visited on 05/29/2016).
- [77] R. H. Telling and M. I. Heggie. "Radiation Defects in Graphite". In: *Philosophical Magazine* 87.31 (Nov. 1, 2007), pp. 4797–4846. ISSN: 1478-6435. DOI: 10.1080/14786430701210023. URL: <http://dx.doi.org/10.1080/14786430701210023> (visited on 05/23/2016).
- [78] J. Eapen et al. "Early Damage Mechanisms in Nuclear Grade Graphite under Irradiation". In: *Materials Research Letters* 2.1 (Jan. 2, 2014), pp. 43–50. ISSN: null. DOI: 10.1080/21663831.2013.841782. URL: <http://dx.doi.org/10.1080/21663831.2013.841782> (visited on 05/23/2016).
- [79] J. Koike and D.F. Pedraza. "Dimensional Changes in Highly Oriented Pyrolytic Graphite due to Electron-Irradiation". In: *Journal of Materials Research* 9 (07 July 1994), pp. 1899–1907. ISSN: 0884-2914, 2044-5326. DOI: 10.1557/JMR.1994.1899. URL: [http://www.journals.cambridge.org/abstract\\_S0884291400074707](http://www.journals.cambridge.org/abstract_S0884291400074707) (visited on 05/29/2016).
- [80] Keisuke Niwase. "Irradiation-Induced Amorphization of Graphite: A Dislocation Accumulation Model". In: *Philosophical Magazine Letters* 82.7 (July 1, 2002), pp. 401–408. ISSN: 0950-0839. DOI: 10.1080/09500830210137416. URL: <http://dx.doi.org/10.1080/09500830210137416> (visited on 05/23/2016).
- [81] Alain Chartier et al. "Atomic Scale Mechanisms for the Amorphisation of Irradiated Graphite". In: *Carbon* 91 (Sept. 2015), pp. 395–407. ISSN: 0008-6223. DOI: 10.1016/j.carbon.2015.05.003. URL: <http://www.sciencedirect.com/science/article/pii/S0008622315003991> (visited on 05/22/2016).
- [82] Rob H. Telling et al. "Wigner Defects Bridge the Graphite Gap". In: *Nature Materials* 2.5 (May 2003), pp. 333–337. ISSN: 1476-1122. DOI: 10.1038/nmat876. URL: <http://www.nature.com/nmat/journal/v2/n5/full/nmat876.html> (visited on 03/31/2016).
- [83] IAEA. *Characterization, Treatment and Conditioning of Radioactive Graphite from Decommissioning of Nuclear Reactors*. TECDOC 1521. International Atomic Energy Agency, 2006. URL: <http://www-pub.iaea.org/books/IAEABooks/7579/Characterization-Treatment-and-Conditioning-of-Radioactive-Graphite-from-Decommissioning-of-Nuclear-Reactors> (visited on 05/29/2016).
- [84] J. A. Auxier. "Windscale Fire". In: (1986). URL: [http://inis.iaea.org/Search/search.aspx?orig\\_q=RN:20011557](http://inis.iaea.org/Search/search.aspx?orig_q=RN:20011557) (visited on 05/29/2016).

- 
- [85] Manuel A. Pouchon et al. "Ceramics Composites for next Generation Nuclear Reactors". In: (). URL: [http://inis.iaea.org/Search/search.aspx?orig\\_q=RN:43102527](http://inis.iaea.org/Search/search.aspx?orig_q=RN:43102527) (visited on 04/05/2016).
- [86] *Our Company*. URL: <http://www.snecma.com/our-company> (visited on 05/22/2016).
- [87] *NRG: Home*. URL: <https://www.nrg.eu/?L=1> (visited on 05/22/2016).
- [88] J. B. J. Hegeman et al. "Mechanical and Thermal Properties of SiCf/SiC Composites Irradiated with Neutrons at High Temperatures". In: *Fusion Engineering and Design*. Proceedings of the 23rd Symposium of Fusion TechnologySOFT 23 75–79 (Nov. 2005), pp. 789–793. ISSN: 0920-3796. DOI: 10.1016/j.fusengdes.2005.06.307. URL: <http://www.sciencedirect.com/science/article/pii/S0920379605001304> (visited on 05/22/2016).
- [89] *The High Flux Reactor (HFR) at Petten*. URL: <http://www.emtr.eu/hfr.html> (visited on 04/02/2014).
- [90] D.J. Ketema and J.K. Aaldijk. *NRG Report K5079/04.63580/I: SICCROWD Neutron Metrology in the HFR*. 2004.
- [91] *Linear Variable Differential Transformer*. In: *Wikipedia, the Free Encyclopedia*. Page Version ID: 714427157. Apr. 9, 2016. URL: [https://en.wikipedia.org/w/index.php?title=Linear\\_variable\\_differential\\_transformer&oldid=714427157](https://en.wikipedia.org/w/index.php?title=Linear_variable_differential_transformer&oldid=714427157) (visited on 05/22/2016).
- [92] *Jannus*. URL: <http://jannus.in2p3.fr/spip.php> (visited on 04/02/2014).
- [93] *MIT Nuclear Reactor Laboratory: Reactor*. URL: <http://web.mit.edu/nrl/www/reactor/reactor.htm> (visited on 04/02/2014).
- [94] *Gamma Engineering, Inc.* URL: <http://www.gammaeng.com/> (visited on 05/22/2016).
- [95] "Improved Multilayer Tube Made from Ceramic-Matrix Composite Material, the Resulting Nuclear Fuel Cladding and Associated Production Methods". WO/2013/017621. Maxime Zabiego et al. Feb. 8, 2013. URL: <http://patentscope.wipo.int/search/en/WO2013017621> (visited on 04/03/2014).
- [96] M. Knoll and E. Ruska. "Das Elektronenmikroskop". In: *Zeitschrift für Physik* 78 (5-6), pp. 318–339. ISSN: 0044-3328. DOI: 10.1007/BF01342199. URL: <http://link.springer.com/article/10.1007/BF01342199> (visited on 02/29/2016).
- [97] D. McMullan. "Scanning Electron Microscopy 1928–1965". In: *Scanning* 17.3 (May 1, 1995), pp. 175–185. ISSN: 1932-8745. DOI: 10.1002/sca.4950170309. URL: <http://onlinelibrary.wiley.com/doi/10.1002/sca.4950170309/abstract> (visited on 02/29/2016).

## Bibliography

---

- [98] Lord Rayleigh F.R.S. “XXXI. Investigations in Optics, with Special Reference to the Spectroscope”. In: *The London, Edinburgh, and Dublin Philosophical Magazine and Journal of Science* (May 13, 2009). DOI: 10.1080/14786447908639684. URL: <http://www.tandfonline.com/doi/abs/10.1080/14786447908639684> (visited on 02/29/2016).
- [99] David B. Williams and C. Barry Carter. *Transmission Electron Microscopy*. Boston, MA: Springer US, 2009. ISBN: 978-0-387-76500-6 978-0-387-76501-3. URL: <http://link.springer.com/10.1007/978-0-387-76501-3> (visited on 07/10/2016).
- [100] R. F. Egerton. “Electron Energy-Loss Spectroscopy in the TEM”. In: *Reports on Progress in Physics* 72.1 (2009), p. 016502. ISSN: 0034-4885. DOI: 10.1088/0034-4885/72/1/016502. URL: <http://stacks.iop.org/0034-4885/72/i=1/a=016502> (visited on 02/25/2016).
- [101] Richard A. Ferrell and John J. Quinn. “Characteristic Energy Loss of Electrons Passing Through Metal Foils: Momentum-Exciton Model of Plasma Oscillations”. In: *Physical Review* 108.3 (Nov. 1, 1957), p. 570. DOI: 10.1103/PhysRev.108.570. URL: <http://journals.aps.org/pr/abstract/10.1103/PhysRev.108.570> (visited on 03/07/2016).
- [102] C. Hébert et al. “ELNES at Magic Angle Conditions”. In: *Ultramicroscopy*. Proceedings of the International Workshop on Enhanced Data Generated by Electrons Proceedings of the International Workshop on Enhanced Data Generated by Electrons 106 (11–12 Oct. 2006), pp. 1139–1143. ISSN: 0304-3991. DOI: 10.1016/j.ultramic.2006.04.030. URL: <http://www.sciencedirect.com/science/article/pii/S030439910600115X> (visited on 03/02/2016).
- [103] P. Schattschneider et al. “Anisotropic Relativistic Cross Sections for Inelastic Electron Scattering, and the Magic Angle”. In: *Physical Review B* 72.4 (July 26, 2005), p. 045142. DOI: 10.1103/PhysRevB.72.045142. URL: <http://link.aps.org/doi/10.1103/PhysRevB.72.045142> (visited on 03/14/2016).
- [104] C. Jeanguillaume and C. Colliex. “Spectrum-Image: The next Step in EELS Digital Acquisition and Processing”. In: *Ultramicroscopy* 28 (1–4 Apr. 1, 1989), pp. 252–257. ISSN: 0304-3991. DOI: 10.1016/0304-3991(89)90304-5. URL: <http://www.sciencedirect.com/science/article/pii/0304399189903045> (visited on 02/23/2016).
- [105] R. F. Egerton and S. C. Cheng. “Measurement of Local Thickness by Electron Energy-Loss Spectroscopy”. In: *Ultramicroscopy* 21.3 (1987), pp. 231–244. ISSN: 0304-3991. DOI: 10.1016/0304-3991(87)90148-3. URL: <http://www.sciencedirect.com/science/article/pii/0304399187901483> (visited on 03/29/2016).



- [106] Friedrich Lenz. “Zur Streuung mittelschneller Elektronen in kleinste Winkel”. In: *Zeitschrift für Naturforschung* 9 (a 1954), pp. 185–204. URL: [http://zfn.mpdl.mpg.de/data/Reihe\\_A/9/ZNA-1954-9a-0185.pdf](http://zfn.mpdl.mpg.de/data/Reihe_A/9/ZNA-1954-9a-0185.pdf) (visited on 03/30/2016).
- [107] Raymond Castaing and Lucien Henry. *OPTIQUE ÉLECTRONIQUE. – Filtrage magnétique des vitesses en Microscopie électronique*. Issue 255. July 1962, pp. 76–78. URL: <http://gallica.bnf.fr/ark:/12148/bpt6k32077> (visited on 02/23/2016).
- [108] Erik Essers et al. “Energy Resolution of an Omega-Type Monochromator and Imaging Properties of the MANDOLINE Filter”. In: *Ultramicroscopy*. PROCEEDINGS OF THE INTERNATIONAL WORKSHOP ON ENHANCED DATA GENERATED BY ELECTRONS 110.8 (July 2010), pp. 971–980. ISSN: 0304-3991. DOI: 10.1016/j.ultramic.2010.02.009. URL: <http://www.sciencedirect.com/science/article/pii/S0304399110000367> (visited on 02/25/2016).
- [109] Rolf Erni. “EFTEM & EELS”. Power Point presentation. EMPA, Nov. 28, 2013.
- [110] Ondrej L. Krivanek et al. “Design and First Applications of a Post-Column Imaging Filter”. In: *Microscopy Microanalysis Microstructures* 3 (2-3 Apr. 1, 1992), pp. 187–199. ISSN: 1154-2799. DOI: 10.1051/mmm:0199200302-3018700. URL: <http://dx.doi.org/10.1051/mmm:0199200302-3018700> (visited on 02/23/2016).
- [111] *Electronic Orbitals*. Oct. 2, 2013. URL: [http://chemwiki.ucdavis.edu/Core/Physical\\_Chemistry/Quantum\\_Mechanics/09.\\_The\\_Hydrogen\\_Atom/Atomic\\_Theory/Electrons\\_in\\_Atoms/Electronic\\_Orbitals](http://chemwiki.ucdavis.edu/Core/Physical_Chemistry/Quantum_Mechanics/09._The_Hydrogen_Atom/Atomic_Theory/Electrons_in_Atoms/Electronic_Orbitals) (visited on 07/02/2016).
- [112] *Media Portfolio*. URL: [http://wps.prenhall.com/wps/media/objects/340/348272/wade\\_ch02.html](http://wps.prenhall.com/wps/media/objects/340/348272/wade_ch02.html) (visited on 07/11/2016).
- [113] R. F. Egerton and M. J. Whelan. “Electron Energy Loss Spectra of Diamond, Graphite and Amorphous Carbon”. In: *Journal of Electron Spectroscopy and Related Phenomena* 3.3 (1974), pp. 232–236. ISSN: 0368-2048. DOI: 10.1016/0368-2048(74)80015-0. URL: <http://www.sciencedirect.com/science/article/pii/0368204874800150> (visited on 10/02/2015).
- [114] J. Bruley et al. “Quantitative near-Edge Structure Analysis of Diamond-like Carbon in the Electron Microscope Using a Two-Window Method”. In: *Journal of Microscopy* 180.1 (Oct. 1, 1995), pp. 22–32. ISSN: 1365-2818. DOI: 10.1111/j.1365-2818.1995.tb03653.x. URL: <http://onlinelibrary.wiley.com/doi/10.1111/j.1365-2818.1995.tb03653.x/abstract> (visited on 12/21/2015).

## Bibliography

---

- [115] Jerome J. Cuomo et al. "Sputter Deposition of Dense Diamond-like Carbon Films at Low Temperature". In: *Applied Physics Letters* 58.5 (Feb. 4, 1991), pp. 466–468. ISSN: 0003-6951, 1077-3118. DOI: 10.1063/1.104609. URL: <http://scitation.aip.org/content/aip/journal/apl/58/5/10.1063/1.104609> (visited on 12/21/2015).
- [116] A. J. Papworth et al. "Electron-Energy-Loss Spectroscopy Characterization of the sp<sup>2</sup> Bonding Fraction within Carbon Thin Films". In: *Physical Review B* 62.19 (Nov. 15, 2000), pp. 12628–12631. DOI: 10.1103/PhysRevB.62.12628. URL: <http://link.aps.org/doi/10.1103/PhysRevB.62.12628> (visited on 08/21/2014).
- [117] Zhi-li Zhang et al. "Investigating the Structure of Non-Graphitising Carbons Using Electron Energy Loss Spectroscopy in the Transmission Electron Microscope". In: *Carbon* 49.15 (Dec. 2011), pp. 5049–5063. ISSN: 0008-6223. DOI: 10.1016/j.carbon.2011.07.023. URL: <http://www.sciencedirect.com/science/article/pii/S0008622311005847> (visited on 10/02/2015).
- [118] B. E. Mironov et al. "Electron Irradiation of Nuclear Graphite Studied by Transmission Electron Microscopy and Electron Energy Loss Spectroscopy". In: *Carbon* 83 (Mar. 2015), pp. 106–117. ISSN: 0008-6223. DOI: 10.1016/j.carbon.2014.11.019. URL: <http://www.sciencedirect.com/science/article/pii/S0008622314010914> (visited on 01/13/2015).
- [119] N. Bernier et al. "A Methodology to Optimize the Quantification of sp<sup>2</sup> Carbon Fraction from K Edge EELS Spectra". In: *Journal of Electron Spectroscopy and Related Phenomena* 164 (1–3 July 2008), pp. 34–43. ISSN: 0368-2048. DOI: 10.1016/j.elspec.2008.04.006. URL: <http://www.sciencedirect.com/science/article/pii/S0368204808000285> (visited on 11/06/2015).
- [120] J. T. Titantah and D. Lamoen. "Technique for the  $s_{p^2}^{p^3}$  Characterization of Carbon Materials: *Ab Initio* Calculation of near-Edge Structure in Electron-Energy-Loss Spectra". In: *Physical Review B* 70.7 (Aug. 31, 2004), p. 075115. DOI: 10.1103/PhysRevB.70.075115. URL: <http://link.aps.org/doi/10.1103/PhysRevB.70.075115> (visited on 12/21/2015).
- [121] Masashi Watanabe and Frances I. Allen. "The SmartEFTEM-SI Method: Development of a New Spectrum-Imaging Acquisition Scheme for Quantitative Mapping by Energy-Filtering Transmission Electron Microscopy". In: *Ultramicroscopy* 113 (Feb. 2012), pp. 106–119. ISSN: 0304-3991. DOI: 10.1016/j.ultramic.2011.10.014. URL: <http://www.sciencedirect.com/science/article/pii/S0304399111002592> (visited on 06/11/2016).



- 
- [122] R.F. Egerton. *Electron Energy-Loss Spectroscopy in the Electron Microscope*. Boston, MA: Springer US, 2011. ISBN: 978-1-4419-9582-7 978-1-4419-9583-4. URL: <http://link.springer.com/10.1007/978-1-4419-9583-4> (visited on 02/26/2016).
- [123] E. Cottureau et al. “ARAMIS: An Ambidextrous 2 MV Accelerator for IBA and MeV Implantation”. In: *Nuclear Instruments and Methods in Physics Research Section B: Beam Interactions with Materials and Atoms* 45 (1–4 Jan. 2, 1990), pp. 293–295. ISSN: 0168-583X. DOI: 10.1016/0168-583X(90)90838-L. URL: <http://www.sciencedirect.com/science/article/pii/0168583X9090838L> (visited on 10/20/2015).
- [124] Jacques Chaumont et al. “A Medium Energy Facility for Variable Temperature Implantation and Analysis”. In: *Nuclear Instruments and Methods in Physics Research* 189.1 (Oct. 1, 1981), pp. 193–198. ISSN: 0167-5087. DOI: 10.1016/0029-554X(81)90145-2. URL: <http://www.sciencedirect.com/science/article/pii/0029554X81901452> (visited on 10/20/2015).
- [125] Bernhard Schaffer, Werner Grogger, and Gerald Kothleitner. “Automated Spatial Drift Correction for EFTEM Image Series”. In: *Ultramicroscopy* 102.1 (Dec. 2004), pp. 27–36. ISSN: 0304-3991. DOI: 10.1016/j.ultramic.2004.08.003. URL: <http://www.sciencedirect.com/science/article/pii/S0304399104001652> (visited on 11/06/2015).
- [126] G. Lucas et al. “Multivariate Statistical Analysis as a Tool for the Segmentation of 3D Spectral Data”. In: *Micron* 52–53 (Sept. 2013), pp. 49–56. ISSN: 0968-4328. DOI: 10.1016/j.micron.2013.08.005. URL: <http://www.sciencedirect.com/science/article/pii/S0968432813001261> (visited on 01/15/2015).
- [127] *Multivariate Statistical Analysis of Spectrum Images | LSME*. URL: <http://lsme.epfl.ch/msa> (visited on 06/12/2016).
- [128] Johannes Schindelin et al. “Fiji: An Open-Source Platform for Biological-Image Analysis”. In: *Nature Methods* 9.7 (June 28, 2012), pp. 676–682. ISSN: 1548-7091, 1548-7105. DOI: 10.1038/nmeth.2019. URL: <http://www.nature.com/doifinder/10.1038/nmeth.2019> (visited on 06/11/2016).
- [129] W. J. Parker et al. “Flash Method of Determining Thermal Diffusivity, Heat Capacity, and Thermal Conductivity”. In: *Journal of Applied Physics* 32.9 (Sept. 1, 1961), pp. 1679–1684. ISSN: 0021-8979, 1089-7550. DOI: 10.1063/1.1728417. URL: <http://scitation.aip.org/content/aip/journal/jap/32/9/10.1063/1.1728417> (visited on 01/12/2016).

## Bibliography

---

- [130] M. Reading, A. Luget, and R. Wilson. “Modulated Differential Scanning Calorimetry”. In: *Thermochimica Acta* 238 (June 1994), pp. 295–307. ISSN: 00406031. DOI: 10.1016/S0040-6031(94)85215-4. URL: <http://linkinghub.elsevier.com/retrieve/pii/S0040603194852154> (visited on 06/25/2016).
- [131] Horst Czichos, Tetsuya Saito, and Leslie Smith, eds. *Springer Handbook of Materials Measurement Methods*. Berlin, Heidelberg: Springer Berlin Heidelberg, 2006. ISBN: 978-3-540-20785-6 978-3-540-30300-8. URL: <http://link.springer.com/10.1007/978-3-540-30300-8> (visited on 01/12/2016).
- [132] Jack P. Holman. *Heat Transfer 10th Edition*. 10th. McGraw-Hill Publishing Company, 2012. ISBN: 978-0-07-352936-3. URL: <http://www.textbooks.com/Heat-Transfer-10th-Edition/9780073529363/Jack-P-Holman.php> (visited on 10/27/2016).
- [133] Elmer. *Elmerfem.org*. URL: <http://elmerfem.org/> (visited on 01/19/2016).
- [134] B. Gebhart. “Surface Temperature Calculations in Radiant Surroundings of Arbitrary Complexity for Gray, Diffuse Radiation”. In: *International Journal of Heat and Mass Transfer* 3.4 (Dec. 1961), pp. 341–346. ISSN: 0017-9310. DOI: 10.1016/0017-9310(61)90048-5. URL: <http://www.sciencedirect.com/science/article/pii/0017931061900485> (visited on 01/12/2016).
- [135] John R. Howell, M. Pinar Mengüç, and Robert Siegel. *Thermal Radiation Heat Transfer, 6th Edition - CRC Press Book*. 6th edition. CRC Press, 2015. ISBN: 978-1-4665-9326-8. URL: <https://www.crcpress.com/Thermal-Radiation-Heat-Transfer-6th-Edition/Howell-Menguc-Siegel/9781466593268> (visited on 01/12/2016).
- [136] S. N. REA. “Rapid Method for Determining Concentric Cylinder Radiation View Factors”. In: *AIAA Journal* 13.8 (1975), pp. 1122–1123. ISSN: 0001-1452. DOI: 10.2514/3.6964. URL: <http://dx.doi.org/10.2514/3.6964> (visited on 11/24/2015).
- [137] H Leuenberger and R. A Person. *Compilation of Radiation Shape Factors for Cylindrical Assemblies*. New York: American Society of Mechanical Engineers, 1956.
- [138] D. C. Hamilton and W. Morgan. *Radiant-Interchange Configuration Factors*. In collab. with NASA. 1952. URL: [http://archive.org/details/nasa\\_techdoc\\_19930083529](http://archive.org/details/nasa_techdoc_19930083529) (visited on 11/24/2015).
- [139] H. Brockmann. “Analytic Angle Factors for the Radiant Interchange among the Surface Elements of Two Concentric Cylinders”. In: *International Journal of Heat and Mass Transfer* 37.7 (May 1994), pp. 1095–1100. ISSN: 0017-9310. DOI: 10.1016/0017-9310(94)90195-3. URL: <http://www.sciencedirect.com/science/article/pii/0017931094901953> (visited on 11/24/2015).

- 
- [140] P.L. Kapitza. *Collected Papers of P.L. Kapitza - ScienceDirect*. URL: <http://www.sciencedirect.com/science/book/9780080109732> (visited on 04/07/2016).
- [141] J. K. Farooqi and M. A. Sheikh. "Finite Element Modelling of Thermal Transport in Ceramic Matrix Composites". In: *Computational Materials Science* 37.3 (Sept. 2006), pp. 361–373. ISSN: 0927-0256. DOI: 10.1016/j.commatsci.2005.11.001. URL: <http://www.sciencedirect.com/science/article/pii/S0927025605003101> (visited on 04/03/2014).
- [142] R. Yamada et al. "Highly Thermal Conductive, Sintered SiC Fiber-Reinforced 3D-SiC/SiC Composites: Experiments and Finite-Element Analysis of the Thermal Diffusivity/Conductivity". In: *Journal of Nuclear Materials* 307–311, Part 2 (Dec. 2002), pp. 1215–1220. ISSN: 0022-3115. DOI: 10.1016/S0022-3115(02)00957-1. URL: <http://www.sciencedirect.com/science/article/pii/S0022311502009571> (visited on 04/03/2014).
- [143] Ba Nghiep Nguyen and Charles H. Henager Jr. "Fiber/Matrix Interfacial Thermal Conductance Effect on the Thermal Conductivity of SiC/SiC Composites". In: *Journal of Nuclear Materials* 440 (1–3 Sept. 2013), pp. 11–20. ISSN: 0022-3115. DOI: 10.1016/j.jnucmat.2013.04.031. URL: <http://www.sciencedirect.com/science/article/pii/S0022311513006314> (visited on 04/03/2014).
- [144] J. D. Eshelby. "The Determination of the Elastic Field of an Ellipsoidal Inclusion, and Related Problems". In: *Proceedings of the Royal Society of London. Series A, Mathematical and Physical Sciences* 241.1226 (Aug. 20, 1957), pp. 376–396. ISSN: 0080-4630. JSTOR: 100095.
- [145] T Mori and K Tanaka. "Average Stress in Matrix and Average Elastic Energy of Materials with Misfitting Inclusions". In: *Acta Metallurgica* 21.5 (May 1973), pp. 571–574. ISSN: 0001-6160. DOI: 10.1016/0001-6160(73)90064-3. URL: <http://www.sciencedirect.com/science/article/pii/0001616073900643> (visited on 04/03/2014).
- [146] Hatta Hiroshi and Taya Minoru. "Equivalent Inclusion Method for Steady State Heat Conduction in Composites". In: *International Journal of Engineering Science* 24.7 (1986), pp. 1159–1172. ISSN: 0020-7225. DOI: 10.1016/0020-7225(86)90011-X. URL: <http://www.sciencedirect.com/science/article/pii/002072258690011X> (visited on 04/03/2014).

## Bibliography

---

- [147] R. C. Progelhof, J. L. Throne, and R. R. Ruetsch. “Methods for Predicting the Thermal Conductivity of Composite Systems: A Review”. In: *Polymer Engineering & Science* 16.9 (Sept. 1, 1976), pp. 615–625. ISSN: 1548-2634. DOI: 10.1002/pen.760160905. URL: <http://onlinelibrary.wiley.com/doi/10.1002/pen.760160905/abstract> (visited on 04/03/2014).
- [148] G. E. Youngblood, D. J. Senor, and R. H. Jones. “Optimizing the Transverse Thermal Conductivity of 2D-SiCf/SiC Composites. I. Modeling”. In: *Journal of Nuclear Materials* 307–311, Part 2 (Dec. 2002), pp. 1112–1119. ISSN: 0022-3115. DOI: 10.1016/S0022-3115(02)00951-0. URL: <http://www.sciencedirect.com/science/article/pii/S0022311502009510> (visited on 04/03/2014).
- [149] G. E. Youngblood et al. “The Transverse Thermal Conductivity of 2D-SiCf/SiC Composites”. In: *Composites Science and Technology* 62.9 (July 2002), pp. 1127–1139. ISSN: 0266-3538. DOI: 10.1016/S0266-3538(02)00069-6. URL: <http://www.sciencedirect.com/science/article/pii/S0266353802000696> (visited on 04/03/2014).
- [150] D. P. H. Hasselman and Lloyd F. Johnson. “Effective Thermal Conductivity of Composites with Interfacial Thermal Barrier Resistance”. In: *Journal of Composite Materials* 21.6 (Jan. 6, 1987), pp. 508–515. ISSN: 0021-9983, 1530-793X. DOI: 10.1177/002199838702100602. URL: <http://jcm.sagepub.com/content/21/6/508> (visited on 04/03/2014).
- [151] A. J. Markworth. “The Transverse Thermal Conductivity of a Unidirectional Fibre Composite with Fibre-Matrix Debonding: A Calculation Based on Effective-Medium Theory”. In: *Journal of Materials Science Letters* 12.19 (Jan. 1, 1993), pp. 1487–1489. ISSN: 0261-8028, 1573-4811. DOI: 10.1007/BF00277073. URL: <http://link.springer.com/article/10.1007/BF00277073> (visited on 04/03/2014).
- [152] James Clerk Maxwell. *A Treatise on Electricity and Magnetism*. 1873. URL: <https://archive.org/details/electricandmagne01maxwrch> (visited on 07/13/2016).
- [153] David S. Smith et al. “Thermal Conductivity of Porous Materials”. In: *Journal of Materials Research* 28.17 (Sept. 2013), pp. 2260–2272. ISSN: 0884-2914, 2044-5326. DOI: 10.1557/jmr.2013.179. URL: [http://www.journals.cambridge.org/abstract\\_S0884291413001799](http://www.journals.cambridge.org/abstract_S0884291413001799) (visited on 07/13/2016).
- [154] Rolf Landauer. “The Electrical Resistance of Binary Metallic Mixtures”. In: *Journal of Applied Physics* 23.7 (1952), p. 779. ISSN: 00218979. DOI: 10.1063/1.1702301. URL: <http://scitation.aip.org/content/aip/journal/jap/23/7/10.1063/1.1702301> (visited on 07/13/2016).

- [155] A. C. Ferrari et al. "Density, sp<sup>3</sup> Fraction, and Cross-Sectional Structure of Amorphous Carbon Films Determined by X-Ray Reflectivity and Electron Energy-Loss Spectroscopy". In: *Physical Review B* 62.16 (Oct. 15, 2000), pp. 11089–11103. DOI: 10.1103/PhysRevB.62.11089. URL: <http://link.aps.org/doi/10.1103/PhysRevB.62.11089> (visited on 08/21/2014).
- [156] J.C. Lascovich, R. Giorgi, and S. Scaglione. "Evaluation of the sp<sup>2</sup>/sp<sup>3</sup> Ratio in Amorphous Carbon Structure by XPS and XAES". In: *Applied Surface Science* 47.1 (Jan. 1991), pp. 17–21. ISSN: 01694332. DOI: 10.1016/0169-4332(91)90098-5. URL: <http://linkinghub.elsevier.com/retrieve/pii/0169433291900985> (visited on 07/15/2016).
- [157] C. Y. Ho et al. *Thermal Conductivity and Thermal Diffusivity of Selected Carbon Steels, Chromium Steels, Nickel Steels, and Stainless Steels*. Springer US, 1978. ISBN: 978-1-4615-9085-9 978-1-4615-9083-5. URL: [http://link.springer.com/chapter/10.1007/978-1-4615-9083-5\\_11](http://link.springer.com/chapter/10.1007/978-1-4615-9083-5_11) (visited on 04/15/2016).
- [158] Yutai Katoh et al. "Thermophysical and Mechanical Properties of near-Stoichiometric Fiber CVI SiC/SiC Composites after Neutron Irradiation at Elevated Temperatures". In: *Journal of Nuclear Materials* 403 (1–3 Aug. 2010), pp. 48–61. ISSN: 0022-3115. DOI: 10.1016/j.jnucmat.2010.06.002. URL: <http://www.sciencedirect.com/science/article/pii/S0022311510002412> (visited on 11/28/2012).
- [159] P.S. Jeon et al. "Thermal Conductivity Measurement of Anisotropic Material Using Photothermal Deflection Method". In: *Thermochimica Acta* 477 (1-2 Oct. 2008), pp. 32–37. ISSN: 00406031. DOI: 10.1016/j.tca.2008.08.004. URL: <http://linkinghub.elsevier.com/retrieve/pii/S0040603108002347> (visited on 08/17/2016).
- [160] Robert L. McMasters and Ralph B. Dinwiddie. "Anisotropic Thermal Diffusivity Measurement Using the Flash Method". In: *Journal of Thermophysics and Heat Transfer* 28.3 (July 2014), pp. 518–523. ISSN: 0887-8722, 1533-6808. DOI: 10.2514/1.T4189. URL: <http://arc.aiaa.org/doi/10.2514/1.T4189> (visited on 07/12/2016).
- [161] Arthur L. Loeb. "Thermal Conductivity: VIII, A Theory of Thermal Conductivity of Porous Materials". In: *Journal of the American Ceramic Society* 37.2 (Feb. 1954), pp. 96–99. ISSN: 00027820. DOI: 10.1111/j.1551-2916.1954.tb20107.x. URL: <http://doi.wiley.com/10.1111/j.1551-2916.1954.tb20107.x> (visited on 07/13/2016).
- [162] D.R. Flynn. "Thermal Conductivity of Ceramics". In: *Mechanical and Thermal Properties of Ceramics: Proceedings*. Ed. by J. B. Wachtman et al. 1969, pp. 63–123.
- [163] W. J. Tropf and M. E. Thomas. "Infrared Refractive Index and Thermo-Optic Coefficient Measurement at APL". In: *Johns Hopkins APL Technical Digest* 19.3 (1998), pp. 293–298.

## Bibliography

---

- [164] A. M. Hofmeister et al. "OPTICAL CONSTANTS OF SILICON CARBIDE FOR ASTRO-PHYSICAL APPLICATIONS. II. EXTENDING OPTICAL FUNCTIONS FROM INFRARED TO ULTRAVIOLET USING SINGLE-CRYSTAL ABSORPTION SPECTRA". In: *The Astrophysical Journal* 696.2 (May 10, 2009), pp. 1502–1516. ISSN: 0004-637X, 1538-4357. DOI: 10.1088/0004-637X/696/2/1502. URL: <http://stacks.iop.org/0004-637X/696/i=2/a=1502?key=crossref.e44f5048e6c19851f5fa536b50a4ef0a> (visited on 06/23/2016).
- [165] *Théorie de Mie*. In: *Wikipédia*. Page Version ID: 127200147. June 19, 2016. URL: [https://fr.wikipedia.org/w/index.php?title=Th%C3%A9orie\\_de\\_Mie&oldid=127200147](https://fr.wikipedia.org/w/index.php?title=Th%C3%A9orie_de_Mie&oldid=127200147) (visited on 06/28/2016).
- [166] NRC. *Tier 2 Chapter 04 - Reactor - Section 4.0 Reactor - 4.1 Summary Description*. AREVA Design Control Document Rev. 5 ML13220A676. United States Nuclear Regulatory Commission, July 19, 2013, p. 11. URL: <http://www.nrc.gov/docs/ML1322/ML13220A676.pdf>.
- [167] Maciej Skrzypek and R. Laskowski. "Thermal-Hydraulic Calculations for a Fuel Assembly in a European Pressurized Reactor Using the RELAP5 Code". In: *Nukleonika* 60.3 (Jan. 1, 2015). ISSN: 0029-5922. DOI: 10.1515/nuka-2015-0110. URL: <http://www.degruyter.com/view/j/nuka.2015.60.issue-3/nuka-2015-0110/nuka-2015-0110.xml> (visited on 08/11/2016).
- [168] Rozhgar Othman. "Steady State and Transient Analysis of Heat Conduction Nuclear Fuel Elements". Master Thesis. Stockholm, Sweden: KTH - Royal Institute of Technology, 2004.
- [169] Hee Cheon No. "Chapter 3: Fuel Thermal Analysis". KAIST, 2013.
- [170] *Nusselt Number*. In: *Wikipedia, the Free Encyclopedia*. Page Version ID: 719312193. May 8, 2016. URL: [https://en.wikipedia.org/w/index.php?title=Nusselt\\_number&oldid=719312193](https://en.wikipedia.org/w/index.php?title=Nusselt_number&oldid=719312193) (visited on 08/11/2016).
- [171] *Hydraulic Diameter*. In: *Wikipedia, the Free Encyclopedia*. Page Version ID: 718186537. May 2, 2016. URL: [https://en.wikipedia.org/w/index.php?title=Hydraulic\\_diameter&oldid=718186537](https://en.wikipedia.org/w/index.php?title=Hydraulic_diameter&oldid=718186537) (visited on 08/11/2016).
- [172] Syeilendra Pramuditya. *Water Thermodynamic Properties (in Polynomials) at Pressure of 155 Bar (Typical PWR Operating Condition)*. 2013-01-23T07:26:57+00:00. URL: <https://syeilendrapramuditya.wordpress.com/2013/01/23/water-thermodynamic-properties-in-polynomials-at-pressure-of-155-bar-typical-pwr-operating-condition/> (visited on 08/11/2016).

- [173] IAEA. *Thermophysical Properties of Materials for Nuclear Engineering: A Tutorial and Collection of Data*. 2009. URL: <http://www-pub.iaea.org/books/IAEABooks/7965/Thermophysical-Properties-of-Materials-for-Nuclear-Engineering-A-Tutorial-and-Collection-of-Data> (visited on 08/11/2016).
- [174] Scott Huxtable et al. "Thermal Conductivity Imaging at Micrometre-Scale Resolution for Combinatorial Studies of Materials". In: *Nature Materials* 3.5 (May 2004), pp. 298–301. ISSN: 1476-1122, 1476-4660. DOI: 10.1038/nmat1114. URL: <http://www.nature.com/doifinder/10.1038/nmat1114> (visited on 09/04/2016).
- [175] David G. Cahill et al. "Nanoscale Thermal Transport". In: *Journal of Applied Physics* 93.2 (2003), p. 793. ISSN: 00218979. DOI: 10.1063/1.1524305. URL: <http://scitation.aip.org/content/aip/journal/jap/93/2/10.1063/1.1524305> (visited on 09/04/2016).
- [176] *MIAMI 2 - University of Huddersfield*. URL: <https://www.hud.ac.uk/research/researchcentres/emma/miamifacility/miami2/> (visited on 09/08/2016).

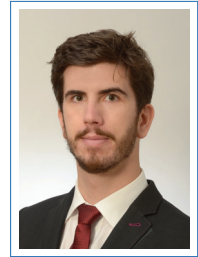




# Loïc Fave

- PhD in materials science and engineering
- thermal conductivity of ceramic matrix composites
- Experience in analytical TEM and STEM
- Experimental design and implementation
- Tutoring of students and interns

Baslerstrasse 60  
4600 Olten  
Switzerland  
☎ +41 78 605 01 71  
✉ loic.fave@alumni.epfl.ch  
Born August 3<sup>rd</sup>, 1987  
Swiss and French citizenships



## Education

- 2012–2016 **PhD in Materials Science & Engineering**, Paul Scherrer Institut, Villigen.  
Student at École Polytechnique Fédérale de Lausanne
- 2010–2012 **MSc in Nuclear Engineering**, EPFL, Lausanne, 5.54/6.  
EPFL and ETHZ joint program, track physics and materials, faculty of physics
- 2007–2010 **BSc in Materials Science & Engineering**, EPFL, Lausanne, 5.02/6.  
2009–2010: Exchange program at the Technical University (TU) of Berlin, Germany

## Academic projects and publications

- PhD thesis** **Investigation of the thermal conductivity of SiC/SiC cladding before and after irradiation**  
supervisors Prof. Cécile Hébert (EPFL) & MER M.A. Pouchon (PSI)  
description Study of irradiation effects in SiC/SiC composites interfaces using energy-filtered transmission electron microscopy (EFTEM) and electron spectroscopic imaging (STEM-EELS), development and implementation of a radial heat flow apparatus to measure the thermal conductivity of hollow cylindrical samples
- Master thesis** **Determination of helium implantation induced swelling in ODS steels**  
supervisors MER M.A. Pouchon (PSI) & Prof. Rakesh Chawla (EPFL)  
description Study of helium implantation induced swelling and hardening in ODS steels using white-light interferometry and nano-indentation
- Bachelor thesis** **Effect of hot-compaction under vacuum on the expansion of  $\text{AlSi}_7$ ,  $\text{AlSi}_6\text{Cu}_4$  and  $\text{AlSi}_8\text{Mg}_4$  foamable alloys**  
supervisors Dr. Catalina Jiménez & Prof. John Banhart (TU Berlin)  
description Determination of the foamability of Al-based alloys under different conditions using X-ray imaging

- Publications**
- L. Fave, M.A. Pouchon, C. Hébert, Journal of Thermal Analysis and Calorimetry, in review, 2016
  - L. Fave, M.A. Pouchon, ANS transactions vol.16, Proceedings of the 2016 HTR conference, Las Vegas, USA, publication en novembre 2016
  - L. Fave, M.A. Pouchon, ANS transactions vol.14, Proceedings of the 2016 ANS annual meeting, New Orleans, USA, May 2016
  - L. Fave, M.A. Pouchon *et al.*, Journal of Nuclear Materials 445 (1-3), 2013
  - L. Fave, M.A. Pouchon *et al.*, Proceedings of the European Nuclear Conference, 2013

## Skills

- Languages** **French**, Native proficiency, **English**, Full professional proficiency.  
**German**, Professional working proficiency, **Swiss-german**, Limited working proficiency.
- Computer** Gimp, Photoshop, Autodesk Inventor, AutoCAD, Digital Micrograph, ImageJ, programming in C and Matlab, L<sup>A</sup>T<sub>E</sub>X.

## Interests

- Teaching**
- Master Student's semester project mentoring in 2015
  - Summer intern at PSI in 2014
- Sports**
- Judo trainer, Vevey-Riviera Judo Club, in charge of a group of teenagers with focus on competition, head of the competition team in 2008
  - climbing, mountaineering, ski touring, judo, basketball
- Photography** Wild animals, landscapes, plants and flowers, wild orchids

